Vertical distribution of aerosols above the Atlantic Ocean, Punta Arenas (Chile), and Stellenbosch (South Africa).

Characterization, solar radiative effects and ice nucleating properties

vorgelegt von
Dipl.-Ing.
Thomas Kanitz
aus Berlin

von der Fakultät für III – Prozesswissenschaften
der Technischen Universität Berlin
zur Erlangung des akademischen Grades

Doktor der Ingenieurwissenschaften
- Dr.-Ing. -

genehmigte Dissertation

Promotionsausschuss:

Vorsitzender:	Prof. Dr. M. Finkbeiner
Berichter:	Prof. Dr. A. Macke
Berichter:	Prof. Dr. W. Rotard

Tag der wissenschaftlichen Aussprache: 24. September 2012

Berlin 2012
D 83

Zusammenfassung:

Im Rahmen der vorliegenden Arbeit wurden Lidarmessungen während dreier meridionaler Transatlantikfahrten des Forschungsschiffs Polarstern durchgeführt. Die Fahrten umfassten einen Zeitraum von insgesamt vier Monaten und eine Strecke von etwa 40000 km. Zusätzlich wurde das Lidar stationär für jeweils vier Monate in Punta Arenas (Chile) und Stellenbosch (Südafrika) betrieben.
Der entstandene Datensatz wurde hinsichtlich dreier Themen untersucht. Im ersten Thema wurden die bestimmten Aerosolprofile analysiert. So wurde reiner Saharastaub und Staub gemischt mit Biomasse–Verbrennungsaerosol an der Westküste Nordafrikas beobachtet. Erstmalig konnten Staubfahnen aus der patagonischen Wüste mit Lidar charakterisiert werden. Unerwarteterweise ergab sich die Möglichkeit, Vulkanascheschichten vom Ausbruch des Eyjafjallajökull zu untersuchen. Ein deutlicher Unterschied in der meridionalen Verteilung von Aerosolschichten in der freien Troposphäre wurde gefunden. Dabei wurden die höchsten optischen Dicken in den nördlichen Tropen bestimmt, die durch hohe Staubemissionen der Sahara zustande kommen. Die niedrigsten Aerosolkonzentrationen in der freien Troposphäre wurden in den südlichen mittleren Breiten gefunden. Während die abgehobenen Aerosolschichten in der freien Atmosphäre in Höhen von bis zu 5 km beobachtet wurden, betrug die mittlere Höhe der maritimen Grenzschicht etwa 0.4–0.9 km. Ihre optische Dicke betrug unabhängig vom Breitengrad rund 0.05. Die schiffsgebundenen Lidarmessungen wurden mit satellitengebundenen Messungen verglichen, wobei eine gute Übereinstimmung gefunden wurde.
Die vertikale Aerosolverteilung ist eine notwendige Information um den direkten Einfluss von Aerosolen auf den Strahlungshalt der Erde zu bestimmen. Im zweiten Teil wurden die Vertikalprofile und die mit Lidar ermittelten optischen Eigenschaften für Strahlungstranportrechnungen verwendet. Die Ergebnisse wurden mit Strahlungsmessungen am Boden und vom Satelliten verglichen. Die Übereinstimmung aller verfügbaren Messungen war hierbei an der Unterkante der Atmosphäre am besten. Eine meridionale Untersuchung hat gezeigt, dass der solare Aerosoleffekt der maritimen Grenzschicht unabhängig von der geographischen Breite ist. In der freien Troposphäre entspricht die Verteilung des solaren Strahlungseffekts von Aerosolen der meridionalen Verteilung der optischen Dicke und zeigt die stärksten Effekte in den nördlichen Tropen.
Aerosole üben ebenfalls einen indirekten Strahlungseffekt aus, da sie die mikrophysikalischen Eigenschaften von Wolken beeinflussen. Einer dieser Prozesse ist die heterogene Eisbildung in unterkühlten Wasserwolken. Mithilfe der Messungen in den südlichen mittleren Breiten (Punta Arenas, 53° S) und vorangegangenen Messungen in den nördlichen mittleren Breiten (Leipzig, 51° N) konnte erstmals der Aerosoleffekt unter verschiedenen Aerosolbedingungen, aber vergleichbaren meteorologischen Bedingungen im dritten Teil dieser Arbeit untersucht werden. Weniger als 20% und rund 70% der beobachteten Wolken mit Oberkantentemperaturen von −15 bis −20 °C zeigten Eisbildung über Punta Arenas bzw. Leipzig. Die starke Differenz zwischen den Beobachtungen wurde durch den Unterschied der Aerosol- und somit Eisnukleationskeimquellen in beiden Hemisphären erklärt.

Abstract:

In the framework of this thesis lidar measurements were performed aboard the research vessel Polarstern during three meridional transatlantic cruises. The shipborne measurements cover a period of four months and a distance of about 40000 km. In addition, the lidar was operated in Punta Arenas (Chile) and Stellenbosch (South Africa) each time for four month. The established data set offered the opportunity to work on three topics. Within the first topic the vertical distribution of aerosols was analyzed. Pure and mixed layers of Saharan dust were observed at the west coast of North Africa. For the first time, plumes of Patagonian desert dust were characterized with lidar. Unexpectedly, layers of volcanic ash from the Eyjafjallajökull eruption in 2010 could be investigated, too. A distinct difference in the meridional distribution of aerosol layers in the free troposphere was found. The highest optical thickness was determined in the northern tropics, which is related to the dust emissions of the Saharan desert. The lowest aerosol load in the free troposphere was found in the southern midlatitudes. While lofted layers were observed up to 5 km height in the free troposphere, the marine boundary layer extended up to about 0.4–0.9 km. The aerosol optical thickness of the boundary layer was about 0.05, independent of the latitude. In a comparative study the shipborne lidar measurements showed a good agreement to spaceborne lidar measurements. The information of the aerosol vertical distribution is a key parameter in modeling the direct effect of aerosols on the Earth's radiation budget. The vertical profiles of lidar–derived particle optical properties were used as input for radiative–transfer calculations in the framework of the second topic. The simulation results were compared to irradiance measurements at the surface and with satellite. The best agreement for all simulations was found for cloud–free conditions at the surface. A meridional analysis showed that the solar aerosol radiative effect is related to the corresponding meridional distribution of the aerosol optical thickness. While the solar aerosol radiative effect of the marine boundary layer was independent from the latitude, the effect of free–tropospheric aerosol was highest in the northern tropics.
Aerosols also indirectly influence the radiation budget by affecting cloud microphysics. One of these effects is the heterogeneous ice formation in supercooled water clouds. Within the third topic, for the first time, this aerosol effect was investigated under different aerosol conditions but comparable meteorological conditions by the use of observations in the southern midlatitudes (Punta Arenas, 53° S) and a previous study in the northern midlatitudes (Leipzig, 51° N). Less than 20% and around 70% of the cloud layers with cloud top temperatures from −15 to −20 °C showed ice formation over Punta Arenas and Leipzig, respectively. More than 90% of the cloud layers contained ice over Leipzig at temperatures from −25 to −30 °C, whereas this level was not reached at Punta Arenas before cloud top temperatures were below −35 °C. The strong contrast found in the cloud observations over Leipzig and Punta Arenas is obviously related to the rather different aerosol conditions at the polluted site in the northern hemisphere and the rather clean maritime site south of 50° S.

"Give way to science"
U. Pahl, Captain of RV Polarstern

Table of Contents

Chapter 1

Introduction

Aerosols, clouds, and aerosol–cloud interactions sensitively influence the radiation budget of the atmosphere, the water cycle, and thus the climate on Earth. This impact is especially sensitive over the oceans [*Stevens and Feingold*, 2009]. However, global atmospheric modeling is associated with high uncertainty, because of gaps in our knowledge regarding the horizontal and vertical abundance and variability of aerosols and clouds around the world. This situation motivated the OCEANET project [*Macke et al.*, 2010] whose goals and observation strategy are explained in Chapter 2.

In the framework of OCEANET unique lidar observations of aerosol and cloud layers were performed aboard the research vessel (RV) Polarstern in 2009 and 2010, and at two coastal measurement sites in the southern hemisphere, at Punta Arenas, Chile, from November 2009 to April 2010 and at Stellenbosch, South Africa, from December 2010 to May 2011. These measurements are presented and discussed in this work. Vertically–resolved observations in the southern hemisphere are rare [*Bösenberg and Hoff*, 2008] and of special interest for modelers. Furthermore, these observations can be contrasted with respective observations of aerosols and clouds in the northern hemisphere to better understand anthropogenic influences on climate, aerosol distributions, and cloud processes.

The work deals with three main topics:

(a) The vertical distribution of aerosols above the North and South Atlantic,
(b) Height–resolved radiative–transfer calculations using optical data from lidar,
(c) Contrasting the impact of aerosols at northern and southern midlatitudes on heterogeneous ice nucleation.

Topic (a) discussed in Chapter 5 includes the aerosol observations that were performed at the three before mentioned sites. Aerosols can occur in layers of pure marine origin or complex mixtures of marine aerosols and continental desert dust, biomass–burning aerosols, and anthropogenic aerosols (industry, domestic, traffic) [*Mattis et al.*, 2008]. Complex aerosol mixtures are often found in the free troposphere as well, where they can be transported over large distances [*Tesche et al.*, 2009]. At the beginning of Chapter 5, a review of previous investigations in this field is given.

The results concerning **topic (b)** are presented in Chapter 6. Radiative–transfer models usually use exponential aerosol height distributions [*Shettle and Fenn*, 1979] despite the known presence of lofted aerosol layers around the globe. Especially investigations of the radiative impact of aerosol layers above clouds showed the strong need of height–dependent calculations [*Haywood and Shine*, 1997; *Wagner et al.*, 2001]. Here, the radiative effect is determined for a selection of observed aerosol and cloud layers using lidar data. An introduction to this topic is given in Sec. 6.1.

Finally, in Chapter 7 the process of heterogeneous ice nucleation is introduced (**topic c**). Heterogeneous ice nucleation is not only a very important process considering precipitation. The thermodynamic state of a cloud (liquid, mixed–phase, pure ice) affects also the radiative impact of clouds [*Sun and Shine*, 1995; *Hogan et al.*, 2003; *Ehrlich et al.*, 2008]. The OCEANET lidar observations of heterogeneous ice nucleation are compared with previous findings of the Leibniz Institute for Tropospheric Research (IfT) at Leipzig (northern hemisphere) and Cape Verde (in the African outflow region). In this way, the influence of aerosols on the heterogeneous ice nucleation between the highly polluted northern hemisphere and the comparably clean southern hemisphere is contrasted.

After the general introduction of the OCEANET project in Chapter 2 the lidar technique is introduced in Chapter 3. Additionally used measurement instruments are presented in Chapter 4. Conclusions and an outlook are given in Chapter 8.

Chapter 2

OCEANET project

2.1 Motivation

Oceans cover about 70% of the Earth's surface. The exchange of energy and material between the ocean and the atmosphere is a key in understanding climate processes. The corresponding fluxes of radiation, heat, water vapor, and CO_2 are driven by the local composition of the upper ocean and the lower troposphere. Aerosols (directly and indirectly via cloud processes [*Lohmann and Feichter*, 2005]) strongly influence the surface radiation budget which in turn is the major part of the surface energy budget. The complex interaction between aerosols, clouds, and radiative fluxes is recognized as the largest source of uncertainties in understanding climate processes [*Forster et al.*, 2007].

According to the report of the Intergovernmental Panel on Climate Change (IPCC, [*Forster et al.*, 2007]) the increase of CO_2 from 1750 until 2005 produced with $1.66\,\mathrm{W\,m^{-2}}$ the largest anthropogenically induced change in the global radiative forcing. Compared to the uncertainty of about $20\,\mathrm{W\,m^{-2}}$ [*Macke et al.*, 2010] in cloud radiative forcing, this number of $1.66\,\mathrm{W\,m^{-2}}$ is small and demonstrates that trustworthy future climate predictions require an improved understanding of aerosol–cloud–radiation interactions.

Figure 2.1 shows a sketch of a feedback loop between biological, chemical, and physical processes above the upper ocean. Aerosols and clouds can disturb this loop. The incident radiation at the ocean surface decreases with increasing scattering and absorption of solar radiation by aerosols and clouds. As a consequence, the temperature and biological production of the upper ocean decrease and less CO_2 is released into the atmosphere. Reduced CO_2 concentration in the atmosphere and decreased evaporation of water–vapor because of lower sea surface temperature (SST) result in lower values of the water vapor

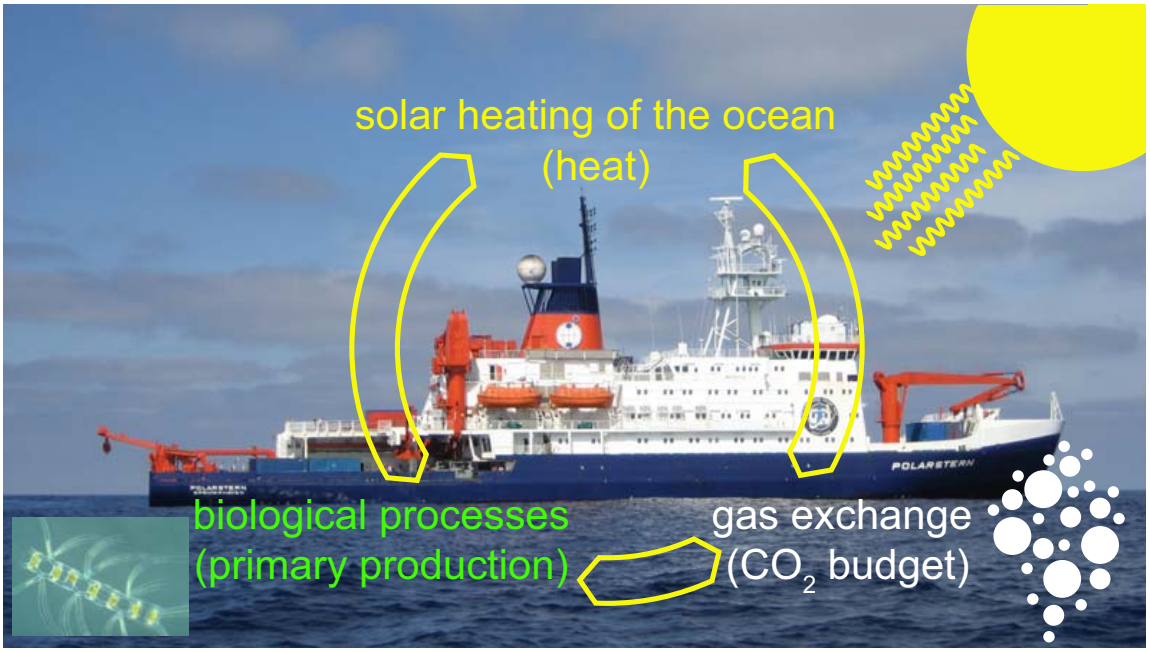

Figure 2.1: Feedback loop between the physical, chemical, and biological processes investigated by OCEANET. Photograph of a diatom from awi.de/LOHAFEX (left, bottom).

mixing ratios [*Minschwaner and Dessler*, 2004]. Thus, cloud formation may then be weakened, as well as the swelling of hygroscopic aerosols. This, in turn, would lead to an increase of downward radiative fluxes and an increase of SST. This is one example of a variety of complex feedback loops which have to be fully understood before a quantitative prediction of future climate conditions can be made.

Within the OCEANET project the first shipborne facility was developed that is able to investigate continuously the transfer of energy and material between ocean and atmosphere. The facility is based on the expertise of the Helmholtz Centre for Ocean Research Kiel (GEOMAR), IfT, the Helmholtz Centre Geesthacht, and the Alfred Wegener Institute (AWI), Bremerhaven. State–of–the art oceanic underway measurement systems observe the CO_2 and O_2 concentrations, type of plankton, temperature, salinity, nutrients, and turbidity to determine the state of the upper ocean [*Petersen et al.*, 2003; *Aßmann et al.*, 2011]. Continuous observations of aerosol, cloud, temperature, and humidity profiles, liquid–water path, incident solar and thermal radiation, sensible and latent heat are performed to determine the influence of the highly variable atmosphere on the radiative energy budget between ocean and atmosphere. Additional satellite observations by Meteosat Second Generation (MSG) are used to estimate the radiative energy budget at the top of atmosphere (TOA).

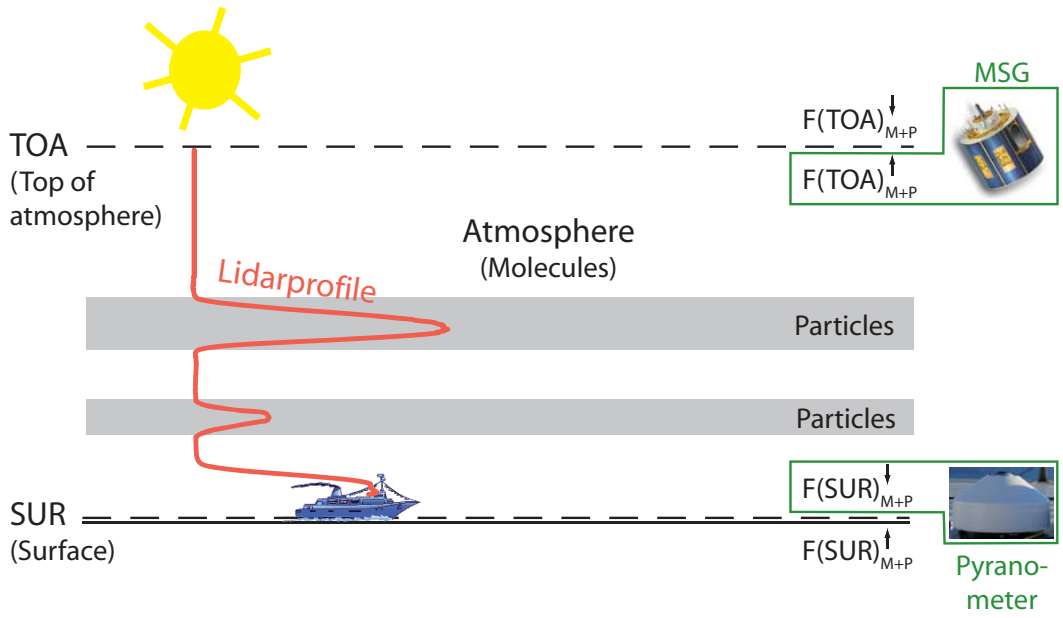

Figure 2.2: Sketch of the possible vertical distribution of aerosol particles in the atmosphere. TOA denotes the top of atmosphere, SUR the surface. Lidar observes single aerosol particle layers at different heights in the atmosphere. This information serves as input for radiative–transfer models. The incident solar radiation at SUR can be determined by a pyranometer, the outgoing solar radiation at TOA by Meteosat Second Generation (MSG).

The vertical profiling of aerosol and cloud layers is performed with the lidar Polly^{XT} (see Chapter 3). As shown in Fig. 2.2, a lidar is able to detect single lofted aerosol and cloud layers in the atmosphere and to resolve cloudy regions when clouds are embedded in aerosol layers. Current assessments of aerosol and cloud impacts on climate remain very uncertain [*Schulz et al.*, 2006] because the assessments rely largely on model simulations of aerosol distributions that differ, in terms of mass concentration ($\mu g\, m^{-3}$), by up to an order of magnitude between different models [*Lohmann et al.*, 2001; *Textor et al.*, 2006]. As shown by *Haywood and Shine* [1997], *Quijano et al.* [2000], and *Wagner et al.* [2001] rather different radiative effects occur depending on whether lofted aerosol layers are above the cloud–free ocean or above a cloud cover of boundary–layer cumuli over the ocean. The cloud–free ocean absorbs almost the entire incident solar radiation due to its low albedo ($\approx$0.05) [*Linke and Baur*, 1970]. In contrast, the albedo of a cloud can be >0.9 [*Liou and Ou*, 1989; *Albrecht*, 1989]. This albedo difference can lead to a change from a negative to a positive radiative impact of a lofted aerosol layer at TOA as reported by *Wagner et al.* [2001] for an Indian aerosol plume.

Above the Atlantic Ocean very different aerosol types are present. Figure 2.3 shows a map of several aerosol source regions and the expected transport direction (indicated by white arrows). Regarding the transport regime 1, *Müller et al.* [2005] observed smoke from Canadian forest fires that was advected across the Atlantic towards Europe. Anthropogenic emissions from North America were investigated during the TARFOX campaign [*Russell et al.*, 1999] at the Atlantic west coast (arrow 2). *Mattis et al.* [2008] showed that anthropogenic haze from North America frequently arrives over Europe in summer in agreement with *Ramanathan et al.* [2007]. European anthropogenic emissions can be advected across the Iberian peninsula to the Atlantic (arrow 3) [*Ansmann et al.*, 2001]. Dust as well as dust mixed with smoke was observed during the SAMUM campaign at Cape Verde at the west coast of Africa [*Ansmann et al.*, 2011a; *Tesche et al.*, 2011; *Groß et al.*, 2011b]. These dust and mixed dust layers are known to cross the entire Atlantic (indicated by arrows 4 and 5) and are detectable in the Caribbean and the Amazon basin [*Formenti et al.*, 2001; *Prospero et al.*, 2002; *Liu et al.*, 2008b; *Ansmann et al.*, 2009; *Baars et al.*, 2011]. Smoke emissions from the Amazon basin are transported to the southeast (arrow 6) [*Fishman et al.*, 1996; *Kaufman et al.*, 1998; *Reid et al.*, 2004]. The southern Atlantic is also influenced by smoke layers advected from southern Africa (arrow 7) [*Swap et al.*, 1996, 2003; *Yu et al.*, 2010; *Wilcox*, 2011]. The transport regime 9 indicates the most southern source of continental aerosols, the Patagonian desert. Patagonian dust was found in Antarctic ice cores and serves perhaps as iron source in the southern oceans [*Iriondo*, 2000; *Gaiero et al.*, 2003; *Gassó et al.*, 2010; *Johnson et al.*, 2011]. Above the entire Atlantic the boundary layer (the lowermost 300–900 m) is dominated by marine aerosol indicated by the white circle 8 [*Heintzenberg et al.*, 2000; *Smirnov et al.*, 2002; *O'Dowd and de Leeuw*, 2007; *Kiliyanpilakkil and Meskhidze*, 2011]. To cover these complex aerosol scenarios by observations, height–resolved measurements of the aerosol distributions are clearly needed.

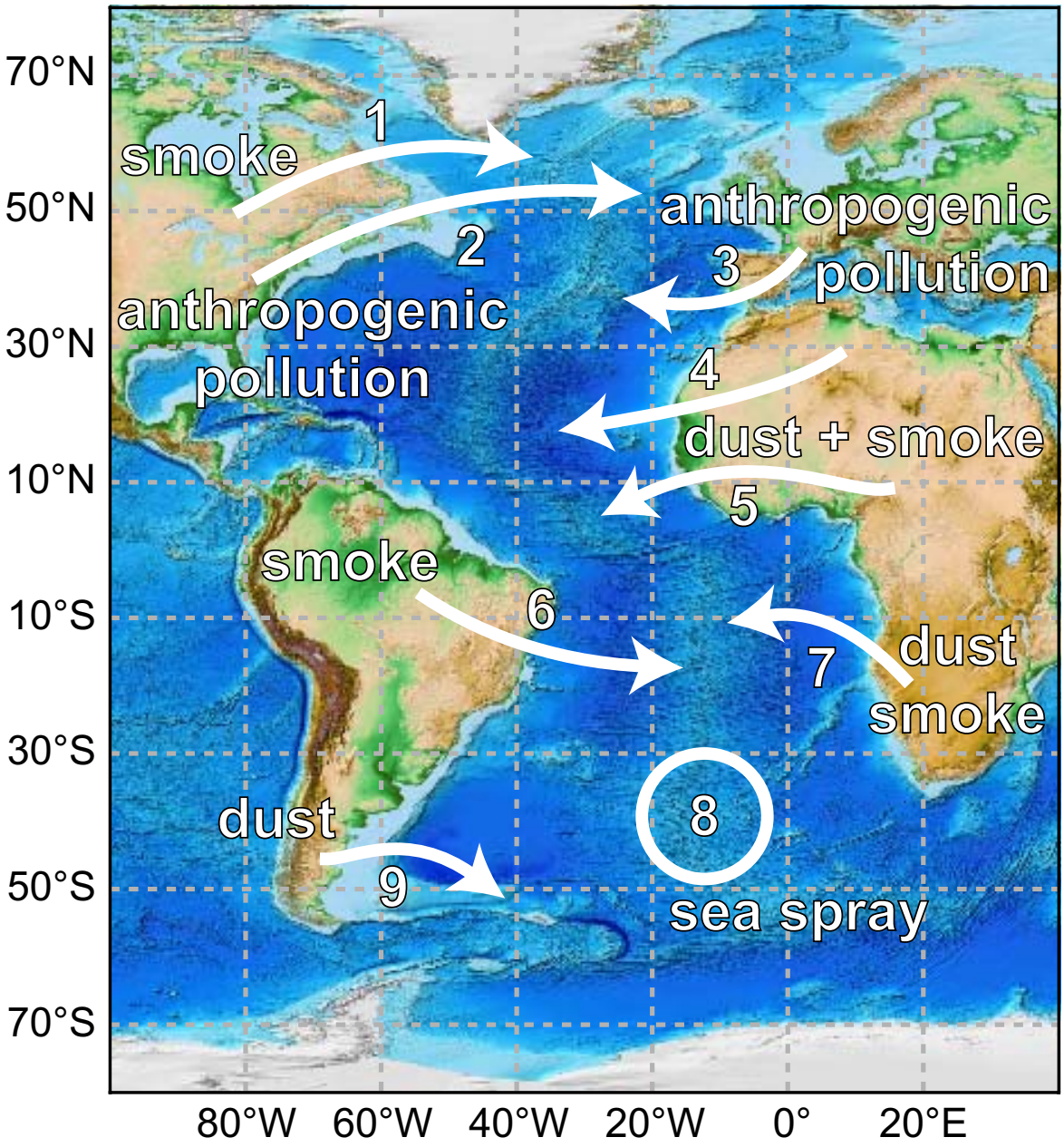

Figure 2.3: Overview of the long–range aerosol transport regimes above the North and South Atlantic. Arrows and numbers indicate the different regimes and aerosol types.

2.2 Instrumentation

The observations were performed (at the Atlantic) aboard the German research vessel Polarstern, which is mostly operating under summer polar conditions either in the Arctic or in the Antarctic. The resulting transfer routes between Germany and either South America or South Africa provide an excellent opportunity to perform atmospheric and oceanic observations under tropical, subtropical, and midlatitudinal conditions in both hemispheres. Thereby, Polarstern passes areas with a known high fraction of free–tropospheric aerosol that is transported over long ranges. During the Antarctic cruises of Polarstern the portable lidar was deployed at coastal sites in the southern hemisphere where, except from satellite observations, vertical aerosol profile information is almost not available [*Bösenberg and Hoff*, 2008]. The Polarstern cruises to the southern hemisphere thus provide an outstanding opportunity to investigate the southern–hemispheric aerosol conditions and to relate these to northern–hemispheric values. For such a comparison, a long–term data set of vertical aerosol profiling is available from measurements at Leipzig, Germany, performed in the framework of the European Aerosol Research LIdar NETwork (EARLINET) [*Bösenberg et al.*, 2003].

The OCEANET–Atmosphere facility was developed to cover the atmospheric observations aboard Polarstern. All measurement instruments are mounted on a 20–feet container shown in Fig. 2.4. Incident solar and thermal radiation are measured with a pyranometer (CMP21) and a pyrgeometer (CGR4), respectively, from Kipp & Zonen (box c in Fig. 2.4). They are part of the SCalable Automatic Weather Station (SCAWS) [*Kleta*, 2010], which was developed in cooperation with the German Weather Service (DWD). Due to the additional recording of temperature, relative humidity, and wind (box a in Fig. 2.4), OCEANET–Atmosphere became an official DWD station. Box d in Fig. 2.4 shows the instrumentation for turbulence and CO_2–flux measurements (METEK USA–1, LICOR 7500), which enables the determination of sensible and latent heat fluxes [*Bumke et al.*, 2002]. Every 15 s a skyimager (box e) takes a picture of the hemisphere above the platform to estimate cloud coverage and cloud type [*Kalisch*, 2011]. Liquid–water path is calculated from the measurements of the Humidity And Temperature PROfiler (HATPRO) [*Rose et al.*, 2005] for further cloud investigations (box f). Vertical aerosol and cloud profiling is performed with the multiwavelength Raman and polarization lidar Polly^{XT} (see Sec. 3). The lidar cabinet is mounted inside OCEANET–Atmosphere and measures through quartz plates in the roof of the container. The emitted visible green laser light can be seen in the nighttime photograph of the container in Fig. 2.4 (top). OCEANET–Atmosphere was deployed at the upperdeck, starboard of Polarstern in about 22 m asl (Fig. 2.4 bottom, right).

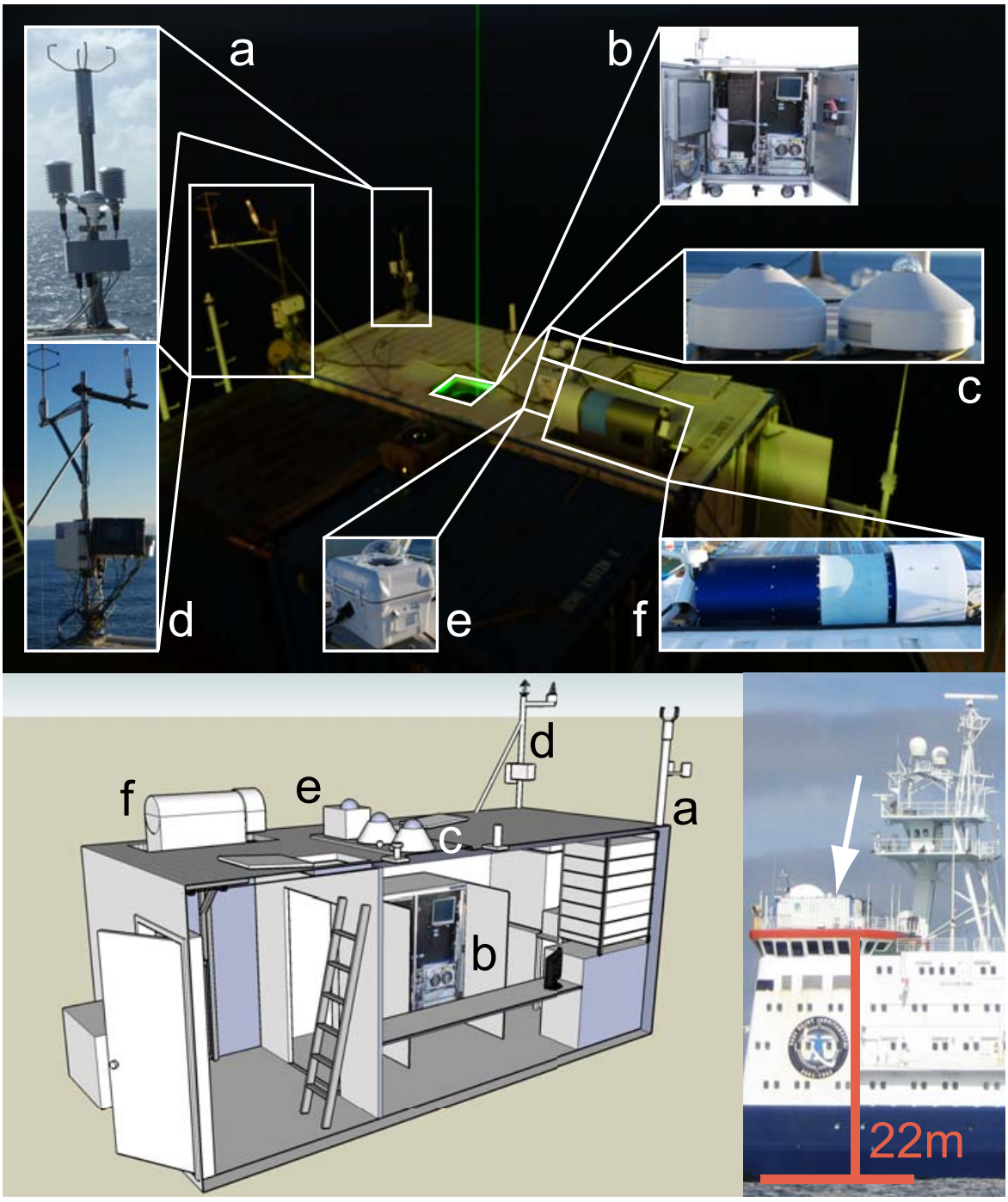

Figure 2.4: Top: Photograph of the OCEANET–Atmosphere facility during nighttime with the green beam of the lidar. Bottom: (left) sketch of the facility with (a) SCAWS temperature-humidity-wind, (b) Polly^{XT}, (c) pyranometer and pyrgeometer, (d) turbulence tower, (e) skyimager, and (f) HATPRO, (right) position of the facility at the upperdeck, starboard of Polarstern.

2.3 Polarstern cruises and southern–hemispheric stations

By the meridional transatlantic cruises of Polarstern from about 50° N to 50° S through different climatic regimes unique data on aerosols, clouds, and related radiative fluxes can be obtained. The performed cruises used in this work are shown in Fig. 2.5.

OCEANET–Atmosphere participated in a meridional cruise of Polarstern in fall 2009 for the first time. The cruise went from Bremerhaven, Germany (16 October 2009, ANT-XXVI/1) to Punta Arenas, Chile (25 November 2009). Polarstern went on to the Antarctica, while the lidar was unmounted from the container and deployed at Punta Arenas (see below). The lidar was remounted into OCEANET–Atmosphere at the pier of Punta Arenas (see Fig. 2.6 a) after the four–month measurement campaign at the University of Magallanes. Figure 2.6 shows impressions of the cruise from Punta Arenas (7 April 2010, ANT-XXVI/4) back to Bremerhaven. The container was lighted at the harbour of Bremerhaven in the

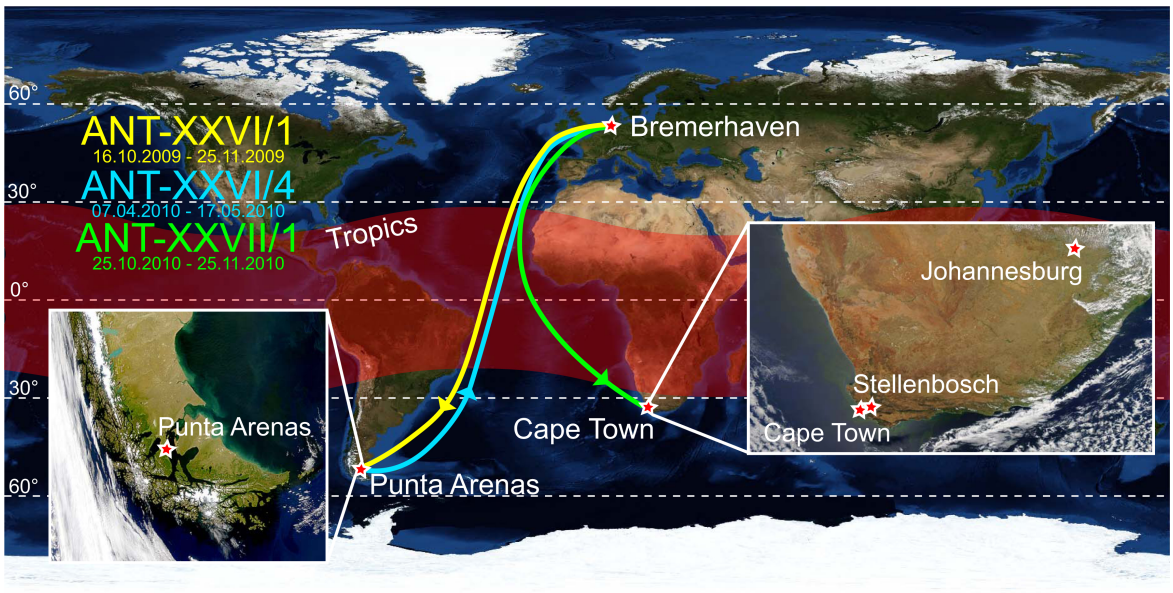

Figure 2.5: Map of the three meridional transatlantic cruises of Polarstern. The first cruise started at Bremerhaven and ended at Punta Arenas (yellow line, fall 2009, ANT-XXVI/1). The second was from Punta Arenas back to Bremerhaven (blue line, spring 2010, ANT-XXVI/4). For the third cruise Polarstern departed from Bremerhaven and arrived at Cape Town (green line, fall 2010, ANT-XXVII/1). The lidar field sites of Punta Arenas and Stellenbosch in the southern hemisphere are indicated by red stars.

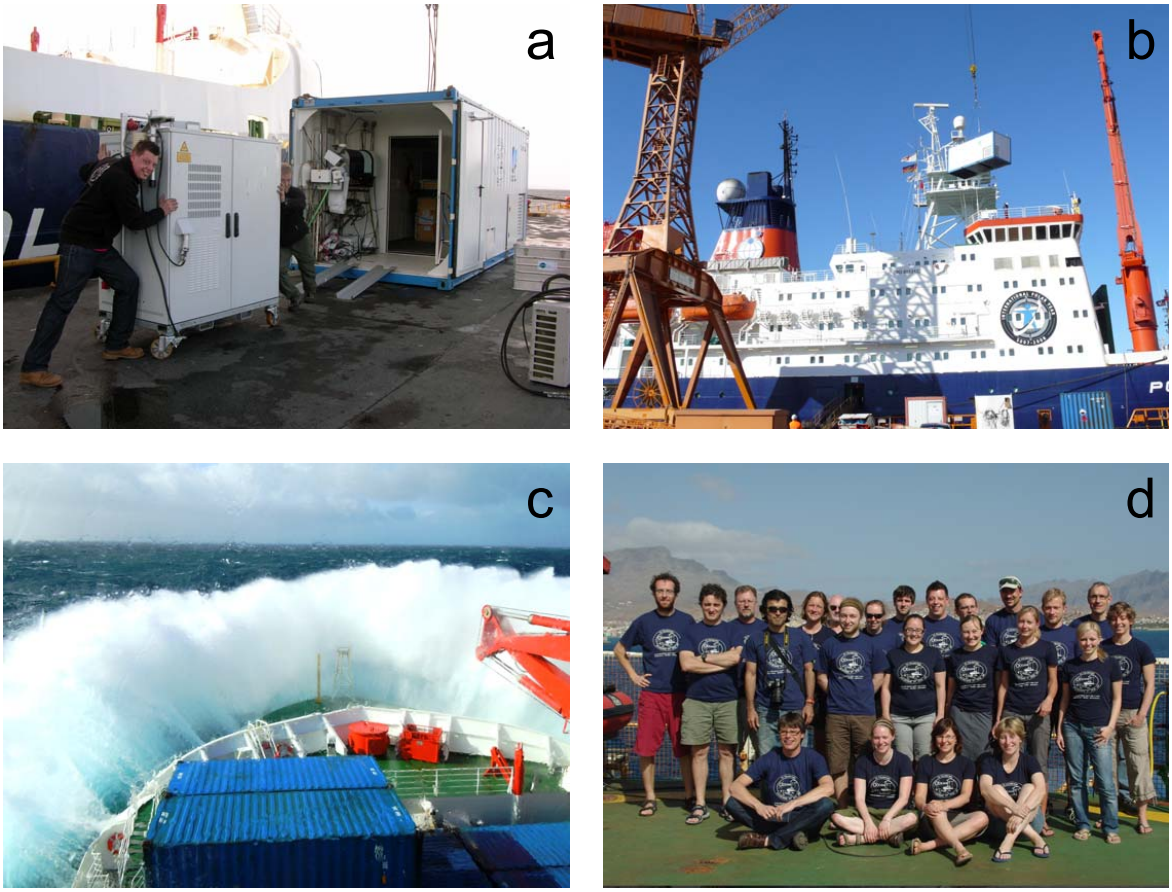

Figure 2.6: Impressions from the research vessel cruise April–May 2010. (a) Mounting the lidar at the pier of Punta Arenas on 7 April 2010. (b) Lightning of OCEANET–Atmosphere at Bremerhaven at the end of the cruise on 17 May 2010. (c) Heavy sea with up to 8 m groundswell and over 28 m s^{-1} wind speed producing sea spray and pitching of the ship during the travel from Punta Arenas towards Cape Verde. (d) The scientific crew from Cape Verde to Las Palmas, the chief scientist Arne Körtzinger (first row, left).

morning of the 17 May 2010 (Fig. 2.6 b). Figure 2.6 d shows the scientific crew of the cruise section from Cape Verde to Las Palmas. The third cruise started in Bremerhaven (25 October 2010, ANT-XXVII/1) towards Cape Town, South Africa (25 November 2010). Detailed information about the scientific work and meteorological conditions at the three transatlantic cruises are offered by the cruise reports of *el Naggar and Macke* [2010], *Körtzinger* [2011], and *Bumke* [2011].

Punta Arenas, Chile

The lidar was deployed at Punta Arenas (53° S, 71° W) in late November 2009, before Polarstern moved on to Antarctica for four month. During the **A**erosol **L**idar observations at **P**unta **A**renas in the framework of a **C**hilean Germ**a**n cooperation (**ALPACA**) campaign (4 December 2009 to 4 April 2010) the lidar site was at the University of Magallanes. Punta Arenas is situated directly at the Strait of the Magellanes (see map in Fig. 2.5). In the west rugged spurs of the Anden Mountains and in the east grassy fields dominate the landscape. *Schneider et al.* [2003] reported an annual mean temperature of about 6 °C and minimum and maximum daily mean temperatures of 2.3 °C and 10.0 °C, respectively. Constant westerly to north–westerly winds prevail through the whole year with a mean surface speed of 4.6 m s^{-1}, which is caused by the Antarctic low–pressure belt. Figure 2.7 shows a map of the southern hemisphere. The most southerly continental area (except Antarctica) is the peak of Southern America, where also Punta Arenas is located. The geopotential height[1] at 500 hPa is denoted by the color code for 1 January 2010 in Fig. 2.7. Dark colors indicate the cold low–pressure systems around the Antarctic. Air masses are advected along the isohypses. As it is cleary shown in Fig. 2.7, the air masses that are advected to Punta Arenas overpass no other continental areas.

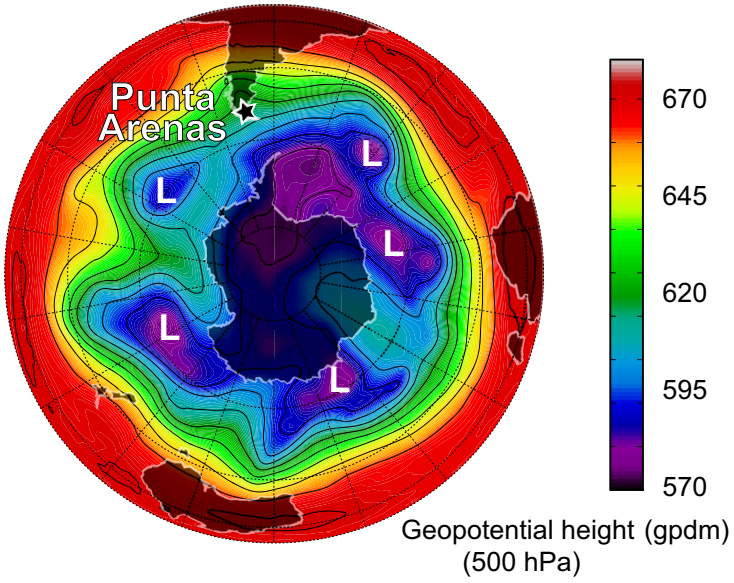

Figure 2.7: Map of the southern hemisphere. The geopotential height at 500 hPa is shown by the color code for 1 January 2010. The location of Punta Arenas is indicated by a black star. L denotes low–pressure systems.

[1] Geopotential height is a vertical coordinate of a certain pressure level. Areas of same geopotential height are indicated with isohypses [*Kraus*, 2004].

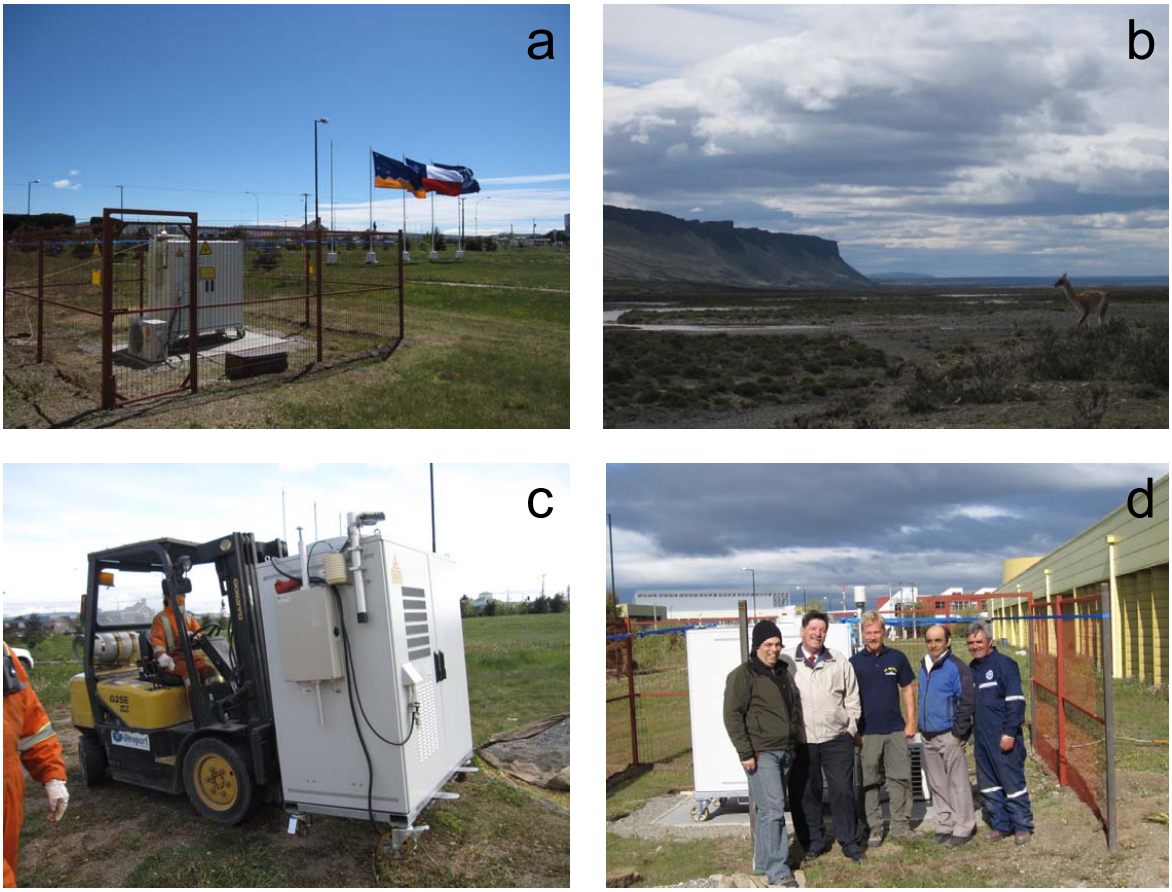

Figure 2.8: Impressions from the measurement site at Punta Arenas, Chile (53° S, 71° W). (a) Clean aerosol conditions prevail during the measurement period from 4 December 2009 to 4 April 2010. (b) Cloud layer over the plains north of Punta Arenas. (c) Installation of the portable lidar. (d) Claudio Casiccia (left), head of the Ozone and RUV Laboratory, University of Magallanes, and further colleagues.

Clean marine air masses dominate the aerosol conditions at Punta Arenas as indicated in Fig. 2.8 a. However, single- and multilayered clouds also occurred frequently (Fig. 2.8 b). Due to the heavy weight of about 700 kg the lidar had to be transported by a pallet truck (Fig. 2.8 c) at the soft and moist ground to its position close to the main building of the university (Fig. 2.8 d). Claudio Casiccia (head of the Ozone and RUV Laboratory, left in Fig. 2.8 d) and staff members helped hard–charging during the installation which last three weeks including bordering and adjustments. Claudio Casiccia and colleagues maintained the lidar during the campaign. An intensive maintenance was carried out together with IfT from 20 to 27 January 2010.

Stellenbosch, South Africa

After the Polarstern cruise ANT/XXVII-1 in October–November 2010 (see Fig. 2.5), the portable lidar was removed from the vessel in Cape Town and deployed at the Physics department of the University of Stellenbosch (34° S, 19° E, Fig 2.9 a and b). The lidar was mounted at the backyard of the institute (Fig. 2.9 c and d). The installations were performed from 27 November to 5 December 2010. The Leipzi**g** Stellenb**o**sch coo**p**eration close to the **H**ottentotten Natur**e** **R**eserve (**GOPHER**) campaign took place from 2 December 2010 to 13 April 2011.

Stellenbosch is located in the Winelands of South Africa about 60 km east of Cape Town (see map in Fig. 2.5). In the east of Stellenbosch are spurs of the Drakensberg and several nature reserves with vegetation from forest to mountain savanna (Fig. 2.9 a). Especially during the summer season, natural forest fires occur and lead to elevated smoke layers as visible in Fig. 2.9 a. Ulli Deutschländer (Fig. 2.9 d) maintained the lidar during GOPHER. An intensive lidar maintenance procedure was necessary after two months of observations (5 to 19 February 2011). Heinrich Schwoerer in Fig. 2.9 d is the head of the Laser Research Institute and Erich G. Rohwer the head of the Physics Department. The lidar was transported back to the harbour of Cape Town on 20 April 2011 and reinstalled at OCEANET–Atmosphere.

Auxiliary meteorological data were offered by the university at http://weather.sun.ac.za/ with 10 min resolution. In 2010 the daily mean temperature was 20 °C, the daily mean relative humidity 66%. The lowest and highest 10–min temperatures were 3.6 °C and 40.7 °C, respectively. The dominating wind direction is southwest and averaged wind speeds of 3.5 $\mathrm{m\,s^{-1}}$ prevail. In this Mediterranean–like climate most of the rain occurs in winter (May–July) [*Tesfaye et al.*, 2011].

Figure 2.10 shows the origin of different aerosol types and favorable aerosol transport pathways (arrows). The aerosol conditions are dominated by marine aerosol from the oceans. About 50% of the time winds are blowing from the Atlantic. Nevertheless, local aerosol sources of dust (savanna and Namibian desert), biomass burning (forests and savanna), urban aerosol from industries around Pretoria and Johannesburg, and long–range transported smoke from South America affect the aerosol conditions in South Africa [*Fishman et al.*, 1996; *Anderson et al.*, 1996; *Swap et al.*, 2003; *Tesfaye et al.*, 2011].

Figure 2.9: Impressions from the measurement site at Stellenbosch, South Africa (34° S, 19° E). (a) Anthropogenic haze, smoke, and dust as well as marine aerosol were observed from 2 December 2010 to 13 April 2011. (b) Transport of the portable lidar from Stellenbosch to Cape Town. (c) The lidar in its safety cage at the backyard of the department. (d) Ulli Deutschländer (left), Heinrich Schwoerer (second right), Erich G. Rohwer (right) from the University of Stellenbosch, Physics Department.

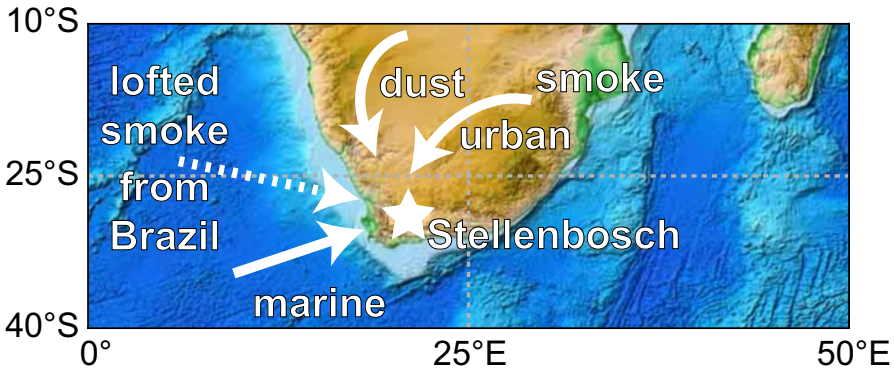

Figure 2.10: Location of the measurement site Stellenbosch, South Africa. Arrows indicate favorable transport paths of different aerosols types.

Chapter 3

Lidar

3.1 Polly^{XT}

The portable Raman and polarization lidar system Polly^{XT} was designed for an unattended, continuous monitoring of aerosol and cloud layers throughout the troposphere [*Althausen et al.*, 2009]. The optical setup of Polly^{XT} is presented in Fig. 3.1.

Laser pulses are transmitted at 355, 532, and 1064 nm with a repetition rate of 20 Hz by a Nd:YAG laser and second– and third–harmonic generators (E0 in Fig. 3.1). The outgoing laser beam is expanded (E2), the light at 355 nm is linearly polarized to enable the measurement of the cross–polarized and total backscatter signal at this wavelength. The whole optical plane is tilted (5° off zenith) to avoid specular reflection by horizontally aligned planar ice crystals which complicates cloud–phase discrimination [*Westbrook et al.*, 2010; *Seifert et al.*, 2010]. The primary mirror (R1) of 300 mm diameter collects the incoming photons. The collected backscattered light is reflected on a secondary mirror (R2) which directs the light through the pinhole (R3). The pinhole defines the receiver field of view (RFOV) of 1 mrad. The segregated light is collimated and transmitted by an achromatic lens (R4) to dichroic and polarizing beamsplitters (the right part of the receiver unit in Fig. 3.1) which split the light into the three elastically scattered wavelengths of 355, 532, and 1064 nm, the Raman–shifted wavelengths of the nitrogen molecule at 387 and 607 nm and the cross–polarized component at 355 nm. During the ALPACA campaign an analog 532–nm channel was replaced by a second depolarization channel which measures the cross–polarized signal component at 532 nm. After the replacement, the depolarization channel was characterized by means of a method described by *Grein* [2006] at IfT in the summer break 2010. Behind the beamsplitters interference filters are placed in front of planconvex lenses which focus the light onto the detection area of photomultipliers. The

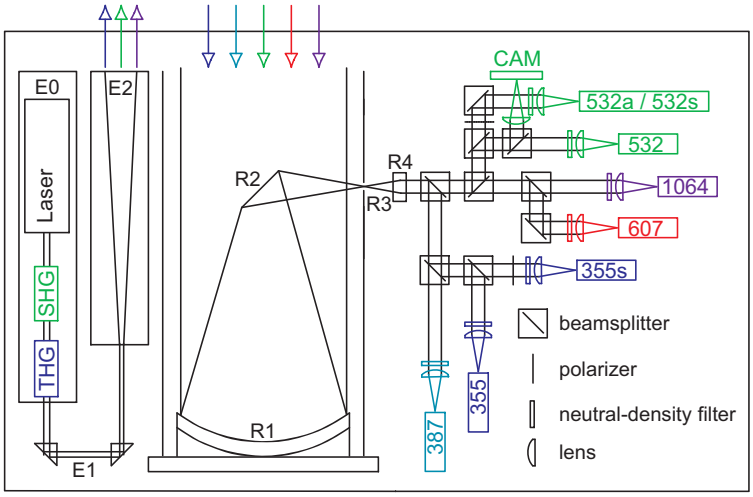

Figure 3.1: Optical setup of Polly^{XT} [adapted from *Althausen et al.*, 2009]. E0 contains the laser head and the second– and third–harmonic generators (Laser, SHG, THG). Prisms (E1) redirect the beam into the beam expander (E2) and into the atmosphere. The primary mirror (R1) reflects the collected photons onto the secondary mirror (R2), to the pinhole / fieldstop (R3), to a achromatic lens (R4), and finally to the receiver unit (right part) which consists of the necessary beamsplitters, filters, lenses, and photomultipliers.

photomultipliers are connected with the computer by data acquisition cards. The recorded profiles are averaged and stored each 30 s with a range resolution of 30 m. The optical setup was characterized by telecover tests and depolarization calibration at IfT before and after each campaign [*Freudenthaler*, 2008; *Grein*, 2006]. In addition, Polly^{XT} participated in the EARLI09 [*Freudenthaler et al.*, 2010] comparison campaign of EARLINET instruments [*Bösenberg et al.*, 2003].

A weatherproof telecommunication cabinet houses the whole optical and electronic setup. Quartz plates in the roof separate the emitter and receiver units from the surrounding and protect the system from pollution. The cabinet ensures temperature stability of the housed hardware by permanent air–conditioning even in different climatic environments. The quartz plates themselves are protected from rain by a roof cover which is closed during rain mode and controlled by a mounted precipitation sensor. The computer controls the entire lidar including the laser power supply and the data acquisition. Thus, it is possible to monitor the whole system by remote desktop via internet from anywhere in the world. The permanent internet connection is also used to upload the data to IfT for quicklook presentation at *http://polly.tropos.de* and back–up management. Simultaneous recording of temperature, pressure, and humidity allows data analysis by using standard atmospheric assumptions [*Ansmann et al.*, 1992].

Inside the OCEANET container Polly^{XT} is mounted on four swinging isolators to protect the sensible optics and electronics from ship vibrations caused by the ship's engine and propeller as well as the scending during heavy sea. Two quartz plates were installed in the roof of the container parallel to the quartz plates of Polly^{XT}. After the first two cruises the angle of the quartz plate mounting in the container roof was increased from 4° to 14° so that droplets can run off the plates. Further, an automatic cleaning system was added which keeps the quartz plates free from sea spray and dust. In 2011 a removable pneumatic lifting arm was mounted on the roof of the container to open the lidar's sheet remotely. Both wash system and the pneumatic lifting arm can be controlled automatically from Polly^{XT}. In addition, the data acquisition of Polly^{XT} was equipped with a position sensor which measures pitch and roll permanently to validate the data sets and to remove potential undesired effects of ship movements on the measured lidar profile.

3.2 Data analysis

3.2.1 Lidar equation

The basic equation of all lidar applications is the so–called lidar equation:

$$P(R,\lambda) = P_0(\lambda)\Delta R A \eta \frac{O(R)}{R^2} \times \left[\beta^{\mathrm{mol}}(R,\lambda) + \beta^{\mathrm{par}}(R,\lambda)\right] \exp\left\{-2\int_0^R \left[\alpha^{\mathrm{mol}}(r,\lambda) + \alpha^{\mathrm{par}}(r,\lambda)\right] \mathrm{d}r\right\}. \tag{3.1}$$

An emitted laser pulse of the power P_0 at wavelength λ is backscattered within a range cell ΔR centered in the range R. The range cell is given by $\frac{c\Delta t}{2}$ with the velocity of light c and the pulse length Δt. The backscatter coefficient $\beta(R,\lambda)$ describes the amount of light which is scattered by aerosols (par) and molecules (mol) at 180° and detected with the telescope mirror of the area A and an overall system efficiency η. Along the atmospheric pathway light gets lost due to absorption and scattering by particles and molecules. $\alpha(r,\lambda)$ is the respective extinction coefficient. $O(R)$ describes the overlap of the laser beam with the RFOV [*Wandinger and Ansmann*, 2002]. $O(R=0) = 0$, and full overlap $O(R) = 1$ is usually given at ranges $R > 1.5\,\mathrm{km}$ for Polly^{XT}. Detailed information is provided by *Wandinger* [2005a].

The molecular backscatter and extinction coefficients (β^{mol}, α^{mol}) can be calculated for given profiles of temperature and pressure [*Bucholtz*, 1995]. To derive β^{par} and α^{par} two approaches are used in the framework of this thesis to solve the lidar equation (3.1).

3.2.2 Klett–Fernald method

The first approach is based on the assumption of a relationship between β^{par} and α^{par}. This is the extinction–to–backscatter ratio or lidar ratio (S^{par}) of the scattering particles:

$$S^{\mathrm{par}}(R) = \frac{\alpha^{\mathrm{par}}(R)}{\beta^{\mathrm{par}}(R)}. \tag{3.2}$$

S^{par} depends on the observed wavelength and aerosol type (shape, size, composition). Thus, it can change with height, if multi–layered aerosol or different aerosol types or mixtures occur. The assumption of a constant lidar ratio can introduce large errors of 100% or more [*Sasano et al.*, 1985]. After *Klett* [1981] and *Fernald* [1984] for a given S^{par} Eq. (3.1) can be solved for β^{par}:

$$\beta^{\mathrm{par}}(R) = -\beta^{\mathrm{mol}}(R) + \frac{A(R_0, R)}{B(R_0) - 2S^{\mathrm{par}} \int_{R_0}^{R} A(R_0, r)\mathrm{d}r}, \tag{3.3}$$

with

$$A(R_0, R) = P(R)R^2 \exp\left[-2(S^{\mathrm{par}} - S^{\mathrm{mol}}) \int_{R_0}^{R} \beta^{\mathrm{mol}}(\xi)\mathrm{d}\xi\right] \tag{3.4}$$

and

$$B(R_0) = \frac{P(R_0)R_0^2}{\beta^{\mathrm{par}}(R_0) + \beta^{\mathrm{mol}}(R_0)}. \tag{3.5}$$

Within Eq. (3.4) the extinction–to–backscatter ratio of air $S^{\mathrm{mol}} = \frac{8\pi}{3}K$ is used, with the King factor K [*Collis and Russell*, 1976]. For simplicity, laser light with a specific wavelength, a full overlap ($O(R) = 1$), and a system term $\Delta R A \eta = 1$ were assumed.

3.2.3 Raman method

The second approach is based on the additionally measured Raman signals of nitrogen during nighttime. The lidar equation for Raman backscattering at wavelength λ_{Ra} is:

$$\begin{aligned} P(R, \lambda_{\mathrm{Ra}}) = {} & P_0 \Delta R A \eta \frac{O(R)}{R^2} \beta_{\mathrm{Ra}}(R, \lambda_0) \\ & \times \exp\left\{-\int_0^R \left[\alpha^{\mathrm{par}}(r, \lambda_0) + \alpha^{\mathrm{mol}}(r, \lambda_0) + \alpha^{\mathrm{par}}(r, \lambda_{\mathrm{Ra}}) + \alpha^{\mathrm{mol}}(r, \lambda_{\mathrm{Ra}})\right] \mathrm{d}r\right\}. \end{aligned} \tag{3.6}$$

From the Raman lidar equation (3.6) the extinction can be computed directly [*Ansmann et al.*, 1990]:

$$\alpha^{\mathrm{par}}(R,\lambda_0) = \frac{\frac{\mathrm{d}}{\mathrm{d}R}\ln\frac{N_{\mathrm{Ra}}(R)}{P(R,\lambda_{Ra})R^2/O(R)} - \alpha^{\mathrm{mol}}(R,\lambda_0) - \alpha^{\mathrm{mol}}(R,\lambda_{\mathrm{Ra}})}{1+\left(\frac{\lambda_0}{\lambda^{\mathrm{Ra}}}\right)^{\mathring{A}_\alpha}}. \tag{3.7}$$

N_{Ra} is the number density of nitrogen molecules and can be calculated for given temperature and pressure profiles [*Bucholtz*, 1995]. The Ångström exponent $\mathring{A}_\alpha$ is given in Eq. (3.10). From two lidar equations, one for elastic backscattering (Eq. (3.1)) and one for Raman backscattering (Eq. (3.6)) the particle backscatter coefficient is obtained by means of [*Ansmann et al.*, 1992]

$$\begin{aligned}\beta^{\mathrm{par}}(R,\lambda_0) = &-\beta^{\mathrm{mol}}(R,\lambda_0) + \left[\beta^{\mathrm{par}}(R_0,\lambda_0) + \beta^{\mathrm{mol}}(R_0,\lambda_0)\right] \\ &\times \frac{P(R_0,\lambda_{Ra})P(R,\lambda_0)N_{\mathrm{Ra}}(R)}{P(R_0,\lambda_0)P(R,\lambda_{\mathrm{Ra}})N_{\mathrm{Ra}}(R_0)} \\ &\times \frac{exp\left\{-\int_{R_0}^{R}\left[\alpha^{\mathrm{par}}(r,\lambda_{\mathrm{Ra}}) + \alpha^{\mathrm{mol}}(r,\lambda_{\mathrm{Ra}})\right]\mathrm{d}r\right\}}{\exp\left\{-\int_{R_0}^{R}\left[\alpha^{\mathrm{par}}(r,\lambda_0) + \alpha^{\mathrm{mol}}(r,\lambda_0)\right]\mathrm{d}r\right\}}.\end{aligned} \tag{3.8}$$

The intensity of Raman scattered light is much lower than the intensity of Rayleigh scattering. Thus, the detection of Raman signals is restricted to nighttime when background noise is minimized. However, the main advantage of the Raman method is the direct determination of the particle extinction coefficient and thus the independent determination of S^{par} to characterize aerosol types [*Müller et al.*, 2007].

Both presented approaches require a reference value $\beta^{\mathrm{par}}(R_0)$ which has to be estimated at the reference height (R_0). This is done at aerosol and cloud–free heights of the free troposphere where $\beta^{\mathrm{par}}(R_0) \ll \beta^{\mathrm{mol}}(R)$ for $\lambda \leq 532\,\mathrm{nm}$ [*Ansmann*, 2002]. Further details are explained by *Ansmann and Müller* [2005].

Besides S^{par}, the depolarization ratio (next section) and the Ångström exponent are useful for the determination of the aerosol type. The Ångström exponent ($\mathring{A}$) describes the spectral slope of a quantity [*Ångström*, 1929]. $\mathring{A}$ is large for fine–mode particles (sulfates) and small for coarse–mode particles like dust [*Müller et al.*, 2007]. The respective $\mathring{A}$ of the backscatter coefficient β measured at the two wavelengths λ_1 and λ_2 is [*Ansmann et al.*, 2002]:

$$\mathring{A}_{\beta,\lambda_1,\lambda_2}(R) = -\frac{\ln\left[\beta_{\lambda_1}(R)/\beta_{\lambda_2}(R)\right]}{\ln(\lambda_1/\lambda_2)}. \tag{3.9}$$

For the extinction coefficient α

$$\begin{aligned} \mathring{A}_{\alpha,\lambda_1,\lambda_2}(R) &= -\frac{\ln\left[\alpha_{\lambda_1}(R)/\alpha_{\lambda_2}(R)\right]}{\ln(\lambda_1/\lambda_2)} \\ &= -\frac{\ln\left\{\left[\beta_{\lambda_1}(R)S_{\lambda_1}(R)\right]/\left[\beta_{\lambda_2}(R)S_{\lambda_2}(R)\right]\right\}}{\ln(\lambda_1/\lambda_2)} \\ &= \mathring{A}_{\beta,\lambda_1,\lambda_2}(R) + \mathring{A}_{S,\lambda_1,\lambda_2}(R) \end{aligned} \tag{3.10}$$

and for the lidar ratio S

$$\mathring{A}_{S,\lambda_1,\lambda_2}(R) = -\frac{\ln\left[S_{\lambda_1}(R)/S_{\lambda_2}(R)\right]}{\ln(\lambda_1/\lambda_2)}. \tag{3.11}$$

3.2.4 Depolarization ratio

Lidars provide also information about the sphericity of the scattering particles, if polarization–sensitive measurement channels are used [*Sassen*, 2005]. Transmitted linearly polarized laser light $P_{0,\parallel}$ is depolarized by non–spherical scatterers (ice crystals, dust particles), which cause a significant cross–polarized ($\perp$) signal component that arrives at the telescope (Tel) of the lidar,

$$P(R)_{\perp}^{\mathrm{Tel}} = P_{0,\parallel}\Delta R A \frac{O(R)}{R^2}\beta_{\perp}(R)\exp\left[-\int_0^R \alpha_{\perp}(r)+\alpha_{\parallel}(r)\mathrm{d}r\right], \tag{3.12}$$

besides the co–polarized signal ($\parallel$)

$$P(R)_{\parallel}^{\mathrm{Tel}} = P_{0,\parallel}\Delta R A \frac{O(R)}{R^2}\beta_{\parallel}(R)\exp\left[-2\int_0^R \alpha_{\parallel}(r)\mathrm{d}r\right]. \tag{3.13}$$

The volume linear depolarization ratio $\delta^{\mathrm{vol}}(R)$ is defined as [*Sassen*, 2005]:

$$\delta^{\mathrm{vol}}(R) = \frac{P_{\perp}^{\mathrm{Tel}}(R)}{P_{\parallel}^{\mathrm{Tel}}(R)} = \frac{\beta_{\perp}(R)}{\beta_{\parallel}(R)} = \frac{\beta_{\perp}^{\mathrm{par}}(R)+\beta_{\perp}^{\mathrm{mol}}(R)}{\beta_{\parallel}^{\mathrm{par}}(R)+\beta_{\parallel}^{\mathrm{mol}}(R)}, \tag{3.14}$$

under the assumption of $\alpha_{\parallel} = \alpha_{\perp}$.

Instrumental effects cause the detection (Det) of co–polarized and cross–polarized components of the received light with the power $P(R)^{\mathrm{Det}}$ [*Grein*, 2006]:

$$P(R)^{\mathrm{Det}} = \eta_{\parallel}^{\mathrm{Det}} P(R)_{\parallel}^{\mathrm{Tel}} + \eta_{\perp}^{\mathrm{Det}} P(R)_{\perp}^{\mathrm{Tel}}, \tag{3.15}$$

with the efficiencies $\eta_{\parallel,\perp}^{Det}$ for both polarization planes. Hence, the incomplete attenuation of the unwanted polarization component between the telescope and the detector has to

be considered in the determination of $\delta^{\mathrm{vol}}(R)$, which is done with the transmission ratio $D^{\mathrm{Det}} = \eta_{\parallel}^{\mathrm{Det}}/\eta_{\perp}^{\mathrm{Det}}$. D^{Det} is determined by the depolarization calibration of *Grein* [2006] and described in detail in *Baars* [2012]. The rearrangement of Eq. (3.14) and (3.15) for the total ($P^t(R)$) and cross–polarized signals ($P^c(R)$) as detected with Polly$^{\mathrm{XT}}$ yields:

$$\delta^{vol,tc}(R) = \frac{C^{tc} - \upsilon^{tc}(R)}{D^c \upsilon^{tc}(R)} - D^t C^{tc}, \tag{3.16}$$

with

$$\upsilon^{tc}(R) = \frac{P^t(R)}{P^c(R)} \qquad \text{and} \qquad C^{tc} = \frac{\eta_{\parallel}^t}{\eta_{\parallel}^c}.$$

$\eta_{\parallel}^t$ and $\eta_{\parallel}^c$ are the corresponding efficiencies for the co–polarized component of $P^t(R)$ and $P^c(R)$. In particle–free heights $C^{t,c}$ can be determined, where $\delta^{\mathrm{vol}}(R_0) = \delta^{\mathrm{mol}}$. δ^{mol} is sensitive to the band with of the interference filter and the temperature [*Behrendt and Nakamura*, 2002; *Wandinger*, 2005b]. A detailed description of calculations with respect to the depolarization measurements of Polly$^{\mathrm{XT}}$ can be found in *Baars* [2012]. Layers dominated by spherical scatterers show $\delta^{\mathrm{vol}} \approx 0$, layers dominated by non–spherical scatterers give $\delta^{\mathrm{vol}} > 0$.

To get an intensive quantity of the scattering volume the particle linear depolarization ratio $\delta^{\mathrm{par}}(R) = \beta_{\perp}^{\mathrm{par}}(R)/\beta_{\parallel}^{\mathrm{par}}(R)$ has to be distinguished from the molecular linear depolarization ratio $\delta^{\mathrm{mol}}(R) = \beta_{\perp}^{\mathrm{mol}}(R)/\beta_{\parallel}^{\mathrm{mol}}(R)$. Rearranging Eq. (3.14) under consideration of $\beta^{\mathrm{mol,par}} = \beta_{\perp}^{\mathrm{mol,par}} + \beta_{\parallel}^{\mathrm{mol,par}} = \beta_{\parallel}^{\mathrm{mol,par}}(1 + \delta^{\mathrm{mol,par}})$ gives:

$$\delta^{\mathrm{par}}(R) = \frac{\beta_{\perp}^{\mathrm{par}}(R)}{\beta_{\parallel}^{\mathrm{par}}(R)} = \frac{(1+\delta^{\mathrm{mol}})\delta^{\mathrm{vol}}(R)\frac{\beta^{\mathrm{mol}}+\beta^{\mathrm{par}}(R)}{\beta^{\mathrm{mol}}(R)} - (1+\delta^{\mathrm{vol}}(R))\delta^{\mathrm{mol}}}{(1+\delta^{\mathrm{mol}})\beta^{\mathrm{mol}}(R) + \beta^{\mathrm{par}}(R)\beta^{\mathrm{mol}}(R) - (1+\delta^{\mathrm{vol}}(R))}. \tag{3.17}$$

δ^{par} allows the distinction of various aerosol types and the separation of spherical and non–spherical scattering compounds in mixed layers [*Tesche et al.*, 2009; *Ansmann et al.*, 2011b; *Groß et al.*, 2011a].

3.2.5 Multiple scattering

When large particles are present in an aerosol or cloud layer the probability increases that photons experience multiple scattering events before they are backscattered to the lidar receiver. Especially in liquid–water clouds which typically feature high concentrations ($N > 100\,\mathrm{cm}^{-3}$) of large droplets ($d > 5\,\mu\mathrm{m}$) the probability of forward scattering increases [*Liou and Schotland*, 1971; *Wandinger*, 1998]. Forward–scattered photons that remain

in the RFOV can be backscattered in a subsequent scattering process (at angles $\neq 180°$) and be detected. As a result the observed extinction coefficient is underestimated and the lidar ratio decreases [*Bissonnette*, 2005; *Wandinger*, 1998; *Seifert et al.*, 2007]. Also the polarization direction changes in the case of multiple scattering by liquid–water droplets because $\delta^{\mathrm{par}} = 0$ is only valid for backscattering at exactly 180°. For small angular deviations from 180°, as it is the case during multiple–scattering events, the depolarization ratio increases [*Bissonnette*, 2005]. *Seifert* [2010] discussed the depolarization effect of multiple scattering in water clouds in detail. The depolarization ratio increases almost linearly with increasing penetration depth into the cloud layer from $\delta^{vol} \approx 0$ at cloud base to $\delta^{vol} \approx 0.15 - 0.25$. *Sassen and Petrilla* [1986] as well as *Ansmann et al.* [2009] observed $\delta^{vol} > 0$ in liquid–water clouds (marine stratus and altocumulus) for a RFOV of 1.0 mrad and 0.8 mrad, respectively.

A detailed overview about the lidar technique is given by *Wandinger* [2005a,b]; *Ansmann and Müller* [2005]; *Sassen* [2005]; *Bissonnette* [2005]. Data correction and error analysis is intensively discussed in *Sasano et al.* [1985]; *Ansmann et al.* [1992]; *Grein* [2006]; *Freudenthaler et al.* [2009]; *Tesche* [2011]; *Groß* [2011]; *Baars* [2012]. The respective data evaluation algorithms are consequently applied in the frame of this thesis.

Chapter 4

Supplementary data sources

A variety of further instruments and methods were applied for the data analysis. The most important ones are introduced briefly in the following.

4.1 Instruments of OCEANET–Atmosphere

In the framework of OCEANET radiation measurements were performed aboard Polarstern and with MSG from space [*Schmetz et al.*, 2002]. The liquid water path (LWP) as well as temperature and humidity profiles were determined with the microwave radiometer HATPRO [*Rose et al.*, 2005]. These data were used in the analysis of the lidar data. The LWP is determined by microwave radiometer with a temporal resolution of 2 s during the whole cruise. Temperature and humidity profiles up to 10 km height were averaged along the time period of interest to increase the signal–to–noise ratio [*Rose et al.*, 2005]. Radiation measurements were performed in the solar range between 305 and 2800 nm with the pyranometer Kipp & Zonen CM21 after ISO9060 with an uncertainty of ±2% each second [*Kipp & Zonen*, 2004, manual]. Because the usual uncertainty is determined under favorable conditions the error was increased to ±4% because of the ship movements and the effect of the ship's superstructure, e. g., the crow's nest [*Kalisch*, 2011]. The skyimager took four pictures of the hemisphere above OCEANET–Atmosphere each minute at daytime. The pictures yield the information about cloud coverage, cloud type, and the atmospheric state [*Kalisch*, 2011].

4.2 Sun photometer

In the framework of the Maritime Aerosol Network (MAN[1]) a number of research vessels, among them the Polarstern, are equipped with handhold Sun photometers (Microtops) to measure the spectral aerosol optical thickness (AOT) above the oceans [*Morys et al.*, 2001; *Porter et al.*, 2001; *Smirnov et al.*, 2009]. AOT is observed at 340, 440, 500, 675, and 870 nm. The particle AOT is defined as the particle extinction coefficient integrated over the vertical column. The derived AOT provides valuable information for the lidar data analysis. In this study the cloud–screened and quality–assured level 2 data was used.

4.3 Cloud–Aerosol Lidar with Orthogonal Polarization (CALIOP)

In April 2006 the Cloud–Aerosol Lidar and Infrared Pathfinder Satellite Observations (CALIPSO) application, a project of the National Aeronautics and Space Administration and Centre National d'Etudes Spatiales was successfully launched and placed into the Afternoon–Train constellation. The satellite is located in an altitude of about 705 km and circles around the globe in a polar orbit within 99 minutes at a velocity of $7\,\mathrm{km\,s^{-1}}$. CALIPSO overpasses the same location each 16th day. CALIOP is aboard the CALIPSO satellite [*Winker et al.*, 2007]. The dual–wavelength backscatter lidar measures backscatter profiles at 532 and 1064 nm, and depolarization at 532 nm. Due to the optical setup the footprint of the laser beam is 70 m in diameter at the ground. The velocity of the satellite and the laser pulse repetition rate of 20.16 Hz determine the distance of 330 m between two laser shots. The vertical resolution is 30 m in the troposphere. The data of CALIOP is processed automatically by an algorithm that is explained in detail in a special issue of the Journal of Atmospheric and Oceanic Technology [*Winker et al.*, 2009].

In terms of CALIOP, it is common to obtain the attenuated backscatter (β^*). By rearrangement of the lidar equation (3.1) (Sec. 3.2) to the range–corrected signal PR^2, divided by the system and geometric constants (summarized in C), the attenuated backscatter is given as

$$\beta^* = \frac{PR^2}{C} = \beta\tau^2, \tag{4.1}$$

where τ is the atmospheric transmission ($\exp\left[-\int \alpha(r)dr\right]$). The attenuated backscatter differs from the backscatter coefficient only by the transmission.

[1]Information and data available at http://aeronet.gsfc.nasa.gov/new_web/maritime_aerosol_network.html

It is worth to mention that the calculation of the level 2 data (backscatter coefficient, extinction coefficient) is based on the region that is overpassed (latitude, longitude), the surface type, and probability density functions of properties of clouds and aerosols. After final data processing profiles of particle backscatter and extinction coefficients are stored (height resolution of 60 m and horizontal averaging as function of aerosol/cloud conditions from 1/3 to 80 km [*Powell et al.*, 2011]) and freely available. These profiles have been validated, e. g., with ground–based lidar [*Anderson et al.*, 2003; *Pappalardo et al.*, 2010; *Wandinger et al.*, 2010] and are widely used in atmospheric science. The data of CALIOP observations are provided by the National Aeronautics and Space Administration (NASA) Langley Research Center, Atmospheric Science Data Center[2] and will also be used in this work (Chapter 5).

4.4 Radiosonde meteorological data

During the cruises of Polarstern daily radiosonde launches (VAISALA, RS92) were performed by the vessel's own meteorological station to obtain profiles of the meteorological standard properties pressure, temperature, and humidity from the heliport (10 m asl) up to heights of 15–37 km. All soundings are stored in the meteorological information system at AWI[3]. At Punta Arenas daily 12:00 UTC radio soundings from the airport were used if available from the data archive of the University of Wyoming[4]. The profile information of temperature and pressure is necessary to calculate the Rayleigh scattering in the atmosphere for the lidar data analysis. Further, the temperature profiles are used to determine cloud top temperatures to investigate heterogeneous ice nucleation in Chapter 7.

4.5 Global data assimilation system (GDAS) meteorological data

At Stellenbosch a close–by radiosonde launch site is missing. Instead, data of the U. S. National Weather Service's National Center for Environmental Prediction was used that is based on GDAS[5] [*Kanamitsu*, 1989]. For a horizontal grid of $1^\circ \times 1^\circ$ meteorological standard properties are stored in the GDAS1 data set which contains 23 vertical layers up to about 30 km height and is available every 3 hours.

[2]Information and data are available at http://eosweb.larc.nasa.gov/PRODOCS/calipso/table_calipso.html
[3]Information and data are available at http://www.pangaea.de/search?q=event:Polarstern+Radiosonde
[4]Data available at http://weather.uwyo.edu/upperair/sounding.html
[5]Information and data of the GDAS archive available at: http://www.arl.noaa.gov/gdas.php

The GDAS1 data were also used to cover periods of missing radio soundings aboard Polarstern and at Punta Arenas. An analysis of the model–derived temperatures and temperatures from launched radiosondes (daily) show a mean difference and a standard deviation of 0.2 ± 0.8 K (Polarstern, for the three cruises), -0.2 ± 1.2 K (Punta Arenas, December 2009 to April 2010), and -0.3 ± 2.2 K (Stellenbosch, December 2010 to April 2011) in the height range from 2 to 11 km (see Appendix A).

4.6 Source apportionment

Air–mass transport analysis was partly based on Flexible Langrangian Particle Dispersion Model (FLEXPART) runs [*Stohl et al.*, 2005]. It simulates long–range and mesoscale transport, as well as diffusion by resolved wind information and parameterized subgrid motions. The model uses archived meteorological data with a temporal resolution of 6 hours and a horizontal resolution of $1° \times 1°$ provided by the Computational & Information Systems Laboratory that is managed by National Center for Atmospheric Research data support[6]. FLEXPART offers daily and cumulative snapshots of a density distribution of backward trajectories of 50.000 air parcels whose anchor points are distributed in the altitude range of interest above the observation site. For statistic approaches in Sec. 7.2 backward and forward trajectories were also calculated with the Hybrid Single–Particle Lagrangian Integrated Trajectory (HYSPLIT) model [*Draxler and Rolph*, 2003]. The local dust load in the area of Polarstern was estimated by Dust Regional Atmospheric Model (DREAM) [*Nickovic et al.*, 2001] computations[7].

4.7 Library Radiative–Transfer (libRadtran)

As one of a few available radiative–transfer models the UVSPEC program [*Kylling*, 1992] of the libRadtran library version 1.6–beta was chosen to calculate the broadband solar downward and upward irradiances at the surface and TOA to derive the solar aerosol radiative effect [*Mayer and Kylling*, 2005]. The libRadtran library includes the discrete ordinate solver DISORT version 2.0 [*Stamnes et al.*, 1988] and the spectral integration by the correlated–k approximation [*Kato et al.*, 1999]. DISORT was applied with sixteen streams with respect to the built–in bidirectional reflectance distribution function (BRDF) [*Cox and Munk*, 1954a,b; *Bellouin et al.*, 2004] for the surface albedo. The dependence of the surface albedo

[6] Information is given at http://dss.ucar.edu/datasets/ds083.2/

[7] Information and data available at http://www.bsc.es/projects/earthscience/DREAM

on the 10–m surface wind speed and salinity was considered whenever data was available[8]. Solar zenith angles were determined from position and time [*Blanco-Muriel et al.*, 2001]. Particle and cloud–free atmospheric conditions were described with standard atmospheres implemented in libRadtran [*Anderson et al.*, 1986] regarding trace gases and radiosonde or GDAS1 profiles of pressure, temperature, and relative humidity. Vertically resolved aerosol conditions were included in terms of the lidar–derived extinction profiles. Single–scattering albedo (SSA) and asymmetry parameter (g) were taken from the literature [*Heinold et al.*, 2011; *Müller et al.*, 2011]. The vertical model grid was set to the maximum resolution of 0.1 km below 6 km and 1 km above to use the lidar–derived extinction profiles which were downscaled to the grid. The comparisons to MSG and pyranometer measurements were performed in the spectral range from 340 to 4000 nm and from 305 to 2800 nm, respectively.

[8]Information and data available at http://dship.awi.de/

Chapter 5

Vertically resolved aerosol characterization above the North and South Atlantic

One goal of OCEANET is a systematic height–resolved characterization of aerosols above the Atlantic. The achievements made in this respect are presented in the following chapter. First, a review of aerosol–related field experiments with shipborne measurements will be presented in Sec. 5.1. Sun photometer measurements performed in the framework of the MAN as part of the AErosol RObotic NETwork (AERONET) will be introduced, because MAN started the first long–term shipborne aerosol observations in October 2004. Afterwards, observed case studies will be presented in detail in Sec. 5.2. At the end of this chapter, a statistical analysis will summarize the general findings in Sec. 5.3.

5.1 Introduction

The vast, hardly accessible oceans embodied a barely characterized area in atmospheric science until the end of the 1960s. First investigations were based on in–situ observations within the Marine Boundary Layer (MBL) [*Fitzgerald*, 1991; *Heintzenberg et al.*, 2000; *Smirnov et al.*, 2002] and until today information about the aerosol distribution in the atmosphere over the ocean is rare. Generally, the size distribution of the particles in the clean MBL is characterized by a sulfate fine mode and a sea–salt coarse mode. The fine mode represents about 90%–95% of the aerosol particle number but only 5% of the total aerosol particle mass [*Hoppel et al.*, 1990]. The fine–mode particles are suggested to originate mostly from gas–to–particle conversion of freshly emitted dimethyl sulfate (DMS) [*Hoppel et al.*, 1990]. Modeling studies estimated emissions of 17.6–34.4 Tg DMS per

year [*Lana et al.*, 2011]. The DMS emissions show a clear dependence on surface wind speed and marine biological activity. Nonprecipitating MBL clouds play an important role in shaping the fine–mode aerosol size distribution in the MBL. Freshly formed aerosol particles that grow to CCN size of around 0.04 µm radius undergo 10–20 cloud cycles within 3–10 days until they deposit [*Hoppel et al.*, 1990]. Within every cycle of cloud evaporation and condensation the particles change in composition and size.

The concentration of coarse–mode sea–salt particles depends mainly on wind speed which determines the strength of sea spray and thus the production of aerosols by bubble bursting at white caps. For wind speeds exceeding $15\,\mathrm{m\,s^{-1}}$ concentrations of $50\,\mu\mathrm{g\,m^{-3}}$ were measured [*Fitzgerald*, 1991; *Gong*, 2003; *Kiliyanpilakkil and Meskhidze*, 2011]. Sea salt accounts for about 44% of the global AOT [*O'Dowd and de Leeuw*, 2007; *Gong*, 2003]. The omnipresence of sea salt above the oceans also explains its leading importance in the radiative budget for the clear–sky ocean [*Haywood et al.*, 1999]. Only in the latitudinal belt of 0° to 30° N crustal material exceeds the mass concentration of sea–salt aerosol due to constant emissions from the subtropical African continent [*Heintzenberg et al.*, 2000].

A systematic global mapping of aerosols above the oceans started with the first spaceborne aerosol observations in the 1970s. An algorithm for the Total Ozone Mapping Spectrometer (TOMS) aboard the Nimbus 7 satellite has enabled the detection and quantification of absorbing aerosols since 1978, and allowed the first continuous observation of the global aerosol distribution [*Herman et al.*, 1997; *Torres et al.*, 1998; *Prospero et al.*, 2002]. TOMS observations provide only column–integrated information about absorbing aerosols in the UV spectral range from 340–380 nm [*Prospero et al.*, 2002]. In the 1990s a variety of satellite sensors were developed and permitted an improved particle characterization on a global scale. The mean AOT (500 nm) above the oceans was determined, e. g., with the Moderate Resolution Imaging Spectroradiometer (MODIS), the Sea–viewing Wide field–of–view sensor (SeaWifs), or the Advanced Very High Resolution Radiometer (AVHRR–2) to be in the range of 0.10–0.16 at 550 nm [*Remer et al.*, 2008; *Myhre et al.*, 2005]. However, AOTs of about 0.2 were determined by the Multi–angle Imaging SpectroRadiometer (MISR) [*Myhre et al.*, 2005].

Continuous ground–based aerosol observations within AERONET have been performed at single islands since June 1994, when observations were started at Mauna Loa, Pacific [*Holben et al.*, 1998; *Holben et al.*, 2001]. A comparison between observations on islands showed values of the AOT at 500 nm from 0.13–0.14 to 0.07–0.08 over the Atlantic and the Pacific,

respectively [*Smirnov et al.*, 2002]. While over the Pacific clean marine conditions prevail, mixed marine conditions increase the AOT above the Atlantic. However, the island–based observations were not able to cover the oceans satisfyingly. Large progress was achieved with the introduction of the handhold Microtops Sun photometer observations that have been used aboard research vessels to determine the AOT above the oceans in the framework of MAN since October 2004 [*Morys et al.*, 2001; *Knobelspiesse et al.*, 2004; *Smirnov et al.*, 2009, 2011]. In Fig. 5.1 mean 500–nm AOT of all currently available Microtops measurements of the years $2004 - 2011$ above the Atlantic are shown as a function of latitude. The presented AOT distribution is dominated by the peak in the latitudinal belt between 15° and 30° N that is caused by dust emissions in the Saharan region [*Heintzenberg et al.*, 2000]. For latitudinal belts of 60°–30° N, 30° N–30° S, and 30°–60° S the mean AOT is 0.13, 0.2, and 0.07, respectively. A more detailed analysis for the tropics yields AOTs of 0.22, 0.27, 0.12, and 0.09 for the latitudinal belts 30°–15° N, 15° N–EQ (equator), EQ–15° S, and 15–30° S, respectively. The mean AOT above the Atlantic is about 0.14 which is comparable to calculations of *Smirnov et al.* [2009]. *Smirnov et al.* [2009] determined a mean AOT of 0.19 above the Atlantic and of 0.11 above all oceans. The handhold Sun photometer observations showed that AOT determined with MODIS are overestimated above regions with surface wind speeds above $6\,\mathrm{m\,s^{-1}}$ and underestimated for wind speeds below $6\,\mathrm{m\,s^{-1}}$. Probably, this finding is caused by a general assumption of constant ocean surface wind speed of $6\,\mathrm{m\,s^{-1}}$ [*Adames et al.*, 2011]. Further satellite measurement validation is presented in *Smirnov et al.* [2011].

The global mean AOT above the oceans does not represent the AOT of the MBL alone. The MBL typically extends to $300 - 900\,\mathrm{m}$ height [*Franke et al.*, 2001; *Sugimoto et al.*, 2001; *Wulfmeyer and Janji*, 2005; *Groß et al.*, 2011a]. As Fig. 5.1 already showed, the AOT is also influenced by aerosol particles originating from continental sources such as the large deserts, areas with systematic biomass burning, and highly industrialized regions (North America, Europe, East Asia). However, frequently these aerosols occur as lofted, free–tropospheric layers that account for 30%–60% of the column–integrated AOT [*Ansmann et al.*, 2001; *Franke et al.*, 2003]. Thus, they are subject to long–range transport over the oceans. The long residence time of these lofted layers, their relevance for the evolution of clouds and precipitation, and their impact on radiative fluxes motivated a number of closure field campaigns in oceanic and coastal regimes (ACE 1 [*Bates et al.*, 1998], TARFOX [*Russell et al.*, 1999], ACE 2 [*Russell and Heintzenberg*, 2000], INDOEX [*Ramanathan et al.*, 2001], ACE–Asia [*Huebert et al.*, 2003], SAFARI 2000 [*Swap et al.*, 2003], ABC [*Nakajima et al.*, 2007], and SAMUM–2 [*Ansmann et al.*, 2011a]).

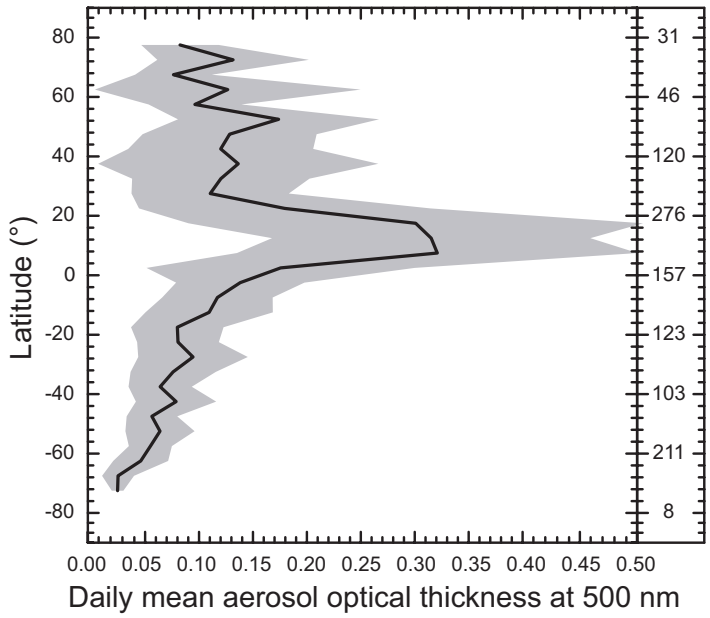

Figure 5.1: Latitudinal distribution of determined mean aerosol optical thickness and its standard deviation at 500 nm in steps of 5° above the Atlantic from October 2004 to June 2011 in the framework of MAN. The right column shows the number of observations in steps of 20° [*Smirnov et al.*, 2009, updated].

Lidars became more and more involved in these intensive field campaigns to provide vertically resolved aerosol observations in the MBL as well as of the lofted layers [*Sugimoto et al.*, 2001; *Groß et al.*, 2011a]. *Ansmann et al.* [2001], *Groß et al.* [2011a], and *Groß et al.* [2011b] determined extinction–to–backscatter ratios (532 nm) of 22.5 ± 2.5, 18 ± 1 sr, and 19 ± 2 sr, respectively, for marine aerosol and subsequently concluded from the measured profiles of the particle backscatter coefficient that the AOT (532 nm) of a clean marine MBL is about 0.05. This value agrees well with the presented MAN observation in the latitudinal belt from 30°–60° S and with the mean AOT (0.06 at 500 nm) of the Southern Ocean which is almost not affected by continental aerosol particles [*Smirnov et al.*, 2009]. However, the high AOT at latitudes >60° N in Fig. 5.1 cannot be explained by marine particles alone, and probably results from the impact of the intercontinental aerosol transport in the northern hemisphere [*Mattis et al.*, 2008; *Mattis et al.*, 2010].

Although complex closure campaigns provided detailed insights into the aerosol properties and the impacts of aerosols on climatically relevant processes above the oceans, the findings are representative for certain areas only. To obtain a vertically resolved, global view on the aerosol distribution, a spaceborne lidar is required. Consequently, CALIPSO was

launched in April 2006 [*Winker et al.*, 2007] (see Sec. 4.3). CALIOP, the dual–wavelength backscatter lidar aboard CALIPSO, provides worldwide observations of lofted aerosol and cloud layers, e. g., cross sections along major advection tracks from the west coast of Africa to the Caribbean or from Patagonia to Antarctica [*Liu et al.*, 2008b; *Nowottnick et al.*, 2011; *Johnson et al.*, 2011]. *Kiliyanpilakkil and Meskhidze* [2011] determined a global mean AOT of 0.052 ± 0.038 caused by clean marine aerosol from CALIOP observations at 532 nm in agreement with the discussions above. But the satellite revolves around the earth with a speed of $7\,\mathrm{km\,s^{-1}}$ and performs measurements with a spatial resolution of 5 km [*Kacenelenbogen et al.*, 2011]. The same footprint is observed every 16th day which inhibits the observation of short–term developments and atmospheric processes such as cloud evolution or the diurnal cycle of the boundary–layer development. Comparisons between MODIS and CALIOP show an uncertainty in AOT of 0.03 to 0.04 [*Redemann et al.*, 2011]. Reasons are probably the general assumption of a fixed lidar ratio in the data analysis of measurements of the simple backscatter lidar CALIOP [*Sasano et al.*, 1985] or the general assumption of constant surface wind speeds of $6\,\mathrm{m\,s^{-1}}$ to derive look–up tables of reflectance for MODIS retrievals [*Levy et al.*, 2003; *Redemann et al.*, 2011; *Kiliyanpilakkil and Meskhidze*, 2011]. Another, often ignored effect is multiple scattering. *Wandinger et al.* [2010] showed that CALIOP underestimates extinction coefficients up to about 30% in the case of Saharan dust plumes over the North Atlantic due to ignoring the significant multiple–scattering effects caused by forward scattering of large dust particles.

Attempts to characterize the aerosol distribution over the ocean with shipborne lidars started in the 1990s. Single–wavelength micropulse lidars (MPL, [*Spinhirne et al.*, 1995; *Campbell et al.*, 2002]) were used during field campaigns like INDOEX [*Welton et al.*, 2002], ACE 2 [*Welton et al.*, 2000], ACE–Asia [*Schmid et al.*, 2003], SAFARI 2000 [*Campbell et al.*, 2003], or during a meridional Atlantic cruise of the RV Ron Brown in the framework of AEROSOL99 [*Bates et al.*, 2001]. Several cruises of the RV Mirai were used to perform dual–wavelength backscatter (532 and 1064 nm) and polarization lidar measurements from 1999 to 2001 in the northern west Pacific region [*Sugimoto et al.*, 2000; *Sugimoto et al.*, 2001]. Recently, a single backscatter and polarization lidar aboard the RV Marion Dufresne observed mixed layers of marine and biomass–burning aerosol in an altitude of about 3 km height at the west coast of South Africa during the Kerguelen Aerosol Measurement from African Sources and plUmes Trajectory Reverse Analysis (KAMASUTRA) campaign [*Duflot et al.*, 2011].

The first lidar aboard Polarstern was set up during the Latitudinal Distribution and Middle Atmospheric Structure (LADIMAS) campaign (October 1991 to January 1992). The Lidar Atmospheric Measurements Program (LAMP) backscatter lidar (355, 532, and 1064 nm) observed the latitudinal distribution of the stratospheric Mt. Pinatubo plume. The highest backscatter intensities were found between 24° N and 16° S and from 22 to 27 km height [*Philbrick et al.*, 1992; *Stevens et al.*, 1994]. The Mobile Aerosol Raman Lidar (MARL) was deployed at Polarstern in 1996 and 2000. *Beyerle et al.* [1998] investigated tropical subvisible cirrus clouds, that were defined by an optical thickness smaller than 0.03 [*Sassen et al.*, 1989]. During 40 h (72%) of the measurement time cirrus clouds were detected. 41% of the cirrus clouds were subvisible. The authors reported that no clouds were observed above 16 km height. During the cruise in 2000 two Saharan dust plumes were observed [*Immler and Schrems*, 2003]. They extended from 2–6 km and from 2–4 km height. This range was below the height of complete overlap of the laser beam and the receiver field of view of MARL which was designed for observations of the upper troposphere and stratosphere only.

Even though shipborne lidar observations have been performed since about 20 years, mostly simple backscatter lidars were used for continuous operation. Such systems however require assumptions on the lidar ratio in the data analysis in order to obtain the radiation–relevant particle extinction coefficient or the AOT. Tropospheric observations with Raman lidar or high–spectral–resolution lidar would be desirable to gain improved knowledge on aerosol extinction over the oceans as it was suggested by the GAW Aerosol Lidar Observation Network (GALION) initiative [*Bösenberg and Hoff*, 2008]. As part of OCEANET–Atmosphere the portable multiwavelength Raman and polarization lidar Polly^{XT} took part at three meridional transatlantic cruises of Polarstern in 2009 and 2010 and demonstrated its potential for continuous long–term observations of aerosols and clouds. The results are presented in the following.

5.2 Case studies

5.2.1 Saharan dust

The Saharan desert covers about 40% of the African continent and is the largest desert on Earth. It is bounded by the Sahel region, the Atlantic, the Mediterranean, and the Red Sea. Annual precipitation ranges from 10 to 50 mm. Higher amounts of precipitation and vegetation occur only at the borders of the desert and in elevated areas like the Ahaggar Mountains. The majority of the Saharan surface is dominated by rocks, gravel, and sand [*Warner*, 2004]. The soil is mobilized by surface winds [*Kok*, 2011; *Knippertz and Todd*, 2012] and suspended into the atmosphere as Saharan dust aerosol. From satellite observations it was found that the emissions of dust show a seasonal pattern with maximum emissions in the first half of the year [*Prospero et al.*, 2002; *Schepanski et al.*, 2007]. The desert dust reaches the free troposphere and is advected across the entire tropical Atlantic to the Caribbean [*Ansmann et al.*, 2009; *Nowottnick et al.*, 2011] or across the Mediterranean and the northern Atlantic to Europe [*Müller et al.*, 2003; *Seifert et al.*, 2010] as pure dust or mixed with biomass–burning smoke [*Prospero and Carlson*, 1972; *Liu et al.*, 2008b; *Tesche et al.*, 2009; *Baars et al.*, 2011].

At the first cruise in fall 2009 Polarstern passed the west coast of northern Africa at the end of October. On 31 October 2009 a lofted aerosol layer was observed with Polly^{XT} (Fig. 5.2, bottom). The aerosol–laden air mass was separated from the MBL, which

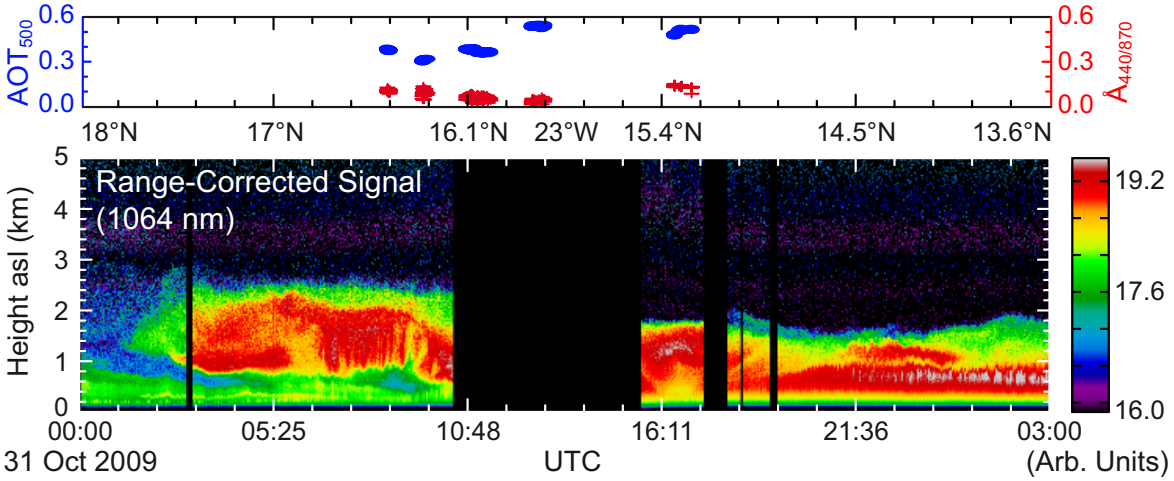

Figure 5.2: Top: Sun–photometer–derived aerosol optical thickness (AOT, 500 nm) and Ångström exponent (440/870 nm) on 31 October 2009. Bottom: Height–time display of 1064–nm range–corrected signal measured with lidar. The lidar observation was interrupted from 10:00 to 15:00 UTC due to high sun.

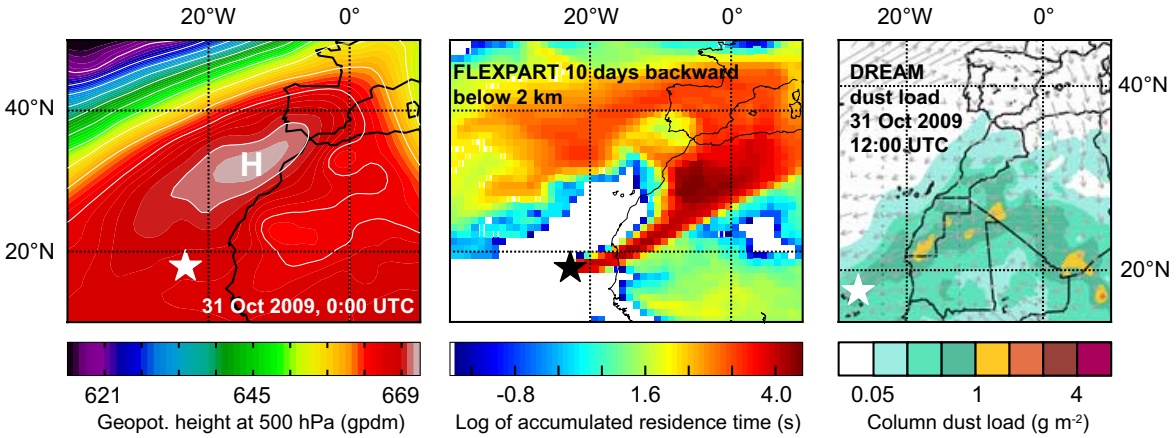

Figure 5.3: Left: Map of geopotential height at 500 hPa on 31 October 2009, 0:00 UTC. Center: FLEXPART 10–day backward simulation related to the lidar observation (Fig. 5.2) between 1200 and 2800 m height from 3:00 to 6:00 UTC on 31 October 2009. Right: Dust column–integrated concentration at 12:00 UTC (DREAM simulation). A star in each figure indicates the position of the RV Polarstern.

reached to heights of 500 to 800 m. The base of the lofted layer was at about 900 m, the top at about 2.5 km. In the afternoon the clear separation of the layer from the MBL disappeared (Fig. 5.2, bottom). Sun–photometer–derived AOT (Fig. 5.2, top) were up to 0.54 at 500 nm and $\mathring{A} < 0.11$ at 440/870 nm indicating the presence and dominance of dust.

Figure 5.3 (left) shows the geopotential height at 500 hPa on 31 October 2009. A high–pressure system above the west coast of Morocco advected air masses along the western flank of the Atlas Mountains. The Mediterranean air masses dried out and heated up above the northern Sahara in Algeria. FLEXPART 10–day backward simulations reveal the Saharan region as origin of the aerosol (dark red colors in Fig. 5.3, center). DREAM dust model results show an increased column dust load above the Atlantic at the position of Polarstern (white star in Fig. 5.3, right) by dark green coloring. According to the available meteorological information (GDAS1, HATPRO, see Fig. 5.4 a), the relative humidity was 40%–60% in the MBL (top height at 600 m according to GDAS1) and 15%–25% in the lower free troposphere (HATPRO, GDAS1).

Mean profiles of the particle backscatter and extinction coefficients for the time period from 3:20 to 5:20 UTC are shown in Fig. 5.4. AOT for dust was only 0.22 for the height range from 800–3000 m. The low extinction and backscatter–related Ångström exponents of 0.09 ± 0.16 and 0.12 ± 0.02, respectively, at heights from $1.1 - 2.4$ km also clearly indicate the presence of Saharan dust. The backscatter coefficient at 1064 nm (red line in 5.4 b) was about 20%

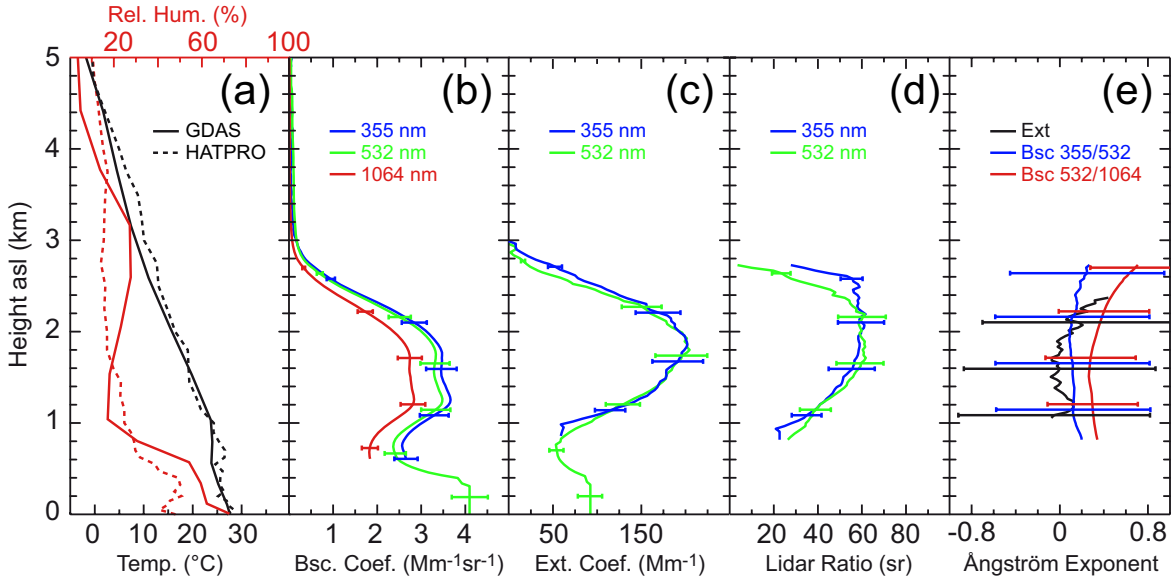

Figure 5.4: (a) Profiles of temperature (black) and relative humidity (red) determined from GDAS1 (solid, 3:00 UTC) and with HATPRO (dotted, averaged between 03:20 and 05:20 UTC) on 31 October 2009. Lidar–derived profiles of mean (b) particle backscatter coefficients, (c) particle extinction coefficients, (d) related lidar ratios and (e) related Ångström exponents for the time period from 3:20 to 5:20 UTC.

lower than at 532 nm, corresponding to an Ångström exponent of 0.33 ± 0.06 (blue curve in Fig 5.4 e). This is in good agreement with SAMUM–1 and SAMUM–2 observations [*Tesche et al.*, 2009, 2011; *Groß et al.*, 2011b]. Mean desert–dust lidar ratios of 50–60 sr at both wavelengths are also in very good agreement with previous observations [*Tesche et al.*, 2009, 2011; *Groß et al.*, 2011b].

It has to be mentioned that the depolarization–dependent transmission in the 355–nm channel could not be corrected by polarization measurements (as described in *Mattis et al.* [2009]) due to a failure of the depolarization channel. Because of the good agreement with SAMUM results, a 355–nm particle depolarization ratio of 26% [*Freudenthaler et al.*, 2009] was assumed to correct the 355–nm signals. After this correction of the raw signals, the 355–nm particle backscatter coefficient was computed. The backscatter coefficients as well as the respective lidar ratios are shown in Fig. 5.4, too. Again, the agreement with findings of SAMUM is very good [*Tesche et al.*, 2009; *Groß et al.*, 2011b].

Three overpasses of CALIPSO occurred in the area of Polarstern on 30 October 2009 and 31 October 2009 (white lines in Fig. 5.5 c). Forward and backward trajectory ensembles

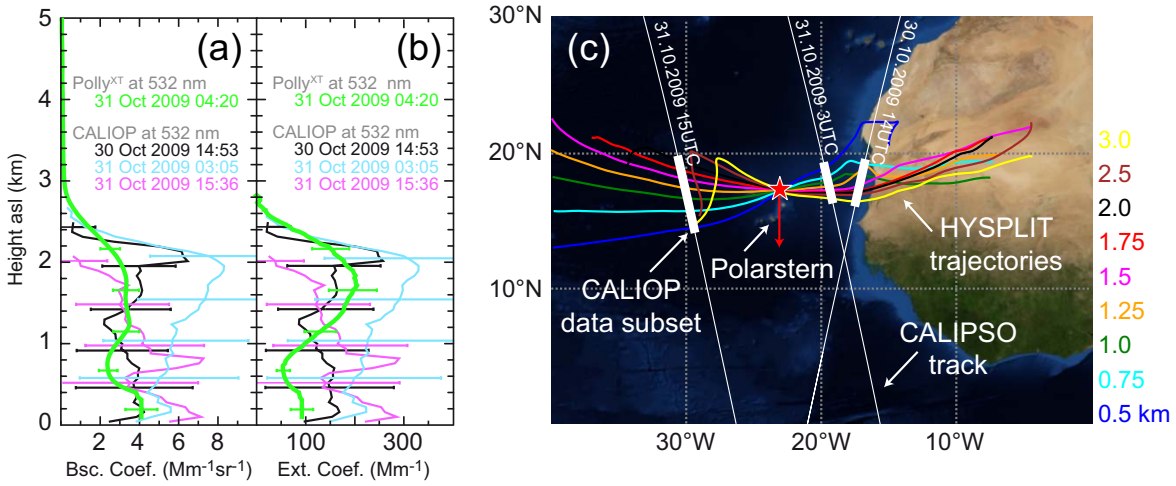

Figure 5.5: Profiles of (a) particle backscatter coefficient and (b) extinction coefficient at 532 nm of CALIOP data subsets from 30 October 2009, 14:53 UTC (black, profiles 1686 to 1749), 31 October 2009, 03:05 UTC (cyan, profiles 2750 to 2803), and 31 October 2009, 15:36 UTC (magenta, profiles 2706 to 2819), and derived with Polly^{XT} on 31 October 2009 between 03:20 and 05:20 UTC (green). (c) Map of the overpasses of CALIPSO (thin white lines), HYSPLIT 72–hours forward and backward trajectory ensembles starting on 31 October 2009 at 4:20 UTC (colored lines), periods of observations of CALIOP (thick solid white lines) used for comparisons, and the position of the RV Polarstern (red star and red arrow).

(colored lines in Fig. 5.5 c) were calculated with HYSPLIT for the analyzed aerosol layers in Fig. 5.4 to determine CALIOP observational periods that can be used for comparisons with the Polarstern lidar data. The CALIOP data in the range of the trajectories were selected under the assumption of stable atmospheric conditions and under consideration of DREAM simulations of the column dust load from 30–31 October 2009. The selected data subsets of CALIOP are shown by thick white lines in Fig. 5.5 c. As an example, Fig. 5.6 (left) shows the height–time display of the attenuated backscatter determined from the CALIOP observations on 31 October 2009, 3:05–3:06 UTC. Above the surface (straight red line) a lofted aerosol layer is observed, indicated by yellow to dark red coloring. An automatic aerosol identification scheme is applied to the CALIOP data (Fig. 5.6, center) [*Liu et al.*, 2010]. The aerosol from the surface to 2.2 km height is categorized as dust and polluted dust as indicated by yellow and brown colors in Fig. 5.6 (right) [*Omar et al.*, 2009].

The profiles of the particle backscatter and extinction coefficients at 532 nm are presented in Fig. 5.5 a and b, respectively. The agreement of the different observations is good, keeping the different positions of CALIOP (laser footprint was 400–800 km west or east of Polarstern), measurement times, and possible variations in the dust load in mind.

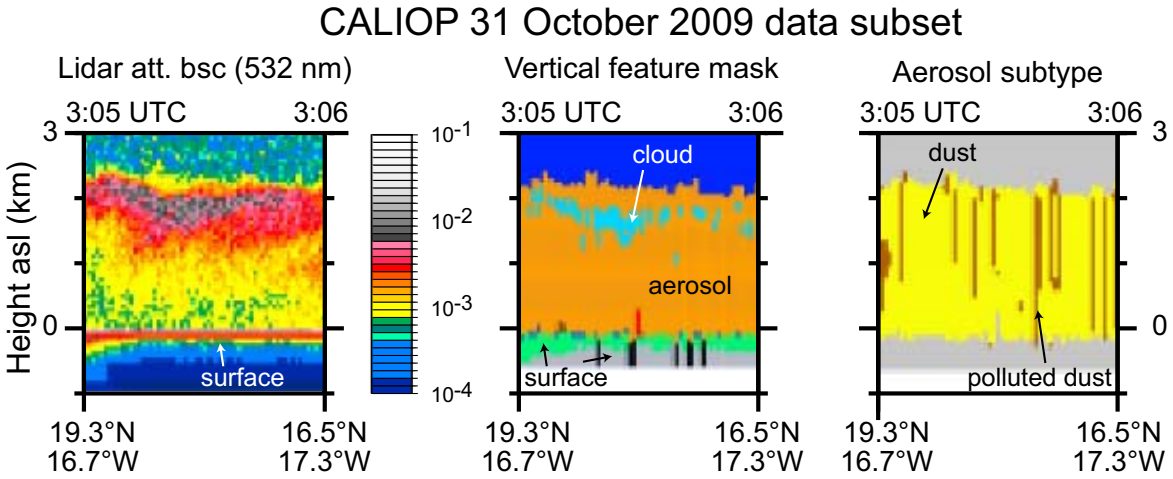

Figure 5.6: Left: Attenuated backscatter coefficient at 532 nm determined from CALIOP measurements on 31 October 2009, 3:05 UTC (profiles 2750 to 2803). Center: The related vertical feature mask indicated an aerosol–free atmosphere (dark blue), clouds (cyan), aerosols (orange), and surface (green and grey). Right: Aerosol typing after *Omar et al.* [2009].

5.2.2 Mixed dust/smoke layers

During the second cruise ANT-XXVI/4 extended lofted aerosol layers were observed at the west coast of northern Africa from 8–21° N, 23° W (over a north–south distance of more than 1400 km) over several days. Figure 5.7 d shows lidar measurements between 30 April 2010 and 5 May 2010 together with simultaneous Sun photometer, HATPRO, and pyranometer measurements. Sun photometer measurements determined maximum 500–nm AOTs of up to 0.3 on 2 May 2010 and corresponding $\AA < 0.3$ (Fig. 5.7 a). Figure 5.7 b shows the LWP determined with HATPRO. The curve of the LWP is in good agreement with the lidar observations. Time periods that show MBL clouds, which totally attenuate the lidar beam, show peaks in the LWP, e. g., during the night from 1–2 May and 3–4 May 2010. The pyranometer measurements in Fig. 5.7 c indicate the frequent occurrence of MBL clouds, e. g., on 1 and 4 May, and almost cloud–free conditions on 2 May. Sky images are presented in Fig 5.8. At 12:00 UTC on 2 May 2010 cloud–free conditions are given, while on 4 May 2010 clouds were observed. Note the effect of the vessel's superstructure.

Figure 5.9 illuminates the origin of the aerosol plumes. On 30 April 2010, 18:00 UTC Polarstern (black star in Fig. 5.9, left) was located more than 1000 km west of an extended area of biomass–burning activity in western Africa (Fig. 5.9, center). Marine aerosols most probably prevailed in the MBL, whereas the lofted aerosol layer contained biomass–burning smoke as well as desert dust (Fig. 5.9, center and right) as the SAMUM observations

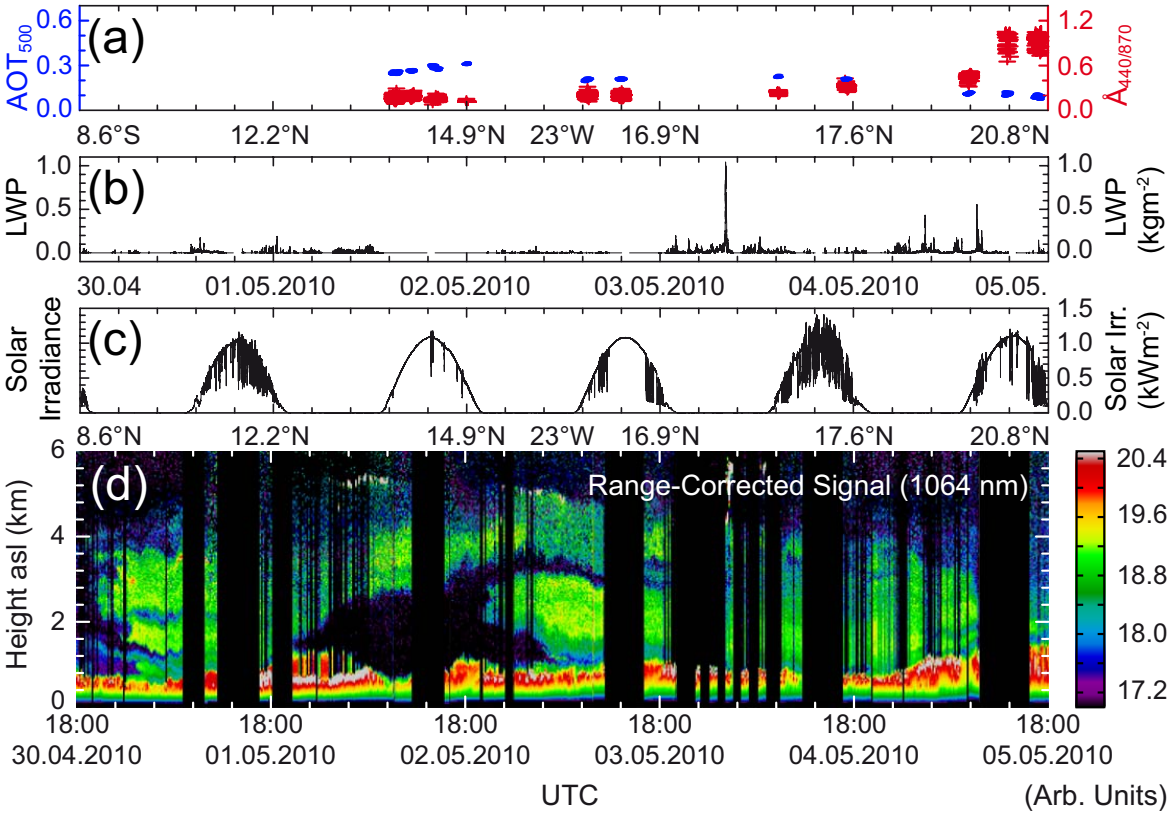

Figure 5.7: (a) Sun–photometer–derived aerosol optical thickness (AOT, 500 nm) and Ångström exponent (440/870 nm) on 30 April 2010, (b) liquid–water path (LWP) derived from HATPRO observations, (c) solar irradiance measured with pyranometer, (d) height–time display of the lidar backscatter signal. Above the MBL (bottom part in red) extended aerosol layers up to 5 km are observed (in green) over several days.

Figure 5.8: Sky images taken on (left) 2 May 2010 at 12:00 UTC and on (right) 4 May 2010 at 18:00 UTC.

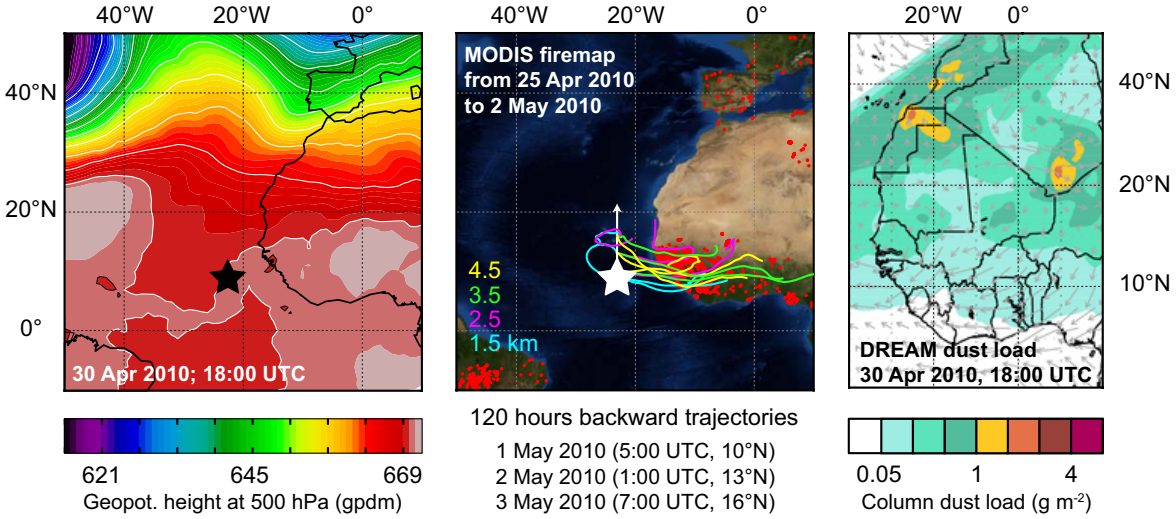

Figure 5.9: Left: Geopotential height at 500 hPa at 18:00 UTC on 30 April 2010. Center: Firemap derived from MODIS measurements and HYSPLIT 120–hour backward trajectories. The observed periods are given at the bottom. Right: DREAM simulations of column dust load at 18:00 UTC. The stars indicate the position of Polarstern on 30 April 2010. The white arrow shows the cruise track from 30 April to 5 May 2010.

show [*Tesche et al.*, 2011; *Groß et al.*, 2011b]. Backward trajectories are presented from 1.5 to 4.5 km height with respect to the lidar observation (Fig. 5.7 d). Only on 3 May 2010 the backward trajectories in the range from 1.5 to 2.5 km height do not cross the area of biomass–burning activity.

Figure 5.10 presents profiles of the particle backscatter coefficient (a–c), extinction coefficient (d–f), and corresponding lidar ratios (g–i), Ångström exponents (j–l), and linear depolarization ratios (m–o), which were determined from lidar measurements between 1 and 3 May 2010. The profiles of the particle backscatter coefficient (a–c) show the layered structure of the MBL and the lofted layers, which are already shown in Fig. 5.7 d. In the top panel of Fig. 5.10 two lofted layers show up in the profiles of the particle backscatter coefficient (Fig. 5.10 a) on 1 May 2010. The lower layer extends from 1.3 to 1.9 km height, the upper layer extends from 2.4 to 3.5 km height in the time period analyzed. Mean AOTs of 0.15 and 0.11 (355 and 532 nm) for the upper layer, and 0.08 and 0.05 for the lower layer result from the extinction profiles. The mean lidar ratios were 61 ± 4 sr and 45 ± 11 sr for the upper layer and 59 ± 5 sr and 45 ± 2 sr for the lower layer at 355 and 532 nm, respectively. The mean extinction–related (355/532) and backscatter–related (355/532 and 532/1064 nm) Ångström exponents of the upper layer (lower layer) were 0.7 ± 0.3 (1.1 ± 0.2), 0.0 ± 0.1 (0.2 ± 0.1), and 0.9 ± 0.0 (1.0 ± 0.1), respectively. The mean particle linear

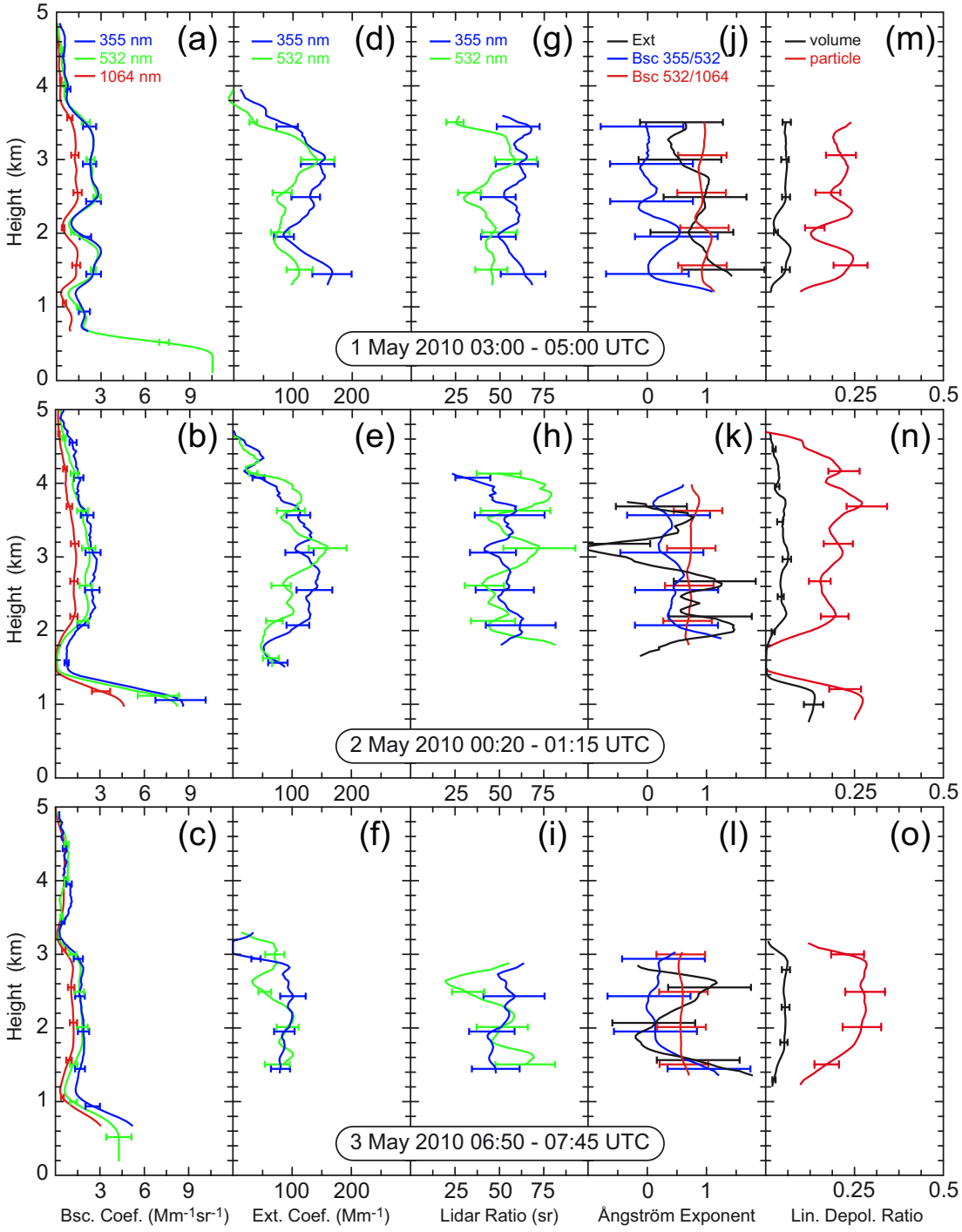

Figure 5.10: Profiles of particle backscatter coefficient (a-c), extinction coefficient (d-f), lidar ratio (g-i), Ångström exponent (j-l), and the particle and volume linear depolarization ratio (m-o). Top panel 1 May 2010 from 3:00 – 5:00 UTC, center 2 May 2010 from 0:20 – 1:15 UTC, and bottom 3 May 2010 from 6:50 – 7:45 UTC.

depolarization ratio was 21% ± 2% in the upper layer and 22% ± 3% in the lower layer. The mean lidar ratio at 355 nm is higher than the typical value for pure dust (=55 sr), and the particle linear depolarization ratio is smaller than the pure–dust values of >26% [*Groß et al.*, 2011b]. Together with the high Ångström exponents with respect to the extinction and the backscatter coefficients at 532 and 1064 nm, these values suggest a mixture of biomass–burning smoke aerosol and dust [*Tesche et al.*, 2011].

On 2 May 2010 only one layer, ranging from 2–5 km height, was observed above the MBL as is shown in the center panel of Fig. 5.10 and Fig. 5.7 (bottom). The mean AOTs were 0.22 (355 nm) and 0.20 (532 nm) and the lidar ratios were 52 ± 5 sr (355 nm) and 58 ± 12 sr (532 nm), respectively. The extinction–related Ångström exponent was 0.4 ± 0.4 as well as the backscatter–related Ångström exponent between 355 and 532 nm. The backscatter–related Ångström exponent between 532 and 1064 nm was 0.8 ± 0.1, the linear particle depolarization ratio was 20% ± 3%, i. e., observed elevated aerosol can be regarded to be of the same type as observed on 1 May 2010.

The bottom panel of Fig. 5.10 shows vertical profiles of the optical properties of a new lofted aerosol layer (Fig. 5.7) that was observed on 3 May 2010. In the time period from 6:50 to 7:45 UTC the layer extended from 1.6 to 2.9 km height. The mean AOTs of the layer were 0.12 and 0.10 (355 and 532 nm). The mean lidar ratios were 52 ± 5 sr (355 nm) and 46 ± 13 sr (532 nm). On average the Ångström exponents were smaller than in the examples before. The mean extinction–related Ångström exponent was 0.4 ± 0.4, the mean backscatter–related Ångströms were 0.2 ± 0.1 (355/532 nm) and 0.6 ± 0.0 (532/1064 nm). The mean particle linear depolarization ratio was 27% ± 2%. The analysis of the observations from 30 April to 5 May 2010 gives evidence that the first observed lofted layers were mixtures of dust and biomass–burning aerosol. After *Tesche et al.* [2009] the fraction of dust and biomass–burning smoke aerosol can be estimated from the particle linear depolarization ratio [*Ansmann et al.*, 2011b; *Baars et al.*, 2011; *Groß et al.*, 2011b]. By assuming a particle linear depolarization ratio of 25%–29% for pure dust, and of 3%–5% for smoke, the first observed lofted layers showed a smoke fraction of 10%–30%. The second lofted layer was found to be of pure dust.

The MBL was affected by the continental aerosols, too. On 1–2 May 2010 the values of the backscatter coefficient in the MBL were comparably high (see Fig. 5.22 below). If the usual AOT of the MBL caused by marine aerosol is ≈0.05 at 532 nm (see below), continental aerosol contributed with an AOT of 0.13 and 0.18 to the MBL AOT and roughly 50%

and 40% to the backscatter coefficient on 1 May and 2 May 2010, respectively. On 3 May 2010 the MBL can be considered as pure marine (MBL AOT of 0.06). The lidar derived AOT values of the MBL and the lofted layers are in agreement with the Sun photometer observations (Fig. 5.7 a).

5.2.3 Patagonian dust

During the first cruise ANT-XXVI/1 below 20° S Polarstern changed its direction towards south west until it reached the Strait of Magellan and finally Punta Arenas. The Strait of Magellan is the southern boundary of the Patagonian desert. The desert is surrounded by the Andean Mountains to the west, the Rio Colorado to the north, and the Atlantic to the east. Its position is highlighted in Fig. 5.11 (left). Patagonia is the only desert in the high southern latitudes. Its climate is dominated by the westerlies which have to cross the Andean Mountains in advance. As a consequence, usually discharged clouds reach Patagonia, resulting in less precipitation and sparse vegetation consisting mainly of grass [*Warner*, 2004]. Troughs of the Antarctic low–pressure belt often force constant and strong winds which exceed 25 m s^{-1} and produce dust emissions from the gravel desert surface by erosion [*Labraga*, 1994; *Gaiero et al.*, 2007; *Gassó et al.*, 2010]. This dust can be transported across the southern Atlantic [*Gassó and Stein*, 2007; *Li et al.*, 2010; *Johnson et al.*, 2011]. Oceanic measurements aboard Polarstern of titanium, which is a tracer for dust, indicate the long–term existence of dust deposition from the Patagonian desert to the Atlantic [*Dammshäuser et al.*, 2011].

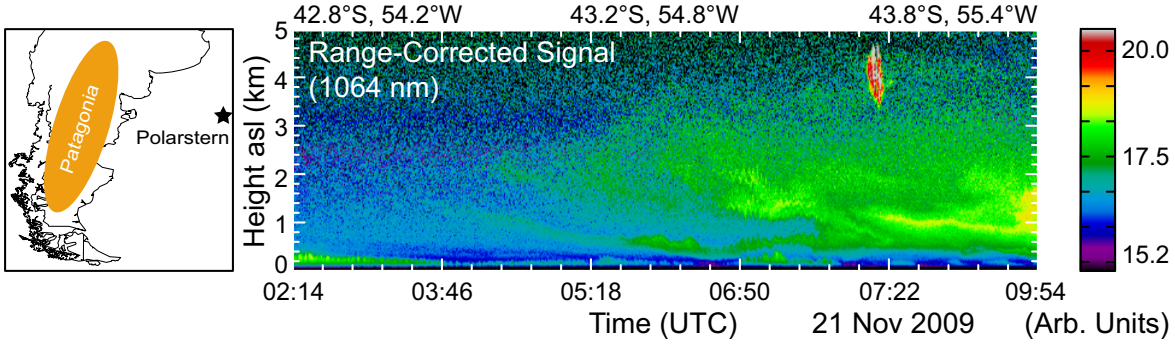

Figure 5.11: Left: Map of South America and location of Patagonia and Polarstern. Right: Lidar observation performed on 21 November 2009. Shown is the height–time display of the range–corrected signal.

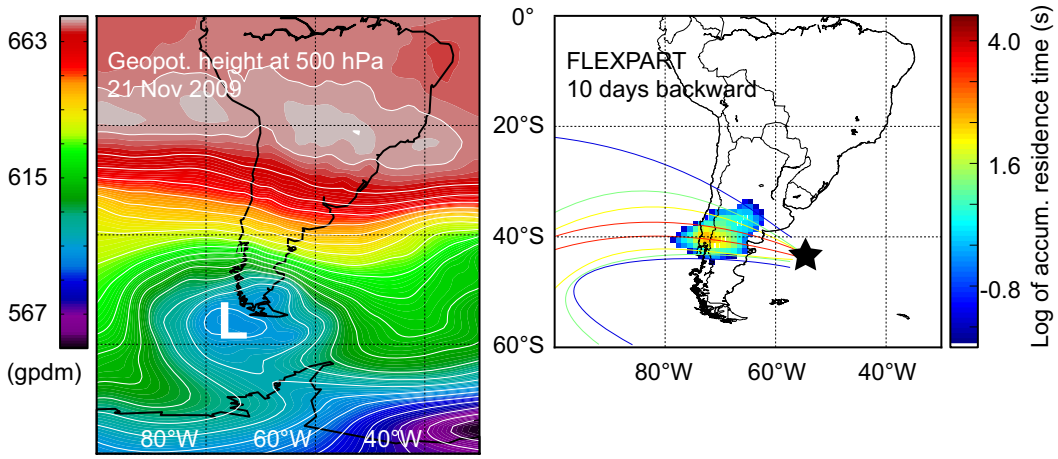

Figure 5.12: Left: Geopotential height at 500 hPa above South America and Antarctica on 21 November 2009, 0:00 UTC. Right: FLEXPART simulations regarding the origin of the air masses observed between 1 and 4 km height above the RV Polarstern (star) on 21 November 2009, 6:00–8:00 UTC. The accumulated residence time distribution of the 10–day backward simulation from 11 November to 21 November 2009 is shown by colored contour lines. A snapshot of the residence time distribution on 20 November 2009 is given by the colored area.

Polarstern passed the Patagonian desert at a distance of about 1000 km to the east. AOTs <0.1 at 500 nm were measured with Sun photometer (Fig. 5.19, see below) and yield no evidence of lofted layers above the MBL. However, the lidar observed optically thin aerosol particle plumes from 13 to 23 November 2009.

Figure 5.11 (right) shows the height–time display of the lidar observation in the morning of 21 November 2009. At the beginning the MBL top was of about 350 m height. At about 4:00 UTC lofted aerosol layers that extended up to 4 km height were observed. On that day a cyclone of the Antarctic low–pressure belt was situated southwest of South America (denoted by L in Fig. 5.12, left). Strong westerly winds occurred in the latitudinal belt from 40°–45° S. According to the isohypse 10–minute average wind speeds at 10 m height were about 25 m s^{-1} and triggered the dust uptake into the atmosphere.

Figure 5.12 (right) shows FLEXPART simulations that were used to determine the origin of the air parcels observed with lidar from 6:00–8:00 UTC on 21 November 2009. The colored area indicates the residence region of the observed air parcels on 20 November 2009, the day before the measurement. Warm colors show the highest residence time of the observed air parcels in the latitudinal belt of the Patagonian desert. The colored contour lines in Fig. 5.12 (right) show the results of the 10–day backward simulations. The highest

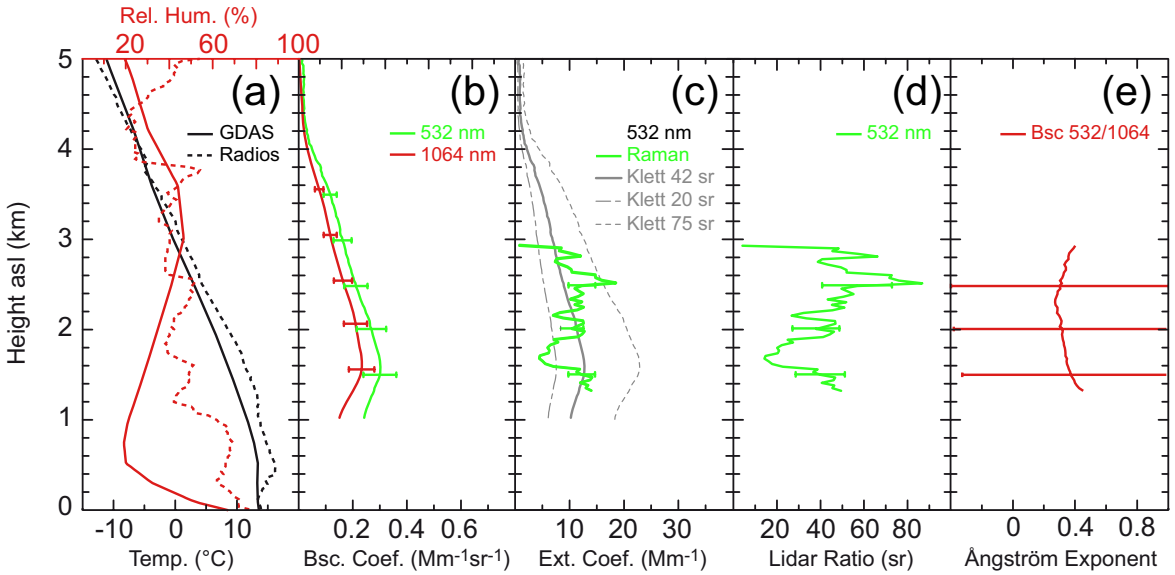

Figure 5.13: (a) Meteorological conditions shown by profiles of temperature (black lines) and relative humidity (red lines) on 21 November 2009 for GDAS–based modeled atmosphere (solid lines) at 06:00 UTC and for the radiosonde launch (dotted line) aboard Polarstern at 11:09 UTC. (b–e) Analysis results from Polly^{XT} observations on 21 November 2009 from 6:00 to 8:00 UTC.

accumulated residence time of the observed air parcels is represented by the red curves which cross the Patagonian desert. The intensive orange–colored area and the red curves provide the information that the air mass detected with lidar crossed the Patagonian desert with very high probability.

The in–depth analysis of the lidar data was difficult because of the rather low AOT of the lofted aerosol plume of 0.02–0.03. Keeping the high surface wind speeds above the Patagonian desert in consideration, the low AOT gives evidence of less available particulate material in the Patagonian desert that can be lifted into the atmosphere than in the Saharan desert due to the permanent high wind speeds. The vertical smoothing length was enlarged to 750 m to reduce signal noise, and the signal profiles could be used only above 1000 m height. With respect to the signal–to–noise ratio the uncertainty was estimated to 40%. The profiles of particle backscatter coefficients (Fig. 5.13 b) show an increased aerosol load up to 4 km height. According to the radiosonde temperature profile in Fig. 5.13 (a) the MBL reached up to 500 m, and the base of the lofted layer was at 1000 m. The 532-nm profile of the extinction coefficient determined with the Raman method is given in Fig. 5.13(c) by the green curve. The extinction coefficient was rather low with values around 10 Mm^{-1}. A mean lidar ratio of 42 ± 17 sr was calculated which is in the range of dust–related lidar

ratios found in the Middle East (42.6 sr) and Kanpur, India (43.8 sr) [*Schuster et al.*, 2012]. In addition, the profile of the extinction coeffcient at 532 nm was reproduced for assumed constant lidar ratios of 42 sr (suggested for Patagonian desert dust), 20 sr (indicating pure marine aerosol [*Ansmann et al.*, 2001]), and 75 sr (indicating smoke [*Tesche et al.*, 2011]) with the Klett method (Sec. 3.2.2). These approximated profiles of extinction lead to AOTs of 0.03, 0.02, and 0.05 for the plume which are much smaller than AOTs of the observed Saharan dust event in Sec. 5.2.1. A low backscatter–related Ångström exponent of 0.4 ± 0.1 at 532 and 1064 nm (see Fig. 5.13 e) indicates the presence of coarse–mode particles. The measured depolarization ratio at 355 nm provided just a qualitative information of the presence of non–spherical scatterers. For low AOT, 355 nm most of the volume linear depolarization information is related to molecular backscattering (see Sec. 3.2.4) causing a volume linear depolarization ratio of a few percent.

Another hint for the observation of large dust particles are the virgae shown at the top of the aerosol layer at about 7:15 UTC in Fig. 5.11 (right). Dust particles are known to be favorable ice nuclei and can trigger heterogeneous ice nucleation at temperatures of above $-38\,^{\circ}\mathrm{C}$ [*Ansmann et al.*, 2005; *Field et al.*, 2006; *Seifert et al.*, 2010]. In the presented case the ice nucleation was initiated at temperatures of roughly $-10\,^{\circ}\mathrm{C}$ (Fig. 5.13 a).

In contrast to the low–AOT case presented here, daily mean AOTs of >0.3 were determined with Sun photometer during the spring cruise in 2008, as presented in Fig. 5.20 (see below). *Gassó et al.* [2010] investigated a plume with AOTs of 0.35–0.45 determined with MODIS over the Southern Atlantic and concluded that dust emissions from the Patagonian desert were the reason for the notably high AOT in this typically rather clean environment.

5.2.4 Volcanic ash from the Eyjafjallajökull volcano

In the final case study, unexpected and unprecedented observations of volcanic ash plumes originating from Eyjafjallajökull (64° N, 20° W) eruptions in May 2010 are discussed. Iceland is known to be an active volcanic island in the Atlantic with seven eruptions in the last two decades. On 20 March 2010 the seismic dormancy of the Eyjafjallajökull was broken, leading to an explosive subglacial eruption on 14 April 2010 whose ash plume disrupted the European air traffic. Until 23 May 2010 ash, tephra, and SO_2 were emitted in maximum estimated fluxes of $750\,\mathrm{Mg\,s^{-1}}$ in a plume up to 9.5 km height with a total emitted mass of about 2.5–50 Tg distal ash and 0.6–23 Tg SO_2 [*Petersen*, 2010; *Schumann et al.*, 2011].

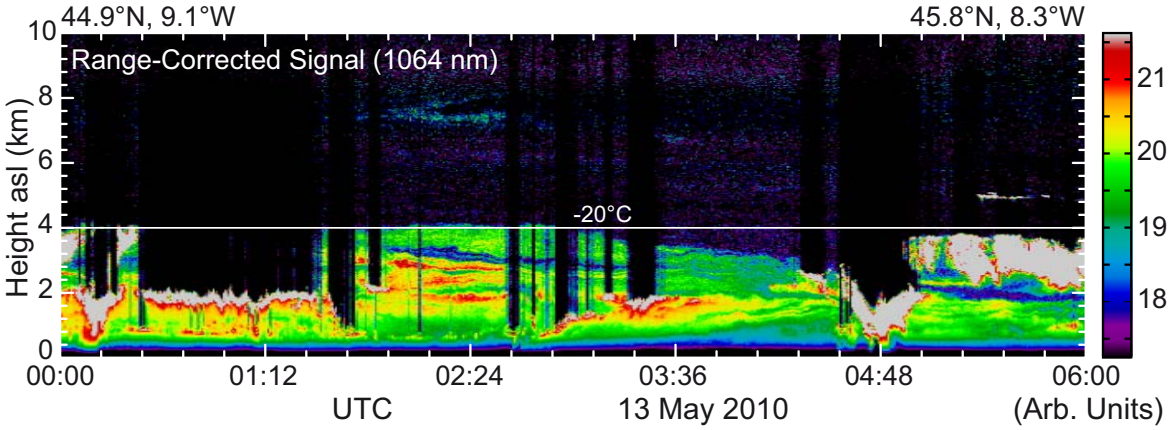

Figure 5.14: Height–time cross section of the range–corrected signal at 1064 nm on 13 May 2010. The white line denotes the cloud top temperature as obtained from GDAS1.

The most active period occurred from 14–17 April 2010. The plume was advected to northern Europe due to a high–pressure system south of Iceland. On 16 April 2010 ash was observed from 2.5 to 6 km at Leipzig, Germany. The volcanic aerosol was characterized by an ash–layer–related AOT of 0.7, a lidar ratio of 55 ± 5 sr at Leipzig and 60 ± 5 sr at Munich, and no spectral slope in the particle backscatter and extinction coefficients [*Ansmann et al.*, 2010].

After a short calm period with decreasing ash production the second active period of Eyjafjallajökull started on 5 May 2010 and was characterized by high SO_2 emission [*Petersen*, 2010]. Aboard Polarstern lofted layers were observed in the lidar measurements between 10 (west coast of Portugal) and 17 May 2010 (harbor of Bremerhaven). The observation on 13 May 2010 is presented in Fig. 5.14. The layers extended up to 4 km height and were observed in the vicinity of cloud layers producing ice virgae. A cloud–top temperature of $-20\,^{\circ}\mathrm{C}$ was determined from the GDAS1 data which indicates heterogeneous ice nucleation within the clouds (for details see Chapter 7). Studies of the ice–nucleation ability of volcanic ash during the Eyjafjallajökull outbreak showed a high efficiency [*Seifert et al.*, 2011; *Steinke et al.*, 2011].

The geopotential height at 500 hPa on 13 May 2010, 0:00 UTC, is presented in Fig. 5.15 (left). High pressure above the North Atlantic and low pressure above Iceland lead to the advection of air masses from Iceland to the Bay of Biscay. FLEXPART modeling results are shown in Fig. 5.14 (right) and confirm the prevalence of the northwesterly advection of the air masses observed aboard Polarstern (green star) from Iceland (green circle).

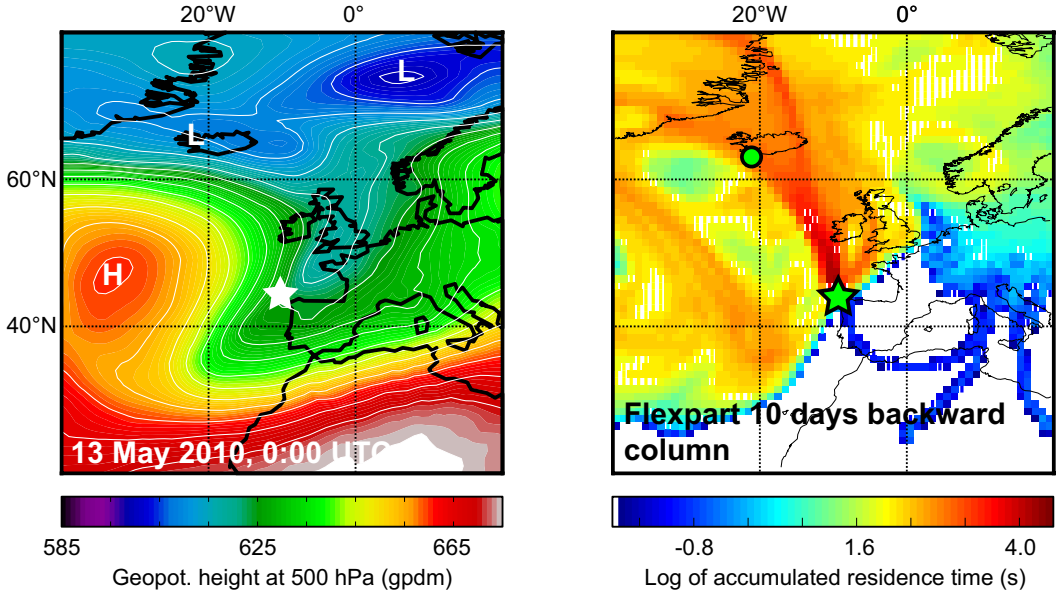

Figure 5.15: Left: Geopotential height at 500 hPa on 13 May 2010, 0:00 UTC. L denotes low–pressure systems, H high–pressure systems. Right: Map of FLEXPART 10–day backward simulations for the observed aerosol layer in 3.3–4 km between 2:20 and 2:36 UTC. The green circle denotes the Eyjafjallajökull at Iceland, stars the RV Polarstern in the Bay of Biscay.

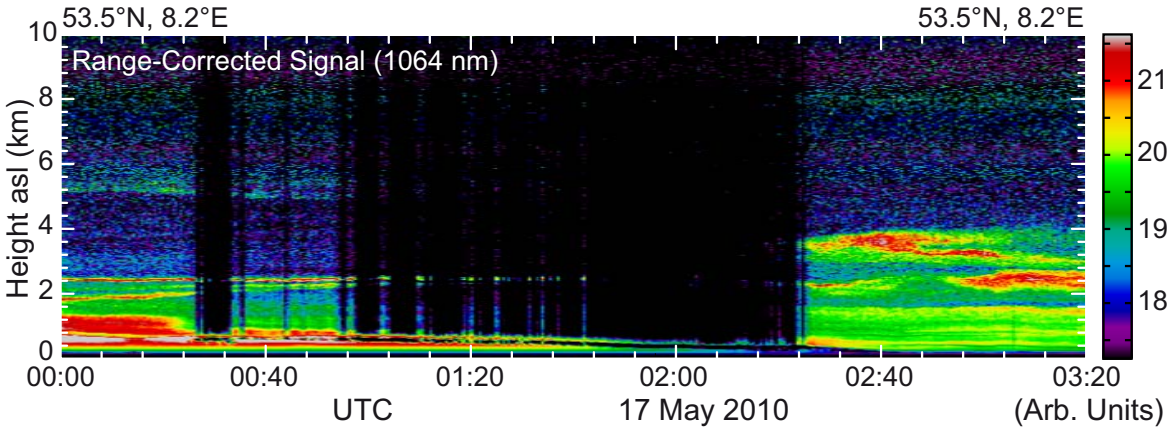

Figure 5.16: Height–time cross section of the range–corrected signal at 1064 nm on 17 May 2010.

The lidar measurements were extended until the lightening of Polarstern started in the harbor of Bremerhaven. Figure 5.16 shows the last measurement period. After the dispersion of boundary–layer clouds at 2:30 UTC two lofted layers were observed between 1.9 and 4 km height. The geopotential height at 500 hPa on 17 May 2010, 0:00 UTC, is presented in Fig. 5.17 (left). A low–pressure system (denoted by L) advected air masses towards Central Europe. FLEXPART simulations, e. g., for the lower layer (2.0–2.6 km height,

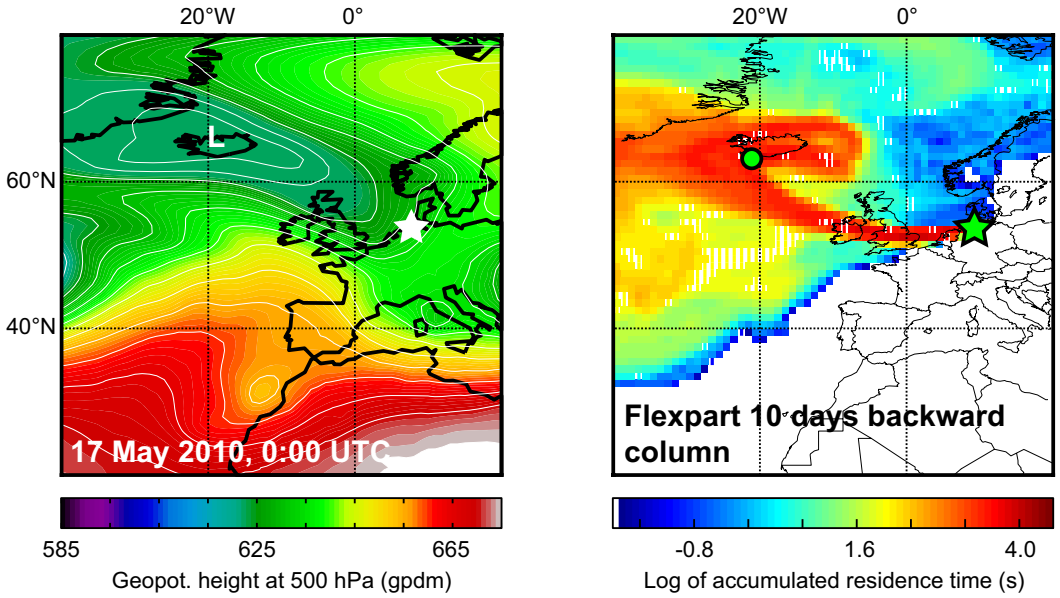

Figure 5.17: Left: Same as Fig. 5.15 for 17 May 2010 and FLEXPART 10–day backward simulations for the observed aerosol layer in 2.0–2.6 km from 2:30–3:20 UTC.

2:30–3:20 UTC) observed at Polarstern in Fig. 5.17 (right), indicate a high probability of air–mass transport from Iceland to Central Europe, too. In both cases, on 13 May 2010 and 17 May 2010, the Eyjafjallajökull (indicated by a green circle in Fig. 5.15, right and 5.17, right) emissions are advected with a high probability to the position of Polarstern (green star).

The lidar observation between 2:20 and 2:36 UTC on 13 May 2010 was analyzed to determine profiles of the particle backscatter and extinction coefficients. The determined profiles are presented in Fig. 5.18 (a–b) by dotted curves. Two lofted layers from 2.2–2.9 km and 3.3–4.2 km height were observed. From the profile of the extinction coefficient an ash–related AOT of 0.06 was determined with lidar (Sun photometer was not available due to cloud coverage). The mean lidar ratio at 355 and 532 nm was 53 ± 10 sr and 45 ± 9 sr, respectively. These values are at the lower end with regard to the values observed during the first strong eruption in April 2010 [*Ansmann et al.*, 2010; *Groß et al.*, 2012]. The mean particle linear depolarization ratios of 15% ± 3% and 13% ± 4% (lower and upper layer, respectively) are comparably small, and mean Ångström exponents of 1.1–1.6 are comparably high. The change in emissions during the dormancy of Eyjafjallajökull might be the reason that predominantly secondary aerosol particles of sulfate were observed on 13 May 2010. As a consequence, the particle depolarization ratio would decrease (more spherical particles) and the Ångström exponents would increase (small particles). Water uptake of ash particles as

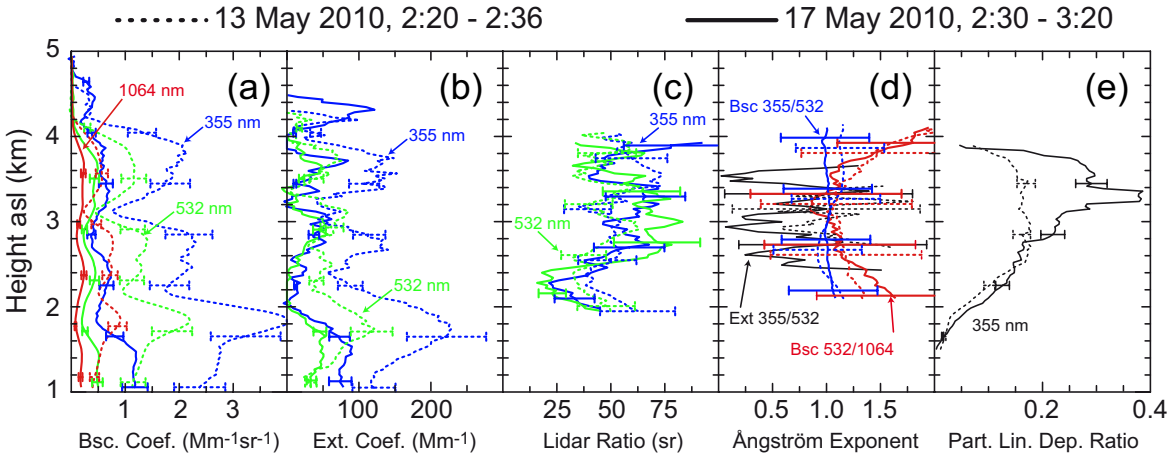

Figure 5.18: Cloud–screened profiles of (a) backscatter coefficients, (b) extinction coefficient, (c) lidar ratio, (d) Ångström exponent, and (e) particle depolarization ratio. Dotted lines denote the results for 13 May 2010, 2:20–2:36 UTC, and solid lines the results for 17 May 2010, 2:30–3:20 UTC.

investigated by *Lathem et al.* [2011] could explain the decrease in the particle depolarization ratio, but not the high Ångström exponents. A mixture with marine aerosol could only explain the low particle depolarization ratio and low lidar ratios.

From the lidar observation on 17 May 2010 the time period from 2:30–3:20 UTC was analyzed to derive the optical aerosol properties (Fig 5.18 solid lines). An AOT of about 0.04 was determined with lidar. Mean lidar ratios of 55 ± 10 sr, and 64 ± 11 sr were determined at 355 and 532 nm, respectively, which are confirmed by the observations before. The upper layer also showed enhanced particle depolarization ratios of up to 38% in a thin layer at about 3.25 km height in agreement with *Groß et al.* [2012]. The Ångström exponents are about 1 and still comparably high. No atmospheric sounding on 17 May 2010 was available from Polarstern and the meteorological station Norderney.

5.3 Statistics

The general aerosol conditions along the three cruises are described by the daily mean AOT determined from Sun photometer observations in the framework of MAN in Fig. 5.19 as function of latitude. Maximum daily mean AOT of 0.46, 0.28, and 0.32 at 500 nm were determined during fall 2009, spring 2010, and fall 2010, respectively. The corresponding Ångström exponents (500/870 nm) show low daily mean values of 0.1, 0.1, and 0.2. The highest AOT values were determined in the latitudinal belt around 14°N where the

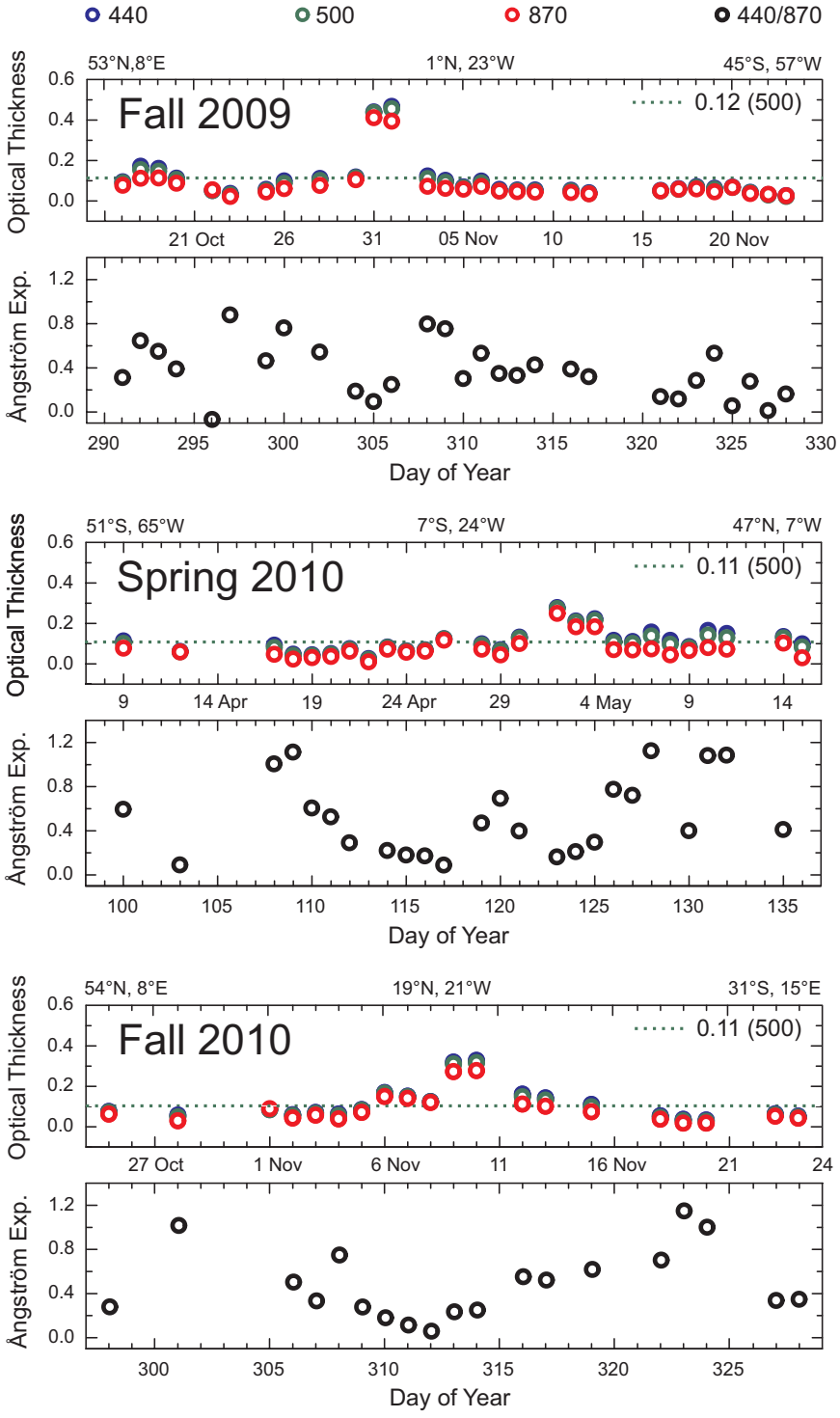

Figure 5.19: Daily mean aerosol optical thickness at 440, 500, and 870 nm and related Ångström exponents at 440/870 nm from Maritime Aerosol Network (MAN) Sun photometer measurements aboard Polarstern during the transatlantic cruises in fall 2009, spring 2010, and fall 2010. Mean 500–nm AOT values for each journey are given as dotted lines.

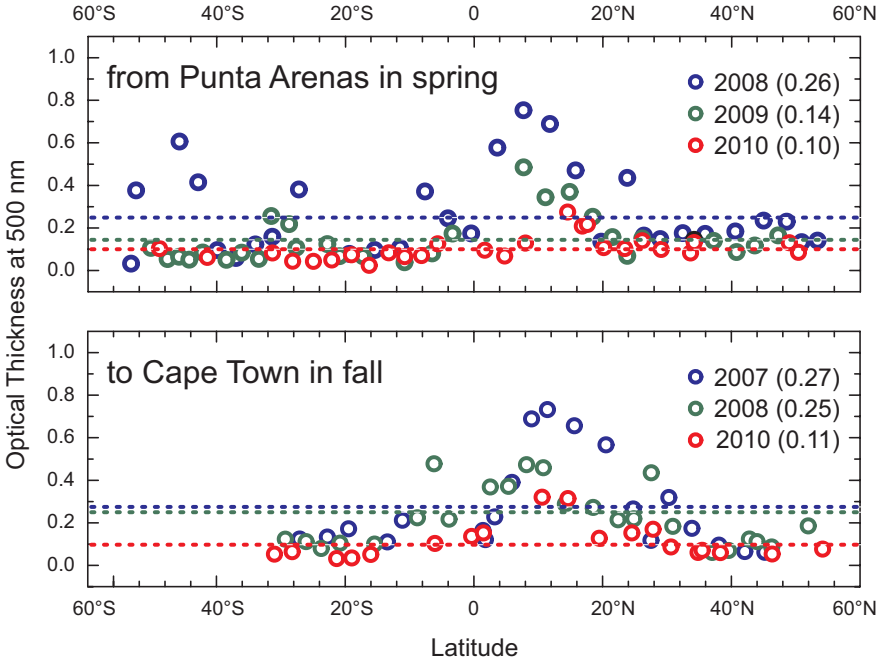

Figure 5.20: Daily mean aerosol optical thickness at 500 nm observed with Maritime Aerosol Network (MAN) Sun photometer measurements aboard Polarstern during seasonally and geographically comparable cruises in spring 2010 and fall 2010. Mean 500–nm AOT values for each journey are given as dotted lines.

Polarstern passed the west coast of Africa in a distance of 400–1000 km. Thus, we assume that large dust particles [*Dubovik et al.*, 2002] were present in the atmospheric column in addition to the marine background aerosol (see Sec. 5.1). Minimum daily mean AOT values of 0.02 (Å of 0.2), 0.02 (Å of 1.7), and 0.03 (Å of 1.0) were determined during the three cruises in the southern hemisphere.

The mean AOTs of about 0.11 ± 0.01 at 500 nm at each cruise are lower than usually above the Atlantic (0.14, Sec. 5.1). The comparison with previous transatlantic cruises of Polarstern with identical departure and arrival harbour (comparable track lines) in Fig. 5.20 shows that during the current cruises in 2009 and 2010 the mean AOT was lower by a factor of 1.4–2.6. Especially in the latitudinal belt of 0°–20° N daily mean AOTs of the previous cruises are higher. Maps of the annual mean AOTs (550 nm, see App. B) above the Atlantic from MODIS observations show that Polarstern crosses each year the outflow of the Saharan dust belt in the tropical region [*Liu et al.*, 2008a; *Ansmann et al.*, 2009; *Baars et al.*, 2011]. The remaining Atlantic regions seem to be less affected by long–range transport of continental aerosol.

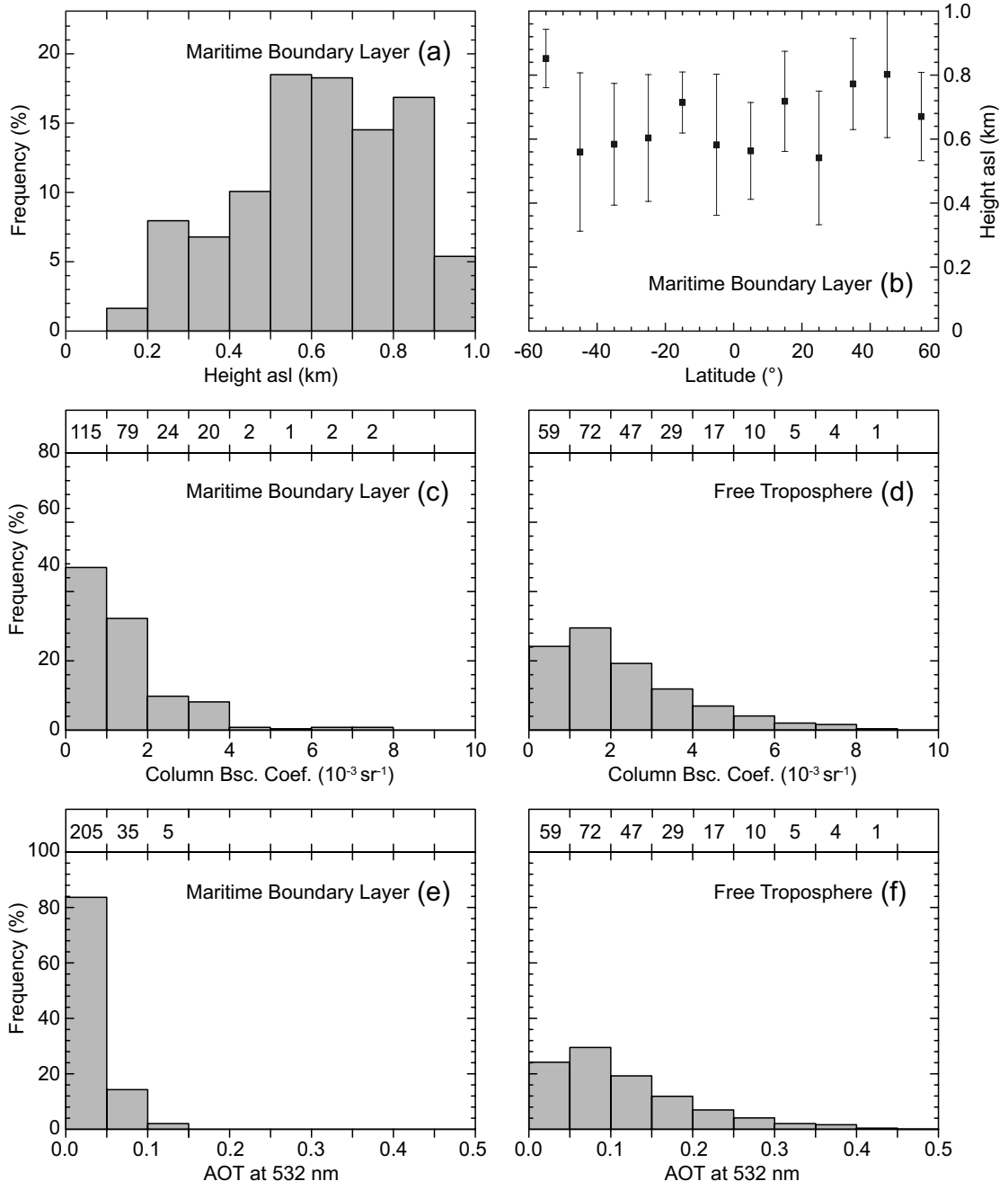

Figure 5.21: Top: Frequency distribution (a) and meridional distribution (b) of the MBL top height. Error bars indicate the mean standard deviation. Center: Frequency distribution of the column–integrated backscatter coefficient (c) within the MBL, (d) within the free troposphere in steps of $10^{-3}\,\mathrm{sr}^{-1}$. The number of cases are given at the top. Bottom: Frequency distribution of the AOT at 532 nm (e) within the MBL, (f) within the free troposphere for intervals of 0.05. The number of cases are given at the top.

The lidar measurements were used in a first step to determine the MBL top height. The MBL typically contains a much higher aerosol load than the free troposphere. Its top height can be determined with the wavelet method explained by *Baars et al.* [2008]. We found in 78% of the measurements MBL top heights of 400–900 m (Fig. 5.21 a). A correlation between latitude and MBL top height was not found. Figure 5.21 (b) shows no latitudinal differences or trends in the MBL top height within the range of the error bars (mean standard deviation). Cloud layers at the MBL top with cloud top heights up to 1.5 km occurred in 21% of the measurement time.

For a statistical analysis 246 cloud–free measurement periods (about 260 hours) were selected. Figures 5.21 (c) and (d) show the frequency of occurrence of the column–integrated backscatter coefficients in the MBL and in the free troposphere, respectively. The number of cases are presented at the top of each figure. The distribution of the column backscatter values in the free troposphere is more variable compared to the one for the MBL. However, ¿70% out of all cases show column backscatter coefficients smaller than $3\times10^{-3}\,\mathrm{sr}^{-1}$ in both the MBL and the free troposphere. The AOT can be roughly estimated from the column backscatter multiplied with a column mean lidar ratio of 20 sr (MBL) and 50 sr (free troposphere). The corresponding frequency distributions of the AOT are shown in Fig. 5.21 (bottom). Here, the reasonable contribution of lofted layers to the aerosol load in the atmospheric column above the Atlantic is shown by the much higher AOT values in the free troposphere. In contrast, the AOT in the MBL is smaller than 0.05 in more than 80% out of all cases.

All single profiles of the particle backscatter coefficients at 532 and 1064 nm for the northern midlatitudes (60°–30° N), the tropics (30° N–30° S), and the southern midlatitudes (30°–60° S) are presented in Fig. 5.22 (a–c) and Fig. 5.23 (a–c). Averaged profiles of the backscatter coefficients in each region are shown by red lines. The error bars indicate the mean standard deviation. The determined profiles of the particle backscatter coefficient over Punta Arenas and Stellenbosch are added in Fig. 5.22 (d–e) and Fig. 5.23 (d–e). Below the MBL top height well–mixed homogeneous particle conditions are assumed. Thus, the particle backscatter coefficient is set constant from the minimum measurement height down to the ground. Signals are smoothed with 330 m vertical window length for the analysis.

The distribution of the backscatter coefficient profiles (532 nm) show that lofted aerosol layers occur most frequently in the tropics (Fig. 5.22 b), and more often in the northern

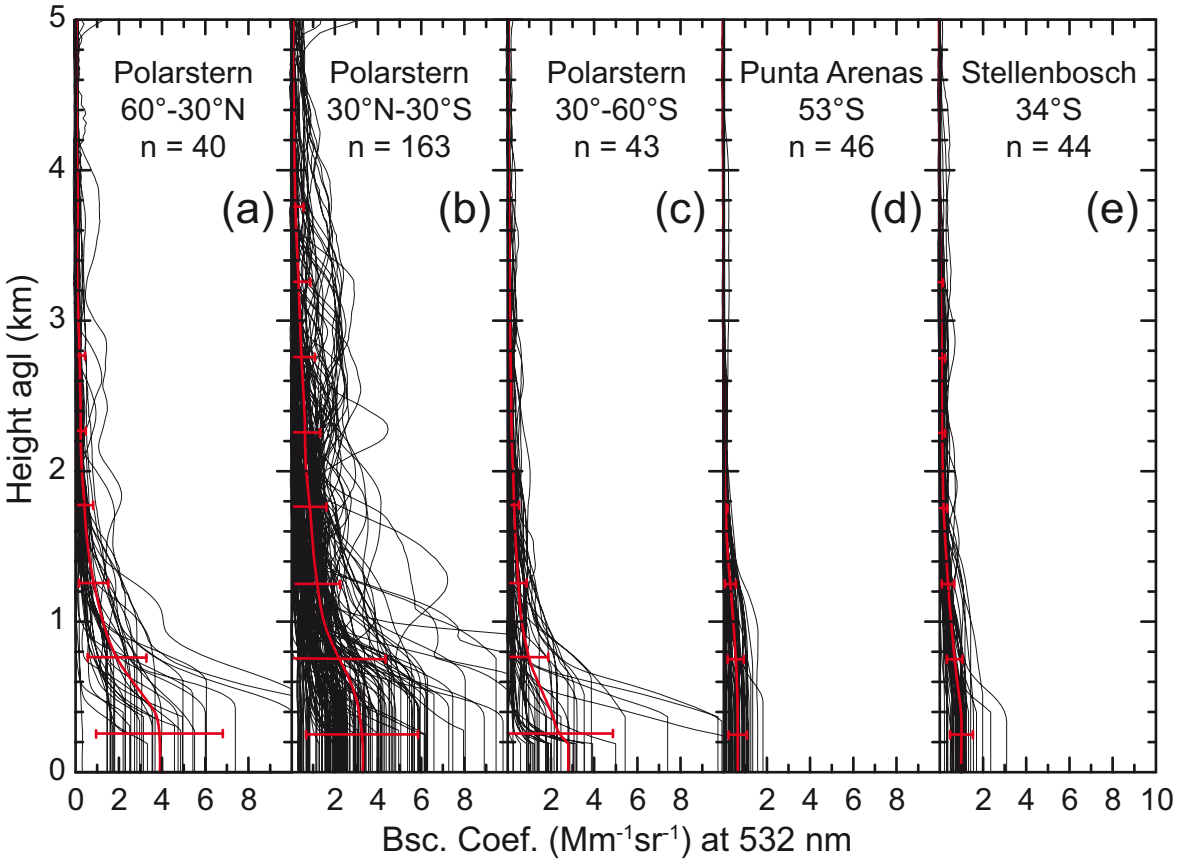

Figure 5.22: Cloud–screened profiles of the backscatter coefficient at 532 nm determined with Polly^{XT} aboard Polarstern in the (a) northern midlatitudes, (b) tropics, and (c) southern midlatitudes. In addition, lidar observations at (d) Punta Arenas and (e) Stellenbosch are shown. Red profiles are the mean profiles. Error bars show the mean standard deviation.

midlatitudes (Fig. 5.22 a) than in the southern midlatitudes (Fig. 5.22 c). Figure 5.23 presents the distribution of the backscatter coefficient profiles at 1064 nm and give further information that the lofted aerosol layers contain a reasonable contribution of coarse–mode particles, because the light scattering of fine–mode particles is less pronounced with increasing wavelength obtained. Note the comparably clean conditions over the field sites of Punta Arenas and Stellenbosch.

Mean profiles of the backscatter coefficient for 30°–15° N, 15° N–EQ, EQ–15° S, and 15°–30° S are presented in Fig. 5.24 (b). The highest aerosol concentration is found in the latitudinal belt from 15° N–EQ (3.32 times higher than the northern midlatitudes shown in Fig. 5.24 a), followed by 30°–15° N (2.51 times higher), EQ–15° S (96%), and 15°–30° S (72%). The high values of the backscatter coefficient in the tropics are mainly caused by

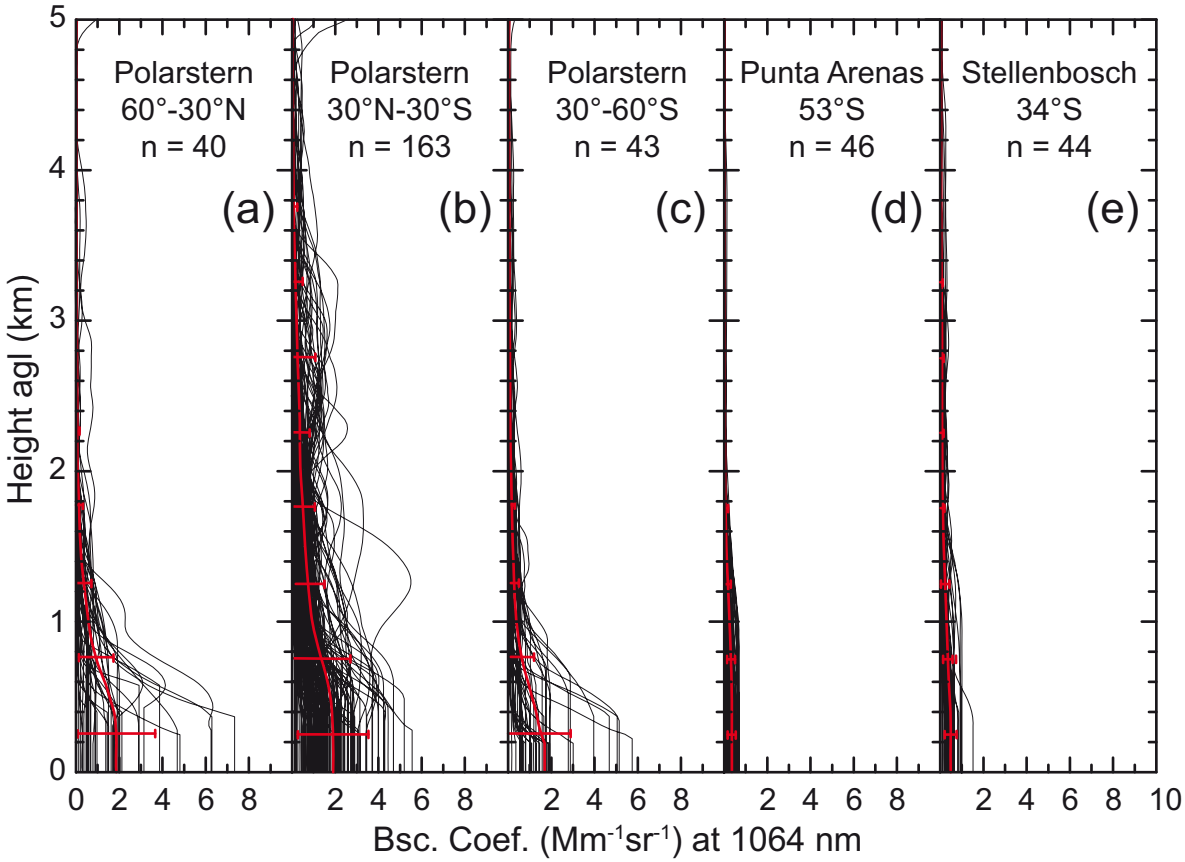

Figure 5.23: Same as in Fig. 5.22 at 1064 nm.

the outflow of dust from the Saharan region which is concentrated in the tropical latitudinal belt of the northern hemisphere. *Tesche* [2011] determined mean particle backscatter coefficients at 532 nm of 0.4 and 1.2 $Mm^{-1}\,sr^{-1}$ in the main lofted layers from 1.5 to 4 km height at Cape Verde during the winter (15 January to 14 February 2008) and summer (24 May to 16 June 2008), respectively. In the same height range we found mean particle backscatter coefficients of 0.8 and 0.65 $Mm^{-1}\,sr^{-1}$ for the latitudinal belts from 15° N–EQ and from 30°–15° N. About 4000 km west of the African coast *Baars* [2012] observed African aerosol in the Amazon basin during the wet season (April–May 2008). On average, particle backscatter coefficients at 532 nm ranged from 0.3–0.7 $Mm^{-1}\,sr^{-1}$ at altitudes from 0.3 to 3 km.

At Stellenbosch lofted layers of smoke and soil from local sources are usually observed up to 4.7 km height (Fig. 5.22 e). The aerosol profiles at Punta Arenas (Fig. 5.22 d), on the other hand, are characterized by pure marine conditions. It should be mentioned that the extinction coefficients over the southern Atlantic and Stellenbosch turn out to be similar

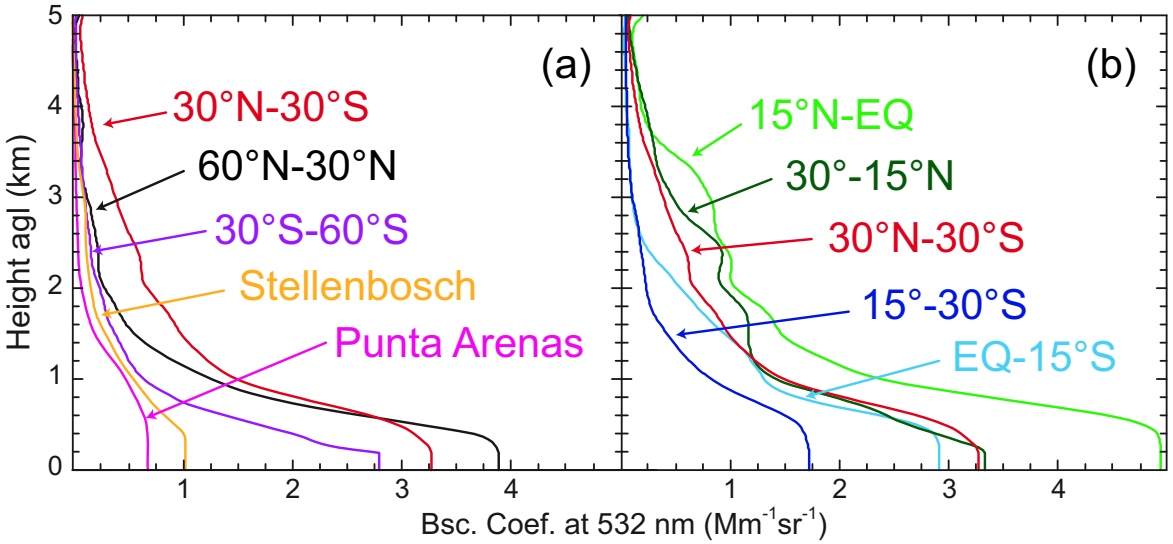

Figure 5.24: Mean particle backscatter coefficients at 532 nm (a) for the northern midlatitudes (60°–30° N), tropics (30° N–30° S), southern midlatitudes (30°–60° S), Punta Arenas, Stellenbosch, and (b) for five latitudinal belts of the tropics.

when the Stellenbosch backscatter values (orange curve in Fig. 5.24 a) are multiplied with 50 sr (lidar ratio of continental aerosol) and the South Atlantic values (dark blue curve in Fig. 5.24 b) are multiplied with 20 sr (lidar ratio of marine aerosol).

From space, CALIOP also performs lidar observations above the Atlantic. Forty one CALIPSO overpasses occurred within a distance of 200 km from Polarstern and within 1 hour of time difference during the three transatlantic cruises. Figure 5.25 (a) shows the distribution of the CALIPSO (foot print) – Polarstern distances. For each overpass the mean profile of the particle backscatter coefficient at 532 nm was determined from the CALIOP data set as described in Sec. 5.2.1. In 93% (38 cases) out of all cases, profiles of particle backscatter coefficients were available in the data subsets. Under consideration of the data confidence flags finally 28 profiles of CALIOP level 2 version 3 data were available for a comparison (see detailed explanation in App. C). These 28 overpasses are indicated by the gray bars in Fig. 5.25 (a).

Figure 5.25 (b) shows the profiles of particle backscatter coefficient at 532 nm obtained with CALIOP and with Polly^{XT}. The CALIOP profiles were vertically smoothed with 300 m, the Polly^{XT} profiles with 330 m. Polly^{XT}–derived particle backscatter coefficients were set constant in the lower MBL due to the overlap problems close to the ground. From space, CALIOP does not suffer from such overlap effects and thus shows the real structures down

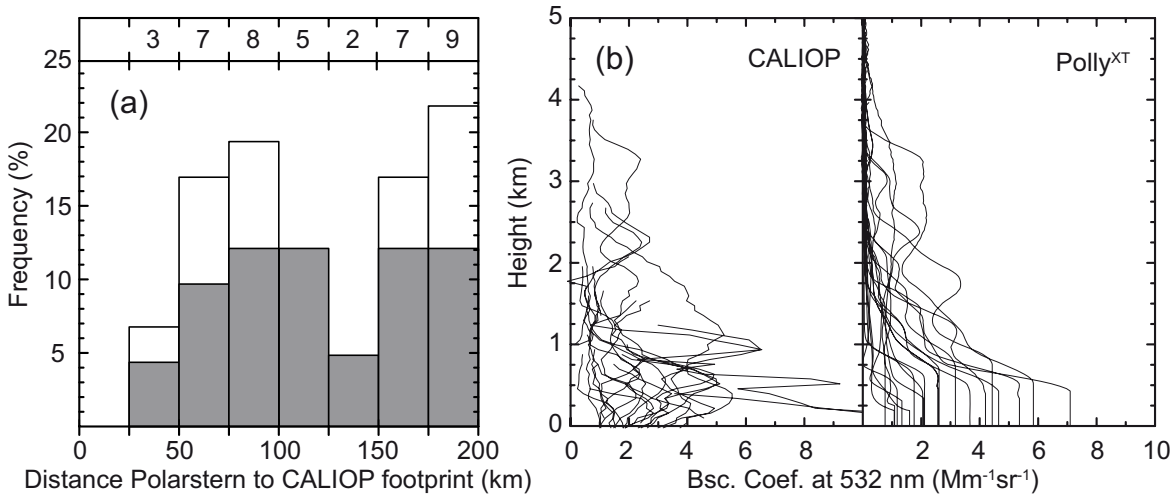

Figure 5.25: (a) Frequency distribution of (white) the distance between CALIOP laser footprint and Polarstern. Number of overpasses is given at the top. Gray bars indicate the quality–assured profiles. (b) Profiles of the particle backscatter coefficient at 532 nm observed with CALIOP (left panel) and with Polly^{XT} (right panel).

to the surface. Nevertheless, a similar vertical layering is observed with both instruments in terms of particle backscatter coefficients.

A more detailed comparison is presented in Fig. 5.26 (b). On 29 October and 9 November 2009 (green and red curves, respectively) lofted aerosol layers were observed with Polly^{XT} and CALIOP. Keeping the influence of atmospheric variability in mind, the observed lofted layers up to 4 km height show good agreement. Below about 600 (red) and 300 m (green) the curves differ from each other because of the overlap effects in the case of Polly^{XT}. In contrast, the observations of Polly^{XT} and CALIOP show good agreement also below 1000 m height on 9 November 2010 (blue curve). On 23 November 2009 and 9 May 2010 (orange and violet curves, respectively) only segments of backscatter profiles were available in the CALIOP database. The agreement is poor for the 23 November 2009, although the CALIOP laser footprint was only 26 km west of Polarstern. The aerosol was characterized as clean marine by CALIOP's data algorithm [*Omar et al.*, 2009]. A horizontal averaging of 80 km was performed by the data algorithm which lead to eight equivalent profiles of CALIOP data. Along such a range thin clouds that were misinterpreted by the cloud–aerosol–discrimination scheme of CALIOP [*Liu et al.*, 2009; *Liu et al.*, 2010] probably contaminate the particle backscatter coefficient profiles.

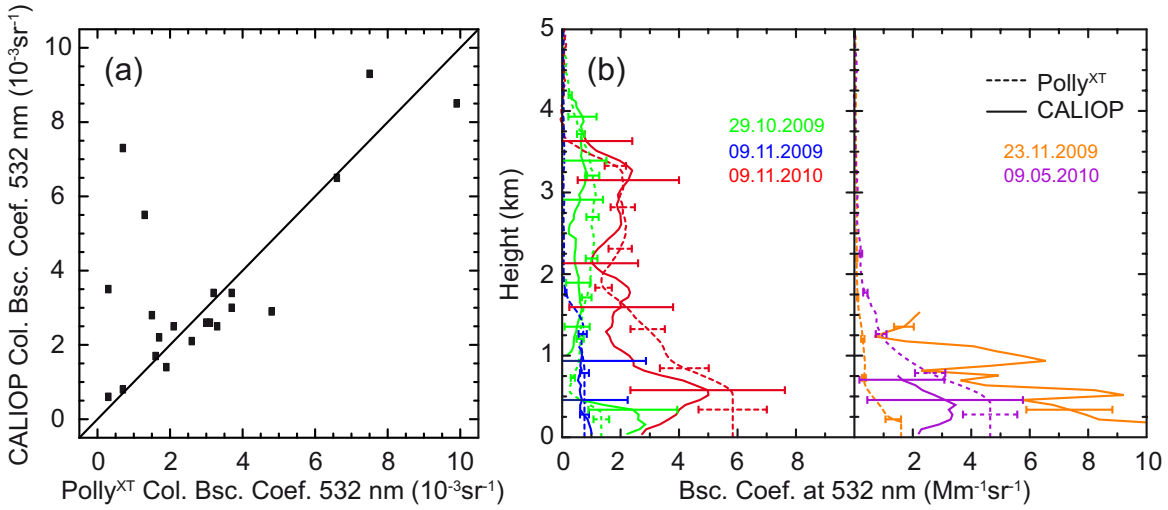

Figure 5.26: (a) Regression of the column backscatter coefficient determined by CALIOP and Polly^{XT}. (b) Same as Fig. 5.25 (b) but for selected cases.

Figure 5.26 (left) presents a correlation study based on column particle backscatter coefficient at 532 nm measured with CALIOP and Polly^{XT}. A good correlation is found, except for a few cases with very low values of the column backscatter coefficient measured with Polly^{XT} ($\approx 10^{-3}\,\mathrm{sr}^{-1}$) but large values of the column backscatter coefficient measured with CALIOP. One of these cases is the observation on 23 November 2009.

As already shown above, high values in the particle backscatter coefficients in the MBL (Fig. 5.22) above the Atlantic indicate strong extinction values. However, the lidar ratio of marine aerosol is low (about 20 sr), i. e. the related extinction coefficient is small even if the backscatter coefficient is comparably large (Fig. 5.21, bottom). In contrast, continental aerosol shows typically a lidar ratio of 50 sr. Thus, continental aerosol layers might show higher extinction coefficients than marine aerosol layers although the backscatter coefficient is small. For an additional comparison, we deal with this issue by differentiating the MBL (<1000 m) and the free troposphere up to 5 km height to estimate the mean AOT in the latitudinal belts as shown in Fig. 5.24.

Figure 5.27 (left) provides an overview of available total AOT (entire atmospheric column) measurements. The AOTs derived in the framework of MAN (500 nm, Sec. 5.1) and AOTs as determined with Polly^{XT} differ by only ± 0.02 which might be due to different aerosol conditions or the assumptions of the lidar ratio. The mean AOT determined from CALIOP observations is lower than the respective one from MAN Sun photometer observations and Polly^{XT} measurements, except for the latitudinal belt from 15° N–EQ.

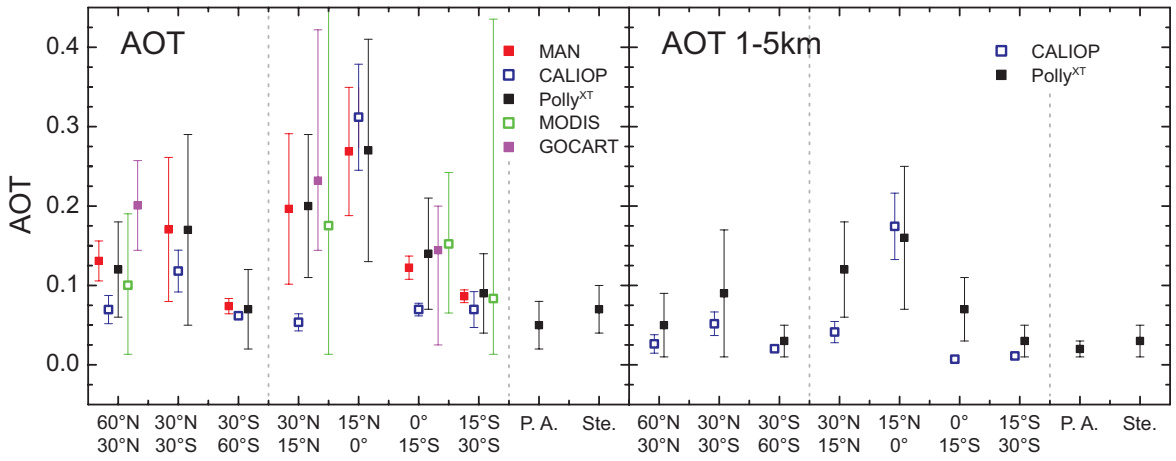

Figure 5.27: Left: Mean AOT at 532 nm for different latitudinal belts derived from Polly^{XT} observations during three transatlantic cruises of Polarstern in 2009 and 2010 (black), mean AOT of CALIOP (532 nm, blue) overpasses, and mean AOT at 500 nm from MAN Sun photometer observations above the Atlantic from 2004 to 2011 (red). Error bars indicate the mean standard deviation (atmospheric variability). AOT retrieved from MODIS satellite observations [*Kaufman et al.*, 2005] are shown in addition (green squares), AOT values modeled with GOCART [*Chin et al.*, 2002] are shown as violet squares. Error bars show the range of AOTs. Exact latitudinal ranges are given in the text. Right: Mean AOT at 532 nm from Polly^{XT} observations and CALIOP observations for the height range from 1 to 5 km height (free troposphere).

Figure 5.27 (left) includes also AOT values published by *Kaufman et al.* [2005] which were determined from MODIS observations (latitudinal belts from 60°–30° N, 30°–5° N, 5° N–20° S, and 20°–30° S), and Global Ozone Chemistry Aerosol Radiation and Transport model (GOCART) results [*Chin et al.*, 2002] for latitudinal belts from 60°–40° N, 30°–10° N, and EQ–20° S. The best agreement of the AOT observations is obtained for the southern tropics. GOCART seems to overestimate the AOT in the northern midlatitudes.

The AOT of the height range from 1 to 5 km (i. e., for the free troposphere) is presented in Fig. 5.27 (right). AOTs in the free troposphere range from 0.01 (CALIOP, 0°–15° S) to 0.17 (CALIOP, 15° N to 0°). The AOT of the MBL (AOT$-$AOT$_{1\text{-}5km}$) is 0.03 to 0.11 in the case of the Polly^{XT} observations and 0.01 to 0.14 in the case of the CALIOP observations.

Figure 5.27 confirms the aerosol features already discussed above. The aerosol load in the free troposphere increases from the northern midlatitudes towards the tropics and then decreases again. The free–tropospheric aerosol amount of the southern midlatitudes is much lower than in northern midlatitudes. Focusing on the AOT values determined from the Polly^{XT} data, the coastal field site Punta Arenas shows the lowest AOT values from 0 to

5 km and 1 to 5 km, although the boundary–layer aerosol backscatter values were multiplied with a lidar ratio of 50 sr which emphasizes the clean aerosol background conditions at Punta Arenas. At Stellenbosch the AOT vertical distribution is comparable to the respective one in the latitudinal belt between 15° and 30° S.

For the first time, an in–depth study of the latitudinal dependence of aerosol layering and associated optical depth is given based on OCEANET, MAN, CALIPSO, satellite as well as modeling data (GOCART). The ability of lidar to separate MBL and free–tropospheric aerosols provide new insights into the contribution of lofted aerosol layers to the column content, which is a prerequisite to study the radiative impact and the influence on cloud–processes in more detail and more realistically.

Chapter 6

Height–resolved radiative–transfer calculations

The Earth's energy budget is a result of complex interactions of a multitude of processes in the atmosphere [*Trenberth et al.*, 2009]. Within this puzzle the OCEANET project focuses on the radiative influence of aerosols and clouds above the Atlantic ocean. In the following, a brief introduction to the terms of radiative transfer is given. The importance of height–resolved atmospheric information is highlighted as one of the key parameters for radiative–transfer calculations. In Sec. 6.2 the presented aerosol lidar observations (Sec. 5.2) are used as input for radiative–transfer calculations to estimate the solar aerosol radiative effect.

6.1 Introduction

The Sun mainly emits electromagnetic radiation at wavelengths between 0.22 and 5 µm (solar range), according to its surface temperature. If a differential amount of such radiant energy ($\mathrm{d}E_\lambda$) penetrates an element of a certain area $\mathrm{d}A$ in the Earth's atmosphere, in a differential solid angle $\mathrm{d}\Omega$, which is oriented at an angle θ to the normal of $\mathrm{d}A$, the specific monochromatic intensity I_λ (radiance) of $\mathrm{d}E_\lambda$ that crosses $\mathrm{d}A$ in a time interval $\mathrm{d}t$, and in a specified wavelength interval $\mathrm{d}\lambda$ can be obtained by:

$$I_\lambda = \frac{\mathrm{d}E_\lambda}{cos\theta \mathrm{d}\Omega \mathrm{d}\lambda \mathrm{d}t \mathrm{d}A}. \tag{6.1}$$

If the intensity is independent of the incident direction, the total flux density of radiant energy F (irradiance) for solar radiation is:

$$F = \int_{0.22}^{5} \pi I_\lambda \mathrm{d}\lambda, \tag{6.2}$$

in units of $\mathrm{W\,m^{-2}}$. The incoming irradiance at TOA is given by the solar constant $S_C \approx 1366\,\mathrm{W\,m^{-2}}$ [*Kraus*, 2004]. The amount of incident solar radiation per day depends on the season (sun–earth distance) and latitude (solar zenith angle – SZA and sunshine duration) [*Bellouin et al.*, 2004]. Within the Earth's atmosphere the solar radiation is scattered and absorbed by gases, aerosols, and clouds. Scattering of the incident radiation can be described with Rayleigh–scattering theory [*Rayleigh*, 1871] if $\lambda \gg 2\pi r_S$ with the radius r_S of the scatterer. For spheres with $2\pi r_S \gtrsim \lambda$ the Lorenz–Mie scattering theory is applied [*Lorenz*, 1890; *Mie*, 1908]. Absorption occurs only in discrete energy levels by atoms according to the Bohr's model. Molecules are able to absorb radiation due to their electric dipole moment and transit it into rotational or vibrational energy. Solids and liquids absorb energy in discrete levels as function of λ and simultaneously emit energy with respect to the temperature of the blackbody in equilibrium conditions in terms of the blackbody laws of Planck, Stefan–Boltzmann, and Kirchhoff. Both processes, scattering and absorption, attenuate the direct downward solar radiation. Considering the change of the intensity $\mathrm{d}I_\lambda$ in an atmospheric layer of thickness $\mathrm{d}s$, the attenuation depends on the density of the atmosphere ρ and the wavelength–dependent mass extinction cross section k_λ. If the concentration of scatterers is low, i. e., in clean conditions, scattered radiation should not affect further scattering processes and independent scattering might be assumed. Considering aerosol layers and especially cloud layers, it may happen that a photon is not only scattered once, because of the high concentration of scatterers and the short distance between them. In that case multiple scattering occurs. This would enhance the solar radiation by diffuse downward radiation, given by a source–function coefficient J_λ. The general radiative–transfer equation combines the sources and sinks of radiation in an atmospheric layer to:

$$\mathrm{d}I_\lambda = -k_\lambda \rho I_\lambda \mathrm{d}s + k_\lambda \rho J_\lambda \mathrm{d}s. \tag{6.3}$$

For a homogeneous layer from $s = 0$ to s_1 with $I_\lambda(s = 0) = I_\lambda(0)$ without multiple scattering Eq. (6.3) can be expressed by the Beer–Bouguer–Law. Further, the integration of $k_\lambda \rho \mathrm{d}s$ from $s = 0$ to ∞ gives the optical thickness.

The direct (total) aerosol effect on the Earth's radiation budget is discussed since the late 1960's [*McCormick and Ludwig*, 1967; *Charlson and Pilat*, 1969; *Charlson et al.*, 1992; *Haywood and Boucher*, 2000; *Yu et al.*, 2006; *Heinold et al.*, 2011; *Torge et al.*, 2011]. The effect can be determined at TOA, the surface, or at any altitude in the atmospheric column by, e. g., measuring the upward ($\uparrow$) and downward ($\downarrow$) irradiances (F_{Real}) at a certain altitude and compare them to modeled irradiances ($F_{\mathrm{Aerosol\_Free}}$) that represent aerosol–free conditions:

$$\Delta F = \left(F^{\uparrow}_{\text{Aerosol\_Free}} - F^{\downarrow}_{\text{Aerosol\_Free}}\right) - \left(F^{\uparrow}_{\text{Real}} - F^{\downarrow}_{\text{Real}}\right). \tag{6.4}$$

The difference gives the solar aerosol radiative effect (ΔF, in the solar range). $\Delta F < 0$ at the TOA indicates an increase of escaping irradiance, i. e., a solar radiative cooling of the atmospheric column caused by aerosols. At the surface $\Delta F < 0$ means a net loss of solar radiation (i.e., cooling) of the atmosphere. In the literature the aerosol effect is sometimes also called aerosol forcing. However, in some publications the aerosol forcing denotes only the anthropogenic effect [e. g. *Sokolik et al.*, 2001; *Yu et al.*, 2006], which is not distinguished here.

Under cloud–free conditions marine aerosol shows the most important solar effect at TOA [*Haywood et al.*, 1999]. *Yu et al.* [2006] reviewed satellite–determined solar aerosol radiative effects above the oceans. The authors reported mean annual averaged effects of -5 to $-6\,\mathrm{W\,m^{-2}}$ at TOA and -8 to $-9\,\mathrm{W\,m^{-2}}$ at the surface. Further, seasonal and regional differences in solar aerosol radiative effects were shown and explained for different aerosol concentrations and predominant aerosol types.

According to radiative–transfer calculations aerosol types are defined by the single–scattering albedo (SSA, [*Haywood and Shine*, 1995]), the ratio of the scattering coefficient and the sum of the scattering and absorption coefficients (extinction coefficient). The angular distribution of scattering by aerosols is described by the phase function that can be retrieved from Mie calculations [*Bohren and Huffman*, 1983] or approximated by the Henyey–Greenstein phase function [*Henyey and Greenstein*, 1941; *Wiscombe and Grams*, 1976; *Boucher*, 1998] which is defined in terms of the asymmetry factor g. As particle size increases, the phase function changes from a symmetric Rayleigh phase function ($g = 0$) to a complex function with increased forward scattering ($g \to 1$, enhanced forward scattering). These properties vary with wavelength [*Ångström*, 1929; *Kiehl and Briegleb*, 1993] and depend on the particle composition [*Sokolik and Toon*, 1999; *Chylek et al.*, 1995], the relative humidity and the hygroscopicity of the aerosol [*Hobbs et al.*, 1997], as well the shape [*Kalashnikova and Sokolik*, 2004] and the size of the aerosols [*Tegen and Lacis*, 1996]. *Tegen and Lacis* [1996] modeled the radiative effect at the tropopause for different extents of dust layers including the thermal spectrum. The dust layer showed an increase of the greenhouse effect with increasing height. Thus, the cooling effect caused by the reduction of solar radiation can change to a warming effect. Focusing on the solar spectrum, the knowledge of the vertical aerosol distribution is of special importance during cloudy sky, because of the change of the reflectance from the ground (surface albedo) to the reflectance of the cloud. [*Haywood and Shine*, 1997; *Liao and Seinfeld*, 1998b; *Sokolik et al.*, 2001; *Chung et al.*, 2005].

The surface albedo of the surface below the observed aerosol layer is key in the solar aerosol radiative effects [e. g., *Russell et al.*, 1997]. *Zhou et al.* [2005] found solar aerosol radiative effects of dust from -17 to $-44\,\mathrm{W\,m^{-2}}$ per unit AOT at the TOA and -48 to $-80\,\mathrm{W\,m^{-2}}$ per unit AOT at the surface from the Saharan desert (surface albedo ≈ 0.35) to the surrounding oceans (surface albedo ≈ 0.05). The surface albedo can even lead to a change of the radiative effect at the TOA from a general cooling effect to a heating effect [*Bierwirth et al.*, 2009; *Tegen et al.*, 2010].

The ocean surface albedo depends on the SZA, wind speed, biological activity, suspended sediments, and surface bubbles [*Jin et al.*, 2002, 2004]. *Li et al.* [2006] compared several parametrization of the ocean surface albedo and found a range of variation of lower than $\pm 10\,\mathrm{W\,m^{-2}}$. Especially above the oceans, elevated aerosol layers in the free troposphere can occur above low–level clouds which have a reflectance tenfold larger than the ocean. Thus, the accurate determination of the height of the aerosol layers is important to know the reflectance below the aerosol layer [e. g. *Haywood and Shine*, 1997; *Liao and Seinfeld*, 1998a; *Quijano et al.*, 2000; *Myhre et al.*, 2003]. However, except for airborne and lidar measurements, aerosol observations include only poor, or low–quality vertical information [*Stevens and Feingold*, 2009], and are often approximated simply by an exponential increase in the aerosol load from the TOA to the surface [*Shettle and Fenn*, 1979] in radiative–transfer models [*Haywood and Shine*, 1997; *Mayer and Kylling*, 2005].

The need for height–resolved measurements was shown by *Wendisch et al.* [1996] who studied combined airborne in–situ and radiation measurements under atmospheric conditions with two temperature inversions that sensitively influenced the vertical distribution of aerosols. Airborne investigations over the Atlantic were performed in the framework of the Saharan Dust Experiment (SHADE) [*Haywood et al.*, 2003] and the Southern African Aerosol Regional Science Initiative (SAFARI 2000) [*Keil and Haywood*, 2003]. Within SHADE a local reflectance over the ocean was found during a Saharan dust event which was 2.7 times higher than during clear–sky conditions. *Keil and Haywood* [2003] observed a conversion from the usual cooling effect of aerosols to a warming effect at TOA by biomass–burning aerosol during cloud–free observations and observations in the presence of clouds, respectively.

In addition to aircraft–based observations, lidars were used to obtain the vertical distribution of lofted aerosol layers, cloud base heights, or profiles of the extinction coefficient to perform radiative–transfer calculations [*Redemann et al.*, 2000; *Podgorny and Ramanathan*, 2001;

Mallet et al., 2008; *Bauer et al.*, 2011]. *Otto et al.* [2009] performed dust–particle–shape–dependent (approximations by spheroids) radiative–transfer calculations and used lidar measurements to evaluate the results with profiles of backscatter and extinction coefficients. *Heinold et al.* [2011] modeled dust and biomass–burning smoke emissions in North Africa to determine their radiative effect during long–range transport. The modeled properties of the mixture of dust and biomass–burning smoke were validated with lidar measurements. To our knowledge, *Wagner et al.* [2001] presented the first radiative–transfer calculations that directly included height–resolved aerosol information derived from lidar. Single–scattering albedo and asymmetry parameter were inverted using the derived optical properties from $3 + 2$ lidar measurements [*Müller et al.*, 1999]. However, a validation of the findings with radiation measurements was missing.

In the following, results from one–dimensional plane–parallel radiative–transfer calculations are shown. The calculations were performed with the UVSPEC program of the libRadtran library (Sec. 4.7). They include the vertical distribution of aerosols above the Atlantic as determined with the shipborne lidar Polly$^{\mathrm{XT}}$ (Sec. 5.2 and 5.3) and are compared to shipborne and spaceborne radiation measurements (see Sec. 2.2).

6.2 Case Studies

6.2.1 Pure dust layer above the MBL

A pure Saharan dust plume was observed on 31 October 2009 (Sec. 5.2.1). The extinction profile as determined with lidar (Fig. 6.1, left) and a dust–related Ångström exponent of 0.1 were used as input for radiative–transfer calculations. The SSA and the asymmetry parameter for dust were adapted from *Heinold et al.* [2011] (see Tab. 6.1). The SSA of marine aerosol was set to 0.99 [*Müller et al.*, 2011] and the asymmetry parameter to 0.65 [*Fiebig and Ogren*, 2006] independent of the spectral band. The MBL–related Ångström exponent was set to 0.0. The surface albedo was estimated with BRDF look–up tables (Sec. 4.7), a mean wind speed of $9\,\mathrm{m\,s^{-1}}$, and a salinity of 36 psu from SCAWS (Sec. 2.2) and Ferrybox [*Petersen et al.*, 2003] measurements. The salinity plays a minor role. A decrease of 60% in the salinity decreases the mean ocean surface albedo by less than 1%. In comparison a decrease of 60% in the mean wind speed increases the mean ocean surface albedo by more than 4%.

Figure 6.1 (right) shows the irradiance at the surface modeled with libRadtran in steps of 15 minutes in comparison to the measured values. The red curve presents the modeled

Table 6.1: Overview of single–scattering albedo (SSA) and asymmetry parameter (g) that were used in radiative–transfer calculations of dust and smoke observations (adapted from *Heinold et al.* [2011]).

	Effective radius (µm)				
	Dust	1.5	3.05	4.6	6.9	Smoke
Spectral band		SSA/g →				
0.245–0.7 µm		0.793/0.817	0.739/0.854	0.685/0.891	0.665/0.901	0.521/0.596
0.7–1.53 µm		0.981/0.673	0.967/0.728	0.952/0.782	0.935/0.795	0.447/0.587
1.53–4.642 µm		0.970/0.689	0.946/0.716	0.921/0.743	0.903/0.765	0.274/0.575

downward irradiance for the observed aerosol conditions (marine and dust aerosol) on 31 October 2009 (Fig. 6.1, left) and the assumption of a dust–related effective radius (r_{eff}) of 1.5 µm. Error bars of the simulation results show the uncertainty based on the uncertainty because of the atmospheric variability during the day as well as the uncertainty of assumed input parameters (e. g., SSA) which were taken from the literature. The extinction profile changed according to the evolution of the dust plume during the day (Fig. 5.2). Changes in the profiles of temperature and relative humidity are considered only with low time resolution in steps of 3 hours (see Sec. 4.5). In addition, the used values presented in Tab. 6.1 were calculated on the basis of Mie–scattering, which treats the non–spherical dust particles

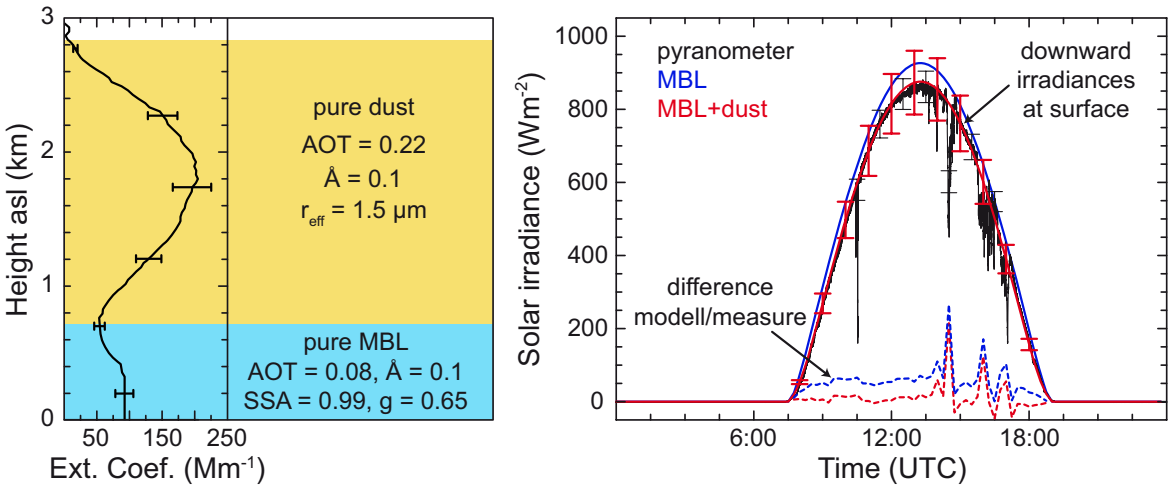

Figure 6.1: Left: Profile of the extinction coefficient as determined with lidar and input as used as for the radiative–transfer calculations (see also Tab. 6.1). Right: Observed and modeled solar irradiance (solid lines) at the surface on 31 October 2009. Differences between observed and modeled irradiance are given by dotted lines. The uncertainty of the simulation results are shown exemplary and are similar for all curves.

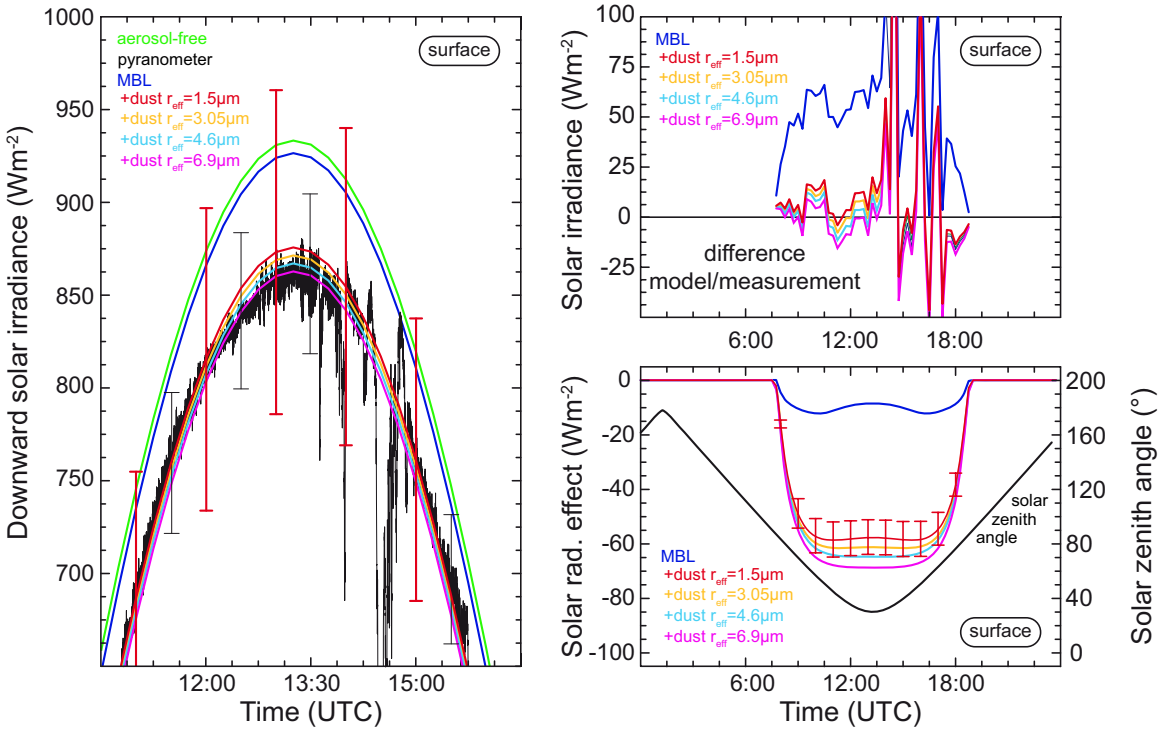

Figure 6.2: Left: Solar irradiance measured (black) and modeled (color lines for different effective radius, r_{eff}) at the surface on 31 October 2009. Right, top: Differences between observed and modeled irradiances at the surface. Right, bottom: Solar radiative effect (color lines) and solar zenith angle (black). Error bars are the same as in Fig. 6.1 and are similar for all curves.

as spherical scatterers. Depolarization caused by scattering by the non–spherical dust particles and three–dimensional effects caused by inhomogeneities of the aerosol layers were not considered in the simulation. The extent of these uncertainties can only be estimated to reach maximum values of 10% which is assumed in the following. However, the results of the performed simulations below are in promising agreement with the pyranometer measurements and are discussed in detail. The uncertainty of the pyranometer measurements were assumed to be 4% due to the ship movement and the ship's superstructure (Sec. 4.1). In addition, the irradiance was modeled for pure marine conditions (blue in Fig. 6.1, right), i. e., ignoring the lofted dust layer. The differences between measurement and simulation (dotted lines) show that the lofted layer contributes significantly to the attenuation of the incident radiation.

Figure 6.2 (left) shows the influence of the assumed size of dust particles on the radiative transfer. The modeled irradiance for the pure marine case (dark blue) differs only slightly from the modeled irradiance for the aerosol–free conditions (light green). The simulations

were extended by three more simulations with increasing dust–related r_{eff} of up to 6.9 µm and constant extinction coefficients. The change in r_{eff} causes a change in the SSA and the asymmetry parameter (Tab. 6.1). The differences between measured and modeled irradiance (Fig. 6.2 right, top) are smallest for a dust size distribution with large r_{eff} from 4.6–6.9 µm (light blue and magenta curve, 6 ± 40 and $3 \pm 40\,\text{W m}^{-2}$). The high fluctuation in the measured irradiance is caused by liquid–water clouds which are not considered in the simulation. However, dust size distributions with $r_{\text{eff}} \geq 4.6$ µm seem to be not very likely to be observed 800 km west of Africa (>1000 km from the Sahara). Dry deposition and turbulent downward mixing cause relatively fast removal of large particles. Nevertheless, CALIOP observations of a dust layer close to Cape Verde (same area) were reproduced by *Wandinger et al.* [2010] with multiple–scattering calculations and $r_{\text{eff}} \geq$ 4–6 µm. For r_{eff} values of 1.5 and 3 µm the difference is 12 ± 40 and $9 \pm 40\,\text{W m}^{-2}$ (Fig. 6.2, right, top). Figure 6.2 (right, bottom) presents the determined radiative effect at the surface according to Fig. 6.2 (left). In addition, the diurnal variation of the solar zenith angle is given. The highest instantaneous aerosol radiative effect of the separated MBL is about -10 to $-12\,\text{W m}^{-2}$ at solar zenith angles from 40° to 70°. With increasing sun elevation the pathway of the photons becomes shorter, less scattering and absorption occur, and the radiative effect decreases during midday. If the dust layer is considered in addition, the effect vanishes with increasing r_{eff}.

The incident radiation is attenuated most efficiently in the case of a dust layer with large r_{eff}. The highest instantaneous solar aerosol radiative effect is about -58 to $-68\,\text{W m}^{-2}$. The daily mean effect (for 24 hours) is -23 to $-27\,\text{W m}^{-2}$ at the surface. The daily mean radiative effect per unit AOT (further denoted as radiative efficiency) is about -78 to $-91\,\text{W m}^{-2}$ on this specific day. During SAMUM–1 *Bierwirth et al.* [2009] estimated a solar aerosol effect of about $-72\,\text{W m}^{-2}$ at the surface for an AOT of 0.41 to 0.46 and SZA = 21°. The radiative efficiency was about -175 to $-157\,\text{W m}^{-2}$.

The modeled upward irradiance at TOA for cloud–free conditions is compared to irradiances determined with MSG according to the pixel (3 km×3 km) above the position of Polarstern [*Clerbaux et al.*, 2001]. The results at TOA are shown in Fig. 6.3 (right, top). A good agreement between the modeled (red) and MSG–derived (black) irradiance is found within the error bars until clouds appeared at about 14:00 UTC. Then the MSG–derived irradiance increases because of enhanced reflectance by the clouds. The uncertainty of the irradiance derived with MSG is about 14% [*Clerbaux et al.*, 2001]. The shift of the irradiances at sunrise and sunset is due the broad–band data algorithm of MSG which does not consider observations with SZA > 80° (Fig. 6.3, right, top), i. e., in the presented case

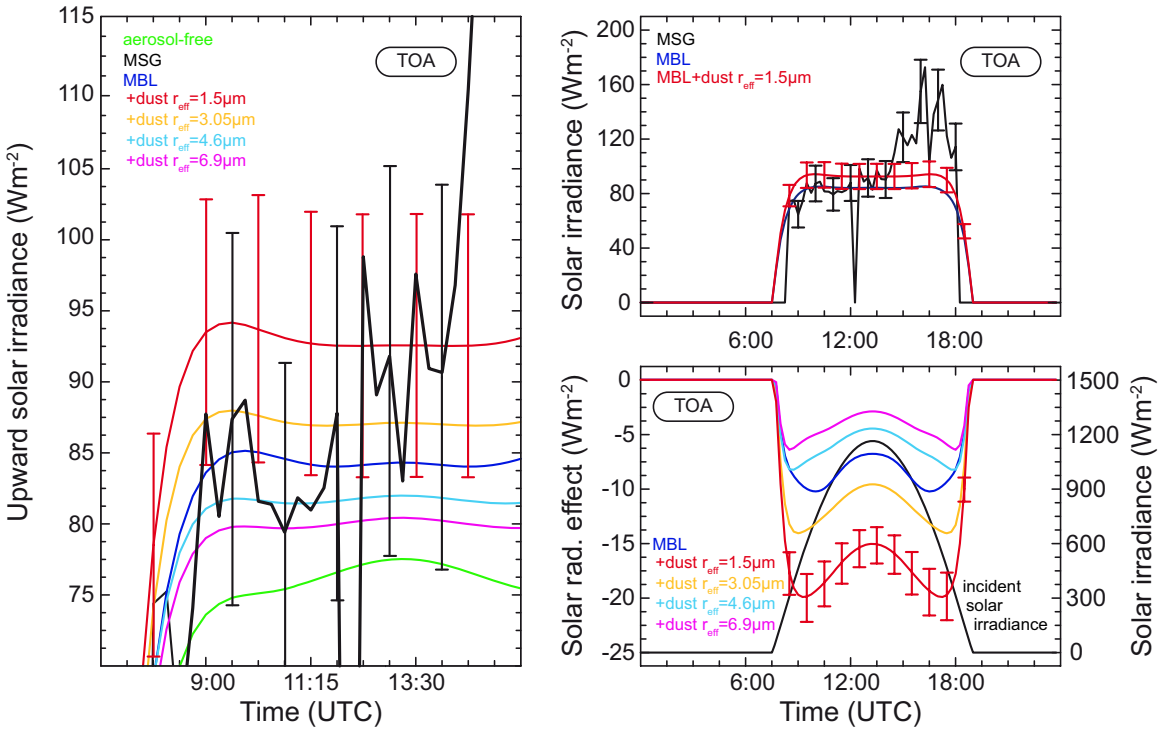

Figure 6.3: Left: Solar irradiance as derived with MSG (black) and modeled (color lines for different effective radius, r_{eff}) at the top of atmosphere (TOA) on 31 October 2009. Right, top: Solar irradiance as derived with MSG and modeled on 31 October 2009 (24 hours). Right, bottom: Solar radiative effect (color lines) and incident solar irradiance at TOA (black). Error bars are determined in the same way as in Fig. 6.1 and are similar for all curves.

before 8:30 and after 18:00 UTC. Figure 6.3 (left) shows the results in more detail. Even if only the MBL (blue, no dust) is considered in the simulation, the estimated irradiance matches the irradiances derived with MSG within the error bars. A mean difference of $0\pm19\,\mathrm{W\,m^{-2}}$ is found for a dust layer with $r_{\text{eff}} = 4.6\,\mu\mathrm{m}$ (light blue), disregarding low sun elevation and cloud–affected measurements. The solar aerosol radiative effect at TOA (Fig. 6.3, right, bottom) is smaller than at the surface (Fig. 6.2, right, bottom) but shows the same patterns with the highest effect at solar zenith angles from 40° to 80° (Fig. 6.2, right, bottom). The dust layer above the MBL does not imply an additional solar radiative effect at TOA. As mentioned, with increasing size of the dust particles, the SSA decreases. As a consequence, the difference between the reflectance of the ocean surface in clear–sky conditions and the increased reflectance due to the aerosol layer above the ocean surface is reduced when large dust particles are present. However, solar aerosol radiative effects of up to $-20\,\mathrm{W\,m^{-2}}$ were found. Thus, a solar radiative efficiency of $-60\,\mathrm{W\,m^{-2}}$ is obtained. The daily mean solar radiative effect is -2 to $-8\,\mathrm{W\,m^{-2}}$, the efficiency -8 to $-26\,\mathrm{W\,m^{-2}}$. At

TOA *Bierwirth et al.* [2009] estimated a solar aerosol efficiency of about $-50\,\mathrm{W\,m^{-2}}$ and SZA = 21°.

In Sec. 5.2.1 another aspect of the case observed on 31 October 2009 was discussed. It was observed that the spaceborne CALIPSO lidar underestimated the dust extinction coefficient by roughly 25% due to the erroneous dust–related lidar ratio. By adapting the extinction profiles with this erroneous dust–related lidar ratio, the solar aerosol radiative effect is instantaneously underestimated by up to $13\,\mathrm{W\,m^{-2}}$ and by about $5\,\mathrm{W\,m^{-2}}$ (≈25%) during the day at the surface. At TOA the solar aerosol radiative effect is instantaneously underestimated by up to $5\,\mathrm{W\,m^{-2}}$ and by about $2\,\mathrm{W\,m^{-2}}$ (≈25%) during the day for a dust r_{eff} of 1.5 µm.

6.2.2 Mixed dust/smoke layer above the MBL

While dust strongly absorbs light in the blue and green spectral range, biomass–burning smoke absorbs in the entire visible spectral region due to the high amount of black carbon in the smoke [*Bond and Bergstrom*, 2006]. For wood smoke, black carbon accounts for 86% of the absorption in the solar range, and organic carbon contributes with 49% to the absorption below 400 nm [*Kirchstetter and Thatcher*, 2012]. However, if a mixture of dust and biomass–burning smoke occurs as observed on 1 and 2 May 2010 (Sec. 5.2.2), it is important to know the individual contributions of dust and smoke particles to light scattering and absorption. The depolarization lidar measurements enable us to estimate the dust fraction in the MBL and in the lofted layers [*Tesche et al.*, 2011] which ranged from 50%–60% in the MBL and from 70%–90% in the lofted layers on 1 and 2 May 2010. The SSA and asymmetry parameter in the simulations were selected by using the values of Tab. 6.1 and by considering the dust and smoke fractions found from the lidar observation. Furthermore, an external mixture with proportional microphysical properties was assumed.

The dust–related r_{eff} is assumed to be 1.5 µm in the presented calculations. An overview of the aerosol conditions used in the following calculations is given in Fig. 6.4. The profile and the spectral dependence of the extinction correspond to the lidar observations. The high values of the extinction coefficients in the MBL are based on the dust fraction found within the MBL (Sec. 5.2.2). As shown in Fig. 6.4, seven different scenarios were assumed in the radiative–transfer simulations. Calculations were performed for lofted layers of pure dust and pure smoke in the presence of a pure marine MBL (cases 1 and 2). In addition, calculations for a mixed MBL with a dust fraction of 50% and a marine aerosol fraction of 50% were performed (cases 3–7). In case 4, the mixing ratio of smoke (10%) and dust

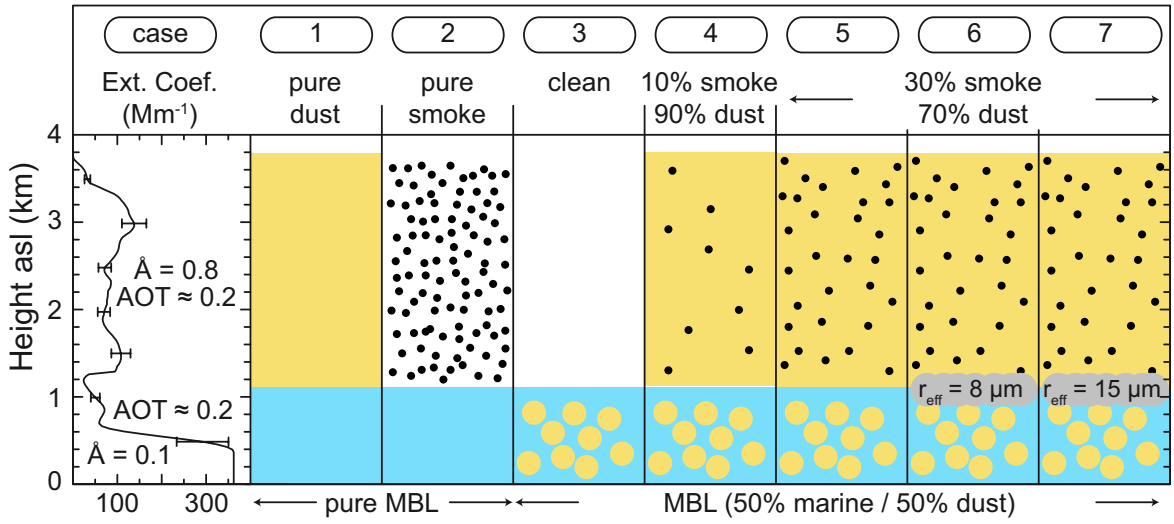

Figure 6.4: Overview of aerosol conditions assumed in the radiative–transfer calculations. Dust with a particle effective radius of 1.5 µm was considered (Tab. 6.1). Case 6 includes boundary–layer clouds with a cloud droplet effective radius of 8 µm, case 7 includes the same with a cloud droplet effective radius of 15 µm.

(90%) in the lofted layer was assumed. For cases 5–7, the mixing ratio of smoke and dust was changed to 30%:70%. Cases 6 and 7 consider boundary–layer clouds with cloud droplet radii of 8 and 15 µm, respectively. The surface albedo was estimated for a mean wind speed of 5.5 m s^{-1} and a salinity of 36 psu in the simulations.

Figure 6.5 (right, top) shows the observed irradiance (black line) at the surface on 1 May 2010. Simplified calculations for non–mixed aerosol layers (cases 1 and 2) are presented, too. In the case of a pure dust layer the modeled irradiance is higher than the observed irradiance during the day, whereas it is too low if a pure smoke layer is considered. The analysis of the lidar observation on 1 May 2010 revealed mixed aerosol within the MBL as well as in the lofted layer. In agreement, the best approximation of the observed irradiance is given by a modeled irradiance that includes an MBL with a fraction of 50% dust and a lofted layer with a smoke fraction of 30% (case 5). However, the uncertainties in the radiative–transfer calculations explained in Sec. 6.2.1 remain high. The time period from 9:00 to 15:00 UTC is shown in more detail in Fig. 6.5 (left). The modeled irradiance in terms of an aerosol–free atmosphere (green) is highest. If the simulations are performed for the mixed MBL only (dark blue, case 3), the modeled irradiance differs slightly from the modeled irradiance of pure marine MBL conditions and a pure dust layer. The simulation of a mixed lofted layer that includes 10% smoke (magenta, case 4) results in a slightly higher irradiance than the simulation with a mixed lofted layer and a smoke fraction of 30%

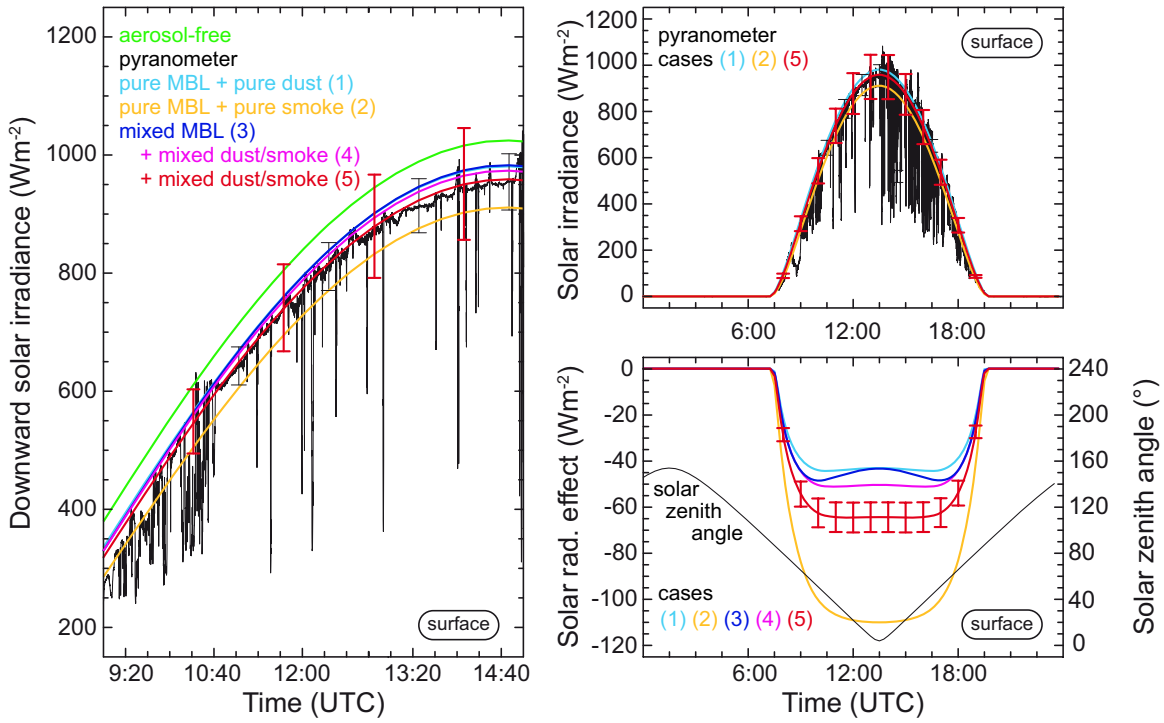

Figure 6.5: Left: Solar irradiance observed (black) and modeled (color lines for scenarios shown in Fig 6.4) at the surface on 1 May 2010. Right, top: Observed and modeled solar irradiance on 1 May 2010 (24 hours). Right, bottom: Solar radiative effect (color lines) and solar zenith angle (black). Error bars are determined in the same way as in Fig. 6.1 and are similar for all curves.

(red, case 5) due to the smaller absorption efficiency. The absorption efficiency of smoke is also indicated in Fig. 6.5 (right, bottom) by the highest solar aerosol radiative effect in the case of pure smoke in the lofted layer (orange, case 2) which reaches up to $-110\,\mathrm{W\,m^{-2}}$ (instantaneous) at a solar zenith angle of 4°. The dependence of the solar aerosol effect on the solar zenith angle is highest when only the MBL is considered in the simulations, because the effect of the related pathway in the atmosphere is strongest. The daily mean solar aerosol radiative effect for aerosol conditions determined with lidar (50% dust in the MBL, 30% smoke in the lofted layer) is $-28 \pm 3\,\mathrm{W\,m^{-2}}$ at the surface and reaches instantaneous values of $-65 \pm 13\,\mathrm{W\,m^{-2}}$.

Figure 6.6 presents the calculation results for TOA. A distinct influence of clouds on the upward irradiance as derived with MSG (black) is found until 10:00 UTC and after 15:00 UTC on 1 May 2010 (Fig. 6.6, right, top). For the period from 10:00 – 15:00 UTC (Fig. 6.6, left) all modeled irradiances that include a dust–containing lofted layer (light blue, magenta, red, cases 1, 4, 5) are in the range of the irradiance derived with MSG under consideration of the

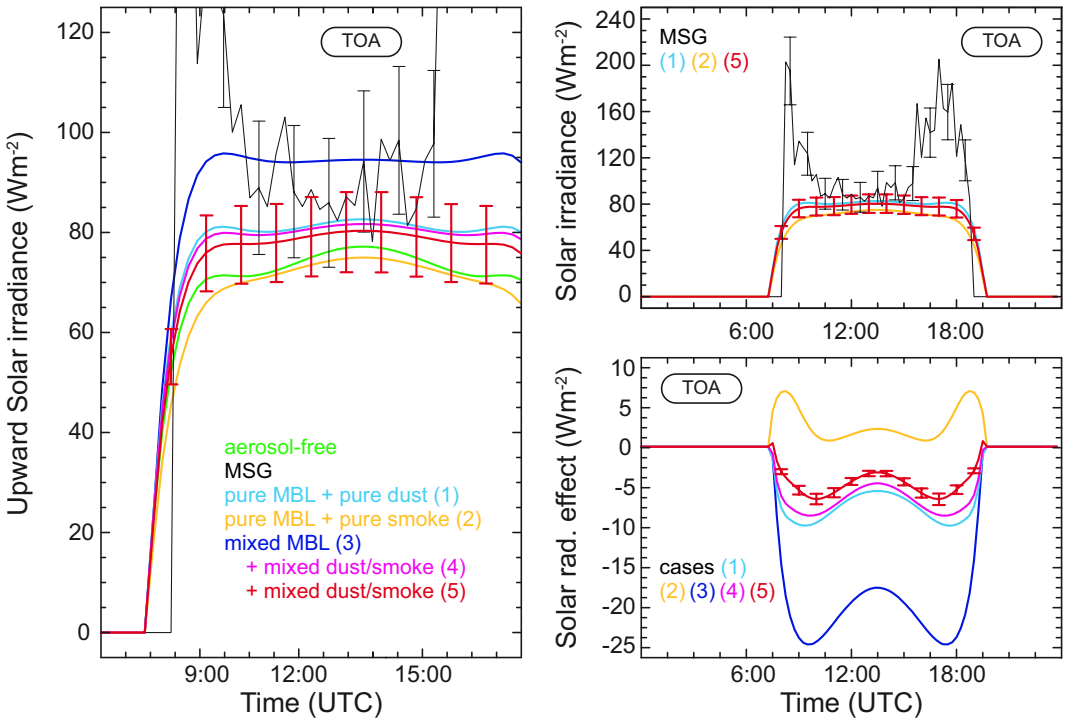

Figure 6.6: Left: Solar irradiance as derived with MSG (black) and modeled (color lines for scenarios shown in Fig 6.4) at the top of atmosphere (TOA) on 1 May 2010. Right, top: Solar irradiance as derived with MSG and modeled on 1 May 2010 (24 hours). Right, bottom: Solar radiative effect at TOA. Error bars are the same as in Fig. 6.1 and are similar for all curves.

uncertainties. The highest upward irradiance was modeled in the case of a mixed aerosol in the MBL itself (blue, case 3) due to the high SSA and thus a low absorption. Hence, the lowest upward irradiance was obtained for the lofted pure smoke layer (orange, case 2). The efficient absorption of solar radiation by smoke leads to a lower upward irradiance at TOA than under aerosol–free conditions (light green) and thus to a positive solar radiative effect (Fig. 6.6, right, bottom). The radiative effect reaches instantaneous values of up to $+7\,\mathrm{W\,m^{-2}}$ and a daily mean of $+1\,\mathrm{W\,m^{-2}}$. In contrast, the solar radiative effect of the aerosol conditions as determined with lidar and supported by the radiative–transfer calculations at the surface (mixed MBL and a smoke fraction of 30% in the lofted layer, case 5) reaches values as low as $-7 \pm 2\,\mathrm{W\,m^{-2}}$. The daily mean radiative effect is $-2 \pm 1\,\mathrm{W\,m^{-2}}$. But even in this case, the smoke fraction leads to a positive radiative effect close to sunrise and sunset (red curve in Fig. 6.6, right, bottom). Because of the decreasing SSA from pure dust (light blue curve, always negative) to pure smoke (orange, always positive), the pathway of the photons at high solar zenith angles (Fig. 6.5, right, bottom) becomes sufficiently long so that more and more photons can be absorbed and less photons are scattered back to space.

Radiative–transfer modeling results of such mixed aerosol layers are rare. During SAMUM–2 *Heinold et al.* [2011] determined mean radiative efficiencies of a mixed dust/smoke plume of $-42\,\mathrm{W\,m^{-2}}$ at the surface and $\pm 0\,\mathrm{W\,m^{-2}}$ at the TOA. The smoke fraction was higher (during the main period of biomass burning in western Africa) than the dust fraction so that the increased reflectance was less pronounced than in the case of this study (at the end of the burning season). In the presented study daily mean solar radiative efficiencies of $-67\,\mathrm{W\,m^{-2}}$ at the surface and of $-5\,\mathrm{W\,m^{-2}}$ at TOA were obtained from the radiative–transfer calculations.

6.2.3 Complex aerosol layering with embedded clouds

The lidar observations of the three cruises showed the frequent occurrence of boundary–layer clouds like on 1 May 2010 (Fig. 5.7). In the following, the cloud–aerosol distribution of cases 6 and 7 in Fig. 6.4 is assumed. The presented simulations of case 5 in Sec. 6.2.2 are extended by boundary–layer clouds with cloud droplet r_{eff} ranging from 8 to 15 µm. The liquid–water content (LWC) was assumed to range from 0.1 to $0.4\,\mathrm{g\,m^{-3}}$ [*Miles et al.*, 2000].

Figure 6.7 presents the results of the radiative–transfer calculations for the surface and an atmosphere that contains an aerosol mixture in the MBL, a mixed lofted layer, and boundary–layer clouds, corresponding to cases 6 and 7 in Fig. 6.4. Within the 24–hour period (Fig. 6.7, right, top) the peaks of the attenuation in the observed downward irradiance are in the range of the simulation results. Peaks in the observed downward irradiance above the modeled irradiance for cloud–free conditions (red curve) are the result of three–dimensional effects by the broken–cloud field. During moments of direct sunlight, diffuse radiation of the broken clouds can lead to enhanced incident irradiance. This effect is not considered in the simulations.

Figure 6.7 (left) shows the period from 9:20 to 14:40 UTC only. The modeled daily mean irradiance for an atmosphere with a cloud with an r_{eff} of 8 µm and an LWC of $0.4\,\mathrm{g\,m^{-3}}$ (dotted, blue) is about 43% lower than the respective value for a cloud with an LWC of $0.1\,\mathrm{g\,m^{-3}}$ (dashed, blue) due to a higher concentration of droplets. A significant difference of the irradiance is given, if r_{eff} is increased to 15 µm (dotted, green). In this case, a lower concentration of larger droplets is present, i. e., less scattering events and less scattering to the sides out of the modeled column. The simulation scenario of a cloud layer with an r_{eff} of 8 µm and with an LWC of $0.4\,\mathrm{g\,m^{-3}}$ matches the strongest observed attenuation of the irradiance (Fig. 6.7, left). In this case, the solar radiative effect of the clouds and aerosols reaches instantaneous values of up to about $-600\,\mathrm{W\,m^{-2}}$ at the surface

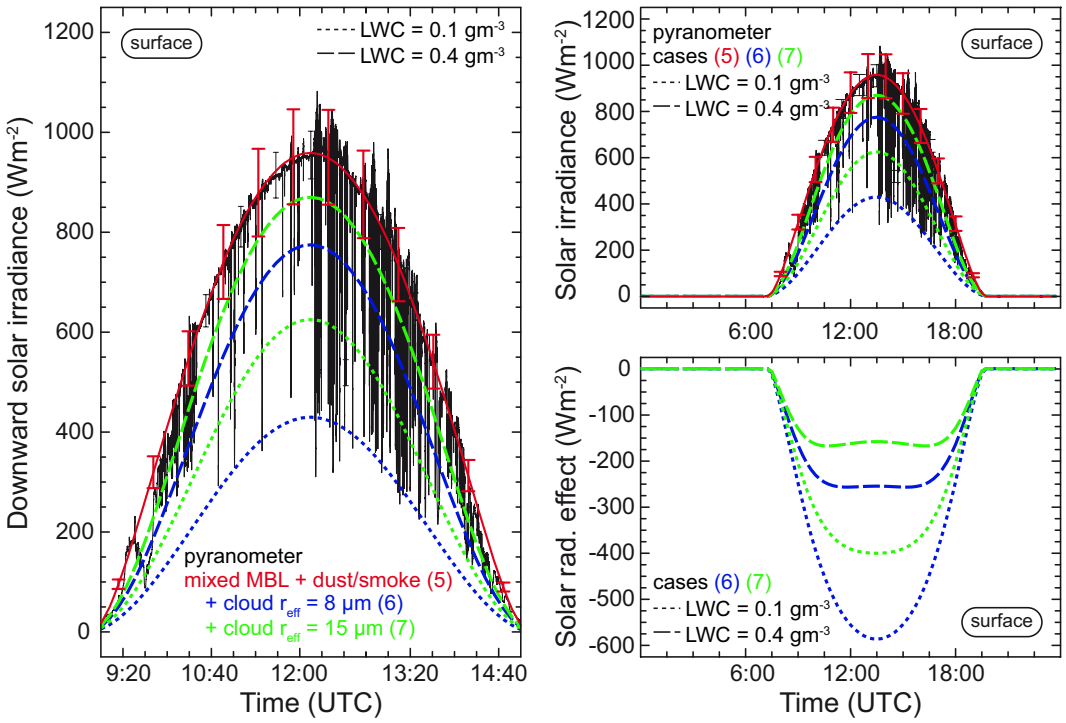

Figure 6.7: Left: Observed (black) and modeled (color lines for aerosol and cloud conditions shown in Fig 6.4) solar irradiance at the surface on 1 May 2010. Red curves show simulation results for a mixed MBL and a mixed lofted layer (30% smoke, case 5). Right, top: Observed and modeled solar irradiance on 1 May 2010 (24 hours). Right, bottom: Solar radiative effect at the surface. Error bars are determined in the same way as in Fig. 6.1 and are similar for all curves.

(Fig. 6.7, dotted, blue). *Kalisch* [2011] determined solar cloud radiative effects of up to $-400\,\mathrm{W\,m^{-2}}$ at the surface for cumulus clouds, and even higher values for altocumulus clouds.

The cloud effect on the upward irradiance at the TOA as derived with MSG (black in Fig. 6.8 left) is most pronounced immediately after sunrise and before sunset. While the strongest peaks of the downward irradiance at the surface are well covered by simulating an additional cloud layer with an r_{eff} of 8 µm and an LWC of $0.4\,\mathrm{g\,m^{-3}}$ (Fig. 6.7, dotted, blue) during the whole day, these atmospheric conditions cannot explain the upward irradiance retrieved at TOA (Fig. 6.8, left). At the surface, the pyranometer measurements are instantaneously affected by scattering of small liquid–water clouds (Fig. 6.7, left, and Fig. 6.9, left). These widespread broken clouds do not significantly increase the mean reflectance to values higher than the reflectance of the aerosol–laden atmosphere in the 3 km×3 km footprint of MSG from 10:30 to 15:00 UTC (Fig. 6.8, left). After 15:00 UTC cloudiness increases (Fig. 6.9, right) which is accompanied by an increase in the reflectance

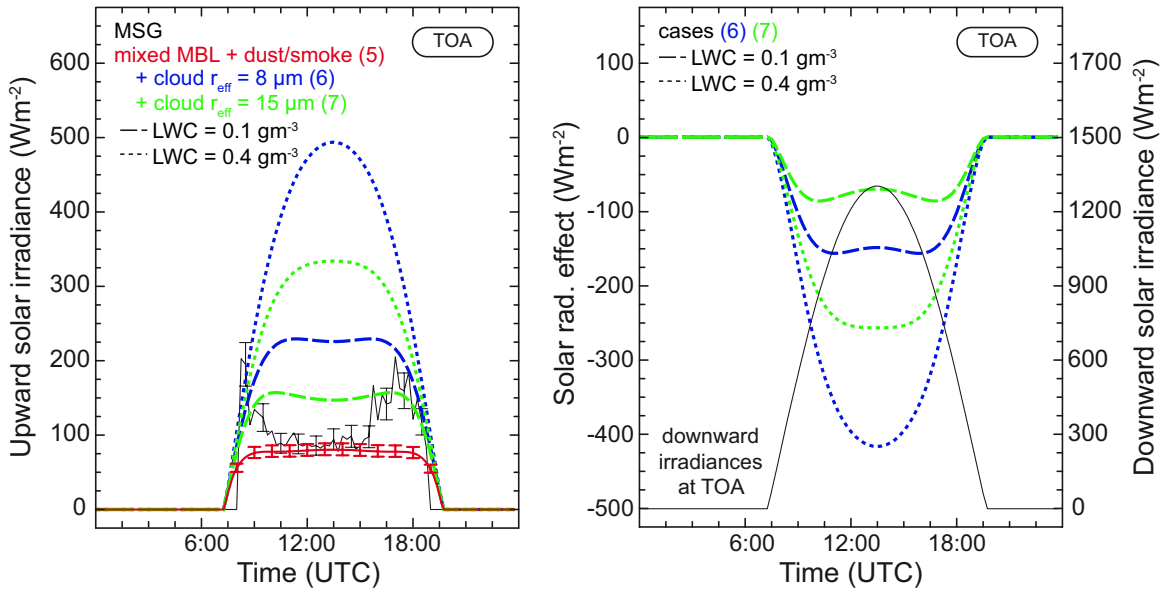

Figure 6.8: Left: Solar irradiance derived with MSG (black) and modeled (aerosol and cloud conditions shown in Fig 6.4, cases 5–7) at the top of atmosphere (TOA) on 1 May 2010. The red curve shows simulation results for a mixed MBL and a mixed lofted layer (30% smoke, case 5). Right: Solar radiative effect and incident solar irradiance at TOA. Error bars are determined in the same way as in Fig. 6.1 and are similar for all curves.

and a higher solar irradiance at TOA (Fig. 6.8, left). However, cloud–free areas remain in the footprint of MSG and lower the mean reflectance. Thus, at TOA the irradiance derived with MSG is approximately obtained with an optically thin cloud layer with an r_{eff} from 8–15 µm and an LWC of 0.1 g m^{-3} (dashed in Fig. 6.8, left) or with a cloud r_{eff} of 15 µm

Figure 6.9: Sky images taken on (left) 1 May 2010 at 12:00 UTC and on (right) 1 May 2010 at 16:30 UTC.

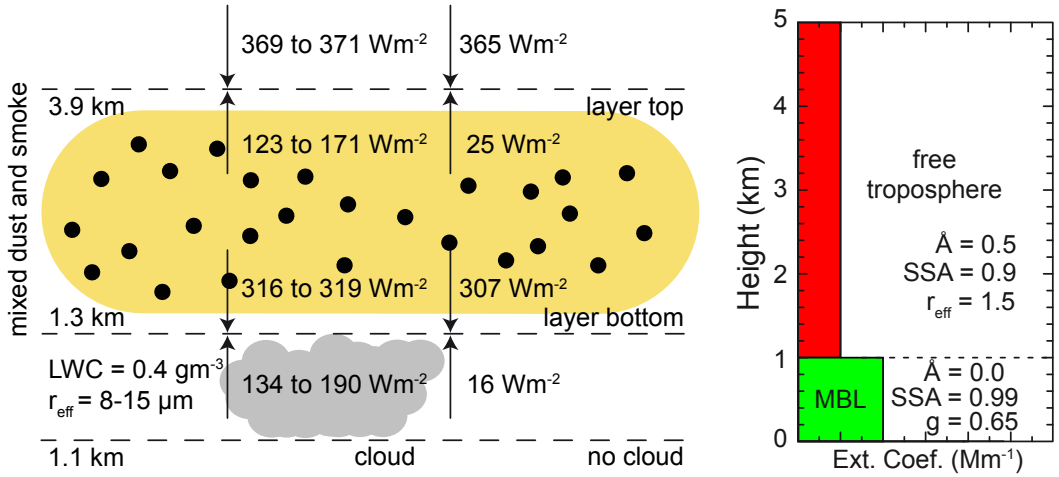

Figure 6.10: Left: Scheme of the downward and upward irradiance at the top and bottom of the mixed Saharan dust and smoke layer on 1 May 2010 in the presence of underlying clouds and without clouds. In this case, the liquid–water content was $0.4\,\mathrm{g\,m^{-3}}$ and the effective droplet radius was 8–15 µm. Right: Overview of the aerosol conditions assumed in radiative–transfer calculations presented in Sec. 6.3. The extinction profile is given by observations with lidar.

and an LWC ranging from 0.1 to $0.2\,\mathrm{g\,m^{-3}}$ (not shown). For the simulated conditions the solar radiative aerosol–cloud effect (Fig. 6.8, right) ranges from -70 to $-417\,\mathrm{W\,m^{-2}}$ close to noon, when the incident irradiance (black) of $1304\,\mathrm{W\,m^{-2}}$ reaches its maximum at TOA. The daily mean effect ranges from -33 to $-139\,\mathrm{W\,m^{-2}}$.

The large range of the observed and modeled radiative effect shows the importance to consider clouds in radiative–transfer studies. An interesting point is the change of the solar aerosol radiative effect of the lofted layer above a cloud layer. Figure 6.10 (left) shows the daily mean irradiance at the top and at the bottom of the observed lofted mixed dust/smoke layer on 1 May 2010, which is located just above a cloud (left, r_{eff} from 8–15 µm, LWC of $0.4\,\mathrm{g\,m^{-3}}$) and during cloud–free conditions (right). The cloud enhances the reflectance of solar radiation towards TOA. The solar albedo of the cloud (≈0.5) is higher than the albedo of the ocean surface (≈0.05). The upward irradiance at the bottom of the layer is about 10 times higher in the case with a cloud layer underneath the aerosol layer, compared to the cloud–free case. The mixed dust/smoke layer enhances the reflectance of the ground in the case of a cloud–free atmosphere and increases the upward irradiance from $16\,\mathrm{W\,m^{-2}}$ at the bottom of the layer to $25\,\mathrm{W\,m^{-2}}$ at the top of the layer. However, in the presence of a cloud layer the irradiance at the top of the aerosol layer is 8%–10% lower than at the bottom. The solar radiative effect of the aerosol layer changes from a cooling effect at the TOA (enhanced upward scattering) to a warming effect when clouds are present.

6.3 Statistics

The radiative–transfer calculations were performed for the entire lidar data set of Sec. 5.3. In this effort, the profiles of extinction were approximated by step functions with MBL aerosol (for heights <1000 m, green in Fig. 6.10, right) and free–troposphic aerosol (from 1–5 km height, red in Fig. 6.10, right). Marine aerosol was treated with an SSA of 0.99 [*Müller et al.*, 2011] and an asymmetry parameter of 0.65 [*Fiebig and Ogren*, 2006]. In the free troposphere continental aerosol was assumed. Keeping the dominance of the Saharan dust belt in consideration, the SSA was set to 0.9, the asymmetry parameter was taken from Tab. 6.1 for an r_{eff} of 1.5 µm. An overview of the idealized aerosol conditions is shown in Fig. 6.10 (right). In addition, the computations were simplified by assuming standard atmospheric conditions [*Anderson et al.*, 1986] and International Geosphere–Biosphere Programme surface–albedo values that are offered in spectral bands for different surface types[1].

The simulation results were then compared with the ground–based pyranometer measurements and the spaceborne observations of MSG. Each analyzed lidar measurement was used to determine the downward irradiance at the surface and the upward irradiance at the TOA during the day (24 hours) of the lidar measurement in steps of 15 minutes. The analyzed lidar data set was cloud–screened to ensure that the simulated irradiance was influenced by aerosols only. However, in the observation of irradiance clouds play an important role. The cloud coverage as determined with the sky imager [*Kalisch and Macke*, 2008] was considered to classify observations during cloud–free conditions. By default, only these observations can be approximated with the simulations.

Figure 6.11 (left) shows a scatterplot of the modeled and measured irradiance at the surface. During cloud coverage of less than 30% (blue dots) a good agreement was found. Usually, in the presence of clouds the model shows overestimated irradiances because the additional cloud radiative effect is not considered [*Ramanathan et al.*, 1989]. Cases with measured irradiance higher than modeled irradiance can occur due to reflections produced by the superstructure of the ship and scattering by broken clouds at high sun elevation. The superstructure of the ship also explains the low measured irradiance under cloud–free conditions due to shadowing.

The irradiance at TOA derived from MSG presented in Fig. 6.11 (right) and the modeled irradiance do not show good agreement. Although most values for cloud–free conditions are

[1] More information and values are given at: http://www-surf.larc.nasa.gov/surf/pages/explan.html

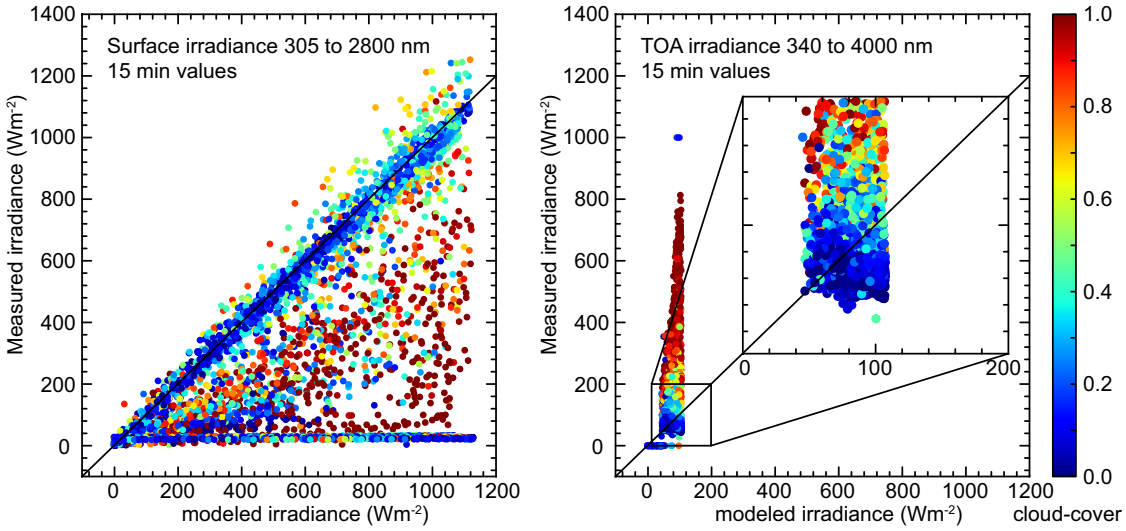

Figure 6.11: Comparison of modeled and measured solar irradiance at the surface (left) and the top of atmosphere (TOA, right). The color code represents the cloud coverage as determined with a sky imager.

close to the 1:1 line through the origin no overall correlation can be found. The effect of clouds on the regression is stronger at TOA than at the surface. In cloud–free conditions the model results (point measurement of the lidar) agree better to the pyranometer observations than to the irradiance as derived with MSG. The obtained pixel of MSG measurements has a footprint of 3 km×3 km at the ground. The pyranometer observes a hemisphere of several kilometers as well. The difference in the correlation between model result and observation at TOA and surface might be caused by the frequent occurrence of broken–cloud fields over the ocean and three–dimensional effects, but is not fully understood until yet.

According to Fig. 5.27 in Sec. 5.3 mean radiative effects at the surface of -24 ± 33, -31 ± 44, and $-15 \pm 22\,\mathrm{W\,m^{-2}}$ were determined by the use of the extinction coefficients from 0–5 km (Fig. 6.10, right) for the latitudinal belts between 60° and 30° N, 30° N and 30° S, and 30° to 60° S, respectively (black circles in Fig. 6.12, left). The strong fluctuations result from the variability of the aerosol conditions and the strong difference between day and night. The highest solar radiative effect occurs in the tropics, especially in the northern tropics from 15° N–EQ ($-43 \pm 59\,\mathrm{W\,m^{-2}}$). The solar radiative effect of the free–tropospheric aerosol (4–5 km height, red squares) shows the same patterns. The effect of the boundary–layer aerosol (0–1 km, green diamonds) is quite constant with mean values in the range of -3 to $-7\,\mathrm{W\,m^{-2}}$ due to the relative constant aerosol load and aerosol type (i. e., sea salt) in the MBL. Another important reason for the difference between the radiative effect of the MBL

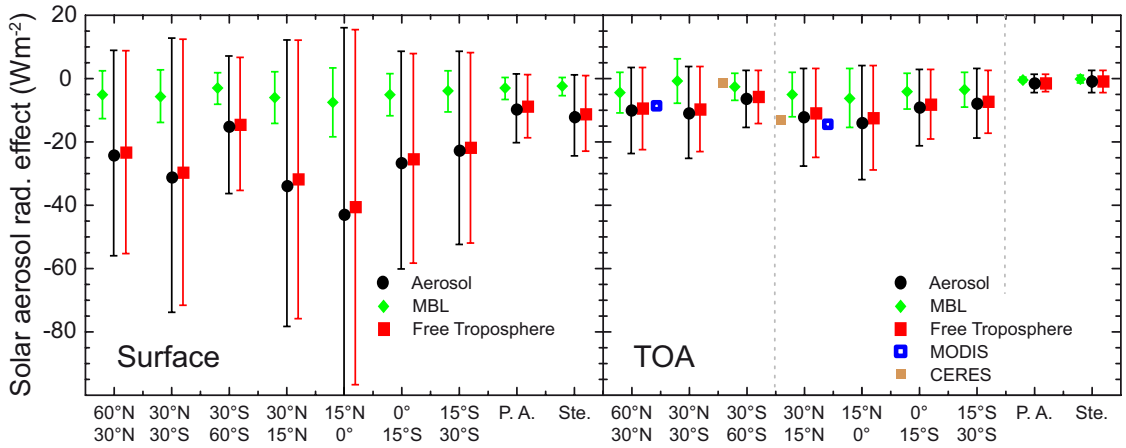

Figure 6.12: Mean solar aerosol radiative effect at the surface (left) and top of atmosphere (TOA, right) for different latitudinal belts as determined from libRadtran simulations with lidar observations during three transatlantic cruises of Polarstern in 2009 and 2010 as input for the vertical aerosol distribution according to Fig. 5.27. Error bars indicate the standard deviation. Derived mean irradiances from CERES [*Christopher and Zhang*, 2002] and MODIS [*Kaufman et al.*, 2005] are added.

and the free troposphere is the non–absorbing sea salt (SSA ≈ 0.99 [*Müller et al.*, 2011]). Continental aerosol, especially black carbon, is known to effectively absorb radiation in the solar range [*Bond and Bergstrom*, 2006]. However, the importance of the contribution of marine aerosol to the global aerosol effect is due to the global distribution of water surfaces on the Earth. The atmosphere over large remote areas in the Pacific Ocean and the Southern Ocean contains marine aerosol only [*Smirnov et al.*, 2009]. The TOA solar aerosol radiative effect (Fig. 6.12, right) shows the same patterns as a function of latitude as the radiative effects that occur at the surface (Fig. 6.12, left). However, they are smaller in range by a factor of 2–3. In the latitudinal belt from 60°–30° N the solar aerosol radiative effect is $-10 \pm 13\,\mathrm{W\,m^{-2}}$, in the latitudinal belt from 30°–60° S it is $-6 \pm 9\,\mathrm{W\,m^{-2}}$. Spaceborne instruments (Fig. 6.12, right) found solar aerosol radiative effects of $-8\,\mathrm{W\,m^{-2}}$ for the latitudinal belt from 60°–30° N above the Atlantic (blue squares) [*Kaufman et al.*, 2005] and $-2\,\mathrm{W\,m^{-2}}$ for the latitudinal belt from 20°–40° S above the Pacific (brown squares) [*Christopher and Zhang*, 2002] and confirm the difference between northern and southern midlatitudes. In the northern tropics solar aerosol radiative effects of $-13\,\mathrm{W\,m^{-2}}$ (latitudinal belt from 30 – 10°N) [*Christopher and Zhang*, 2002] and $-14\,\mathrm{W\,m^{-2}}$ (30°–5° N) [*Kaufman et al.*, 2005] were determined. Based on the lidar measurements of this study solar aerosol radiative effects of -12 ± 16 and $-14 \pm 18\,\mathrm{W\,m^{-2}}$ were estimated from the simulations for the tropical belts from 30°–15° N and from 15°–0° N at TOA, i. e., very good agreement is obtained.

The solar aerosol radiative effect was also determined for both measurement campaigns in the southern hemisphere. The surface type was changed from ocean surface to grassland (Punta Arenas) and savanna (Stellenbosch). Thus, the absorption efficiency of the surface was reduced. In the boundary layer and the free troposphere continental aerosol was assumed with the same microphysical properties as in the settings before (Fig. 6.10, right). At the surface (Fig. 6.12, left) a solar aerosol radiative effect of about -12 and $-10\,\mathrm{W\,m^{-2}}$ was determined at Stellenbosch and Punta Arenas, respectively. At Punta Arenas the lowest AOT values (Fig. 5.27, left) in this study lead also to the lowest determined solar aerosol radiative effect. At TOA the change of the surface albedo from ocean surface ($\approx$0.05) to savanna ($\approx$0.18) strongly affects the radiative influence of the aerosol. Although the mean AOT value (Fig. 5.27, left) determined at Stellenbosch (0.07) is in the range of the determined AOT for the latitudinal belts from 30°–60° S (AOT of 0.08, solar aerosol radiative effect of $-6\,\mathrm{W\,m^{-2}}$) and 15°–30° S (AOT of 0.08, solar aerosol radiative effect of $-8\,\mathrm{W\,m^{-2}}$), the solar aerosol radiative effect is $-1\,\mathrm{W\,m^{-2}}$. The aerosol effectively enhances the reflectance above the ocean surface, but a distinct influence on the reflectance above savanna or grassland cannot be found.

The presented simulations show that height–resolved extinction coefficients and different SSA and asymmetry parameter for free–tropospheric and MBL aerosol are key input variables for accurate, realistic radiative–transfer modeling. However, more detailed spectral information about the extinction coefficients in at least equivalent bands of the correlated–k approximation (Sec. 4.7) should be aspired as well as routinely determined, spectrally resolved SSA and asymmetry parameter for more accurate radiative–transfer calculations.

Chapter 7

Contrasting the impact of aerosols at northern and southern midlatitudes on heterogeneous ice nucleation

Aerosol particles can influence cloud evolution processes in a variety of ways. *Lohmann and Feichter* [2005] distinguished between the cloud albedo effect (the higher the amount of small cloud particles, the higher the cloud reflectivity), the cloud lifetime effect (the smaller the cloud droplets, the less precipitation), the semi–direct effect (the more radiation is absorbed in the atmosphere, the higher the evaporation), the thermodynamic effect (the smaller the liquid–water droplets, the more time and colder temperatures are needed for freezing), the glaciation indirect effect (the more aerosol particles serve as ice nuclei, the more precipitation), the riming indirect effect (the smaller the cloud droplets, the less riming), and the surface energy budget effect (the higher the attenuation of the incoming radiation, the smaller the net surface solar radiation). The complexity of possible influences motivate ongoing strong observational and laboratory efforts because of the lack of a detailed knowledge of aerosol–cloud interactions and, consequently, the large uncertainties in their description and parametrization in atmospheric models. In particular, the process of heterogeneous ice nucleation is poorly understood [*Cantrell and Heymsfield*, 2005], so that especially in this scientific field more research (including atmospheric observation for a variety of aerosol and meteorological conditions) is needed. In the next section, heterogeneous ice nucleation is described and experimental approaches in the research field are briefly reviewed. The advantage of lidar in this field of research will be shown. Afterwards, the results of a study on heterogeneous ice formation will be presented, which was focused on the comparison of findings at northern and southern midlatitudes.

7.1 Introduction

Aerosol particles are required to initiate ice nucleation in the atmosphere at temperatures down to −37 °C [*Pruppacher and Klett*, 1997]. Besides aerosol properties (number concentration, size, aerosol type), ambient meteorological conditions (temperature, relative humidity, vertical motions, turbulent mixing) as well as cloud microphysical properties (e. g., droplet concentration and size, dynamics) control the nucleation of first ice crystals in supercooled liquid–water clouds. There is no doubt that aerosol particles serving as cloud condensation nuclei (CCN) or ice nuclei (IN) sensitively influence cloud processes. One of the basic questions is however, how important this impact is (compared to ambient meteorological influences and cloud dynamics) and whether global models [*Chen et al.*, 2008; *Hoose et al.*, 2010], used to predict future climate change, properly reflect aerosol effects on ice nucleation and the subsequent impact on the production of rain in different clean to heavily polluted areas around the globe.

Below −38 °C homogeneous ice formation takes place, i. e., spontaneous ice formation in supercooled liquid water droplets at high ice supersaturation levels without the need for IN [*Heymsfield and Sabin*, 1989; *Koop et al.*, 2000; *Ansmann et al.*, 2009]. Between −38 and 0 °C IN offer a pre–crystalline structure for aggregating single water molecules that enables the nucleation of ice crystals [*Lundheim*, 2002] which can, e. g., be described with the active–site theory [*Niedermeier et al.*, 2011]. Thereby, four general mechanisms can be distinguished. Heterogeneous ice nucleation is possible by (a) deposition freezing that denotes the direct deposition of water vapor on an IN at $RH_{Ice} > 100\%$, (b) contact freezing when a supercooled droplet collides with a dry IN at $RH_{Water} > 100\%$, (c) condensation freezing which happens when the insoluble fraction of a CCN leads to instantaneous ice nucleation of a freshly formed droplet at $RH_{Water} > 100\%$, and (d) immersion freezing (same as condensation freezing but further cooling is needed after condensation). Ice formation processes including so–called secondary ice production are summarized by *Seifert* [2010].

Laboratory measurements of ice nucleation triggered by several aerosol types were performed in the Aerosol Interactions and Dynamics in the Atmosphere cloud chamber (AIDA) [*Möhler et al.*, 2001] and the Leipzig Aerosol Cloud Interaction Simulator (LACIS) [*Stratmann et al.*, 2004; *Hartmann et al.*, 2011]. According to many publications dust seems to be the most important IN due to its high abundance [*Liu et al.*, 2008a; *Dentener et al.*, 2006], high active fraction (favorable surface properties), and high temperature of activation. *Möhler et al.* [2008a] and *Connolly et al.* [2009] found activation temperatures of −20 °C for pure dust in agreement to observations of *Ansmann et al.* [2008].

Soot particles may also be favorable IN. The freezing efficiency of soot strongly depends on the generating process (forest fire, volcanic eruptions, fuel combustion, biomass burning) that determines the shape and hygroscopic behavior of the soot [*Gorbunov et al.*, 2001]. Activation temperatures of −18 to −26 °C for soot IN were found [*Gorbunov et al.*, 2001; *Diehl et al.*, 2006]. A third class, assumed to be favorable IN, are bacteria. They show ice nucleation at temperatures of −7 to −11 °C, but a very low fraction becomes activated [*Levin and Yankofsky*, 1983; *Lundheim*, 2002; *Christner et al.*, 2008; *Möhler et al.*, 2008b].

At atmospheric conditions, mixtures of aerosol types develop during regional to long–range transport [*Tesche et al.*, 2011; *Ansmann et al.*, 2011b]. Coating of, e. g., dust particles by sulfuric acid or organics lower the IN efficiency and temperature of activation [*Möhler et al.*, 2005, 2008a; *Cziczo et al.*, 2009; *Niedermeier et al.*, 2010] which indicates that the soluble part of particles determines its efficiency to serve as CCN whereas the insoluble part is responsible for the ice activation potential or efficiency [*DeMott et al.*, 1997; *Diehl and Wurzler*, 2004; *Diehl et al.*, 2006]. However, the controlling mechanisms that define the ice activation temperature of a given particle population with a specific size distribution and chemical composition are complex and not fully understood yet. In–situ sampling and analysis of ice residues within the atmosphere provide valuable indications regarding the IN properties of aged (coated, mixed) atmospheric aerosol particles [*DeMott et al.*, 2003; *Prenni et al.*, 2009; *Pratt et al.*, 2009; *Stith et al.*, 2011]. Evidence of an increase in the active fraction and temperature of activation of particle mixtures with anthropogenic metals was found recently by *Ebert et al.* [2011], especially for lead–bearing particles.

In contrast, marine particles seem to be bad IN. Samples taken in marine environments showed a negligible ice nucleation efficiency of marine aerosols (DMS, sea salt, and marine bacteria) [*Prenni et al.*, 2009; *Ebert et al.*, 2011; *Alpert et al.*, 2011] up to a suppression of ice nucleation by DMS and soluble sea salt containing particles [*Vortisch et al.*, 2000; *Zobrist et al.*, 2008].

Atmospheric investigations were mainly based on aircraft in–situ studies until 2005. Aircraft observations are suitable to investigate the relationships between cloud–droplet, ice–crystal, and IN number concentration in mixed–phase clouds [*Peppler*, 1940; *Hobbs and Rangno*, 1985; *Heymsfield and Miloshevich*, 1993; *Hobbs and Rangno*, 1998; *Cober et al.*, 2001; *Korolev et al.*, 2003; *Hogan et al.*, 2003; *Field et al.*, 2004; *Heymsfield*, 2007; *Lance et al.*, 2011]. *Hobbs and Rangno* [1985, 1998] found, for instance, a strong correlation between the occurrence of ice formation and the occurrence of a broad drop size spectrum. Ice crystals

were observed at temperatures above −10 °C only for clouds that showed a significant number of droplets with diameters larger than 20 µm.

In the probed mixed–phase clouds IN concentrations were often smaller than ice crystal concentrations by several orders of magnitude [*Hobbs and Rangno*, 1985]. This difference was explained by secondary nucleation processes (e. g., the Hallet–Mossop process [*Hallett and Mossop*, 1974], crystal–crystal collisions [*Vardiman*, 1978]) that enhanced the ice crystal concentration above that produced by the primary heterogeneous ice crystal production [*Hobbs and Rangno*, 1985, 1990; *Rangno and Hobbs*, 2001]. However, aircraft studies are performed at high ground speeds and perhaps affected by ice crystal shattering at the probe inlets, too [*Korolev et al.*, 2003; *Heymsfield*, 2007]. Uncertainties in the discrimination of the ice and liquid phases for a wide range of cloud particle sizes was discussed by *Korolev et al.* [2003]. One remarkable result from aircraft studies is the temperature independence found for ice nucleation [*Hobbs and Rangno*, 1998; *Fleishauer et al.*, 2002] although a relation would be expected from laboratory studies, as discussed above. This confusing result may be related to the fact that cloud top (and cloud top temperature) is usually not well known and the in–situ measurements along flight tracks are frequently performed up to several kilometers below cloud top [*Mossop et al.*, 1970]. Thus, the initial height of the primary ice nucleation, the cloud top [*Rauber and Tokay*, 1991; *Harrington et al.*, 1999; *Lebo et al.*, 2008], and the respective temperature are not observed. Aircraft frequently observe ice crystals that nucleated at higher altitudes and at colder temperatures than assumed in the data analysis (temperature at flight level) [*Fleishauer et al.*, 2002].

Ice crystal formation starts in supercooled clouds under most favorable temperature and water–vapor conditions. This favorable environment is usually given at cloud top. After nucleation, ice crystals grow fast and immediately start to fall [*Song and Lamb*, 1994]. *Heymsfield et al.* [2011] deduced mean linear ice crystal growth rates of $1.4\,\mu m\,s^{-1}$ independent of the ice crystal size in the range of 100 to 400 µm. Falling velocities of 0.2 to $1.0\,m\,s^{-1}$ for ice crystal ensembles were observed with Doppler lidar at Leipzig [*Ansmann et al.*, 2008]. *Heymsfield* [2003] found even falling velocities of 2.5 to $3\,m\,s^{-1}$ for ice crystal ensembles with 1 mm median ice crystal radius. Because of the rapid ice crystal growth and high falling velocities ice crystals need only a couple of minutes to fall from cloud top to cloud base in layered clouds of 200–500 m vertical extent. Thus, they become visible as virgae below cloud base and can also easily be detected with lidar. As a consequence of this sedimentation effect and possible secondary ice production, it is important to observe the entire cloud when studying heterogeneous ice nucleation effects.

Ground–based polarization lidar observations have the advantage that the cloud top can be resolved, if the cloud is optically not too thick, and simultaneously cloud virgae can be studied with respect to the phase to unambiguously identify ice nucleation in clouds [*Sassen*, 2002; *Sassen et al.*, 2003; *Sassen*, 2005; *Ansmann et al.*, 2005, 2008, 2009; *Seifert et al.*, 2010; *de Boer et al.*, 2011; *Seifert et al.*, 2011]. In the following, the results of the current IfT lidar cloud data with focus on heterogeneous ice formation and height–resolved mixed–phase cloud characterization will be presented [*Kanitz et al.*, 2011].

7.2 Results

A series of lidar studies were already performed at IfT regarding the role of desert dust and tropical aerosols in heterogeneous nucleation of ice crystals in supercooled clouds at Ouarzazate (Morocco), Cape Verde, and Leipzig [*Ansmann et al.*, 2008, 2009; *Seifert et al.*, 2010]. Here the same method is applied to the three cloud data sets, each covering four months of observations, that were recorded at Punta Arenas, at Stellenbosch, and aboard Polarstern [*Kanitz et al.*, 2011].

Aboard Polarstern and at Punta Arenas and Stellenbosch 3352 clouds were observed with lidar in the framework of OCEANET from 16 October 2009 to 13 April 2011. The geometrical properties of the clouds were determined by means of the lidar backscatter information as shown in Fig. 7.1 (top). Two defined cloud layers are highlighted in Fig. 7.1 by square boxes. Strong backscattering at 355 nm occurred at heights around 1.5 and 5 km. A cloud layer is defined as single cloud layer, if it is separated from adjacent clouds by 500 m in the vertical and 5 min in time. The time of occurrence of a cloud layer is defined as the time from the first to the last signal profile that shows enhanced backscattering. All signal profiles that were recorded within the time of occurrence of the cloud were averaged to yield one single profile. From that profile the cloud top height (H_{top}) is determined. It is the height at which the signal decreases to a value below the signal at cloud base (the height bin above which the signal starts to increase). In Fig. 7.1 (top) H_{top} of 2.2 (lower layer) and 6.4 km (upper layer) were determined.

In terms of the volume linear depolarization ratio (δ^{vol}, see Sec. 3.2) cloud layers that are dominated by ice crystals reach δ^{vol} on the order of 30%–50%. Liquid–water clouds of spherical water droplets cause δ^{vol} of 0% [*Schotland et al.*, 1971; *Liou and Lahore*, 1974; *Sassen*, 2005].

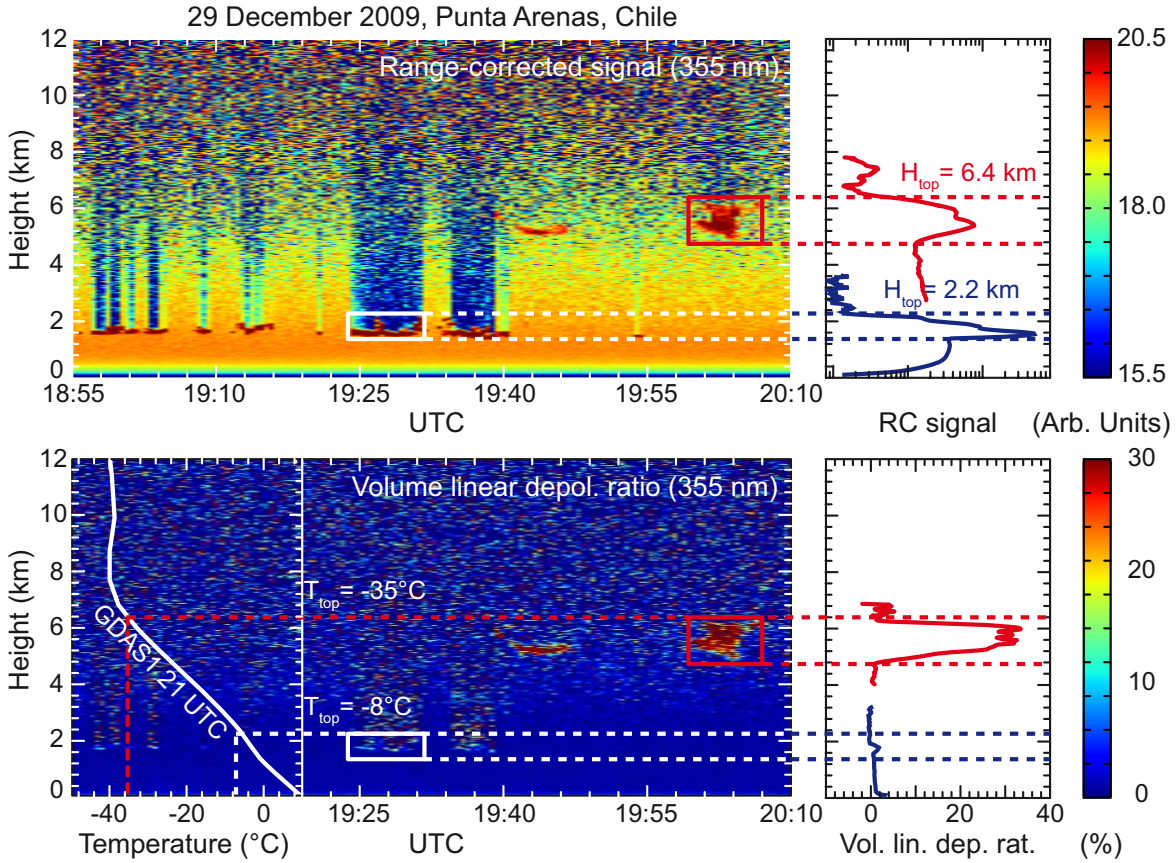

Figure 7.1: Top: Range–corrected signal at 355 nm. Cloud top height H_{top} is derived from the signal profiles (top, right). Bottom: In terms of the volume linear depolarization ratio cloud layers at around 2 and 6 km are detected and identified as liquid–water layers below 2 km and ice–containing cloud layers above 5 km. The GDAS1 temperature profile is used to determine cloud top temperatures T_{top} (given as numbers).

Fig. 7.1 (bottom) shows the height–time display of δ^{vol} (left) and the averaged δ^{vol}–profiles in the lower right panel according to the cloud examples of 29 December 2009 above. The upper cloud layer with H_{top} = 6.4 km (red box) causes high depolarization (red). The averaged δ^{vol}–profile shows δ^{vol} of 30%. Thus, the cloud layer is categorized as ice–containing layer. The lower cloud layer with H_{top} = 2.2 km (white box) appears dark blue in the height–time display of δ^{vol}. The laser light sustains its state of polarization throughout the cloud which points to a liquid–water cloud. However, in the averaged δ^{vol}–profile a small peak can be seen. This peak is caused by multiple scattering (see Sec. 3.2) which has to be considered in the cloud–phase discrimination. GDAS1 temperature profiles are available every 3 hours. We selected the 21 UTC profile (Fig. 7.1, bottom, left) to estimate cloud top temperatures T_{top} as indicated in Fig. 7.1 (bottom).

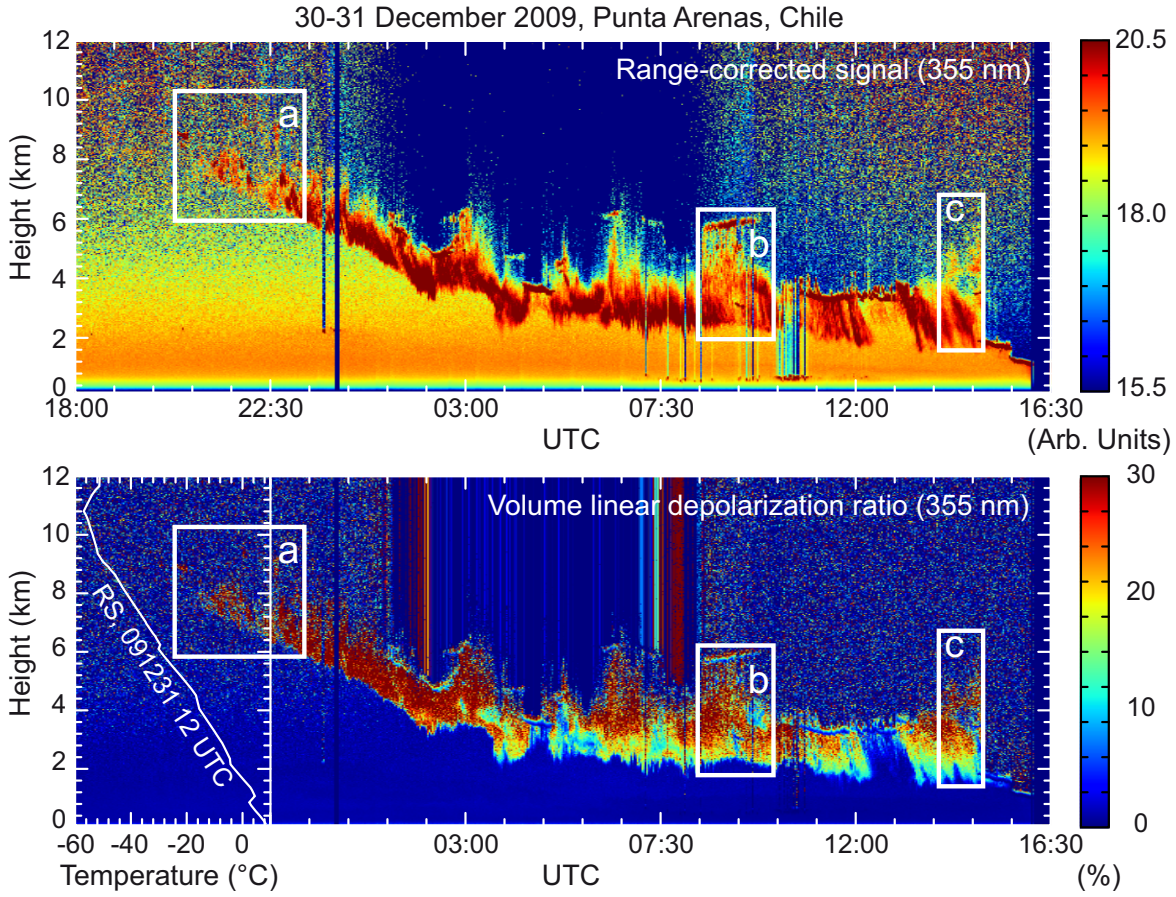

Figure 7.2: Lidar observation of a complex cloud system in terms of the range–corrected signal (top) and volume linear depolarization ratio (bottom) height–time displays for 30–31 December 2009. Temperature profile measured with radiosonde (RS) at Punta Arenas at 12 UTC is shown in addition (bottom, left). Several transparent cloud layers (box a, b, c) are identified and may allow the determination of cloud top and top temperature. However, such complex, optically thick cloud decks widely prohibit the detection of the uppermost cloud layer in which first ice crystals nucleate.

Complex cloud systems as shown in Figure 7.2 are not considered in the cloud statistics discussed below. The shown cloud system developed during the passage of a warm front. Such cloud decks are optically thick so that laser light cannot penetrate the layer up to the cloud top during most of the time (see periods between the boxes a and b in Fig. 7.2). Even during time periods with partly transparent clouds (a, b, c in Fig. 7.2) it usually remains unclear at what height ice nucleation was initiated. Several cloud layers at different heights may be detected but the uppermost may not be visible in the lidar profiles.

Table 7.1: Cloud statistics from the lidar cloud data records at Punta Arenas (Chile, December–January, January–April), RV Polarstern (Atlantic), and Stellenbosch (South Africa). Out of the total number of cloud cases observed (928 in December–January, 593 in January–April, 1316, 515) 95% (Punta Arenas, RV Polarstern) and 76% (Stellenbosch) were well defined in terms of cloud phase and top height. Additionally, the cloud data set of an 11–year study at Leipzig (Germany) is presented [*Seifert et al.*, 2010].

	Punta Arenas 2009/2010 Dec–Jan Cases (%)	Punta Arenas 2010 Jan–Apr Cases (%)	RV Polarstern 2009/2010 Cases (%)	Stellenbosch 2010/2011 Cases (%)	Leipzig 1997–2008 Apr–Sep Cases (%)
Well–defined clouds	884	564	1251	389	1134
Clouds, phase state					
Liquid–water clouds	646 (73%)	416 (74%)	980 (78%)	253(65%)	555 (49%)
Mixed–phase clouds	72 (8%)	52 (9%)	58 (5%)	41 (11%)	105 (9%)
Pure ice clouds	166 (19%)	96 (17%)	213 (17%)	95 (24%)	474 (42%)
Clouds, top temperature					
$< -40\,^{\circ}$C	163 (18%)	132 (23%)	208 (17%)	87 (22%)	415 (37%)
$-40\,^{\circ}$C to $0\,^{\circ}$C	631 (71%)	373 (66%)	228 (18%)	122 (31%)	417 (37%)
$> 0\,^{\circ}$C	90 (10%)	59 (10%)	815 (65%)	180 (46%)	302 (27%)

Cloud seeding effects may have caused ice production in lower cloud layers. In box (b) ice nucleation is most probably initiated at the top of the highest observed layer (6.2 km, -30° C). Immediately, precipitation below the cloud is observed. However, it remains unclear, whether cloud seeding [*Rutledge and Hobbs*, 1983; *Ansmann et al.*, 2009] from above also contributed to the detailed ice production. According to the *seeder–feeder mechanism* falling ice crystals grow by the Bergeron–Findeisen process after entering lower cloud layers from above and cause the supercooled droplets within these lower cloud layers to transfer water vapor onto the crystals [*Findeisen*, 1938]. The grown ice crystals fall through the cloud and form virgae below the lower cloud. In box (c) cloud layers up to 4.5 km height were observed and suggest that the precipitation at 16:00 UTC is caused by precipitating overlying clouds that are invisible due to the optical thickness of the underlying clouds.

Table 7.1 lists all observed cloud layers that were characterized by T_{top} and cloud phase at the three measurement sites. In addition, observations at Leipzig, Germany are included. The cloud data set is divided into three classes according to cloud phase and T_{top}. Liquid–water, mixed–phase, and pure ice clouds were distinguished as well as warm clouds ($T_{top} > 0°$C).

At Punta Arenas 884 clouds were characterized during the first seven weeks (December–January) of the four–month campaign. 27% out of all clouds contained ice crystals (pure ice and mixed–phase). 71% had a cloud top temperature between 0 and −40 °C. The last months (January–April) of the ALPACA campaign were treated separately. The 355–nm depolarization channel did not work properly from the end of January until the end of the campaign. In this period, clouds were counted as mixed–phase clouds, when the extinction coefficient was clearly >1.0 km^{-1} (i. e., clearly above the values for typical cirrus) and the cloud produced virgae. According to our experience during the first two months of the campaign we assumed that all virgae consist of ice crystals and indicate ice nucleation. The statistics of liquid–water, mixed–phase, and pure ice clouds for the December–January period and the entire period from December to April are rather similar as Tab 7.1 indicates so that it is sufficient to use the December–January cloud data set for further studies. In this way, the entire lidar study focusing on the comparison of cloud observations at very different sites is solely based on polarization lidar measurements.

Aboard Polarstern the highest fractions of warm clouds were found. 65% out of all cases are pure liquid–water clouds with top temperature above 0 °C. Most of these clouds were shallow clouds at the MBL top. The liquid–water cloud fraction (78%) and the fraction of warm clouds show that only 13% of the characterized clouds were supercooled liquid–water clouds ($T_{top} < 0$ °C). In total 210, 785, and 256 clouds were defined in the northern mid-latitudes (60°–30° N), the tropics (30° N–30° S), and the southern midlatitudes (30°–60°S), respectively. The lidar was running whenever weather conditions were appropriate and the sun elevation was <80°.

A comparably small amount of cloud layers (515 total) was recorded at Stellenbosch during the four–month period. 389 clouds (76%) were well defined (i. e., cloud top could be detected, volume linear depolarization ratio profile was of high quality). 35% of the well–defined clouds were ice–containing clouds. The measurements at Stellenbosch had to be interrupted during noon. The air conditioning system of Polly^{XT} was not able to cool down the lidar cabin at high sun conditions during the subtropical southern hemispheric summer (air temperature >35 °C). Therefore, the measurements were performed between 10:00 UTC and 16:00 UTC only for 10 minutes each hour to document the daily development of aerosol and cloud layers above Stellenbosch. Between 16:00 UTC and 10:00 UTC the measurements were continuously running.

The Leipzig cloud data set [*Seifert et al.*, 2010] selected for this study contains only clouds measured during the summer periods from April to September in the years 1997 to 2008. The summer period was chosen only because the measurements at Punta Arenas and Stellenbosch were also performed during the summer season.

Table 7.1 shows that the fraction of mixed–phase clouds is comparably low (<11%) at all stations and aboard Polarstern. Liquid–water clouds dominate at Punta Arenas, Stellenbosch, and aboard Polarstern, but not at Leipzig (almost similar number for liquid–water and pure ice clouds).

In Fig. 7.3 the observed clouds are given as a function of H_{top} (left). Fig. 7.3 (right) presents the frequency distribution of cloud depth for the three defined cloud classes. As can be seen, similar distributions of cloud heights and depths were observed at the different lidar sites. As mentioned above, complex cloud decks are excluded from the statistics. This holds also for the Leipzig cloud data set. The maximum cirrus top height is 18 km (Polarstern, includes tropical cirrus), <15 km (Stellenbosch, subtropics), <14 km (Leipzig, midlatitudes), and <13 km (Punta Arenas, midlatitudes). Cloud top heights of mixed–phase clouds range from 4–11 km (Polarstern), 5–10 km (Stellenbosch), 2–10 km (Leipzig), and 3–8 km height (Punta Arenas). The comparably large H_{top} range observed aboard the Polarstern shows that tropical as well as midlatitudinal cloud layers are included in the statistics. In contrast, at Punta Arenas almost polar climate conditions dominate (as discussed below). Cloud top heights of liquid–water cloud layers are all <8 km with the highest frequency of occurrence below 3 km height at all sites.

In Fig. 7.3 (right) cloud depth distributions show similar features for the different sites. Roughly 80% out of all liquid–water cloud layers show depths of <1 km, 80% out of all mixed–phase cloud layers had a vertical extension <2 km (from top to the bottom of the virgae), and 80% out of all cirrus depths were <3 km. Thus, the lidar observations include mostly layered clouds (altocumulus, altostratus). Convective clouds are excluded for the reasons discussed above.

Figure 7.4 shows the fraction of ice–containing clouds as a function of cloud top temperature (T_{top}). Besides the OCEANET and the Leipzig observations, measurements performed at the tropical site of Praia, Cape Verde, are included. These measurements were conducted in the framework of SAMUM–2 in the winter of 2008 [*Ansmann et al.*, 2009].

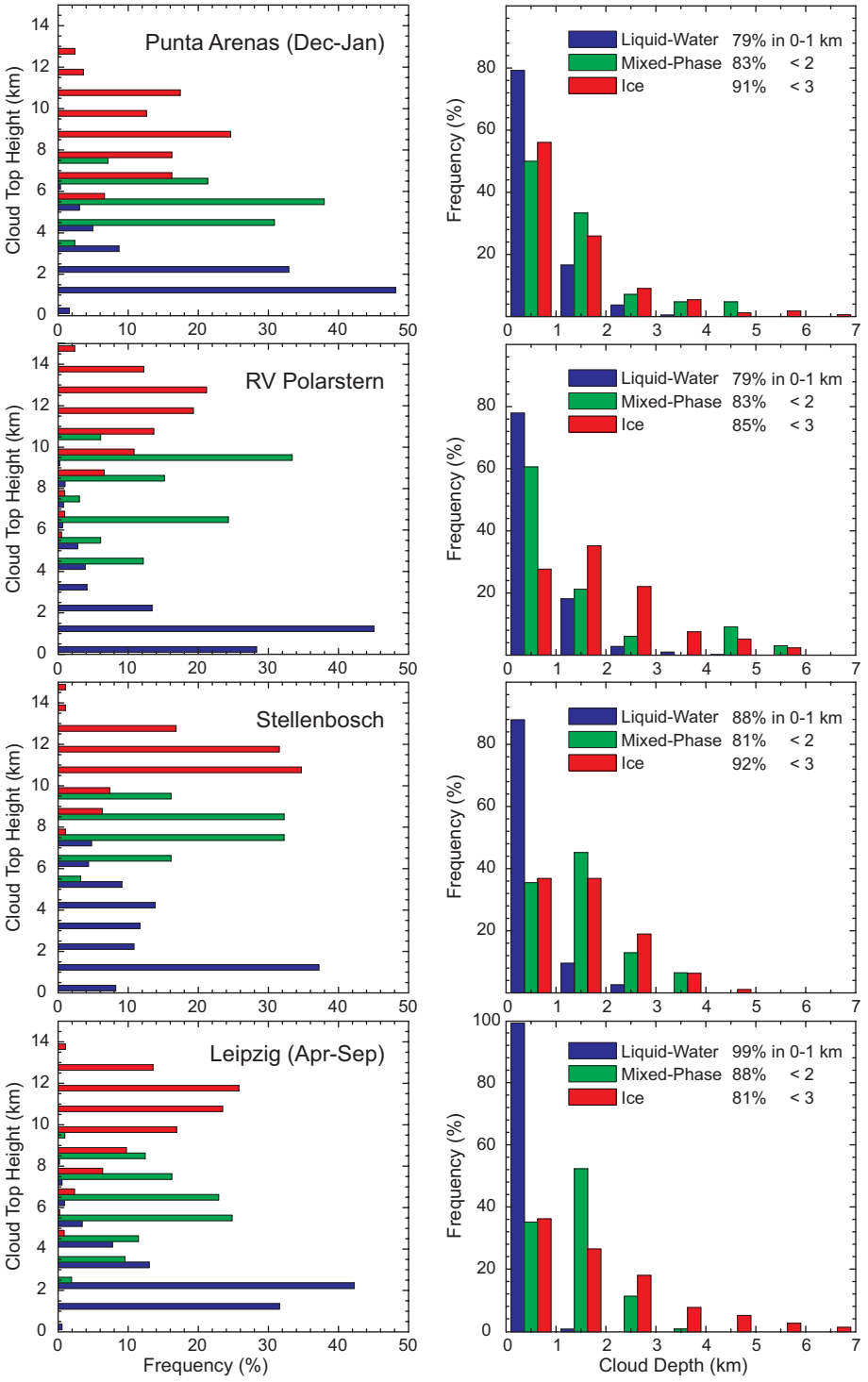

Figure 7.3: Frequency of occurrence of cloud top heights and cloud depths, separately for liquid–water cloud layers (blue), mixed–phase cloud layers (green), and pure ice cloud layers (red). Cumulative frequency of occurrence of cloud layers in certain cloud depth ranges is given for each site. The statistics are based on the 884, 1251, 389, and 1134 cloud layers at Punta Arenas, Chile (December–January), RV Polarstern, Stellenbosch, South Africa, and Leipzig, Germany (summer half year), respectively.

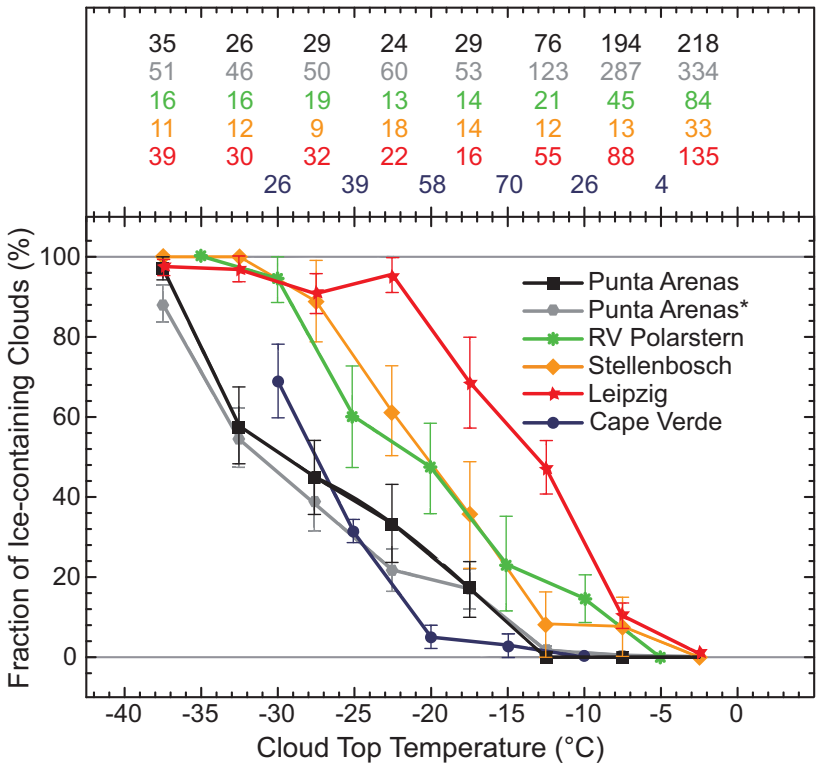

Figure 7.4: Frequency of occurrence of ice–containing (mixed–phase and pure ice) cloud layers as a function of cloud top temperature. Clouds with cloud top temperatures between −40 and 0 °C are considered. Observational sites are Punta Arenas (black, Dec–Jan, grey and denoted with *, Jan–Apr), RV Polarstern (green), Stellenbosch (orange), Leipzig (red, summer periods from *Seifert et al.* 2010), and Cape Verde (navy blue, seeding–corrected clouds from *Ansmann et al.* 2009). Error bars indicate the standard deviation [*Seifert et al.*, 2010]. The total number of observed cloud layers for each 5–K temperature interval is given on top.

The error bars in Fig. 7.4 are calculated from the standard deviation σ of binomial distributions (see Eq. 7.1) which depends on the number of sampled cloud events n and the fraction of ice–containing clouds f representing the likelihood that an ice–containing cloud is observed [*Seifert et al.*, 2010]:

$$\sigma = \sqrt{f(1-f)/n}. \tag{7.1}$$

As can be seen in Fig. 7.4, a significant fraction of ice–containing clouds of 20% is found over Leipzig already at temperatures around −10 °C. In contrast, less than 15% and even <5% of the clouds contain ice at this temperature over Stellenbosch and Punta Arenas, respectively. With decreasing T_{top} the fraction of ice–containing clouds increases at all sites. However, the slopes of the curves are very different in Fig. 7.4. At $T_{top} = -15$ °C about 60%

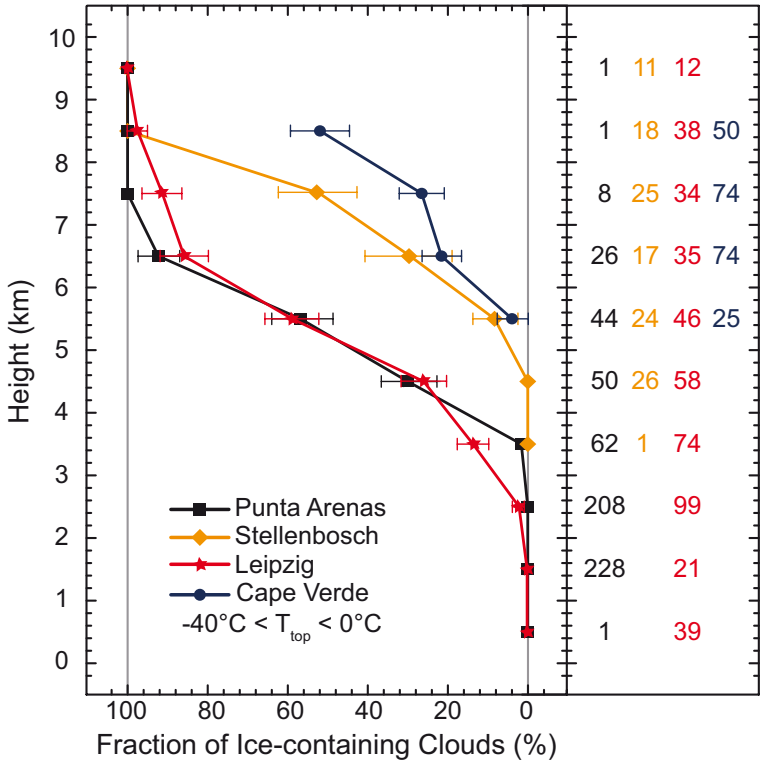

Figure 7.5: Frequency of occurrence of ice–containing clouds as a function of height. The cloud fractions are computed for 10 cloud top height intervals of 1 km vertical extent. Error bars indicate the standard deviation [*Seifert et al.*, 2010]. The total number of observed cloud layers for each interval is given at the right.

(Leipzig), <25% (Stellenbosch, Polarstern), and <10% (Punta Arenas) are mixed–phase or pure ice clouds. The 90%–100% level of ice–containing clouds is reached at $T_{top} > -25\,°C$ (Leipzig), around $-30\,°C$ (Stellenbosch, Polarstern), and $<-35\,°C$ (Punta Arenas). The curve for Cape Verde is rather similar to the one for Punta Arenas. This strong contrast in the results (Leipzig versus Punta Arenas) clearly points to a significant influence of aerosol particles on ice formation. However, atmospheric (meteorological) and geographic influences may have contributed to this strong contrast. Whereas at Punta Arenas (and also at Stellenbosch and over Polarstern) marine environmental conditions prevail, Leipzig is clearly a continental site. Orographic effects by mountains up to 3–4 km height about 500 km south west of Leipzig and 100 km west of Punta Arenas may significantly influence the weather patterns in addition.

To check the influence of different atmospheric conditions, in Fig. 7.5 and 7.6 the cloud statistics are presented as a function of height. In this way, also the aerosol effects can be

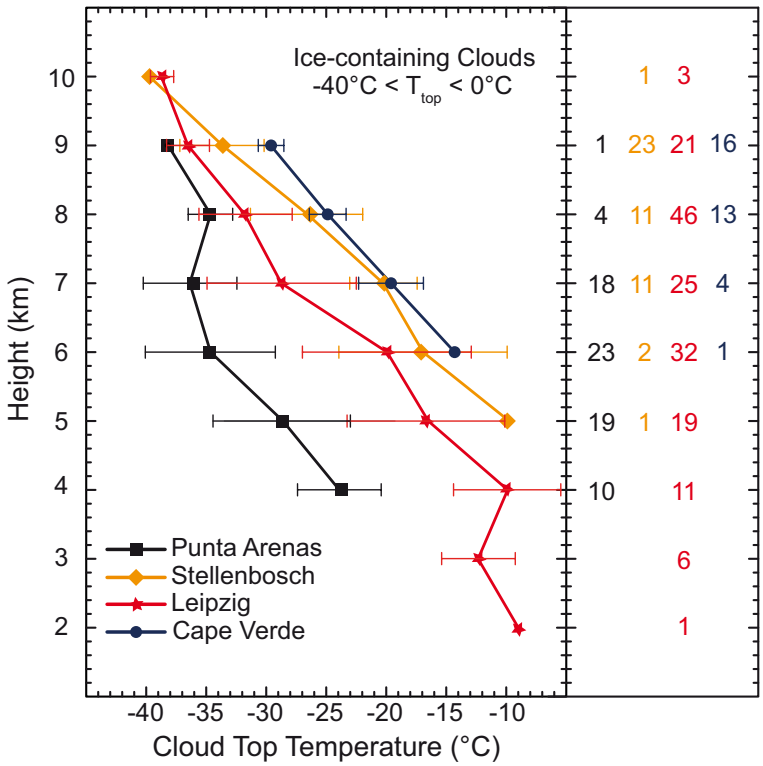

Figure 7.6: Mean cloud top temperature of all ice–containing clouds observed within each of the nine height intervals from 1.5 to 10.5 km height over four different sites. Vertical extent of each height interval is 1 km. Error bars indicate the mean standard deviation. Total number of observed cloud layers for each interval is given at the right.

further investigated, because the strongest influence of particles is expected to occur at low height (close to the sources of atmospheric particles). On the other hand, longe–range transport of particles (desert dust, forest–fire smoke) typically takes place at heights from 2–6 km [*Müller et al.*, 2005; *Mattis et al.*, 2008].

Figure 7.5 shows the fraction of ice–containing clouds and the increase of this fraction as a function of height. As can be seen, similar height–dependent distributions of ice–containing clouds are found at Punta Arenas and Leipzig. Significant ice nucleation starts at heights >4 km and the range of strongest change in the fraction of ice–containing clouds extents from 3.5–6.5 km height. This suggests that atmospheric aspects can be widely ruled out in the explanation of the differences of cloud statistics for Punta Arenas and Leipzig. In the subtropics (Stellenbosch) and tropics (Cape Verde), ice nucleation starts at heights >6 km (and thus even above most of the lofted aerosol layers).

According to Fig. 7.6, which shows the distribution of cloud top temperatures of ice–containing clouds as a function of height, the clouds over Punta Arenas are however much colder (10–15 K) than over Leipzig in the range from 3.5–6.5 km height. Whereas Leipzig is a representative station of the northern midlatitudes (temperate region), Punta Arenas seems to be strongly influenced by polar weather regimes (polar region). Consequently, the subtropical and tropical datasets show even higher cloud temperatures for a given height (e. g., at 6 km). All in all, the results in Fig. 7.5 and 7.6 corroborate that the observed strong contrast in the statistics of ice–containing clouds shown in Fig. 7.4 is related to strong differences in aerosol conditions in the free troposphere rather than meteorological conditions.

At northern midlatitudes, the aerosol conditions in the free troposphere are widely determined by anthropogenic pollution from North America, Europe, and East Asia, desert dust emissions in Africa, America, and Asia, and releases of forest–fire and other biomass–burning smoke in the latitudinal belt from 35° to 65° N [*Müller et al.*, 2005; *Mattis et al.*, 2008; *Uno et al.*, 2011]. In addition, biological material (pollen, bacteria, leaf fragments) may contribute to efficient ice nucleation. At high southern latitudes over remote oceanic areas (>50° S), continental aerosol particles are widely absent and, even if present, the most favorable large IN may already be removed by dry and wet deposition [*Bigg*, 1973]. From a review of in–situ observations *Heintzenberg et al.* [2000] show that the most favorable IN are present in much lower concentrations in the southern hemisphere compared to the northern hemisphere (e. g., dust roughly 88% less, metals roughly 82% less). Here, clean marine conditions prevail as confirmed by *Minikin et al.* [2003].

An interesting point is visible in Fig. 7.5 and remains to be discussed. Although the fraction of ice–containing clouds increases in a similar way between 4 and 6 km height over Punta Arenas and Leipzig, there is a significant deviation at heights from 2–4 km. This is in agreement with Fig. 7.4, which shows the heterogeneous ice nucleation over Leipzig begins already at temperatures >–10 °C. The reasons are not clear, but it may be another hint that anthropogenic pollution as well as biological material are responsible for this effect found over Leipzig. Summertime planetary–boundary–layer heights are frequently above 2 km so that turbulent mixing causes an efficient upward flux of, e. g., urban haze into the lower free troposphere. In contrast, the free troposphere above Punta Arenas shows very low aerosol concentration (see Sec. 5.3).

Figure 7.7 corroborates this argumentation. HYSPLIT 120–hours backward trajectories for each cloud layer considered in the statistics are shown. In the top and center panel

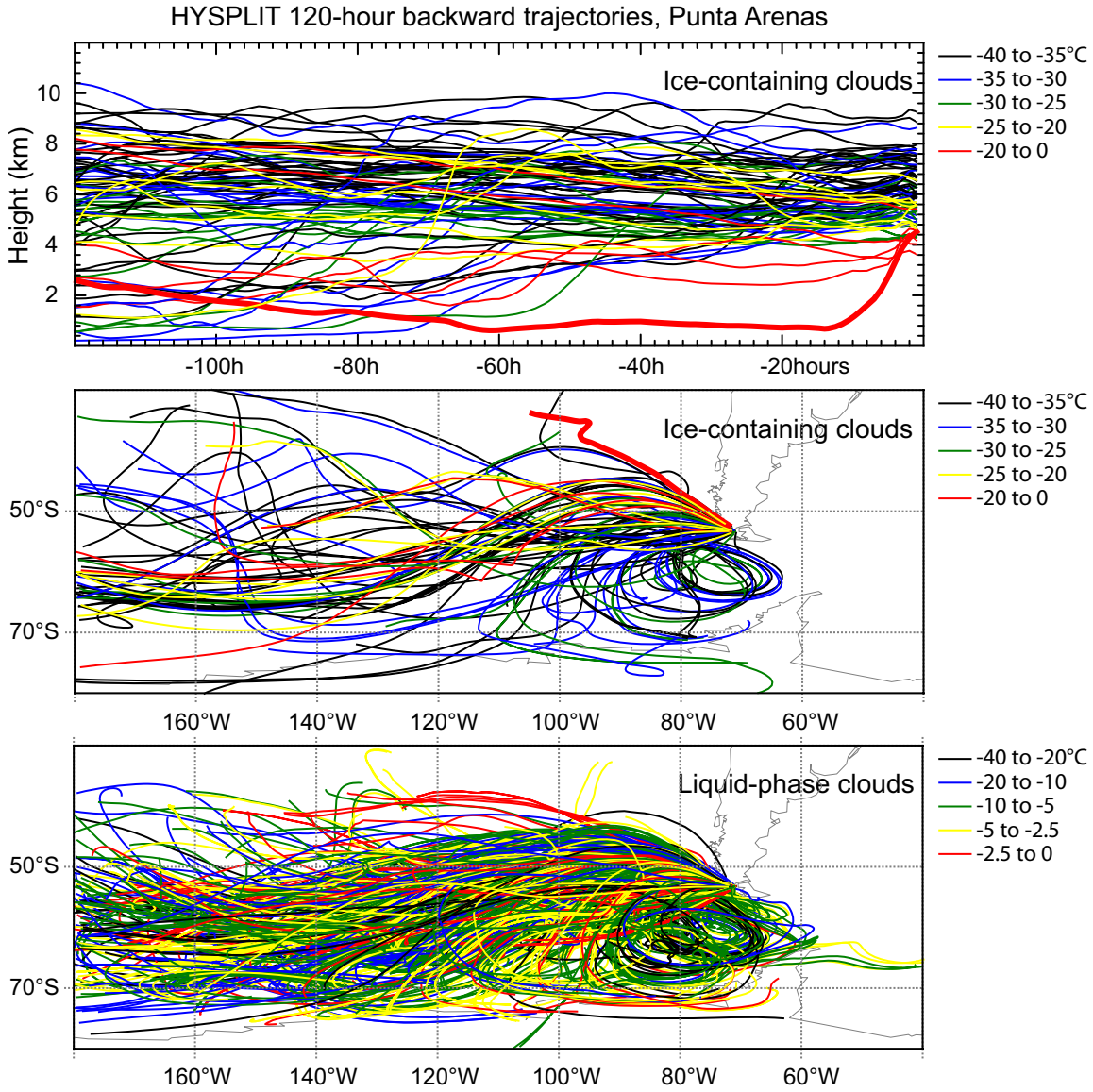

Figure 7.7: 120–hour HYSPLIT backward trajectories of ice–containing clouds over Punta Arenas as function of time and height (top), location (center). Respective backward trajectories for liquid–water clouds (bottom). Only clouds observed in December 2009 to January 2010 are shown.

the height and location of the backward trajectories for ice–containing clouds is shown classified by T_{top} with a color code. The lower panel shows the location of the backward trajectories for liquid–water clouds classified by T_{top}, too. Almost all observed air parcels were advected from west to east, from the Pacific to Punta Arenas. Some of the trajectories show by rising air parcels from start heights <2 km to final heights >4 km (e. g., red thick trajectory) that a turbulent mixing with the boundary layer may inject IN into the

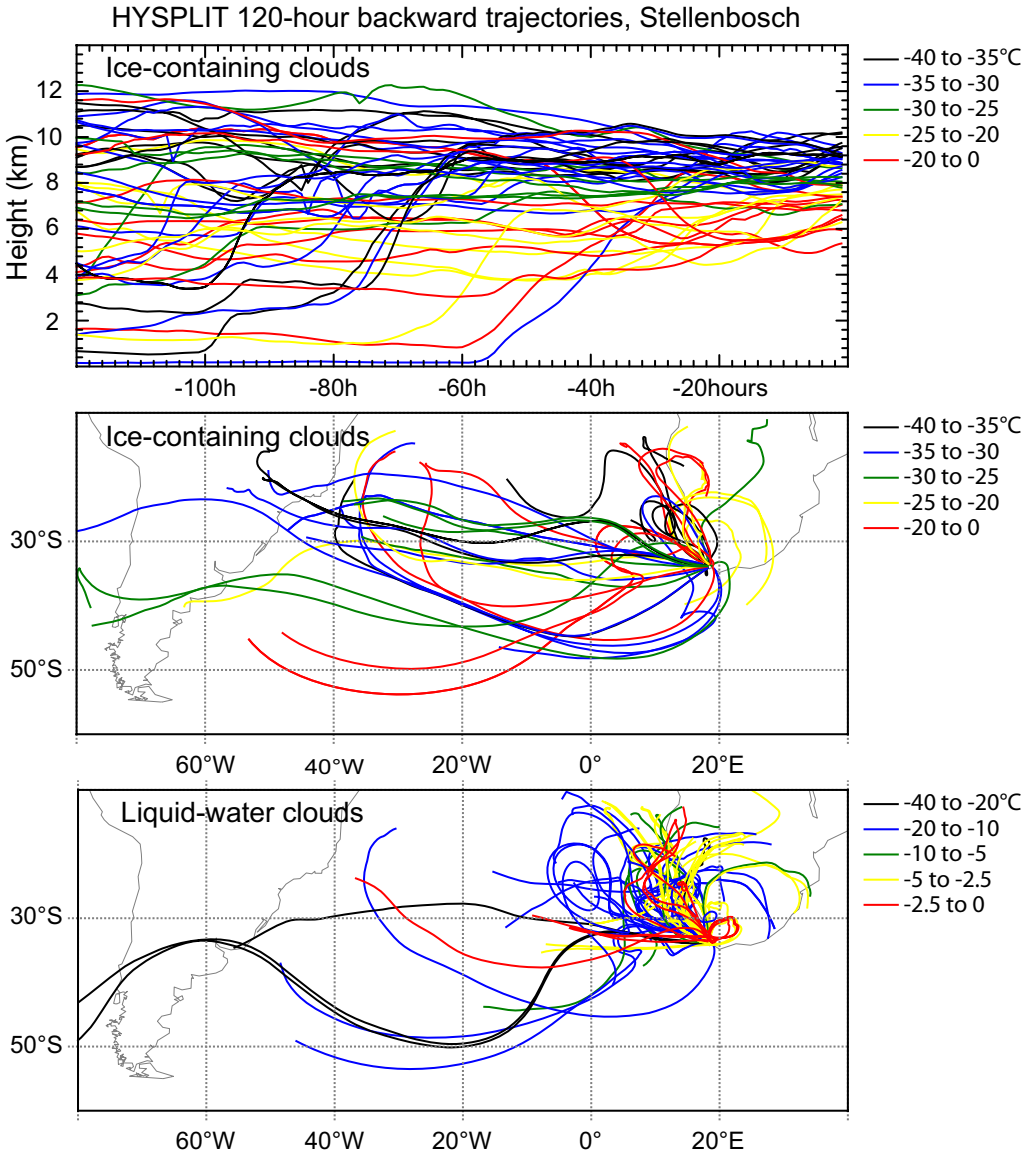

Figure 7.8: Same as Fig. 7.7, except for Stellenbosch (December 2010 to March 2011).

observed air masses. Most of the trajectories of ice–containing clouds with temperature >–25 °C (red and yellow curves) pass the west coast of Chile north of Punta Arenas and cover a longer distance over the continent which enhances the probability of an uptake of continental IN, too. However, most of the trajectories remain above 3 km height and show a marine origin. Thus, the IN availability is defined by the background aerosol concentration.

At Stellenbosch the aerosol conditions are influenced by desert dust from Namibia, smoke from South Africa and Madagascar, and anthropogenic pollution from the industrial region

around Johannesburg and Pretoria [*Tesfaye et al.*, 2011]. In addition, smoke from South America can be advected to South Africa [*Kaufman et al.*, 1998; *Reid et al.*, 2004]. During the GOPHER campaign lofted layers of soil and smoke were frequently observed with lidar. Figure 7.8 shows the calculated 120–hour HYSPLIT backward trajectories of each observed cloud layer at Stellenbosch. The trajectories of ice–containing clouds show a much higher contribution of continental air to the free–tropospheric aerosol load. Most of the ice–containing clouds with $T_{top} > -25\,^{\circ}C$ (red and yellow curves) were observed when air masses were advected along the west coast of South Africa. The probability for dust uptake is high as long as the trajectories are below 4–5 km when they pass desert areas, as SAMUM observations indicate [*Tesche et al.*, 2009]. Trajectories for ice–containing clouds with $T_{top} < -25^{\circ}C$ frequently indicate long–range transport from South America at large heights and a marine origin without significant amounts of IN.

Chapter 8

Summary and Outlook

The Earth's climate is sensitively influenced by aerosols and clouds. Their horizontal and vertical variability and their interactions produce high uncertainties in global atmospheric modeling. Within this thesis the vertical distribution of aerosols above the North and South Atlantic was analyzed with multiwavelength Raman and polarization lidar measurements. The retrieved height–resolved aerosol particle optical properties were used to determine the direct aerosol radiative effect. In addition, the polarization lidar measurements enabled the investigation of the glaciation effect.

The presented results were based on lidar measurements in the framework of OCEANET aboard the research vessel Polarstern during three transfer cruises over the Atlantic ocean, between Germany and either South America or South Africa. Each of the meridional cruises covered a distance of about 10000–14000 km and corresponding time periods of 4–6 weeks. The observations were performed within tropical, subtropical, and midlatitudinal conditions in both hemispheres and frequently downwind of various continental aerosol sources. In addition, measurements in the southern hemisphere were carried out during the southern hemispheric summer half year in Punta Arenas, Chile (2009/2010), and Stellenbosch, South Africa (2010/2011).

Within the first topic of the thesis, the vertical distribution of aerosols above the North and South Atlantic was analyzed. Pure and mixed layers of Saharan dust with an AOT of about 0.2 were observed at the west coast of North Africa. The pure Saharan dust layer showed distinctive wavelength–independent lidar ratios of 50–60 sr and an extinction–related Ångström exponent of about 0.1. Based on the lidar depolarization measurements a biomass–burning smoke fraction of up to 30% was found in an observed mixed layer. For the first time, plumes of Patagonian desert dust were characterized with lidar. The shipborne

lidar observations revealed a lidar ratio of 42 ± 17 sr (532 nm) and a backscatter–related Ångström exponent of 0.4 ± 0.1. The dust particles were found up to 3 km height. Although the wind speed above the Patagonian desert was high with $\approx 25\,\mathrm{m\,s^{-1}}$, the AOT was low with $0.02 - 0.03$. In contrast to African deserts and Sahel areas there are apparently only small amounts of particulate material available in Patagonia that can be lifted and advected eastwards. Unexpectedly, layers of volcanic ash from the Eyjafjallajökull eruption in 2010 could be investigated, too. The ash–related AOT was $0.04 - 0.06$. Determined mean lidar ratios of 45–64 sr, Ångström exponents of ≥ 1, and strong depolarization of more than 30% indicated a mixture of sulfate aerosol and volcanic ash. From a statistical analysis distinct difference in the meridional distribution of aerosol layers in the free troposphere was found. While the MBL showed AOTs of about 0.05, independent of the latitude, the free–tropospheric aerosol can feature AOTs roughly tenfold higher. The highest optical thickness was determined in the northern tropics (0.27), mainly in the outflow regime of Saharan dust. South of the equator a sharp decrease in the amount of free–tropospheric aerosol in the tropics was found. The strong north–to–south difference in the aerosol load also hold for the midlatitudes in both hemispheres. In the northern midlatitudes an AOT of 0.12 was found, in the southern midlatitudes an AOT of 0.07 was determined. While lofted layers were observed up to 5 km height in the free troposphere, the marine boundary layer extended up to about 0.4–0.9 km height. In a comparative study the shipborne lidar measurements showed a good agreement to collocated Sun photometer measurements. The first ground validation of the spaceborne lidar CALIOP with a Raman lidar above the Atlantic was performed. Based on 41 satellite overpasses a good agreement was found in the backscatter coefficient at 532 nm. However, a distinct bias of mistreated thin marine boundary clouds in the data of CALIOP was observed and had to be removed from the data set.

While the site at Stellenbosch is located close to the subtropics and was affected by regional continental aerosol sources, free–tropospheric aerosol layers were almost absent over Punta Arenas. The determined AOT statistic at Stellenbosch (AOT of 0.07) was similar to the AOT statistic for the latitudinal band from 15° to 30° S (AOT of 0.08) obtained from the shipborne observations during the three cruises. At Punta Arenas clean marine conditions prevailed (AOT of about 0.05), because constantly marine air masses were advected to the measurement site by the Antarctic low–pressure belt.

The information of the aerosol vertical distribution is a key parameter in modeling the effect of aerosols on the Earth's radiation budget. The vertical profiles of lidar–derived particle

optical properties were used as input for radiative–transfer calculations which represent the second topic of this thesis. During the presence of a lofted Saharan dust plume a solar radiative effect of -23 to $-27\,\mathrm{W\,m^{-2}}$ at the surface and -2 to $-8\,\mathrm{W\,m^{-2}}$ at TOA was determined with libRadtran. In the case of a lofted mixed layer with Saharan dust and biomass–burning smoke a daily solar aerosol radiative effect of $-2\,\mathrm{W\,m^{-2}}$ at TOA and $-28\,\mathrm{W\,m^{-2}}$ at the surface was determined. Additional radiative–transfer calculations showed that the lofted mixed dust/smoke layer has a cooling effect at TOA in cloud–free conditions. This effect changes to a warming effect, if underlying boundary–layer clouds occur. The albedo at the bottom of the lofted layer was increased by a factor of 10 from 0.05 (over the cloud–free ocean) to 0.5 when clouds are present below the lofted layers. The complete lidar data set served for for the first latitude–dependent investigation of the solar aerosol radiative effect of free–tropospheric and boundary–layer aerosol with ground–based lidar data. According to the determined frequent occurrence of free–tropospheric aerosol layers the solar aerosol radiative effect was highest in the latitudinal belt of the northern tropics from 15° N to the equator with $-43\,\mathrm{W\,m^{-2}}$ at the surface and $-14\,\mathrm{W\,m^{-2}}$ at TOA. The radiative effect of the marine boundary layer alone showed low mean values of -3 to $-7\,\mathrm{W\,m^{-2}}$ at the surface and -3 to $-6\,\mathrm{W\,m^{-2}}$ at the TOA in all obtained latitudinal belts. The entire simulation results were compared to irradiance measurements at the surface and with satellite. The best agreement for all simulations was found for cloud–free conditions at the surface. However, the uncertainties in the single–scattering albedo and the phase function of the atmospheric aerosol particles remain as significant error sources in radiative simulation.

Aerosols also indirectly influence the radiation budget by affecting cloud microphysics. One of these effects is the heterogeneous ice formation in supercooled water clouds. Within the third topic of this thesis, for the first time, this aerosol effect was investigated under different aerosol conditions but comparable meteorological conditions by the use of observations in the southern midlatitudes (Punta Arenas, 52° S) and a previous study in the northern midlatitudes (Leipzig, 51° N). Less than 20% and around 70% of the cloud layers with cloud top temperatures from -15 to $-20\,^{\circ}\mathrm{C}$ showed ice formation over Punta Arenas and Leipzig, respectively. More than 90% of the cloud layers contained ice over Leipzig at temperatures from -25 to $-30\,^{\circ}\mathrm{C}$, whereas this level was not reached at Punta Arenas before cloud top temperatures were below $-35\,^{\circ}\mathrm{C}$. Half of the observed cloud layers contained ice at $-13\,^{\circ}\mathrm{C}$ at Leipzig and at $-30\,^{\circ}\mathrm{C}$ at Punta Arenas. Favorable ice nuclei were almost absent at Punta Arenas as was confirmed by the lidar aerosol observations. In contrast, a mixture of favorable mineral and anthropogenic ice nuclei are ubiquitous in Central Europe. In addition, at Stellenbosch and aboard Polarstern about 30%–40% of the observed cloud layers

with cloud top temperatures from −15 to −20 °C were classified as ice–containing clouds. In total, the existing cloud data set of IfT was increased from 2546 to 5898 clouds. The IfT lidar cloud data can be regarded as one of the most comprehensive cloud libraries with focus on heterogeneous ice formation and height–resolved mixed–phase cloud characterization.

The scientific potential of long–term observations aboard Polarstern during the meridional transatlantic cruises was already recognized during the OCEANET cruises. Thus, the mobile measurement facility OCEANET–Atmosphere was extended by including radiation measurements of the Leipzig Institute of Meteorology in 2011 and in–situ aerosol measurements of IfT. The facility will routinely perform measurements aboard Polarstern in the future. The height–resolved observations of the atmospheric state, of free–tropospheric aerosol layers, of downmixing from lofted layers, and the presence of embedded clouds will be possible with the ongoing lidar measurements. The increasing lidar data set will enable a more detailed latitudinal investigation of tropospheric aerosols and their glaciation effect. Combinations of further radiation measurements of OCEANET–Atmosphere, especially highly spectral–resolved observations, with the lidar–derived height–resolved extinction coefficient and the lidar–derived particle linear depolarization ratio will give more insights into the solar radiative effect of aerosols and clouds. In doing so, the simulations should be extended to three–dimensional Monte Carlo simulations and also to the terrestrial spectral range. An improved understanding of the global influence of aerosols and clouds will be obtained with the shipborne lidar observations, which also serve as a unique ground–based validation of height–resolved spaceborne observations above the Atlantic. Especially in the barely investigated southern hemisphere, possibilities for ground truthing are missing. Modelers and laboratory studies benefit already from the unique observations at Punta Arenas. New routes, like along the Saharan dust outflow from Africa to America, will improve the knowledge about aerosol effects caused by freshly emitted to aged particles.

Appendix A

Comparison of radiosonde and modeled (GDAS1 data set) temperature profiles

In Sec. 7.2 the cloud top temperature is used to investigate the fraction of ice–containing clouds under consideration of aerosol–particle and meteorology–related influences. Since Polly^{XT} is not able to determine the temperature profile, and under consideration of the barely available radiosonde launches aboard Polarstern (daily, 12:00 UTC), Punta Arenas, Chile (Airport of Punta Arenas[1], from December 2009 to April 2010, unsteady daily, 12:00 UTC), and Stellenbosch, South Africa (Airport of Cape Town[2], from December 2010 to April 2011, daily, 12:00 UTC), GDAS1 modeled temperature profiles were utilized. A statistical comparison of temperature profiles measured with radiosondes and the corresponding GDAS1 temperature profiles was performed. Figure A.1 shows the scatterplots of the temperatures measured with radiosondes and the related GDAS1 temperatures. At all three measurement sites measured and modeled temperature show a significant correlation by the coefficient of determination ($R \geq 0.99$) and p-value of less than 0.0001. The mean difference and its standard deviation of measured and modeled temperature is 0.158 ± 0.84 K (Polarstern), -0.214 ± 1.23 K (Punta Arenas), and -0.284 ± 2.22 K (Stellenbosch).

[1] http://weather.uwyo.edu/upperair/sounding.html

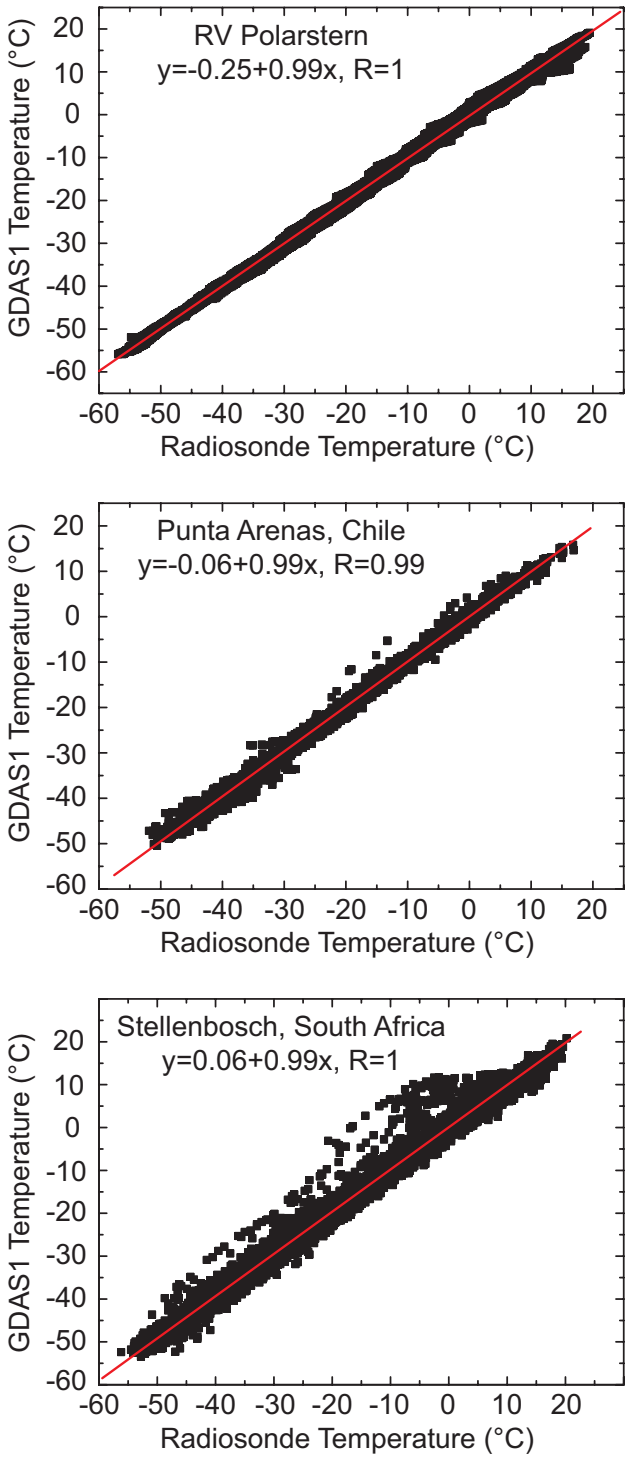

Figure A.1: Linear regressions of interpolated radiosonde temperature profiles to GDAS1 modeled temperature profiles. Top: Comparison of the temperature profiles aboard Polarstern during the transatlantic cruises results in $y = -0.25 + 0.99x$, $R = 1$. Center: Comparison of the temperature profiles at Punta Arenas, Chile (53°S, 71°W) from December 2009 to April 2010 results in $y = -0.06 + 0.99x$, $R = 0.99$. Bottom: Comparison of the temperature profiles at Stellenbosch, South Africa (34°S, 19°E) from December 2010 to April 2011 results in $y = 0.06 + 0.99x$, $R = 1$.

Appendix B

MODIS maps of annual AOT

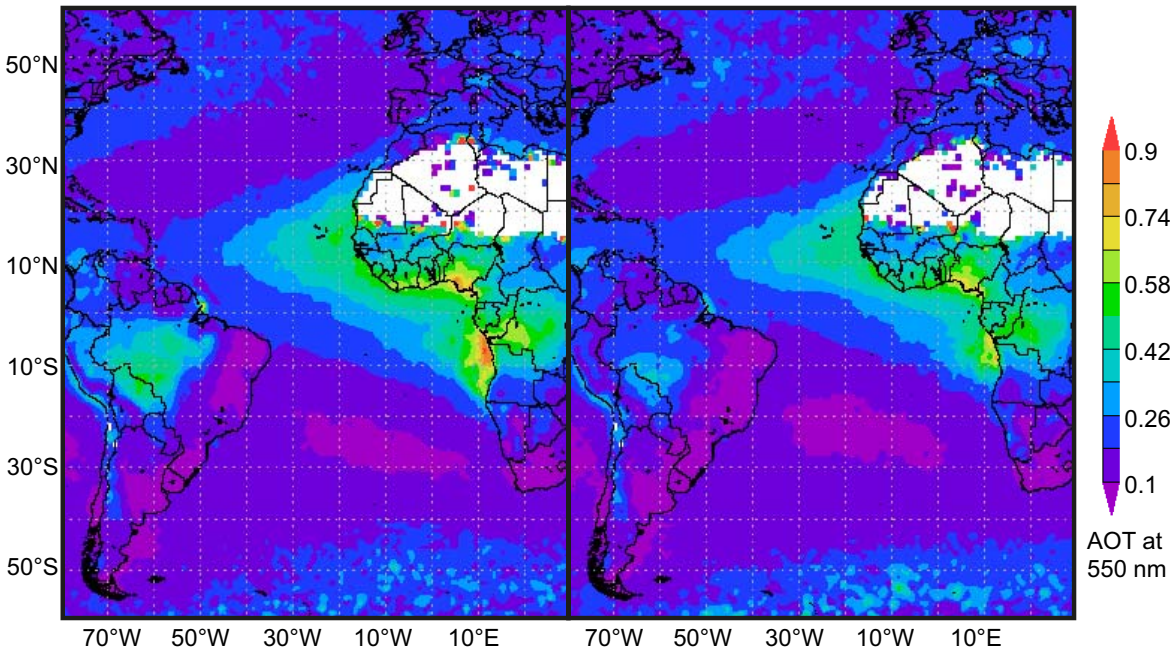

Figure B.1: Maps of the annual mean AOT at 550 nm for the years 2005 and 2006 derived with MODIS. High AOTs are denoted by bright colors.

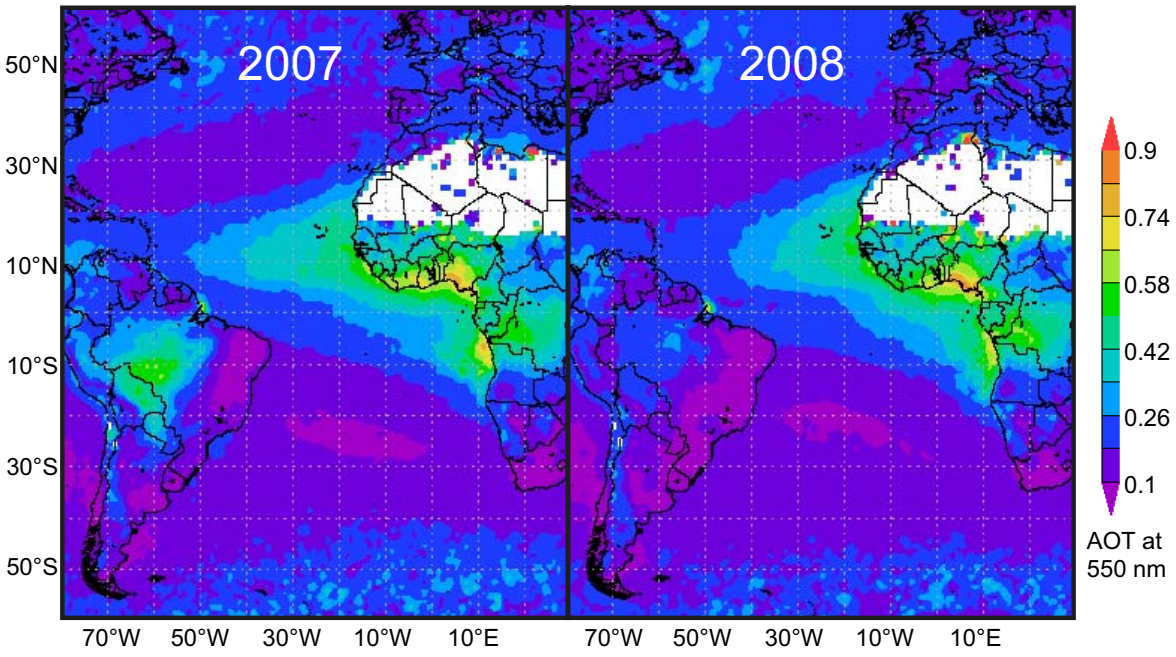

Figure B.2: Same as in Fig. B.1, but for 2007 and 2008.

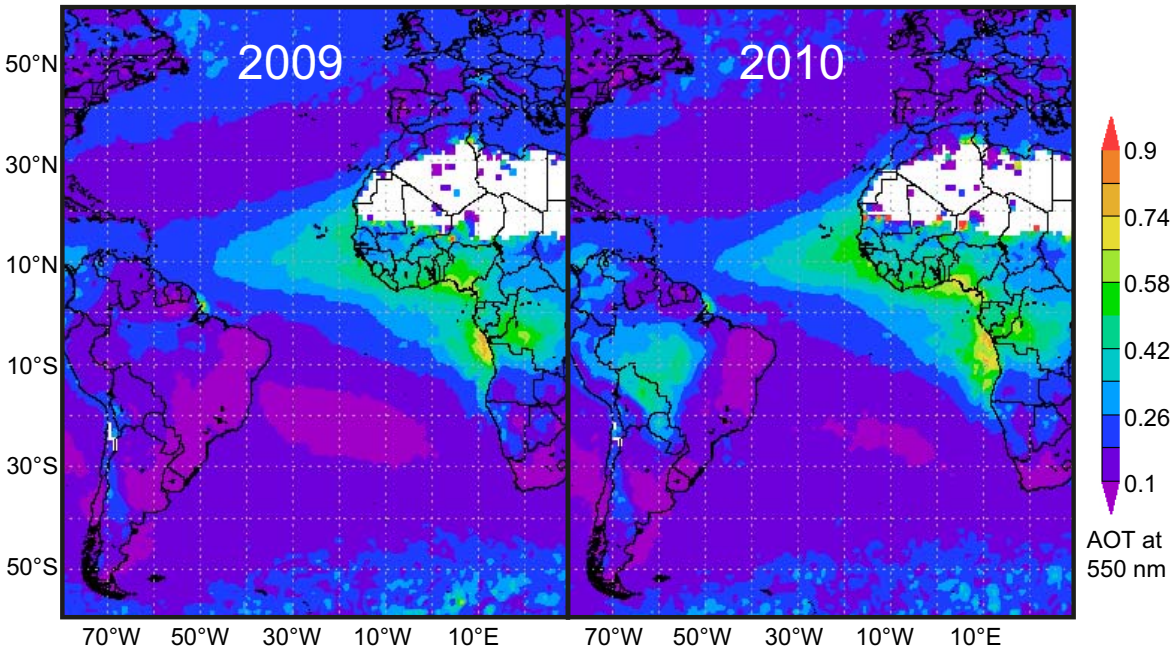

Figure B.3: Same as in Fig. B.1, but for 2009 and 2010.

Appendix C

Quality assurance of CALIOP level 2 version 3 data

The CALIOP level 2 data set provides profiles of backscatter and extinction coefficients at 532 and 1064 nm. Version 3 denotes the current state of the data analysis algorithm [e. g., *Liu et al.*, 2010]. The data of CALIOP were extracted as described before in Sec. 5.3. Further, the extracted data were checked by the provided Cloud–Aerosol–Discrimination score (CAD score), the information of the Feature Classification Flag (FCF), and the extinction flags, as well as the backscatter and extinction uncertainty. The CAD score is -1 to -100, if aerosol was observed as defined by the probability distribution functions [*Liu et al.*, 2004, 2009; *Liu et al.*, 2010]. Values closer to -100 suggest a high probability and an unambiguous assignment as aerosol. The FCF contains confidence level information for the discrimination in clouds and aerosols (feature type, ft) and the discrimination in different aerosol types (feature subtype, fst) [*Omar et al.*, 2009]. The quality assurance within the extinction flags describes the last process of the data analysis of the CALIOP data to retrieve particle backscatter and extinction coefficients. Within the Hybrid Extinction Retrieval Algorithm (HERA) [*Young and Vaughan*, 2009] the data analysis might fail for fixed lidar ratios [*Omar et al.*, 2009]. Thus, the lidar ratio is varied, e. g., to prevent negative extinction coefficients. Values of <8 in the extinction flags allow for these changes. Values >7 describe other possible problems, e. g., the calculated backscatter coefficient exceeds the maximum allowable value and is neglected.

In the quality assurance lots of geometrically and optically thin cloud layers (especially embedded clouds and boundary–cloud layers) were found which were treated as aerosol layers ($-90 \geq \mathrm{CAD} \geq -100$) by mistake and were not refused by other quality assurance flags. Single profiles that contained such clouds showed a distinct peak in the particle

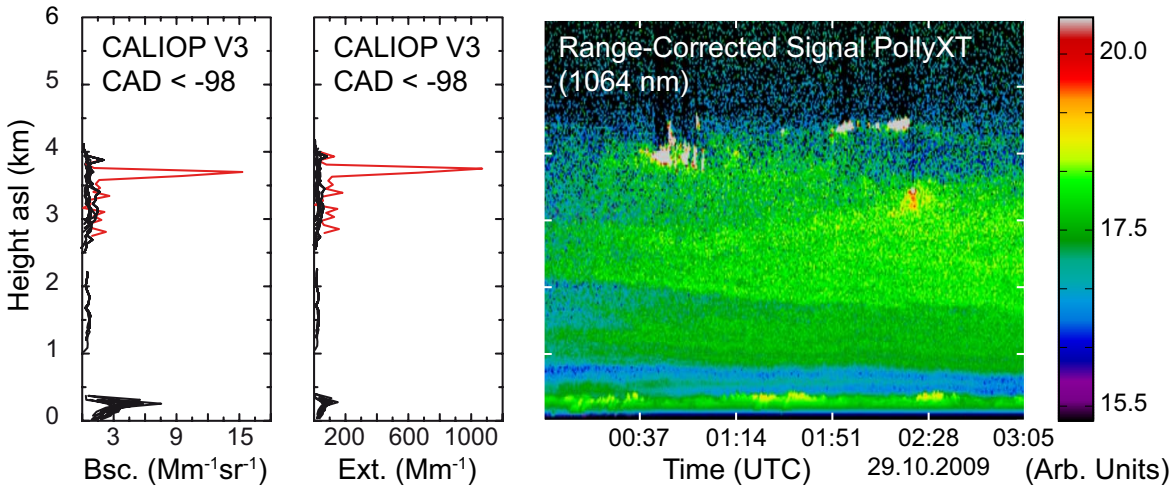

Figure C.1: Left: Profiles of the particle backscatter and extinction coefficient extracted from CALIOP level 2 version 3 data of 29 October 2009, 03:16 UTC (profiles 1570 to 1586). Right: Height–time display of lidar observation aboard Polarstern.

backscatter coefficient (Fig. C.1, left). Within an intensive study it was found that the contrast in the extinction coefficient (Fig. C.1, center) was even better to determine cloud–contaminated aerosol backscatter profiles. The red curve in Fig. C.1 (center) indicates a cloud layer with values of the extinction coefficient $>1000\,\mathrm{Mm}^{-1}$. Below the sharp peak the extinction coefficient remains increased due to multiple scattering (see Sec. 3.2.5). The intensive study of all cloud–contaminated aerosol profiles results in a threshold value of the particle extinction coefficient of $400\,\mathrm{Mm}^{-1}$. Most of the cloud–containing profiles showed also multiple–scattering effects. As a consequence, profiles of aerosols below well–treated cloud layers were unconsidered in the data analysis, too.

The particle backscatter and extinction uncertainty is determined within HERA in terms of a propagation of the errors of the total, the normalized, and the molecular backscatter and the molecular and particle transmittance (see Uncertainty Analysis for Particulate Backscatter, Extinction and Optical Depth Retrievals reported in the CALIPSO Level 2, Version 3 Data Release[1]). However, the uncertainty does not help to find confidential values because low values in the particle backscatter coefficient with relative high uncertainties are not wrong per se. The applied thresholds in this thesis are summarized in Tab. C.1.

During the three cruises of Polarstern CALIPSO passed the ship 41 times within 200 km spatial and 1 hour temporal distance. The selected data contained 38 times profiles of backscat-

[1] http://eosweb.larc.nasa.gov/PRODOCS/calipso/pdf/CALIOP_Version3_Extinction_Error_Analysis.pdf

Table C.1: Boundaries for the quality assurance of CALIOP level 2 version 3 data

Criterion	Allowed values	Meaning
CAD score	−90 to −100	aerosol with high probability
Feature Type	>1	middle and high confidence
Feature Subtype	1	confident
Extinction flag	<8	allow only changes in LR
Extinction	$<400\,\mathrm{Mm}^{-1}$	find mistreated boundary–layer clouds
Overlying clouds		account for multiple scattering

Table C.2: Availability of CALIOP level 2 version 3 data.

Distance (km)	Overpasses	Aerosol	Val. Aerosol	Data Points	Val. Points (%)
0–25	–	–	–	–	–
25–50	3	2	2	556	449 (81)
50–75	7	7	4	713	510 (71)
75–100	8	8	5	1506	848 (56)
100–125	5	5	5	1934	848 (44)
125–150	2	2	2	248	210 (85)
150–175	7	6	5	992	479 (48)
175–200	9	8	5	1457	1051 (72)
Sum	41	38	28	7406	4395 (59)

ter and extinction coefficients. After the quality assurance process 28 cases remained. In average, 41% of the available data were refused. Details are presented in Tab. C.2.

Bibliography

Adames, A. F., M. Reynolds, A. Smirnov, D. S. Covert, and T. P. Ackerman (2011), Comparison of Moderate Resolution Imaging Spectroradiometer ocean aerosol retrievals with ship–based Sun photometer measurements from the Around the Americas expedition, *Journal of Geophysical Research*, *116*, D16303, doi:10.1029/2010JD015440.

Albrecht, B. A. (1989), Aerosols, cloud microphysics, and fractional cloudiness, *Science*, *245*, 1227–1230, doi:10.1126/science.245.4923.1227.

Alpert, P. A., J. Y. Aller, and D. A. Knopf (2011), Ice nucleation from aqueous NaCl droplets with and without marine diatoms, *Atmospheric Chemistry and Physics*, *11*, 5539–5555, doi:10.5194/acp-11-5539-2011.

Althausen, D., R. Engelmann, H. Baars, B. Heese, A. Ansmann, D. Müller, and M. Komppula (2009), Portable Raman lidar Polly^{XT} for automated profiling of aerosol backscatter, extinction, and depolarization, *Journal of Atmospheric and Oceanic Technology*, *26*, 2366–2378, doi:10.1175/2009JTECHA1304.1.

Anderson, B. E., W. B. Grant, G. L. Gregory, E. V. Browell, J. E. Collins, G. W. Sachse, D. R. Bagwell, C. H. Hudgins, D. R. Blake, and N. J. Blake (1996), Aerosols from biomass burning over the tropical South Atlantic region: Distributions and impacts, *Journal of Geophysical Research*, *101*, 24117–24138, doi:10.1029/96JD00717.

Anderson, G. P., S. A. Clough, F. X. Kneizys, J. H. Chetwynd, and E. P. Shettle (1986), AFGL atmospheric constituent profiles (0.120km), Technical Report AFGL-TR-86-0110, *Air Force Geophysical Laboratory*, Hanscom Air Force Base, Mass.

Anderson, T. L., R. J. Charlson, D. M. Winker, J. A. Ogren, and K. Holmén (2003), Mesoscale variations of tropospheric aerosols, *Journal of the Atmospheric Sciences*, *60*, 119–136, doi:10.1175/1520-0469(2003)060⟨0119:MVOTA⟩2.0.CO;2.

Ångström, A. (1929), On the atmospheric transmission of sun radiation and on dust in the air, *Geografiska Annaler*, *11*, 156–166.

Ansmann, A. (2002), Molecular backscatter lidar profiling of the volume scattering coefficient in cirrus, in *Cirrus*, D. K. Lynch, K. Sassen, D. O. Starr and G. l. Stephens (ed.), pp. 197–210, Oxford University Press.

Ansmann, A., and D. Müller (2005), Lidar and atmospheric aerosol particles, in *Lidar: Range–resolved optical remote sensing of the atmosphere*, C. Weitkamp (ed.), pp. 105–138, Springer.

Ansmann, A., M. Riebesell, and C. Weitkamp (1990), Measurement of atmospheric aerosol extinction profiles with a Raman lidar, *Optics Letters*, *15*, 746–748, doi:10.1364/OL.15.000746.

Ansmann, A., U. Wandinger, M. Riebesell, C. Weitkamp, and W. Michaelis (1992), Independent measurement of extinction and backscatter profiles in cirrus clouds by using a combined Raman elastic–backscatter lidar, *Applied Optics*, *31*, 7113–7131, doi:10.1364/AO.31.007113.

Ansmann, A., F. Wagner, D. Althausen, D. Müller, A. Herber, and U. Wandinger (2001), European pollution outbreaks during ACE 2: Lofted aerosol plumes observed with Raman lidar at the Portuguese coast, *Journal of Geophysical Research*, *106*, 20725–20734, doi:10.1029/2000JD000091.

Ansmann, A., F. Wagner, D. Müller, D. Althausen, A. Herber, W. von Hoyningen-Huene, and U. Wandinger (2002), European pollution outbreaks during ACE 2: Optical particle properties inferred from multiwavelength lidar and star-Sun photometry, *Journal of Geophysical Research*, *107*, 4259, doi:10.1029/2001JD001109.

Ansmann, A., I. Mattis, D. Müller, U. Wandinger, M. Radlach, D. Althausen, and R. Damoah (2005), Ice formation in Saharan dust over central Europe observed with temperature/humidity/aerosol Raman lidar, *Journal of Geophysical Research*, *110*, D18S12, doi:10.1029/2004JD005000.

Ansmann, A., M. Tesche, D. Althausen, D. Müller, P. Seifert, V. Freudenthaler, B. Heese, M. Wiegner, G. Pisani, P. Knippertz, and O. Dubovik (2008), Influence of Saharan dust on cloud glaciation in southern Morocco during the Saharan Mineral Dust Experiment, *Journal of Geophysical Research*, *113*, 4210, doi:10.1029/2007JD008785.

Ansmann, A., H. Baars, M. Tesche, D. Müller, D. Althausen, R. Engelmann, T. Pauliquevis, and P. Artaxo (2009), Dust and smoke transport from Africa to South America: Lidar profiling over Cape Verde and the Amazon rainforest, *Geophysical Research Letters*, *36*, 11802, doi:10.1029/2009GL037923.

Ansmann, A., M. Tesche, P. Knippertz, E. Bierwirth, D. Althausen, D. Müller, and O. Schulz (2009), Vertical profiling of convective dust plumes in southern Morocco during SAMUM, *Tellus Series B*, *61*, 340–353, doi:10.1111/j.1600-0889.2008.00384.x.

Ansmann, A., M. Tesche, P. Seifert, D. Althausen, R. Engelmann, J. Fruntke, U. Wandinger, I. Mattis, and D. Müller (2009), Evolution of the ice phase in tropical altocumulus: SAMUM lidar observations over Cape Verde, *Journal of Geophysical Research*, *114*, D17208, doi:10.1029/2008JD011659.

Ansmann, A., M. Tesche, S. Groß, V. Freudenthaler, P. Seifert, A. Hiebsch, J. Schmidt, U. Wandinger, I. Mattis, D. Müller, and M. Wiegner (2010), The 16 April 2010 major volcanic ash plume over central Europe: EARLINET lidar and AERONET photometer observations at Leipzig and Munich, Germany, *Geophysical Research Letters*, *371*, L13810, doi:10.1029/2010GL043809.

Ansmann, A., A. Petzold, K. Kandler, I. Tegen, M. Wendisch, D. Müller, B. Weinzierl, T. Müller, and J. Heintzenberg (2011a), Saharan mineral dust experiments SAMUM-1 and SAMUM-2: what have we learned?, *Tellus Series B*, *63*, 403–429, doi:10.1111/j.1600-0889.2011.00555.x.

Ansmann, A., M. Tesche, P. Seifert, S. Groß, V. Freudenthaler, A. Apituley, K. M. Wilson, I. Serikov, H. Linné., B. Heinold, A. Hiebsch, F. Schnell, J. Schmidt, I. Mattis, U. Wandinger, and M. Wiegner (2011b), Ash and fine–mode particle mass profiles from EARLINET–AERONET observations over central Europe after the eruptions of the Eyjafjallajökull volcano in 2010, *Journal of Geophysical Research*, *116*, D00U02, doi:10.1029/2010JD015567.

Aßmann, S., C. Frank, and A. Körtzinger (2011), Spectrophotometric high-precision seawater ph determination for use in underway measuring systems, *Ocean Science*, *7*, 597–607, doi:10.5194/os-7-597-2011.

Baars, H. (2012), Aerosol profiling with lidar in the Amazon basin during the wet and dry season 2008, Ph.D. thesis, Faculty of Physics and Geoscience, University of Leipzig.

Baars, H., A. Ansmann, R. Engelmann, and D. Althausen (2008), Continuous monitoring of the boundary-layer top with lidar, *Atmospheric Chemistry and Physics*, *8*, 7281–7296, doi:10.5194/acp-8-7281-2008.

Baars, H., A. Ansmann, D. Althausen, R. Engelmann, P. Artaxo, T. Pauliquevis, and R. Souza (2011), Further evidence for significant smoke transport from Africa to Amazonia, *Geophysical Research Letters*, *382*, 20802, doi:10.1029/2011GL049200.

Bates, T. S., B. J. Huebert, J. L. Gras, F. B. Griffiths, and P. A. Durkee (1998), International Global Atmospheric Chemistry (IGAC) Project's First Aerosol Characterization Experiment (ACE 1): Overview, *Journal of Geophysical Research*, *1031*, 16297–16318, doi:10.1029/97JD03741.

Bates, T. S., P. K. Quinn, D. J. Coffman, J. E. Johnson, T. L. Miller, D. S. Covert, A. Wiedensohler, S. Leinert, A. Nowak, and C. Neusüss (2001), Regional physical and chemical properties of the marine boundary layer aerosol across the Atlantic during Aerosols99: An overview, *Journal of Geophysical Research*, *106*, 20767–20782, doi:10.1029/2000JD900578.

Bauer, S., E. Bierwirth, M. Esselborn, A. Petzold, A. Macke, T. Trautmann, and M. Wendisch (2011), Airborne spectral radiation measurements to derive solar radiative forcing of Saharan dust mixed with biomass burning smoke particles, *Tellus Series B*, *63*, 742–750,doi:10.1111/j.1600-0889.2011.00567.x.

Behrendt, A., and T. Nakamura (2002), Calculation of the calibration constant of polarization lidar and its dependency on atmospheric temperature, *Optics Express*, *10*, 805–817.

Bellouin, N., O. Boucher, M. Vesperini, and D. E. Tanré (2004), Estimating the direct aerosol radiative perturbation: Impact of ocean surface representation and aerosol nonsphericity, *Quarterly Journal of the Royal Meteorological Society*, *130*, 2217–2232, doi:10.1256/qj.03.136.

Beyerle, G., H.-J. Schäfer, R. Neuber, O. Schrems, and I. S. McDermid (1998), Dual wavelength lidar observation of tropical high-altitude cirrus clouds during the ALBATROSS 1996 campaign, *Geophyical Research Letters*, *25*, 919–922, doi:10.1029/98GL00491.

Bierwirth, E., M. Wendisch, A. Ehrlich, B. Heese, M. Tesche, D. Althausen, A. Schladitz, D. Müller, S. Otto, T. Trautmann, T. Dinter, W. von Hoyningen-Huene, and R. Kahn (2009), Spectral surface albedo over Morocco and its impact on radiative forcing of Saharan dust, *Tellus Series B*, *61*, 252–269, doi:10.1111/j.1600-0889.2008.00395.x.

Bigg, E. K. (1973), Ice nucleus concentrations in remote areas, *Journal of the Atmospheric Sciences*, *30*, 1153–1157, doi:10.1175/1520-0469(1973)030⟨1153:INCIRA⟩2.0.CO;2.

Bissonnette, L. R. (2005), Lidar and multiple scattering, in *Lidar: Range-resolved optical remote sensing of the atmosphere*, C. Weitkamp (ed.), pp. 43–100, Springer.

Blanco-Muriel, M., D. C. Alarcón-Padilla, T. López-Moratalla, and M. Lara-Coira (2001), Computing the solar vector, *Solar Energy*, *70*, 431–441, doi:10.1016/S0038-092X(00)00156-0.

Bohren, C. F., and D. R. Huffman (1983), Absorption and scattering of light by small particles, *Wiley-VCH Verlag GmbH*, doi:10.1002/9783527618156.refs.

Bond, T. C., and R. W. Bergstrom (2006), Light absorption by carbonaceous particles: An investigative review, *Aerosol Science and Technology*, *40*, 27–67, doi:10.1080/02786820500421521.

Bösenberg, J., V. Matthias, A. Amodeo, V. Amoridis, A. Ansmann, J. M. Baldasano, I. Balin, D. Balis, C. Böckmann, A. Boselli, G. Carlsson, A. Chaikovsky, G. Chourdakis, A. Comeron, F. De Tomasi, R. Eixmann, V. Freudenthaler, H. Giehl, I. Grigorov, A. Hågård, M. Iarlori, A. Kirsche, G. Kolarov, L. Komguem, S. Kreipl, W. Kumpf, G. Larchevêque, H. Linné, R. Matthey, I. Mattis, A. Mekler, I. Mironova, V. Mitev, L. Mona, D. Müller, S. Music, S. Nickovic, M. Pandolfi, A. Papayannis, G. Pappalardo, J. Pelon, C. Pérez, R. M. Perrone, R. Persson, D. P. Resendes, V. Rizi, F. Rocadenbosch, J. A. Rodrigues, L. Sauvage, L. Schneidenbach, R. Schumacher, V. Shcherbakov, V. Simeonov, P. Sobolewski, N. Spinelli, I. Stachlewska, D. Stoyanov, T. Trickl, G. Tsaknakis, G. Vaughan, U. Wandinger, X. Wang, M. Wiegner, M. Zavrtanik, and C. Zerefos (2003), EARLINET: a European Aerosol Research lidar network to establish an aerosol climatology, Rep. 348, Max–Planck–Institut für Meteorologie, Hamburg, Germany, http://lidarb.dkrz.de/earlinet/.

Bösenberg, J., and R. Hoff (2007), Plan for the implementation of the GAW aerosol lidar observation network GALION, World Meteorological Organization Rep. 178, 53 pp.

Boucher, O. (1998), On aerosol direct shortwave forcing and the Henyey-Greenstein phase function., *Journal of the Atmospheric Sciences*, *55*, 128–134, doi:10.1175/1520-0469(1998)055⟨0128:OADSFA⟩2.0.CO;2.

Bucholtz, A. (1995), Rayleigh-scattering calculations for the terrestrial atmosphere, *Applied Optics*, *34*, 2765–2773.

Bumke, K. (Ed.) (2011), The expedition of the research vessel Polarstern to the Antarctic in 2010 (ANT–XXVII/1), in *Reports on polar and marine research*, vol. 628, Alfred Wegener Institute for Polar and Marine Research.

Bumke, K., U. Karger, and K. Uhlig (2002), Measurements of turbulent fluxes of momentum and sensible heat over the Labrador Sea, *Journal of Physical Oceanography*, *32*, 401–410, doi:10.1175/1520-0485(2002)032⟨0401:MOTFOM⟩2.0.CO;2.

Campbell, J. R., D. L. Hlavka, E. J. Welton, C. J. Flynn, D. D. Turner, J. D. Spinhirne, V. S. Scott III, and I. H. Hwang (2002), Full-time, eye-safe cloud and aerosol lidar observation at Atmospheric Radiation Measurement program sites: Instruments and data processing, *Journal of Atmospheric and Oceanic Technology*, *19*, 431–442, doi:10.1175/1520-0426(2002)019⟨0431:FTESCA⟩2.0.CO;2.

Campbell, J. R., E. J. Welton, J. D. Spinhirne, Q. Ji, S.-C. Tsay, S. J. Piketh, M. Barenbrug, and B. N. Holben (2003), Micropulse lidar observations of tropospheric aerosols over northeastern South Africa during the ARREX and SAFARI 2000 dry season experiments, *Journal of Geophysical Research*, *108*, 8497, doi:10.1029/2002JD002563.

Cantrell, W., and A. Heymsfield (2005), Production of ice in tropospheric clouds: A review, *Bulletin of the American Meteorological Society*, *86*, 795–807, doi:10.1175/BAMS-86-6-795.

Charlson, R. J., and M. J. Pilat (1969), Climate: The influence of aerosols, *Journal of Applied Meteorology*, *8*, 1001–1002, doi:10.1175/1520-0450(1969)008⟨1001:CTIOA⟩2.0.CO;2.

Charlson, R. J., S. E. Schwartz, J. M. Hales, R. D. Cess, J. A. Coakley, J. E. Hansen, and D. J. Hofmann (1992), Climate forcing by anthropogenic aerosols, *Science*, *255*, 423–430, doi:10.1126/science.255.5043.423.

Chen, J. P., A. Hazra, and Z. Levin (2008), Parameterizing ice nucleation rates using contact angle and activation energy derived from laboratory data, *Atmospheric Chemistry and Physics*, *8*, 7431–7449, doi:10.5194/acp-8-7431-2008.

Chin, M., P. Ginoux, S. Kinne, O. Torres, B. N. Holben, B. N. Duncan, R. V. Martin, J. A. Logan, A. Higurashi, and T. Nakajima (2002), Tropospheric aerosol optical thickness from the GOCART model and comparisons with satellite and Sun photometer measurements, *Journal of the Atmospheric Sciences*, *59*, 461–483, doi:10.1175/1520-0469(2002)059⟨0461:TAOTFT⟩2.0.CO;2.

Christner, B. C., R. Cai, C. E. Morris, K. S. McCarter, C. M. Foreman, M. L. Skidmore, S. N. Montross, and D. C. Sands (2008), Geographic, seasonal, and precipitation chemistry influence on the abundance and activity of biological ice nucleators in rain and snow, *Proceedings of the National Academy of Sciences*, *105*, 18854–18859, doi:10.1073/pnas.0809816105.

Christopher, S. A., and J. Zhang (2002), Shortwave aerosol radiative forcing from MODIS and CERES observations over the oceans, *Geophysical Research Letters*, *29*, 1859, doi:10.1029/2002GL014803.

Chung, C. E., V. Ramanathan, D. Kim, and I. A. Podgorny (2005), Global anthropogenic aerosol direct forcing derived from satellite and ground–based observations, *Journal of Geophysical Research*, *110*, D24207, doi:10.1029/2005JD006356.

Chylek, P., G. Videen, D. Ngo, R. G. Pinnick, and J. D. Klett (1995), Effect of black carbon on the optical properties and climate forcing of sulfate aerosols, *Journal of Geophysical Research*, *100*, 16,325–16,332, doi:10.1029/95JD01465.

Clerbaux, N., S. Dewitte, L. Gonzalez, A. Ipe, and B. Nicula (2001), Derivation of the top of the atmosphere radiative fluxes from SEVIRI: Methodology, accuracy and perspectives, in *Proc. of the 2001 EUMETSAT Meteorological Satellite Data Users Conference, Antalya*, pp. 69–76.

Cober, S. G., G. A. Isaac, A. V. Korolev, and J. W. Strapp (2001), Assessing cloud–phase conditions., *Journal of Applied Meteorology*, *40*, 1967–1983, doi:10.1175/1520-0450(2001)040⟨1967:ACPC⟩2.0.CO;2.

Collis, R. T. H., and P. B. Russell (1976), Lidar measurement of particles and gases by elastic backscattering and differential absorption, *Laser Monitoring of the Atmosphere*, *14*, 71–151, doi:10.1007/3-540-07743-X_18.

Connolly, P. J., O. Möhler, P. R. Field, H. Saathoff, R. Burgess, T. Choularton, and M. Gallagher (2009), Studies of heterogeneous freezing by three different desert dust samples, *Atmospheric Chemistry and Physics*, *9*, 2805–2824, doi:10.5194/acp-9-2805-2009.

Cox, C., and W. Munk (1954a), Measurement of the roughness of the sea surface from photographs of the sun's glitter, *Journal of the Optical Society of America (1917-1983)*, *44*, 838–850, doi:10.1364/JOSA.44.000838.

Cox, C., and W. Munk (1954b), Statistics of the sea surface derived from sun glitter, *Journal of Marine Research*, *13*, 198–227.

Cziczo, D., K. D. Froyd, S. J. Gallavardin, O. Möhler, S. Benz, H. Saathoff, and D. M. Murphy (2009), Deactivation of ice nuclei due to atmospherically relevant surface coatings, *Environmental Research Letters*, *4*, 044013, doi:10.1088/1748-9326/4/4/044013.

Dammshäuser, A., T. Wagener, and P. L. Croot (2011), Surface water dissolved aluminum and titanium: Tracers for specific time scales of dust deposition to the Atlantic?, *Geophysical Research Letters*, *38*, L24601, doi:10.1029/2011GL049847.

de Boer, G., H. Morrison, M. D. Shupe, and R. Hildner (2011), Evidence of liquid dependent ice nucleation in high–latitude stratiform clouds from surface remote sensors, *Geophysical Research Letters*, *380*, L01803, doi:10.1029/2010GL046016.

DeMott, P. J., D. C. Rogers, and S. M. Kreidenweis (1997), The susceptibility of ice formation in upper tropospheric clouds to insoluble aerosol components, *Journal of Geophysical Research*, *102*, 19,575–19,584, doi:10.1029/97JD01138.

DeMott, P. J., D. J. Cziczo, A. J. Prenni, D. M. Murphy, S. M. Kreidenweis, D. S. Thomson, R. Borys, and D. C. Rogers (2003), Measurements of the concentration and composition of nuclei for cirrus formation, *Proceedings of the National Academy of Sciences*, *100*, 14655–14660, doi:10.1073/pnas.2532677100.

Dentener, F., S. Kinne, T. Bond, O. Boucher, J. Cofala, S. Generoso, P. Ginoux, S. Gong, J. J. Hoelzemann, A. Ito, L. Marelli, J. E. Penner, J. P. Putaud, C. Textor, M. Schulz, G. R. van der Werf, and J. Wilson (2006), Emissions of primary aerosol and precursor gases in the years 2000 and 1750, prescribed data-sets for AeroCom, *Atmospheric Chemistry and Physics*, *6*, 4321–4344, doi:10.5194/acp-6-4321-2006.

Diehl, K., and S. Wurzler (2004), Heterogeneous drop freezing in the immersion mode: Model calculations considering soluble and insoluble particles in the drops., *Journal of the Atmospheric Sciences*, *61*, 2063–2072, doi:10.1175/1520-0469(2004)061⟨2063:HDFITI⟩2.0.CO;2.

Diehl, K., M. Simmel, and S. Wurzler (2006), Numerical sensitivity studies on the impact of aerosol properties and drop freezing modes on the glaciation, microphysics, and dynamics of clouds, *Journal of Geophysical Research*, *111*, D07202, doi:10.1029/2005JD005884.

Draxler, R. R., and G. D. Rolph (2003), HYSPLIT (HYbrid Single-Particle Lagrangian Integrated Trajectory) model access via NOAA ARL READY website (http://www. arl. noaa. gov/ready/hysplit4. html). NOAA Air Resources Laboratory, Silver Spring.

Dubovik, O., B. Holben, T. F. Eck, A. Smirnov, Y. J. Kaufman, M. D. King, D. Tanré, and I. Slutsker (2002), Variability of absorption and optical properties of key aerosol types observed in worldwide locations., *Journal of the Atmospheric Sciences*, *59*, 590–608, doi:10.1175/1520-0469(2002)059⟨0590:VOAAOP⟩2.0.CO;2.

Duflot, V., P. Royer, P. Chazette, J. L. Baray, Y. Courcoux, and R. Delmas (2011), Marine and biomass burning aerosols in the southern Indian Ocean: Retrieval of aerosol optical properties from shipborne lidar and Sun photometer measurements, *Journal of Geophysical Research*, *116*, D18208, doi:10.1029/2011JD015839.

Ebert, M., A. Worringen, N. Benker, S. Mertes, E. Weingartner, and S. Weinbruch (2011), Chemical composition and mixing–state of ice residuals sampled within mixed phase clouds, *Atmospheric Chemistry and Physics*, *11*, 2805–2816, doi:10.5194/acp-11-2805-2011.

Ehrlich, A., A. Wendisch, E. Bierwirth, A. Herber, and A. Schwarzenböck (2008), Ice crystal shape effects on solar radiative properties of Arctic mixed–phase clouds — Dependence on microphysical properties, *Atmospheric Research*, *88*, 266–276, doi:10.1016/j.atmosres.2007.11.018.

el Naggar, S., and A. Macke (Eds.) (2010), The expedition of the research vessel Polarstern to the Antarctic in 2009 (ANT–XXVI/1), in *Reports on polar and marine research*, vol. 614, Alfred Wegener Institute for Polar and Marine Research.

Fernald, F. G. (1984), Analysis of atmospheric lidar observations: some comments, *Applied Optics*, *23*, 652–653, doi:10.1364/AO.23.000652.

Fiebig, M., and J. A. Ogren (2006), Retrieval and climatology of the aerosol asymmetry parameter in the NOAA aerosol monitoring network, *Journal of Geophysical Research*, *111*, D21204, doi:10.1029/2005JD006545.

Field, P. R., R. J. Hogan, P. R. A. Brown, A. J. Illingworth, T. W. Choularton, P. H. Kaye, E. Hirst, and R. Greenaway (2004), Simultaneous radar and aircraft observations of mixed–phase cloud at the 100 m scale, *Quarterly Journal of the Royal Meteorological Society*, *130*, 1877–1904, doi:10.1256/qj.03.102.

Field, P. R., O. Möhler, P. Connolly, M. Krämer, R. Cotton, A. J. Heymsfield, H. Saathoff, and M. Schnaiter (2006), Some ice nucleation characteristics of Asian and Saharan desert dust, *Atmospheric Chemistry and Physics*, *6*, 2991–3006, doi:10.5194/acp-6-2991-2006.

Findeisen, W. (1938), Kolloid–meterologische Vorgänge bei Niederschlagsbildung, *Meteorologische Zeitschrift*, *55*, 121–133.

Fishman, J., J. M. Hoell, R. D. Bendura, R. J. McNeal, and V. W. J. H. Kirchhoff (1996), NASA GTE TRACE A Experiment (September–October 1992): Overview, *Journal of Geophysical Research*, *101*, 23,865–23,880, doi:10.1029/96JD00123.

Fitzgerald, J. W. (1991), Marine aerosols: A review, *Atmospheric Environment*, *25*, 533–545, doi:10.1016/0960-1686(91)90050-H.

Fleishauer, R. P., V. E. Larson, and T. H. Vonder Haar (2002), Observed microphysical structure of midlevel, mixed–phase clouds, *Journal of the Atmospheric Sciences*, *59*, 1779–1804, doi:10.1175/1520-0469(2002)059⟨1779:OMSOMM⟩2.0.CO;2.

Formenti, P., M. O. Andreae, L. Lange, G. Roberts, J. Cafmeyer, I. Rajta, W. Maenhaut, B. N. Holben, P. Artaxo, and J. Lelieveld (2001), Saharan dust in Brazil and Suriname during the Large–Scale Biosphere–Atmosphere Experiment in Amazonia (LBA)–Cooperative LBA Regional Experiment (CLAIRE) in March 1998, *Journal of Geophysical Research*, *106*, 14,919–14,934, doi:10.1029/2000JD900827.

Forster, P., V. Ramaswamy, P. Artaxo, T. Berntsen, R. Betts, D. W. Fahey, J. Haywood, J. Lean, D. C. Lowe, G. Myhre, J. Nganga, R. Prinn, G. Raga, M. Schulz, and R. V. Dorland (2007), Changes in Atmospheric Constituents and in Radiative Forcing, in *Climate change 2007: The physical science basis. Contribution of working group I to the fourth assessment report of the Intergovernmental Panel on Climate Change*, S. Solomon, D. Qin, M. Manning, Z. Chen, M. Marquis, K. B. Averyt, M. Tignor and H. L. Miller, pp. 129–234, Cambridge University Press, doi:9780521705967.

Franke, K., A. Ansmann, D. Müller, D. Althausen, F. Wagner, and R. Scheele (2001), One-year observations of particle lidar ratio over the tropical Indian Ocean with Raman lidar, *Geophysical Research Letters*, *28*, 4559–4562, doi:10.1029/2001GL013671.

Franke, K., A. Ansmann, D. Müller, D. Althausen, C. Venkataraman, M. S. Reddy, F. Wagner, and R. Scheele (2003), Optical properties of the Indo–Asian haze layer over the tropical Indian Ocean, *Journal of Geophysical Research*, *108*, 4059, doi:10.1029/2002JD002473.

Freudenthaler, V. (2008), The telecover test: A quality assurance tool for the optical part of a lidar system, in *Reviewed and revised papers presented at the 25 th International Laser Radar Conference*, Boulder, Colorado, USA.

Freudenthaler, V., M. Esselborn, M. Wiegner, B. Heese, M. Tesche, A. Ansmann, D. Müller, D. Althausen, M. Wirth, A. Fix, G. Ehret, P. Knippertz, C. Toledano, J. Gasteiger, M. Garhammer, and M. Seefeldner (2009), Depolarization ratio profiling at several wavelengths in pure Saharan dust during SAMUM 2006, *Tellus Series B*, *61*, 165–179, doi: 10.1111/j.1600-0889.2008.00396.x.

Freudenthaler, V., S. Groß, R. Engelmann, I. Mattis, U. Wandinger, G. Pappalardo, A. Amodeo, A. Giunta, G. D'Amico, A. Chaikovsky, F. Osipenko, A. Slesar, D. Nicolae, L. Belegante, C. Talianu, I. Serikov, H. Linne, F. Jansen, K. Wilson, M. de Graaf, A. Apituley, T. Trickl, H. Giehl, and M. Adam (2010), EARLI09 - Direct intercomparison of eleven EARLINET lidar systems, in *Reviewed and revised papers presented at the 26 th International Laser Radar Conference*, St. Petersburg, Russia.

Gaiero, D. M., J. L. Probst, P. J. Depetris, S. M. Bidart, and L. Leleyter (2003), Iron and other transition metals in Patagonian riverborne and windborne materials: Geochemical control and transport to the southern South Atlantic Ocean, *Geochimica et Cosmochimica Acta*, *67*, 3603–3623, doi:10.1016/S0016-7037(03)00211-4.

Gaiero, D. M., F. Brunet, J. L. Probst, and P. J. Depetris (2007), A uniform isotopic and chemical signature of dust exported from Patagonia: Rock sources and occurrence in southern environments, *Chemical Geology*, *238*, 107–120, doi:10.1016/j.chemgeo.2006.11.003.

Gassó, S., and A. F. Stein (2007), Does dust from Patagonia reach the sub–Antarctic Atlantic Ocean?, *Geophysical Research Letters*, *34*, L01801, doi:10.1029/2006GL027693.

Gassó, S., A. Stein, F. Marino, E. Castellano, R. Udisti, and J. Ceratto (2010), A combined observational and modeling approach to study modern dust transport from the Patagonia desert to East Antarctica, *Atmospheric Chemistry and Physics*, *10*, 8287–8303, doi:10.5194/acp-10-8287-2010.

Gong, S. L. (2003), A parameterization of sea–salt aerosol source function for sub– and super–micron particles, *Global Biogeochemical Cycles*, *17*, 1097, doi:10.1029/2003GB002079.

Gorbunov, B., A. Baklanov, N. Kakutkina, H. L. Windsor, and R. Toumi (2001), Ice nucleation on soot particles, *Journal of Aerosol Science*, *32*, 199–215, doi:10.1016/S0021-8502(00)00077-X.

Grein, M. (2006), Charakterisierung und Erweiterung der Empfängeroptik des IFT–Ramanlidars MARTHA für kombinierte Aerosol- und Wolkenmessungen, Master's thesis, Universität Leipzig, Fakultät für Physik und Geowissenschaften.

Groß, S., J. Gasteiger, V. Freudenthaler, M. Wiegner, A. Geiß, A. Schladitz, C. Toledano, K. Kandler, M. Tesche, A. Ansmann, and A. Wiedensohler (2011a), Characterization of the planetary boundary layer during SAMUM–2 by means of lidar measurements, *Tellus Series B*, *63*, 695–705, doi:10.1111/j.1600-0889.2011.00557.x.

Groß, S., M. Tesche, V. Freudenthaler, C. Toledano, M. Wiegner, A. Ansmann, D. Althausen, and M. Seefeldner (2011b), Characterization of Saharan dust, marine aerosols and mixtures of biomass–burning aerosols and dust by means of multi–wavelength depolarization and Raman lidar measurements during SAMUM–2, *Tellus Series B*, *63*, 706–724, doi:10.1111/j.1600-0889.2011.00556.x.

Groß, S., V. Freudenthaler, M. Wiegner, J. Gasteiger, A. Geiß, and F. Schnell (2012), Dual-wavelength linear depolarization ratio of volcanic aerosols: Lidar measurements of the Eyjafjallajökull plume over Maisach, Germany, *Atmospheric Environment*, *48*, 85-96, doi:10.1016/j.atmosenv.2011.06.017.

Groß, S. M. (2011), Aerosol characterization by multi–wavelength Raman– and depolarization lidar observations, Ph.D. thesis, Fakultät der Physik an der Ludwig–Maximilians–Universität München.

Hallett, J., and S. C. Mossop (1974), Production of secondary ice crystals during the riming process, *Nature*, *249*, 26–28, doi:10.1038/249026a0.

Harrington, J. Y., T. Reisin, W. R. Cotton, and S. M. Kreidenweis (1999), Cloud resolving simulations of Arctic stratus: Part II: Transition-season clouds, *Atmospheric Research*, *51*, 45–75, doi:10.1016/S0169-8095(98)00098-2.

Hartmann, S., D. Niedermeier, J. Voigtländer, T. Clauss, R. A. Shaw, H. Wex, A. Kiselev, and F. Stratmann (2011), Homogeneous and heterogeneous ice nucleation at LACIS: operating principle and theoretical studies, *Atmospheric Chemistry and Physics*, *11*, 1753–1767, doi:10.5194/acp-11-1753-2011.

Haywood, J., and O. Boucher (2000), Estimates of the direct and indirect radiative forcing due to tropospheric aerosols: A review, *Reviews of Geophysics*, *38*, 513–543, doi:10.1029/1999RG000078.

Haywood, J., P. Francis, S. Osborne, M. Glew, N. Loeb, E. Highwood, D. Tanré, G. Myhre, P. Formenti, and E. Hirst (2003), Radiative properties and direct radiative effect of Saharan dust measured by the C–130 aircraft during SHADE: 1. Solar spectrum, *Journal of Geophysical Research*, *108*, 8577, doi:10.1029/2002JD002687.

Haywood, J. M., and K. P. Shine (1995), The effect of anthropogenic sulfate and soot aerosol on the clear sky planetary radiation budget, *Geophysical Research Letters*, *22*, 603–606, doi:10.1029/95GL00075.

Haywood, J. M., and K. P. Shine (1997), Multi–spectral calculations of the direct radiative forcing of tropospheric sulphate and soot aerosols using a column model, *Quarterly Journal of the Royal Meteorological Society*, *123*, 1907–1930, doi:10.1002/qj.49712354307.

Haywood, J. M., V. Ramaswamy, and B. J. Soden (1999), Tropospheric aerosol climate forcing in clear–sky satellite observations over the oceans, *Science*, *283*, 1299–1303, doi:10.1126/science.283.5406.1299.

Heinold, B., I. Tegen, S. Bauer, and M. Wendisch (2011), Regional modelling of Saharan dust and biomass-burning smoke. Part 2: Direct radiative forcing and atmospheric dynamic response, *Tellus Series B*, *63*, 800–813, doi:10.1111/j.1600-0889.2011.00574.x.

Heintzenberg, J., D. C. Covert, and R. van Dingenen (2000), Size distribution and chemical composition of marine aerosols: a compilation and review, *Tellus Series B*, *52*, 1104–1122, doi:10.1034/j.1600-0889.2000.00136.x.

Henyey, L. G., and J. L. Greenstein (1941), Diffuse radiation in the Galaxy, *Astrophysical Journal*, *93*, 70–83, doi:10.1086/144246.

Herman, J. R., P. K. Bhartia, O. Torres, C. Hsu, C. Seftor, and E. Celarier (1997), Global distribution of UV–absorbing aerosols from Nimbus 7/TOMS data, *Journal of Geophysical Research*, *1021*, 16,911–16,922, doi:10.1029/96JD03680.

Heymsfield, A. J. (2003), Properties of tropical and midlatitude ice cloud particle ensembles. Part I: Median mass diameters and terminal velocities., *Journal of the Atmospheric Sciences*, *60*, 2573–2591, doi:10.1175/1520-0469(2003)060⟨2573:POTAMI⟩2.0.CO;2.

Heymsfield, A. J. (2007), On measurements of small ice particles in clouds, *Geophysical Research Letters*, *34*, L23812, doi:10.1029/2007GL030951.

Heymsfield, A. J., and L. M. Miloshevich (1993), Homogeneous ice nucleation and supercooled liquid water in orographic wave clouds, *Journal of the Atmospheric Sciences*, *50*, 2335–2353, doi:10.1175/1520-0469(1993)050⟨2335:HINASL⟩2.0.CO;2.

Heymsfield, A. J., and R. M. Sabin (1989), Cirrus crystal nucleation by homogeneous freezing of solution droplets, *Journal of the Atmospheric Sciences*, *46*, 2252–2264, doi:10.1175/1520-0469(1989)046⟨2252:CCNBHF⟩2.0.CO;2.

Heymsfield, A. J., P. R. Field, M. Bailey, D. Rogers, J. Stith, C. Twohy, Z. Wang, and S. Haimov (2011), Ice in Clouds Experiment Layer Clouds. Part I: Ice growth rates derived from lenticular wave cloud penetrations, *Journal of the Atmospheric Sciences*, *68*, 2628–2654, doi:10.1175/JAS-D-11-025.1.

Hobbs, P. V., and A. L. Rangno (1985), Ice particle concentrations in clouds, *Journal of the Atmospheric Sciences*, *42*, 2523–2549, doi:10.1175/1520-0469(1985)042⟨2523:IPCIC⟩2.0.CO;2.

Hobbs, P. V., and A. L. Rangno (1990), Rapid development of high ice particle concentrations in small polar maritime cumuliform clouds, *Journal of the Atmospheric Sciences*, *47*, 2710–2724, doi:10.1175/1520-0469(1990)047⟨2710:RDOHIP⟩2.0.CO;2.

Hobbs, P. V., and A. L. Rangno (1998), Microstructures of low and middle–level clouds over the Beaufort Sea, *Quarterly Journal of the Royal Meteorological Society*, *124*, 2035–2071, doi:10.1002/qj.49712455012.

Hobbs, P. V., J. S. Reid, R. A. Kotchenruther, R. J. Ferek, and R. Weiss (1997), Direct radiative forcing by smoke from biomass burning, *Science*, *275*, 1777–1778, doi:10.1126/science.275.5307.1777.

Hogan, R. J., P. N. Francis, H. Flentje, A. J. Illingworth, M. Quante, and J. Pelon (2003), Characteristics of mixed–phase clouds. I: Lidar, radar and aircraft observations from CLARE'98, *Quarterly Journal of the Royal Meteorological Society*, *129*, 2089–2116, doi: 10.1256/rj.01.208.

Holben, B. N., T. F. Eck, I. Slutsker, D. Tanre, J. P. Buis, A. Setzer, E. Vermote, J. A. Reagan, Y. J. Kaufman, T. Nakajima, F. Lavenu, I. Jankowiak, and A. Smirnov (1998), AERONET–a federated instrument network and data archive for aerosol characterization, *Remote Sensing of Environment*, *66*, 1–16, doi:10.1016/S0034-4257(98)00031-5.

Holben, B. N., D. Tanré, A. Smirnov, T. F. Eck, I. Slutsker, N. Abuhassan, W. W. Newcomb, J. S. Schafer, B. Chatenet, F. Lavenu, Y. J. Kaufman, J. V. Castle, A. Setzer, B. Markham, D. Clark, R. Frouin, R. Halthore, A. Karneli, N. T. O'Neill, C. Pietras, R. T. Pinker, K. Voss, and G. Zibordi (2001), An emerging ground-based aerosol climatology: Aerosol optical depth from AERONET, *Journal of Geophysical Research*, *106*, 12,067–12,098, doi: 10.1029/2001JD900014.

Hoose, C., J. E. Kristjánsson, J. P. Chen, and A. Hazra (2010), A classical–theory–based parameterization of heterogeneous ice nucleation by mineral dust, soot, and biological particles in a global climate model, *Journal of the Atmospheric Sciences*, *67*, 2483–2503, doi:10.1175/2010JAS3425.1.

Hoppel, W. A., J. W. Fitzgerald, G. M. Frick, R. E. Larson, and E. J. Mack (1990), Aerosol size distributions and optical properties found in the marine boundary layer over the Atlantic Ocean, *Journal of Geophysical Research*, *95*, 3659–3686, doi:10.1029/ JD095iD04p03659.

Huebert, B. J., T. Bates, P. B. Russell, G. Shi, Y. J. Kim, K. Kawamura, G. Carmichael, and T. Nakajima (2003), An overview of ACE–Asia: Strategies for quantifying the relationships between Asian aerosols and their climatic impacts, *Journal of Geophysical Research*, *108*, 8633, doi:10.1029/2003JD003550.

Immler, F., and O. Schrems (2003), Vertical profiles, optical and microphysical properties of Saharan dust layers determined by a ship–borne lidar, *Atmospheric Chemistry and Physics*, *3*, 1353–1364, doi:10.5194/acp-3-1353-2003.

Iriondo, M. (2000), Patagonian dust in Antarctica, *Quaternary International*, *68*, 83–86, doi:10.1016/S1040-6182(00)00035-5.

Jin, Z., T. P. Charlock, and K. Rutledge (2002), Analysis of broadband solar radiation and albedo over the ocean surface at COVE, *Journal of Atmospheric and Oceanic Technology*, *19*, 1585–1601, doi:10.1175/1520-0426(2002)019⟨1585:AOBSRA⟩2.0.CO;2.

Jin, Z., T. P. Charlock, W. L. Smith, and K. Rutledge (2004), A parameterization of ocean surface albedo, *Geophysical Research Letters*, *31*, L22301, doi:10.1029/2004GL021180.

Johnson, M. S., N. Meskhidze, V. P. Kiliyanpilakkil, and S. Gassó (2011), Understanding the transport of Patagonian dust and its influence on marine biological activity in the South Atlantic Ocean, *Atmospheric Chemistry and Physics*, *11*, 2487–2502, doi:10.5194/ acp-11-2487-2011.

Kacenelenbogen, M., M. A. Vaughan, J. Redemann, R. M. Hoff, R. R. Rogers, R. A. Ferrare, P. B. Russell, C. A. Hostetler, J. W. Hair, and B. N. Holben (2011), An accuracy assessment of the CALIOP/CALIPSO version 2/version 3 daytime aerosol extinction product based on a detailed multi–sensor, multi–platform case study, *Atmospheric Chemistry and Physics*, *11*, 3981–4000, doi:10.5194/acp-11-3981-2011.

Kalashnikova, O. V., and I. N. Sokolik (2004), Modeling the radiative properties of nonspherical soil–derived mineral aerosols, *Journal of Quantitative Spectroscopy and Radiative Transfer*, *87*, 137–166, doi:10.1016/j.jqsrt.2003.12.026.

Kalisch, J. (2011), Der Einfluss von Wolken auf den Strahlungsantrieb der Erde, Ph.D. thesis, Mathematisch–Naturwissenschaftliche Fakultät der Christian–Albrechts–Universität zu Kiel.

Kalisch, J., and A. Macke (2008), Estimation of the total cloud cover with high temporal resolution and parametrization of short-term fluctuations of sea surface insolation, *Meteorologische Zeitschrift*, *17*, 603–611.

Kanamitsu, M. (1989), Description of the NMC global data assimilation and forecast system, *Weather and Forecasting*, *4*, 335–342, doi:10.1175/1520-0434(1989)004⟨0335:DOTNGD⟩2.0.CO;2.

Kanitz, T., P. Seifert, A. Ansmann, R. Engelmann, D. Althausen, C. Casiccia, and E. G. Rohwer (2011), Contrasting the impact of aerosols at northern and southern midlatitudes on heterogeneous ice formation, *Geophysical Research Letters*, *38*, L17802, doi:10.1029/2011GL048532.

Kato, S., T. P. Ackerman, J. H. Mather, and E. E. Clothiaux (1999), The k–distribution method and correlated–k approximation for a shortwave radiative transfer model, *Journal of Quantitative Spectroscopy and Radiative Transfer*, *62*, 109–121, doi:10.1016/S0022-4073(98)00075-2.

Kaufman, Y., I. Koren, L. Remer, D. Rosenfeld, and Y. Rudich (2005), The effect of smoke, dust, and pollution aerosol on shallow cloud development over the Atlantic Ocean, *Proceedings of the National Academy of Sciences of the United States of America*, *102*, 11207–11212, doi:10.1073/pnas.0505191102.

Kaufman, Y. J., P. V. Hobbs, V. Kirchhoff, P. Artaxo, L. A. Remer, B. N. Holben, M. D. King, D. E. Ward, E. M. Prins, and K. M. Longo (1998), Smoke, Clouds, and Radiation–Brazil (SCAR–B) experiment, *Journal of Geophysical Research*, *103*, 783–808, doi:10.1029/98JD02281.

Keil, A., and J. M. Haywood (2003), Solar radiative forcing by biomass burning aerosol particles during SAFARI 2000: A case study based on measured aerosol and cloud properties, *Journal of Geophysical Research*, *108*, 8467, doi:10.1029/2002JD002315.

Kiehl, J. T., and B. P. Briegleb (1993), The relative roles of sulfate aerosols and greenhouse gases in climate forcing, *Science*, *260*, 311–314, doi:10.1126/science.260.5106.311.

Kiliyanpilakkil, V. P., and N. Meskhidze (2011), Deriving the effect of wind speed on clean marine aerosol optical properties using the A–Train satellites, *Atmospheric Chemistry and Physics*, *11*, 11401–11413, doi:10.5194/acp-11-11401-2011.

Kipp & Zonen (2004), Instruction manual CM 21. – Manual version: 0904. Kipp & Zonen B.V., Delftechpark 36, 2628 Delft, Niederlande.

Kirchstetter, T. W., and T. L. Thatcher (2012), Contribution of organic carbon to wood smoke particulate matter absorption of solar radiation, *Atmospheric Chemistry and Physics Discussions*, *12*, 5803–5816, doi:10.5194/acpd-12-5803-2012.

Kleta, H. (2010), Launch of 1000 ships: A look at voluntary observing ships (vos) scheme, *Meterological Technology International*, 80–81.

Klett, J. D. (1981), Stable analytical inversion solution for processing lidar returns, *Applied Optics*, *20*, 211–220, doi:10.1364/AO.20.000211.

Knippertz, P., and M. C. Todd (2012), Mineral dust aerosols over the Sahara: Meteorological controls on emission and transport and implications for modeling, *Review of Geophysics*, *50*, RG1007, doi:10.1029/2011RG000362.

Knobelspiesse, K. D., C. Pietras, G. S. Fargion, M. Wang, R. Frouin, M. A. Miller, A. Subramaniam, and W. M. Balch (2004), Maritime aerosol optical thickness measured by handheld sun photometers, *Remote Sensing of Environment*, *93*, 87–106, doi:10.1016/j.rse.2004.06.018.

Kok, J. F. (2011), Does the size distribution of mineral dust aerosols depend on the wind speed at emission?, *Atmospheric Chemistry and Physics*, *11*, 10,149–10,156, doi:10.5194/acp-11-10149-2011.

Koop, T., B. Luo, A. Tsias, and T. Peter (2000), Water activity as the determinant for homogeneous ice nucleation in aqueous solutions, *Nature*, *406*, 611–614, doi:10.1038/35020537.

Korolev, A. V., G. A. Isaac, S. G. Cober, J. W. Strapp, and J. Hallett (2003), Microphysical characterization of mixed–phase clouds, *Quarterly Journal of the Royal Meteorological Society*, *129*, 39–65, doi:10.1256/qj.01.204.

Körtzinger, A. (Ed.) (2011), The expedition of the research vessel "Polarstern" to the Antarctic in 2010 (ANT–XXVI/4), in *Reports on polar and marine research*, vol. 631, Alfred Wegener Institute for Polar and Marine Research..

Kraus, H. (2004), *Die Atmosphäre der Erde*, 108 pp., 305 pp., Springer, Berlin, Germany.

Kylling, A. (1992), Radiation transport in cloudy and aerosol loaded atmospheres, Ph.D. thesis, Alaska University, Fairbanks.

Labraga, J. (1994), Extreme winds in the Pampa del Castillo Plateau, Patagonia, Argentina, with reference to wind farm settlement, *Journal of Applied Meteorology*, *33*, 85–95, doi:10.1175/1520-0450(1994)033⟨0085:EWITPD⟩2.0.CO;2.

Lana, A., T. G. Bell, R. Simó, S. M. Vallina, J. Ballabrera-Poy, A. J. Kettle, J. Dachs, L. Bopp, E. S. Saltzman, J. Stefels, J. E. Johnson, and P. S. Liss (2011), An updated climatology of surface dimethlysulfide concentrations and emission fluxes in the global ocean, *Global Biogeochemical Cycles*, *25*, GB1004, doi:10.1029/2010GB003850.

Lance, S., M. D. Shupe, G. Feingold, C. A. Brock, J. Cozic, J. S. Holloway, R. H. Moore, A. Nenes, J. P. Schwarz, J. R. Spackman, K. D. Froyd, D. M. Murphy, J. Brioude, O. R. Cooper, A. Stohl, and J. F. Burkhart (2011), Cloud condensation nuclei as a modulator of ice processes in Arctic mixed–phase clouds, *Atmospheric Chemistry and Physics*, *11*, 8003–8015, doi:10.5194/acp-11-8003-2011.

Lathem, T. L., P. Kumar, A. Nenes, J. Dufek, I. N. Sokolik, M. Trail, and A. Russell (2011), Hygroscopic properties of volcanic ash, *Geophysical Research Letters*, *381*, L11802, doi:10.1029/2011GL047298.

Lebo, Z. J., N. C. Johnson, and J. Y. Harrington (2008)), Radiative influences on ice crystal and droplet growth within mixed–phase stratus clouds, *Journal of Geophysical Research*, *113*, D09203, doi:10.1029/2007JD009262.

Levin, Z., and S. A. Yankofsky (1983), Contact versus immersion freezing of freely suspended droplets by bacterial ice nuclei., *Journal of Applied Meteorology*, *22*, 1964–1966, doi:10.1175/1520-0450(1983)022⟨1964:CVIFOF⟩2.0.CO;2.

Levy, R. C., L. A. Remer, D. Tanré, Y. J. Kaufman, C. Ichoku, B. N. Holben, J. M. Livingston, P. B. Russell, and H. Maring (2003), Evaluation of the Moderate–Resolution Imaging Spectroradiometer (MODIS) retrievals of dust aerosol over the ocean during PRIDE, *Journal of Geophysical Research*, *108*, 8594, doi:10.1029/2002JD002460.

Li, F., P. Ginoux, and V. Ramaswamy (2010), Transport of Patagonian dust to Antarctica, *Journal of Geophysical Research*, *115*, D18217, doi:10.1029/2009JD012356.

Li, J., J. Scinocca, M. Lazare, N. McFarlane, K. von Salzen, and L. Solheim (2006), Ocean surface albedo and its impact on radiation balance in climate models, *Journal of Climate*, *19*, 6314–6333, doi:10.1175/JCLI3973.1.

Liao, H., and J. H. Seinfeld (1998a), Effect of clouds on direct aerosol radiative forcing of climate, *Journal of Geophysical Research*, *103*, 3781–3788, doi:10.1029/97JD03455.

Liao, H., and J. H. Seinfeld (1998b), Radiative forcing by mineral dust aerosols: sensitivity to key variables, *Journal of Geophysical Research*, *103*, 31,637–31,646, doi:10.1029/1998JD200036.

Linke, F., and F. Baur (1970), *Meteorologisches Taschenbuch II*, 712 pp., Akademische Verlagsgesellschaft Geest and Portig, Leipzig, Germany.

Liou, K.-N., and H. Lahore (1974), Laser sensing of cloud composition: A backscattered depolarization technique, *Journal of Applied Meteorology*, *13*, 257–263, doi:10.1175/1520-0450(1974)013⟨0257:LSOCCA⟩2.0.CO;2.

Liou, K. N., and S. C. Ou (1989), The role of cloud microphysical processes in climate: An assessment from a one–dimensional perspective, *Journal of Geophysical Research*, *94*, 8599–8607, doi:10.1029/JD094iD06p08599.

Liou, K. N., and R. M. Schotland (1971), Multiple backscattering and depolarization from water clouds for a pulsed lidar system, *Journal of the Atmospheric Sciences*, *28*, 772–784, doi:10.1175/1520-0469(1971)028⟨0772:MBADFW⟩2.0.CO;2.

Liu, D., Z. Wang, Z. Liu, D. Winker, and C. Trepte (2008a), A height resolved global view of dust aerosols from the first year CALIPSO lidar measurements, *Journal of Geophysical Research*, *113*, D16214, doi:10.1029/2007JD009776.

Liu, Z., M. A. Vaughan, D. M. Winker, C. A. Hostetler, L. R. Poole, D. Hlavka, W. Hart, and M. McGill (2004), Use of probability distribution functions for discriminating between cloud and aerosol in lidar backscatter data, *Journal of Geophysical Research*, *109*, D15202, doi:10.1029/2004JD004732.

Liu, Z., A. Omar, M. Vaughan, J. Hair, C. Kittaka, Y. Hu, K. Powell, C. Trepte, D. Winker, C. Hostetler, R. Ferrare, and R. Pierce (2008b), CALIPSO lidar observations of the optical properties of Saharan dust: A case study of long-range transport, *Journal of Geophysical Research*, *113*, D07207, doi:10.1029/2007JD008878.

Liu, Z., M. Vaughan, D. Winker, C. Kittaka, B. Getzewich, R. Kuehn, A. Omar, K. Powell, C. Trepte, and C. Hostetler (2009), The CALIPSO lidar cloud and aerosol discrimination: Version 2 algorithm and initial assessment of performance, *Journal of Atmospheric and Oceanic Technology*, *26*, 1198–1213, doi:10.1175/2009JTECHA1229.1.

Liu, Z., R. Kuehn, M. Vaughan, D. Winker, A. Omar, K. Powell, C. Trepte, Y. Hu, and C. Hostetler (2010), The CALIPSO cloud and aerosol discrimination: Version 3 algorithm and test results, in *25th International Laser Radar Conference (ILRC), St. Petersburg, Russia*.

Lohmann, U., and J. Feichter (2005), Global indirect aerosol effects: A review, *Atmospheric Chemistry and Physics*, *5*, 715–737, doi:10.5194/acp-5-715-2005.

Lohmann, U., W. R. Leaitch, L. Barrie, K. Law, Y. Yi, D. Bergmann, C. Bridgeman, M. Chin, J. Christensen, R. Easter, J. Feichter, A. Jeuken, E. Kjellström, D. Koch, C. Land, P. Rasch, and G. J. Roelofs (2001), Vertical distributions of sulfur species simulated by large scale atmospheric models in COSAM: Comparison with observations, *Tellus Series B*, *53*, 646–672, doi:10.1034/j.1600-0889.2001.530508.x.

Lorenz, L. (1890), Lysbevaegelsen i og uden for en af plane lysbolger belyst kulge vidensk, *Selsk. Skr*, *6*, 1–62.

Lundheim, R. (2002), Physiological and ecological significance of biological ice nucleators, *Philosophical Transactions of the Royal Society of London. Series B: Biological Sciences*, *357*, 937–943, doi:10.1098/rstb.2002.1082.

Macke, A., J. Kalisch, Y. Zoll, and K. Bumke (2010), Radiative effects of the cloudy atmosphere from ground and satellite based observations, *EPJ Web of Conferences*, *9*, 83–94, doi:10.1051/epjconf/201009006.

Mallet, M., V. Pont, C. Liousse, L. Gomes, J. Pelon, S. Osborne, J. Haywood, J. C. Roger, P. Dubuisson, A. Mariscal, V. Thouret, and P. Goloub (2008), Aerosol direct radiative forcing over Djougou (northern Benin) during the African Monsoon Multidisciplinary Analysis dry season experiment (Special Observation Period-0), *Journal of Geophysical Research*, *113*, D00C01, doi:10.1029/2007JD009419.

Mattis, I., D. Müller, A. Ansmann, U. Wandinger, J. Preißler, P. Seifert, and M. Tesche (2008), Ten years of multiwavelength Raman lidar observations of free–tropospheric aerosol layers over central Europe: Geometrical properties and annual cycle, *Journal of Geophysical Research*, *113*, D009636, doi:10.1029/2007JD009636.

Mattis, I., M. Tesche, M. Grein, V. Freudenthaler, and D. Müller (2009), Systematic error of lidar profiles caused by a polarization–dependent receiver transmission: quantification and error correction scheme, *Applied Optics*, *48*, 2742–2751, doi:10.1364/AO.48.002742.

Mattis, I., P. Seifert, D. Müller, M. Tesche, A. Hiebsch, T. Kanitz, J. Schmidt, F. Finger, U. Wandinger, and A. Ansmann (2010), Volcanic aerosol layers observed with multiwavelength Raman lidar over Central Europe in 2008–2009, *Journal of Geophysical Research*, *115*, D00L99, doi:10.1029/2010JD014895.

Mayer, B., and A. Kylling (2005), Technical note: The libRadtran software package for radiative transfer calculations — description and examples of use, *Atmospheric Chemistry and Physics*, *5*, 1855–1877.

McCormick, R. A., and J. H. Ludwig (1967), Climate modification by atmospheric aerosols, *Science*, *156*, 1358–1359, doi:10.1126/science.156.3780.1358.

Mie, G. (1908), Beiträge zur Optik trüber Medien, speziell kolloidaler Metallösungen, *Annalen der Physik*, *330*, 377–445.

Miles, N. L., J. Verlinde, and E. E. Clothiaux (2000), Cloud droplet size distributions in low–level stratiform clouds, *Journal of Atmospheric Sciences*, *57*, 295–311, doi:10.1175/1520-0469(2000)057⟨0295:CDSDIL⟩2.0.CO;2.

Minikin, A., A. Petzold, J. Ström, R. Krejci, M. Seifert, P. van Velthoven, H. Schlager, and U. Schumann (2003), Aircraft observations of the upper tropospheric fine particle aerosol in the Northern and Southern Hemispheres at midlatitudes, *Geophysical Research Letters*, *30*, 1503, doi:10.1029/2002GL016458.

Minschwaner, K., and A. E. Dessler (2004), Water vapor feedback in the tropical upper troposphere: Model results and observations, *Journal of Climate*, *17*, 1272–1282, doi:10.1175/1520-0442(2004)017⟨1272:WVFITT⟩2.0.CO;2.

Möhler, O., A. Nink, H. Saathoff, S. Schaefers, M. Schnaiter, W. Schock, and U. Schurath (2001), The Karlsruhe aerosol chamber facility AIDA: Technical description and first

results of homogeneous and heterogeneous ice nucleation experiments, *Cern European Organization for Nuclear Research–Reports–Cern*, *7*, 163–168.

Möhler, O., S. Büttner, C. Linke, M. Schnaiter, H. Saathoff, O. Stetzer, R. Wagner, M. Krämer, A. Mangold, V. Ebert, et al. (2005), Effect of sulfuric acid coating on heterogeneous ice nucleation by soot aerosol particles, *Journal of Geophysical Research*, *110*, D11210, doi:10.1029/2004JD005169.

Möhler, O., S. Benz, H. Saathoff, M. Schnaiter, R. Wagner, J. Schneider, S. Walter, V. Ebert, and S. Wagner (2008a), The effect of organic coating on the heterogeneous ice nucleation efficiency of mineral dust aerosols, *Environmental Research Letters*, *3*, 025007, doi:10.1088/1748-9326/3/2/025007.

Möhler, O., D. G. Georgakopoulos, C. E. Morris, S. Benz, V. Ebert, S. Hunsmann, H. Saathoff, M. Schnaiter, and R. Wagner (2008b), Heterogeneous ice nucleation activity of bacteria: New laboratory experiments at simulated cloud conditions, *Biogeosciences*, *5*, 1425–1435, doi:10.5194/bg-5-1425-2008.

Morys, M., F. M. Mims III, S. Hagerup, S. E. Anderson, A. Baker, J. Kia, and T. Walkup (2001), Design, calibration, and performance of MICROTOPS II handheld ozone monitor and Sun photometer, *Journal of Geophysical Research*, *106*, 573–582, doi:0148-0227/01/2001JD900103.

Mossop, S. C., A. Ono, and E. R. Wishart (1970), Ice particles in maritime clouds near Tasmania, *Quarterly Journal of the Royal Meteorological Society*, *96*, 487–508, doi:10.1002/qj.49709640910.

Müller, D., U. Wandinger, and A. Ansmann (1999), Microphysical particle parameters from extinction and backscatter lidar data by inversion with regularization: Theory, *Applied Optics*, *38*, 2346–2357, doi:10.1364/AO.38.002346.

Müller, D., I. Mattis, U. Wandinger, A. Ansmann, D. Althausen, O. Dubovik, S. Eckhardt, and A. Stohl (2003), Saharan dust over a central European EARLINET–AERONET site: Combined observations with Raman lidar and Sun photometer, *Journal of Geophysical Research*, *108*, 4345, doi:10.1029/2002JD002918.

Müller, D., I. Mattis, U. Wandinger, A. Ansmann, D. Althausen, and A. Stohl (2005), Raman lidar observations of aged Siberian and Canadian forest fire smoke in the free troposphere over Germany in 2003: Microphysical particle characterization, *Journal of Geophysical Research*, *110*, D17201, doi:10.1029/2004JD005756.

Müller, D., A. Ansmann, I. Mattis, M. Tesche, U. Wandinger, D. Althausen, and G. Pisani (2007), Aerosol–type–dependent lidar ratios observed with Raman lidar, *Journal of Geophysical Research*, *112*, D16202, doi:10.1029/2006JD008292.

Müller, T., A. Schladitz, K. Kandler, and A. Wiedensohler (2011), Spectral particle absorption coefficients, single scattering albedos and imaginary parts of refractive indices from ground based in situ measurements at Cape Verde Island during SAMUM–2, *Tellus Series B*, *63*, 573–588, doi:10.1111/j.1600-0889.2011.00572.x.

Myhre, G., T. K. Berntsen, J. M. Haywood, J. K. Sundet, B. N. Holben, M. Johnsrud, and F. Stordal (2003), Modeling the solar radiative impact of aerosols from biomass burning during the Southern African Regional Science Initiative (SAFARI–2000) experiment, *Journal of Geophysical Research*, *108*, 8501, doi:10.1029/2002JD002313.

Myhre, G., F. Stordal, M. Johnsrud, D. J. Diner, I. V. Geogdzhayev, J. M. Haywood, B. N. Holben, T. Holzer-Popp, A. Ignatov, R. A. Kahn, Y. J. Kaufman, N. Loeb, J. V. Martonchik, M. I. Mishchenko, N. R. Nalli, L. A. Remer, M. Schroedter-Homscheidt, D. Tanré, O. Torres, and M. Wang (2005), Intercomparison of satellite retrieved aerosol optical depth over ocean during the period September 1997 to December 2000, *Atmospheric Chemistry and Physics*, *5*, 1697–1719, doi:10.5194/acp-5-1697-2005.

Nakajima, T., S.-C. Yoon, V. Ramanathan, G.-Y. Shi, T. Takemura, A. Higurashi, T. Takamura, K. Aoki, B.-J. Sohn, S.-W. Kim, H. Tsuruta, N. Sugimoto, A. Shimizu, H. Tanimoto, Y. Sawa, N.-H. Lin, C.-T. Lee, D. Goto, and N. Schutgens (2007), Overview of the Atmospheric Brown Cloud East Asian Regional Experiment 2005 and a study of the aerosol direct radiative forcing in east Asia, *Journal of Geophysical Research*, *112*, D24S91, doi:10.1029/2007JD009009.

Nickovic, S., G. Kallos, A. Papadopoulos, and O. Kakaliagou (2001), A model for prediction of desert dust cycle in the atmosphere, *Journal of Geophysical Research*, *106*, 18,113–18,130, doi:10.1029/2000JD900794.

Niedermeier, D., S. Hartmann, R. A. Shaw, D. Covert, T. F. Mentel, J. Schneider, L. Poulain, P. Reitz, C. Spindler, and T. Clauss (2010), Heterogeneous freezing of droplets with immersed mineral dust particles—measurements and parameterization, *Atmospheric Chemistry and Physics*, *10*, 3601–3614, doi:10.5194/acp-10-3601-2010.

Niedermeier, D., R. A. Shaw, S. Hartmann, H. Wex, T. Clauss, J. Voigtländer, and F. Stratmann (2011), Heterogeneous ice nucleation: exploring the transition from stochastic to singular freezing behavior, *Atmospheric Chemistry and Physics*, *11*, 8767–8775, doi:10.5194/acp-11-8767-2011.

Nowottnick, E., P. Colarco, A. da Silva, D. Hlavka, and M. McGill (2011), The fate of Saharan dust across the Atlantic and implications for a central American dust barrier, *Atmospheric Chemistry and Physics*, *11*, 8415–8431, doi:10.5194/acp-11-8415-2011.

O'Dowd, C. D., and G. de Leeuw (2007), Marine aerosol production: a review of the current knowledge, *Royal Society of London Philosophical Transactions Series A*, *365*, 1753–1774, doi:10.1098/rsta.2007.2043.

Omar, A. H., D. M. Winker, C. Kittaka, M. A. Vaughan, Z. Liu, Y. Hu, C. R. Trepte, R. R. Rogers, R. A. Ferrare, K. P. Lee, R. E. Kuehn, and C. A. Hostetler (2009), The CALIPSO automated aerosol classification and lidar ratio selection algorithm, *Journal of Atmospheric and Oceanic Technology*, *26*, 1994–2014, doi:10.1175/2009JTECHA1231.1.

Otto, S., E. Bierwirth, B. Weinzierl, K. Kandler, M. Esselborn, M. Tesche, A. Schladitz, M. Wendisch, and T. Trautmann (2009), Solar radiative effects of a Saharan dust plume

observed during SAMUM assuming spheroidal model particles, *Tellus Series B*, *61*, 270–296, doi:10.1111/j.1600-0889.2008.00389.x.

Pappalardo, G., U. Wandinger, L. Mona, A. Hiebsch, I. Mattis, A. Amodeo, A. Ansmann, P. Seifert, H. Linné, A. Apituley, L. Alados Arboledas, D. Balis, A. Chaikovsky, G. D'Amico, F. De Tomasi, V. Freudenthaler, E. Giannakaki, A. Giunta, I. Grigorov, M. Iarlori, F. Madonna, R.-E. Mamouri, L. Nasti, A. Papayannis, A. Pietruczuk, M. Pujadas, V. Rizi, F. Rocadenbosch, F. Russo, F. Schnell, N. Spinelli, X. Wang, and M. Wiegner (2010), EARLINET correlative measurements for CALIPSO: First intercomparison results, *Journal of Geophysical Research*, *115*, D00H19, doi:10.1029/2009JD012147.

Peppler, W. (1940), Unterkühlte Wasserwolken und Eiswolken, *Forschung und Erfahrung - Reichsamt für Wetterdienst*, *Band 1*, 3–68.

Petersen, G. N. (2010), A short meteorological overview of the Eyjafjallajökull eruption 14 April–23 May 2010, *Weather*, *65*, 203–207, doi:10.1002/wea.634.

Petersen, W., M. Petschatnikov, F. Schroeder, and F. Colijn (2003), Ferrybox systems for monitoring coastal waters, *Elsevier Oceanography Series*, *69*, 325–333, doi:10.1016/S0422-9894(03)80052-1.

Philbrick, C. R., D. B. Lysak, T. D. Stevens, P. A. T. Haris, and Y. C. Rau (1992), Atmospheric measurements using the LAMP lidar during the LADIMAS campaign, in *16 th International Laser Radar Conference*, Cambridge, Massachusetts, USA.

Podgorny, I. A., and V. Ramanathan (2001), A modeling study of the direct effect of aerosols over the tropical Indian Ocean, *Journal of Geophysical Research*, *106*, 24097–24106, doi:10.1029/2001JD900214.

Porter, J. N., M. Miller, C. Pietras, and C. Motell (2001), Ship–based Sun photometer measurements using Microtops Sun photometers, *Journal of Atmospheric and Oceanic Technology*, *18*, 765–774, doi:10.1175/1520-0426(2001)018⟨0765:SBSPMU⟩2.0.CO;2.

Powell, K., M. Vaughan, D. Winker, K. P. Lee, M. Pitts, C. Trepte, P. Detweiler, W. Hunt, J. Lambeth, P. Lucker, T. Murray, O. Hagolle, A. Lifermann, M. Faivre, A. Garnier, and J. Pelon (2011), Cloud–Aerosol Lidar Infrared Pathfinder Satellite Observations data management system, data products catalog release 3.3 document no: Pc-sci-503, *Tech. rep.*, National Aeronautics and Space Administration, Langley Research Center, Hampton, Virginia 23681–2199.

Pratt, K. A., P. J. DeMott, J. R. French, Z. Wang, D. L. Westphal, A. J. Heymsfield, C. H. Twohy, A. Prenni, and K. Prather (2009), In situ detection of biological particles in cloud ice–crystals, *Nature Geoscience*, *2*, 398–401, doi:10.1038/ngeo521.

Prenni, A. J., M. D. Petters, S. M. Kreidenweis, C. L. Heald, S. T. Martin, P. Artaxo, R. M. Garland, A. G. Wollny, and U. Pöschl (2009), Relative roles of biogenic emissions and Saharan dust as ice nuclei in the Amazon basin, *Nature Geoscience*, *2*, 402–405, doi:10.1038/ngeo517.

Prospero, J. M., and T. N. Carlson (1972), Vertical and areal distribution of Saharan dust over the western equatorial North Atlantic Ocean, *Journal of Geophysical Research*, *77*, 5255–5265, doi:10.1029/JC077i027p05255.

Prospero, J. M., P. Ginoux, O. Torres, S. E. Nicholson, and T. E. Gill (2002), Environmental characterization of global sources of atmospheric soil dust identified with the NIMBUS 7 Total Ozone Mapping Specrometer (TOMS) absorbing aerosol product, *Reviews of Geophysics*, *40*, 1002, doi:10.1029/2000RG000095.

Pruppacher, H. R., and J. D. Klett (1997), *Microphysics of clouds and precipitation*, 954 pp., Springer.

Quijano, A. L., I. N. Sokolik, and O. B. Toon (2000), Radiative heating rates and direct radiative forcing by mineral dust in cloudy atmospheric conditions, *Journal of Geophysical Research*, *105*, 12,207–12,220, doi:10.1029/2000JD900047.

Ramanathan, V., R. D. Cess, E. F. Harrison, P. Minnis, B. R. Barkstrom, E. Ahmad, and D. Hartmann (1989), Cloud–radiative forcing and climate: Results from the Earth Radiation Budget Experiment, *Science*, *243*, 57–63, doi:10.1126/science.243.4887.57.

Ramanathan, V., P. J. Crutzen, J. Lelieveld, A. P. Mitra, D. Althausen, J. Anderson, M. O. Andreae, W. Cantrell, G. R. Cass, C. E. Chung, A. D. Clarke, J. A. Coakley, W. D. Collins, W. C. Conant, F. Dulac, J. Heintzenberg, A. J. Heymsfield, B. Holben, S. Howell, J. Hudson, A. Jayaraman, J. T. Kiehl, T. N. Krishnamurti, D. Lubin, G. McFarquhar, T. Novakov, J. A. Ogren, I. A. Podgorny, K. Prather, K. Priestley, J. M. Prospero, P. K. Quinn, K. Rajeev, P. Rasch, S. Rupert, R. Sadourny, S. K. Satheesh, G. E. Shaw, P. Sheridan, and F. P. J. Valero (2001), Indian Ocean experiment: An integrated analysis of the climate forcing and effects of the great Indo–Asian haze, *Journal of Geophysical Research*, *106*, 28,371–28,398, doi:10.1029/2001JD900133.

Ramanathan, V., F. Li, M. V. Ramana, P. S. Praveen, D. Kim, C. E. Corrigan, H. Nguyen, E. A. Stone, J. J. Schauer, G. R. Carmichael, B. Adhikary, and S. C. Yoon (2007), Atmospheric brown clouds: Hemispherical and regional variations in long-range transport, absorption, and radiative forcing, *Journal of Geophysical Research*, *112*, D22S21, doi:10.1029/2006JD008124.

Rangno, A. L., and P. V. Hobbs (2001), Ice particles in stratiform clouds in the Arctic and possible mechanisms for the production of high ice concentrations, *Journal of Geophysical Research*, *106*, 15,065–15,076, doi:10.1029/2000JD900286.

Rauber, R. M., and A. Tokay (1991), An explanation for the existence of supercooled water at the top of cold clouds, *Journal of the Atmospheric Sciences*, *48*, 1005–1023, doi:10.1175/1520-0469(1991)048⟨1005:AEFTEO⟩2.0.CO;2.

Rayleigh, L. (1871), On the scattering of light by small particles, *Philosophical Magazine*, *41*, 447–454.

Redemann, J., R. P. Turco, K. N. Liou, P. V. Hobbs, W. S. Hartley, R. W. Bergstrom, E. V. Browell, and P. B. Russell (2000), Case studies of the vertical structure of the direct

shortwave aerosol radiative forcing during TARFOX, *Journal of Geophysical Research*, *105*, 9971–9980, doi:10.1029/1999JD901042.

Redemann, J., M. A. Vaughan, Q. Zhang, Y. Shinozuka, P. B. Russell, J. M. Livingston, M. Kacenelenbogen, and L. A. Remer (2011), The comparison of MODIS–Aqua (C5) and CALIOP (V2, V3) aerosol optical depth, *Atmospheric Chemistry and Physics*, *112*, 22,987–23,027, doi:10.5194/acpd-11-22987-2011.

Reid, J. S., E. M. Prins, D. L. Westphal, C. C. Schmidt, K. A. Richardson, S. A. Christopher, T. F. Eck, E. A. Reid, C. A. Curtis, and J. P. Hoffman (2004), Real–time monitoring of South American smoke particle emissions and transport using a coupled remote sensing/box–model approach, *Geophysical Research Letters*, *31*, L06107, doi: 10.1029/2003GL018845.

Remer, L. A., R. G. Kleidman, R. C. Levy, Y. J. Kaufman, D. Tanré, S. Mattoo, J. V. Martins, C. Ichoku, I. Koren, H. Yu, and B. N. Holben (2008), Global aerosol climatology from the MODIS satellite sensors, *Journal of Geophysical Research*, *113*, D14S07, doi: 10.1029/2007JD009661.

Rose, T., S. Crewell, U. Löhnert, and C. Simmer (2005), A network suitable microwave radiometer for operational monitoring of the cloudy atmosphere, *Atmospheric Research*, *75*, 183–200, doi:10.1016/j.atmosres.2004.12.005.

Russell, P. B., and J. Heintzenberg (2000), An overview of the ACE–2 clear sky column closure experiment, *Tellus Series B*, *52*, 463–483, doi:10.1034/j.1600-0889.2000.00013.x.

Russell, P. B., S. A. Kinne, and R. W. Bergstrom (1997), Aerosol climate effects: Local radiative forcing and column closure experiments, *Journal of Geophysical Research*, *102*, 9397–9408, doi:10.1029/97JD00112.

Russell, P. B., P. V. Hobbs, and L. L. Stowe (1999), Aerosol properties and radiative effects in the United States East Coast haze plume: An overview of the Tropospheric Aerosol Radiative Forcing Observational Experiment (TARFOX), *Journal of Geophysical Research*, *104*, 2213–2222, doi:10.1029/1998JD200028.

Rutledge, S. A., and P. V. Hobbs (1983), The mesoscale and microscale structure and organization of clouds and precipitation in midlatitude cyclones: A model for the seeder–feeder process in warm–frontal rainbands, *Journal of the Atmospheric Sciences*, *40*, 1185–1206, doi:10.1175/1520-0469(1983)040⟨1185:TMAMSA⟩2.0.CO;2.

Sasano, Y., E. V. Browell, and S. Ismail (1985), Error caused by using a constant extinction/backscattering ratio in the lidar solution, *Applied Optics*, *24*, 3929–3932, doi: 10.1364/AO.24.003929.

Sassen, K. (2002), Indirect climate forcing over the western US from Asian dust storms, *Geophysical Research Letters*, *29*, 1465, doi:10.1029/2001GL014051.

Sassen, K. (2005), Polarization lidar, in *Lidar: Range–resolved optical remote sensing of the atmosphere*, C. Weitkamp (ed.), pp. 19–40, Springer.

Sassen, K. (2005), Meteorology: Dusty ice clouds over Alaska, *Nature*, *434*, 456, doi:10.1038/434456a.

Sassen, K., and R. L. Petrilla (1986), Lidar depolarization from multiple scattering in marine stratus clouds, *Applied Optics*, *25*, 1450–1459, doi:10.1364/AO.25.001450.

Sassen, K., M. K. Griffin, and G. C. Dodd (1989), Optical scattering and microphysical properties of subvisual cirrus clouds, and climatic implications, *Journal of Applied Meteorology*, *28*, 91–98, doi:10.1175/1520-0450(1989)028⟨0091:OSAMPO⟩2.0.CO;2.

Sassen, K., P. J. DeMott, J. M. Prospero, and M. R. Poelot (2003), Saharan dust storms and indirect aerosol effects on clouds: CRYSTAL–FACE results, *Geophysical Research Letters*, *30*, 1633, doi:10.1029/2003GL017371.

Schepanski, K., I. Tegen, B. Laurent, B. Heinold, and A. Macke (2007), A new Saharan dust source activation frequency map derived from MSG-SEVIRI IR-channels, *Geophysical Research Letters*, *341*, L18803, doi:10.1029/2007GL030168.

Schmetz, J., P. Pili, S. Tjemkes, D. Just, J. Kerkmann, S. Rota, and A. Ratier (2002), An introduction to Meteosat Second Generation (MSG), *Bulletin of the American Meteorological Society*, *83*, 977–992, doi:10.1175/1520-0477(2002)083⟨0977:AITMSG⟩2.3.CO;2.

Schmid, B., D. A. Hegg, J. Wang, D. Bates, J. Redemann, P. B. Russell, J. M. Livingston, H. H. Jonsson, E. J. Welton, J. H. Seinfeld, R. C. Flagan, D. S. Covert, O. Dubovik, and A. Jefferson (2003), Column closure studies of lower tropospheric aerosol and water vapor during ACE–Asia using airborne Sun photometer and airborne in situ and ship–based lidar measurements, *Journal of Geophysical Research*, *108*, 8656, doi:10.1029/2002JD003361.

Schneider, C., M. Glaser, R. Kilian, A. Santana, N. Butorovic, and G. Casassa (2003), Weather observations across the southern Andes at 53° S, *Physical Geography*, *24*, 97–119.

Schotland, R. M., K. Sassen, and R. Stone (1971), Observations by lidar of linear depolarization ratios for hydrometeors, *Journal of Applied Meteorology*, *10*, 1011–1017, doi:10.1175/1520-0450(1971)010⟨1011:OBLOLD⟩2.0.CO;2.

Schulz, M., C. Textor, S. Kinne, Y. Balkanski, S. Bauer, T. Berntsen, T. Berglen, O. Boucher, F. Dentener, S. Guibert, I. S. A. Isaksen, T. Iversen, D. Koch, A. Kirkevåg, X. Liu, V. Montanaro, G. Myhre, J. E. Penner, G. Pitari, S. Reddy, Ø. Seland, P. Stier, and T. Takemura (2006), Radiative forcing by aerosols as derived from the AeroCom present–day and pre–industrial simulations, *Atmospheric Chemistry and Physics*, *6*, 5225–5246.

Schumann, U., B. Weinzierl, O. Reitebuch, H. Schlager, A. Minikin, C. Forster, R. Baumann, T. Sailer, K. Graf, H. Mannstein, C. Voigt, S. Rahm, R. Simmet, M. Scheibe, M. Lichtenstern, P. Stock, H. Rüba, D. Schäuble, A. Tafferner, M. Rautenhaus, T. Gerz, H. Ziereis, M. Krautstrunk, C. Mallaun, J.-F. Gayet, K. Lieke, K. Kandler, M. Ebert, S. Weinbruch, A. Stohl, J. Gasteiger, S. Groß, V. Freudenthaler, M. Wiegner, A. Ansmann, M. Tesche, H. Olafsson, and K. Sturm (2011), Airborne observations of the Eyjafjalla volcano ash cloud over Europe during air space closure in April and May 2010, *Atmospheric Chemistry and Physics*, *11*, 2245–2279, doi:10.5194/acp-11-2245-2011.

Schuster, G. L., M. Vaughan, D. MacDonnell, W. Su, D. Winker, O. Dubovik, T. Lapyonok, and C. Trepte (2012), Comparison of CALIPSO aerosol optical depth retrievals to AERONET measurements, and a climatology for the lidar ratio of dust, *Atmospheric Chemistry and Physics Discussions*, *12*, 11641–11697, doi:10.5194/acpd-12-11641-2012.

Seifert, P. (2010), Dust-related ice formation in the troposphere – A statistical analysis based on 11 years of lidar observations of aerosols and clouds over Leipzig, Ph.D. thesis, Faculty of Physics and Geoscience, University of Leipzig.

Seifert, P., A. Ansmann, D. Müller, U. Wandinger, D. Althausen, A. J. Heymsfield, S. T. Massie, and C. Schmitt (2007), Cirrus optical properties observed with lidar, radiosonde, and satellite over the tropical Indian Ocean during the aerosol-polluted northeast and clean maritime southwest monsoon, *Journal of Geophysical Research*, *112*, D17205, doi: 10.1029/2006JD008352.

Seifert, P., A. Ansmann, I. Mattis, U. Wandinger, M. Tesche, R. Engelmann, D. Müller, C. Pérez, and K. Haustein (2010), Saharan dust and heterogeneous ice formation: Eleven years of cloud observations at a central European EARLINET site, *Journal of Geophysical Research*, *115*, D20201, doi:10.1029/2009JD013222.

Seifert, P., A. Ansmann, S. Groß, V. Freudenthaler, B. Heinold, A. Hiebsch, J. Schmidt, F. Schnell, M. Tesche, U. Wandinger, I. Mattis, and M. Wiegner (2011), Ice formation in ash–influenced clouds after the eruption of the Eyjafjallajökull volcano in April 2010, *Journal of Geophysical Research*, *116*, D00U04, doi:10.1029/2011JD015702.

Shettle, E. P., and R. W. Fenn (1979), Models for the aerosols of the lower atmosphere and the effects of humidity variations on their optical properties (1979), Air Force Geophysics Laboratory Report No. AFGL-TR-79-0214, Hanscom AFB, Massachusetts.

Smirnov, A., B. N. Holben, Y. J. Kaufman, O. Dubovik, T. F. Eck, I. Slutsker, C. Pietras, and R. N. Halthore (2002), Optical properties of atmospheric aerosol in maritime environments, *Journal of the Atmospheric Sciences*, *59*, 501–523, doi:10.1175/1520-0469(2002)059⟨0501:OPOAAI⟩2.0.CO;2.

Smirnov, A., B. N. Holben, I. Slutsker, D. M. Giles, C. R. McClain, T. F. Eck, S. M. Sakerin, A. Macke, P. Croot, G. Zibordi, P. K. Quinn, J. Sciare, S. Kinne, M. Harvey, T. J. Smyth, S. Piketh, T. Zielinski, A. Proshutinsky, J. I. Goes, N. B. Nelson, P. Larouche, V. F. Radionov, P. Goloub, K. Krishna Moorthy, R. Matarrese, E. J. Robertson, and F. Jourdin (2009), Maritime Aerosol Network as a component of Aerosol Robotic Network, *Journal of Geophysical Research*, *114*, D06204, doi:10.1029/2008JD011257.

Smirnov, A., B. N. Holben, D. M. Giles, I. Slutsker, N. T. O'Neill, T. F. Eck, A. Macke, P. Croot, Y. Courcoux, S. M. Sakerin, T. J. Smyth, T. Zielinski, G. Zibordi, J. I. Goes, M. J. Harvey, P. K. Quinn, N. B. Nelson, V. F. Radionov, C. M. Duarte, R. Losno, J. Sciare, K. J. Voss, S. Kinne, N. R. Nalli, E. Joseph, K. Krishna Moorthy, D. S. Covert, S. K. Gulev, G. Milinevsky, P. Larouche, S. Belanger, E. Horne, M. Chin, L. A. Remer, R. A. Kahn, J. S. Reid, M. Schulz, C. L. Heald, J. Zhang, K. Lapina, R. G. Kleidman, J. Griesfeller, B. J. Gaitley, Q. Tan, and T. L. Diehl (2011), Maritime Aerosol Network

as a component of AERONET — first results and comparison with global aerosol models and satellite retrievals, *Atmospheric Measurement Techniques*, *4*, 583–597, doi:10.5194/amt-4-583-2011.

Sokolik, I. N., and O. B. Toon (1999), Incorporation of mineralogical composition into models of the radiative properties of mineral aerosol from UV to IR wavelengths, *Journal of Geophysical Research*, *104*, 9423–9444, doi:10.1029/1998JD200048.

Sokolik, I. N., D. M. Winker, G. Bergametti, D. A. Gillette, G. Carmichael, Y. J. Kaufman, L. Gomes, L. Schuetz, and J. E. Penner (2001), Introduction to special section: Outstanding problems in quantifying the radiative impacts of mineral dust, *Journal of Geophysical Research*, *106*, 18,015–18,028, doi:10.1029/2000JD900498.

Song, N., and D. Lamb (1994), Experimental investigations of ice in supercooled clouds. part 1: System description and growth of ice by vapor deposition, *Jounral of the Atmospheric Sciences*, *51*, 91–103, doi:10.1175/1520-0469(1994)051⟨0091:EIOIIS⟩2.0.CO;2.

Spinhirne, J. D., J. A. R. Rall, and V. S. Scott (1995), Compact eye safe lidar systems, *Review of Laser Engineering–Laser Society of Japan*, *23*, 26–132.

Stamnes, K., S.-C. Tsay, K. Jayaweera, and W. Wiscombe (1988), Numerically stable algorithm for discrete–ordinate–method radiative transfer in multiple scattering and emitting layered media, *Atmospheric Optics*, *27*, 2502–2509, doi:10.1364/AO.27.002502.

Steinke, I., O. Möhler, A. Kiselev, M. Niemand, H. Saathoff, M. Schnaiter, J. Skrotzki, C. Hoose, and T. Leisner (2011), Ice nucleation properties of fine ash particles from the Eyjafjallajökull eruption in April 2010, *Atmospheric Chemistry and Physics*, *111*, 17665–17698, doi:10.5194/acpd-11-17665-2011.

Stevens, B., and G. Feingold (2009), Untangling aerosol effects on clouds and precipitation in a buffered system, *Nature*, *461*, 607–613, doi:10.1038/nature08281.

Stevens, T. D., P. A. T. Haris, Y.-C. Rau, and C. R. Philbrick (1994), Latitudinal lidar mapping of stratospheric particle layers, *Advances in Space Research*, *14*, 193–198, doi:10.1016/0273-1177(94)90136-8.

Stith, J. L., C. H. Twohy, P. J. DeMott, D. Baumgardner, T. Campos, R. Gao, and J. Anderson (2011), Observations of ice nuclei and heterogeneous freezing in a Western Pacific extratropical storm, *Atmospheric Chemistry and Physics*, *11*, 6229–6243, doi:10.5194/acp-11-6229-2011.

Stohl, A., C. Forster, A. Frank, P. Seibert, and G. Wotawa (2005), Technical note: The Lagrangian particle dispersion model FLEXPART version 6.2, *Atmospheric Chemistry and Physics*, *5*, 2461–2474, doi:10.5194/acp-5-2461-2005.

Stratmann, F., A. Kiselev, S. Wurzler, M. Wendisch, J. Heintzenberg, R. J. Charlson, K. Diehl, H. Wex, and S. Schmidt (2004), Laboratory studies and numerical simulations of cloud droplet formation under realistic supersaturation conditions, *Journal of Atmospheric and Oceanic Technology*, *21*, 876–887, doi:10.1175/1520-0426(2004)021⟨0876:LSANSO⟩2.0.CO;2.

Sugimoto, N., I. Matsui, Z. Liu, A. Shimizu, I. Tamamushi, and K. Asai (2000), Observation of aerosols and clouds using a two–wavelength polarization lidar during the Nauru99 experiment, *Sea and Sky*, *76*, 90–95.

Sugimoto, N., I. Matsui, Z. Liu, A. Shimizu, K. Asai, K. Yoneyama, and M. Katsumata (2001), Latitudinal distribution of aerosols and clouds in the western Pacific observed with a lidar on board the research vessel Mirai, *Geophysical Research Letters*, *28*, 4187–4190, doi:10.1029/2001GL013510.

Sun, Z., and K. P. Shine (1995), Parameterization of ice cloud radiative properties and its application to the potential climatic importance of mixed–phase clouds., *Journal of Climate*, *8*, 1874–1888, doi:10.1175/1520-0442(1995)008⟨1874:POICRP⟩2.0.CO;2.

Swap, R., M. Garstang, S. A. Macko, P. D. Tyson, W. Maenhaut, P. Artaxo, P. Kallberg, and R. Talbot (1996), The long–range transport of southern African aerosols to the tropical South Atlantic, *Journal of Geophysical Research*, *101*, 23,777–23,792, doi:10.1029/95JD01049.

Swap, R. J., H. J. Annegarn, J. T. Suttles, M. D. King, S. Platnick, J. L. Privette, and R. J. Scholes (2003), Africa burning: A thematic analysis of the Southern African Regional Science Initiative (SAFARI 2000), *Journal of Geophysical Research*, *108*, 8465, doi:10.1029/2003JD003747.

Tegen, I., and A. A. Lacis (1996), Modeling of particle size distribution and its influence on the radiative properties of mineral dust aerosol, *Journal of Geophysical Research*, *101*, 19,237-19,244, doi:10.1029/95JD03610.

Tegen, I., E. Bierwirth, B. Heinold, J. Helmert, and M. Wendisch (2010), Effect of measured surface albedo on modeled Saharan dust solar radiative forcing, *Journal of Geophysical Research*, *115*, D24312, doi:10.1029/2009JD013764.

Tesche, M. (2011), Vertical profiling of aerosol optical properties with multiwavelength aerosol lidar during the Saharan Mineral Dust Experiments, Ph.D. thesis, Faculty of Physics and Geoscience, University of Leipzig.

Tesche, M., A. Ansmann, D. Müller, D. Althausen, R. Engelmann, V. Freudenthaler, and S. Groß (2009), Vertically resolved separation of dust and smoke over Cape Verde using multiwavelength Raman and polarization lidars during Saharan Mineral Dust Experiment 2008, *Journal of Geophysical Research*, *114*, D13202, doi:10.1029/2009JD011862.

Tesche, M., A. Ansmann, D. Müller, D. Althausen, I. Mattis, B. Heese, V. Freudenthaler, M. Wiegner, M. Esselborn, G. Pisani, and P. Knippertz (2009), Vertical profiling of Saharan dust with Raman lidars and airborne HSRL in southern Morocco during SAMUM, *Tellus Series B*, *61*, 144–164, doi:10.1111/j.1600-0889.

Tesche, M., S. Gross, A. Ansmann, D. Müller, D. Althausen, V. Freudenthaler, and M. Esselborn (2011), Profiling of Saharan dust and biomass-burning smoke with multiwavelength polarization Raman lidar at Cape Verde, *Tellus Series B*, *63*, 649–676, doi:10.1111/j.1600-0889.2011.00548.x.

Tesfaye, M., V. Sivakumar, J. Botai, and G. Mengistu Tsidu (2011), Aerosol climatology over South Africa based on 10 years of Multiangle Imaging Spectroradiometer (MISR) data, *Journal of Geophysical Research*, *116*, D20216, doi:10.1029/2011JD016023.

Textor, C., M. Schulz, S. Guibert, S. Kinne, Y. Balkanski, S. Bauer, T. Berntsen, T. Berglen, O. Boucher, M. Chin, F. Dentener, T. Diehl, R. Easter, H. Feichter, D. Fillmore, S. Ghan, P. Ginoux, S. Gong, A. Grini, J. Hendricks, L. Horowitz, P. Huang, I. Isaksen, I. Iversen, S. Kloster, D. Koch, A. Kirkevåg, J. E. Kristjansson, M. Krol, A. Lauer, J. F. Lamarque, X. Liu, V. Montanaro, G. Myhre, J. Penner, G. Pitari, S. Reddy, Ø. Seland, P. Stier, T. Takemura, and X. Tie (2006), Analysis and quantification of the diversities of aerosol life cycles within AeroCom, *Atmospheric Chemistry and Physics*, *6*, 1777–1813, doi:10.5194/acp-6-1777-2006.

Torge, A., A. Macke, B. Heinold, and J. Wauer (2011), Solar radiative transfer simulations in Saharan dust plumes: particle shapes and 3–D effect, *Tellus Series B*, *63*, 770–780, doi:10.1111/j.1600-0889.2011.00560.x.

Torres, O., P. K. Bhartia, J. R. Herman, Z. Ahmad, and J. Gleason (1998), Derivation of aerosol properties from satellite measurements of backscattered ultraviolet radiation: Theoretical basis, *Journal of Geophysical Research*, *1031*, 17,099–17,110, doi:10.1029/98JD00900.

Trenberth, K. E., J. T. Fasullo, and J. Kiehl (2009), Earth's global energy budget, *Bulletin of the American Meteorological Society*, *90*, 311–323, doi:10.1175/2008BAMS2634.1.

Uno, I., K. Eguchi, K. Yumimoto, Z. Liu, Y. Hara, N. Sugimoto, A. Shimizu, and T. Takemura (2011), Large Asian dust layers continuously reached North America in April 2010, *Atmospheric Chemistry and Physics*, *111*, 12251–12268, doi:10.5194/acpd-11-12251-2011.

Vardiman, L. (1978), The generation of secondary ice particles in clouds by crystal-crystal collision, *Journal of the Atmospheric Sciences*, *35*, 2168–2180, doi:10.1175/1520-0469(1978)035⟨2168:TGOSIP⟩2.0.CO;2.

Vortisch, H., B. Krämer, I. Weidinger, L. Wöste, T. Leisner, M. Schwell, H. Baumgärtel, and E. Rühl (2000), Homogeneous freezing nucleation rates and crystallization dynamics of single levitated sulfuric acid solution droplets, *Physical Chemistry Chemical Physics*, *2*, 1407–1413, doi:10.1039/A908225E.

Wagner, F., D. Müller, and A. Ansmann (2001), Comparison of the radiative impact of aerosols derived from vertically resolved (lidar) and vertically integrated (Sun photometer) measurements: Example of an Indian aerosol plume, *Journal of Geophysical Research*, *106*, 22,861–22,870, doi:10.1029/2001JD000320.

Wandinger, U. (1998), Multiple–scattering influence on extinction- and backscatter–coefficient measurements with Raman and high–spectral–resolution lidars, *Applied Optics*, *37*, 417–427, doi:10.1364/AO.37.000417.

Wandinger, U. (2005a), Introduction to lidar, in *Lidar - Range–resolved optical remote sensing of the atmosphere*, C. Weitkamp (ed.), pp. 1—18, Springer Science + Business Media Inc.

Wandinger, U. (2005b), Raman lidar, in *Lidar - Range–resolved optical remote sensing of the atmosphere*, C. Weitkamp (ed.), pp. 241–267, Springer Science + Business Media Inc.

Wandinger, U., and A. Ansmann (2002), Experimental determination of the lidar overlap profile with Raman lidar, *Applied Optics*, *41*, 511–514, doi:10.1364/AO.41.000511.

Wandinger, U., M. Tesche, P. Seifert, A. Ansmann, D. Müller, and D. Althausen (2010), Size matters: Influence of multiple–scattering on CALIPSO light–extinction profiling in desert dust, *Geophysical Research Letters*, *37*, L10801, doi:10.1029/2010GL042815.

Warner, T. T. (2004), *Desert Meteorology*, 79–126, Cambridge University Press, New York, USA.

Welton, E. J., K. J. Voss, H. R. Gordon, H. Maring, A. Smirnov, B. Holben, B. Schmid, J. M. Livingston, P. B. Russell, and P. A. Durkee (2000), Ground–based lidar measurements of aerosols during ACE–2: Instrument description, results, and comparisons with other ground–based and airborne measurements, *Tellus B*, *52*, 636–651, doi:10.1034/j.1600-0889.2000.00025.x.

Welton, E. J., K. J. Voss, P. K. Quinn, P. J. Flatau, K. Markowicz, J. R. Campbell, J. D. Spinhirne, H. R. Gordon, and J. E. Johnson (2002), Measurements of aerosol vertical profiles and optical properties during INDOEX 1999 using micropulse lidars, *Journal of Geophysical Research*, *107*, 8019, doi:10.1029/2000JD000038.

Wendisch, M., S. Mertes, A. Ruggaber, and T. Nakajima (1996), Vertical profiles of aerosol and radiation and the influence of a temperature inversion: Measurements and radiative transfer calculations, *Journal of Applied Meteorology*, *35*, 1703–1715, doi:10.1175/1520-0450(1996)035⟨1703:VPOAAR⟩2.0.CO;2.

Westbrook, C. D., A. J. Illingworth, E. J. O'Connor, and R. J. Hogan (2010), Doppler lidar measurements of oriented planar ice crystals falling from supercooled and glaciated layer clouds, *Quarterly Journal of the Royal Meteorological Society*, *136*, 260–276, doi:10.1002/qj.528.

Wilcox, E. M. (2011), Direct and semi-direct radiative forcing of smoke aerosols over clouds, *Atmospheric Chemistry and Physics*, *11*, 20947–20972, doi:10.5194/acpd-11-20947-2011.

Winker, D. M., W. H. Hunt, and M. J. McGill (2007), Initial performance assessment of CALIOP, *Geophysical Research Letters*, *341*, L19803, doi:10.1029/2007GL030135.

Winker, D. M., M. A. Vaughan, A. Omar, Y. Hu, K. A. Powell, Z. Liu, W. H. Hunt, and S. A. Young (2009), Overview of the CALIPSO mission and CALIOP data processing algorithms, *Journal of Atmospheric and Oceanic Technology*, *26*, 2310–2323, doi:10.1175/2009JTECHA1281.1.

Wiscombe, W. J., and G. W. Grams (1976), The backscattered fraction in two–stream approximations, *Journal of the Atmospheric Sciences*, *33*, 2440–2451, doi:10.1175/1520-0469(1976)033⟨2440:TBFITS⟩2.0.CO;2.

Wulfmeyer, V., and T. Janji (2005), Twenty–four–hour observations of the marine boundary layer using shipborne NOAA high–resolution Doppler lidar, *Journal of Applied Meteorology*, *44*, 1723–1744, doi:10.1175/JAM2296.1.

Young, S. A., and M. A. Vaughan (2009), The retrieval of profiles of particulate extinction from Cloud–Aerosol Lidar Infrared Pathfinder Satellite Observations (CALIPSO) data: Algorithm description, *Journal of Atmospheric and Oceanic Technology*, *26*, 1105–1119, doi:10.1175/2008JTECHA1221.1.

Yu, H., Y. Kaufman, M. Chin, G. Feingold, L. Remer, T. Anderson, Y. Balkanski, N. Bellouin, O. Boucher, and S. Christopher (2006), A review of measurement–based assessments of the aerosol direct radiative effect and forcing, *Atmospheric Chemistry and Physics*, *6*, 613–666, doi:10.5194/acp-6-613-2006.

Yu, H., M. Chin, D. M. Winker, A. H. Omar, Z. Liu, C. Kittaka, and T. Diehl (2010), Global view of aerosol vertical distributions from CALIPSO lidar measurements and GOCART simulations: Regional and seasonal variations, *Journal of Geophysical Research*, *115*, D00H30, doi:10.1029/2009JD013364.

Zhou, M., H. Yu, R. E. Dickinson, O. Dubovik, and B. N. Holben (2005), A normalized description of the direct effect of key aerosol types on solar radiation as estimated from Aerosol Robotic Network aerosols and Moderate Resolution Imaging Spectroradiometer albedos, *Journal of Geophysical Research*, *110*, D19202, doi:10.1029/2005JD005909.

Zobrist, B., C. Marcolli, T. Peter, and T. Koop (2008), Heterogeneous ice nucleation in aqueous solutions: the role of water activity, *The Journal of Physical Chemistry A*, *112*, 3965–3975, doi:10.1021/jp7112208.

List of Figures

List of Tables

List of Symbols

Symbol	Description	Unit
$\parallel$	parallel–polarized component of a quantity	
$\perp$	cross–polarized component of a quantity	
c	channel measuring cross–polarized component of a quantity	
t	channel measuring the total of a quantity	
$\downarrow$	downward–directed orientation of a quantity	
$\uparrow$	upward–directed orientation of a quantity	
Greek Symbol		
α^{mol}	molecular extinction coefficient	m^{-1}
α^{par}	particle extinction coefficient	m^{-1}
β^{*}	attenuated backscatter coefficient	$m^{-1}\,sr^{-1}$
β^{mol}	molecular backscatter coefficient	$m^{-1}\,sr^{-1}$
β^{par}	particle backscatter coefficient	$m^{-1}\,sr^{-1}$
β_{Ra}	particle backscatter coefficient	$m^{-1}\,sr^{-1}$
δ^{mol}	molecular depolarization ratio	
δ^{par}	particle depolarization ratio	
δ^{vol}	volume depolarization ratio	
η	system efficiency	
θ	zenith angle	
λ	wavelength	m
λ_0	emitted wavelength	m
λ_{Ra}	wavelength of Raman–scattered light	m
π	constant value	
ρ	density	$kg\,m^{-3}$
σ	standard deviation	
τ	transmission	
Ω	solid angle	sr

Latin Symbol		
A	surface area	m^2
$\mathring{A}$	Ångström exponent	
$\mathring{A}_\alpha$	extinction–related Ångström exponent	
$\mathring{A}_\beta$	backscatter–related Ångström exponent	
$\mathring{A}_S$	lidar–ratio–related Ångström exponent	
C	system and geometric constant	W m^3 sr
C_{tc}	ratio of efficiencies	
D	transmission ratio	
d	diameter	m
E_λ	energy	J
f	likelihood	
F	irradiance (flux density)	W m^{-2}
g	asymmetry parameter	
H	height	m
I_λ	radiance (intensity)	W m^{-2} sr^{-1}
J_λ	source function of radiance	W m^{-2} sr^{-1}
K	King factor	sr
k_λ	mass extinction cross section	m^2 kg^{-1}
n	number of cases	
N	number concentration	m^{-3}
N_{Ra}	number concentration of inelastically scattering molecules	m^{-3}
O	overlap function	
P	lidar signal/detected energy	W
P_0	emitted laser energy	W
R	range	m
R_0	reference height	m
r	range	m
r_S	radius of a scattering object	m
RH	relative humidity	%
s	distance	m
S^{mol}	molecular lidar ratio	sr
S^{par}	particle lidar ratio	sr
S_C	solar constant	W m^{-2}
T	temperature	K
t	time	s

List of Abbreviations

ACE–1	Southern Hemisphere Marine Aerosol Characterization Experiment
ACE–2	North Atlantic Regional Aerosol Characterization Experiment 2
ACE–Asia	Asian Pacific Regional Aerosol Characterization Experiment
ABC	Atmospheric Brown Cloud East Asian Regional Experiment 2005
AERONET	Aerosol Robotic Network
AEROSOL99	Atlantic AEROSOL experiment 1999
AIDA	Aerosol Interactions and Dynamics in the Atmosphere cloud chamber
ALPACA	Aerosol Lidar observations at Punta Arenas in the framework of a Chilean German cooperation
ANT	Antarctic cruise
AOT	Aerosol Optical Thickness
asl	above sea level
AVHRR	Advanced Very High Resolution Radiometer
AWI	Alfred Wegener Institute
BRDF	Bidirectional Reflectance Distribution Function
CAD	Cloud–Aerosol Discrimination
CALIOP	Cloud–Aerosol Lidar with Orthogonal Polarisation
CALIPSO	Cloud–Aerosol Lidar and Infrared Pathfinder Satellite Observations
CCN	Cloud Condensation Nuclei
CG4	Kipp and Zonen Pyrgeometer
CM21	Kipp and Zonen Pyranometer
Det	Detector
DISORT	Discrete ordinate solver
DMS	Dimethyl Sulfate
DREAM	Dust Regional Atmospheric Model
DWD	Deutscher Wetterdienst (German Meteorological Service)
EARLINET	European Aerosol Research Lidar Network
EARLI09	EARLINET Reference Lidar Intercomparison 2009
EQ	equator
FCF	Feature–Classification–Flag
FST	Feature Subtype
FT	Feature Type
FLEXPART	Flexible Langrangian Particle Dispersion Model

GALION	GAW Aerosol Lidar Observation Network
GDAS	Global data assimilation system
GEOMAR	Helmholtz Centre for Ocean Research Kiel (former IFM–Geomar, *Leibniz–Institut für Meereswissenschaften an der Universität Kiel* (German for 'Leibniz Institute for Marine Research at the University Kiel')
GFS	Global Forecast System
GOPHER	Leipzig Stellenbosch cooperation close to the Hottentotten nature reserve
H	High–pressure
HATPRO	Humidity and Temperature Profiler
HERA	Hybrid Extinction Retrieval Algorithm
HYSPLIT	Hybrid Single–Particle Lagrangian Integrated Trajectory
i. e.	that is
IfT	*Leibniz–Institut für Troposphärenforschung* (German for 'Leibniz Institute for Tropospheric Research')
IGBP	International Geosphere–Biosphere Programme
IN	Ice Nuclei
INDOEX	Indian Ocean Experiment
ISO	International Organization for Standardization
IPCC	Intergovernmental Panel on Climate Change
KAMASUTRA	Kerguelen Aerosol Measurement from African Sources and plUmes Trajectory Reverse Analysis
L	Low–pressure
LACIS	Leipzig Aerosol Cloud Interaction Simulator
LADIMAS	Latitudinal Distribution and Middle Atmospheric Structure
LAMP	Lidar Atmospheric Measurements Program
laser	Light Amplification by Stimulated Emission of Radiation
libRadtran	library Radiative transfer
LWC	Liquid Water Content
LWP	Liquid Water Path
MAN	Maritime Aerosol Network
MARL	Mobile Aerosol Raman lidar
MBL	Marine Boundary Layer
METEK	Meteorologische Messtechnik GmbH (Meteorological measurement technic)
MISR	Multiangle Imaging Spectroradiometer
MODIS	Moderate Resolution Imaging Spectroradiometer
MPL	Micropulse lidar
MSG	Meteosat Second Generation
NASA	National Aeronautics and Space Administration
Nd:YAG	Neodymium–doped yttrium aluminum garnet
OCEANET	OCEANET project
PMT	Photomultiplier
RFOV	Receiver field of view
RV	Research vessel

SAMUM–1	Saharan Mineral Dust Experiment, Morocco, 2007
SAMUM–2	Saharan Mineral Dust Experiment, Cape Verde, 2008
SAFARI	Southern African Fire–Atmosphere Research Initiative
SAFARI 2000	Southern African Fire–Atmosphere Research Initiative 2000
SCAWS	Scalable automatic weather station
SeaWifis	Sea–viewing Wide field–of–view sensor
SHADE	Saharan Dust Experiment
SHG	Second Harmonic Generator
SSA	Single Scattering Albedo
SST	Sea Surface Temperature
SUR	Surface
SZA	Solar Zenith Angle
TARFOX	Tropospheric Aerosol Radiative Forcing Observational Experiment
Tel	Telescope
THG	Third Harmonic Generator
TOA	Top of Atmosphere
TOMS	Total Ozone Mapping Spectrometer
U. S., USA	United States of America
UTC	Universal time coordinated
UV	Ultra Violet

Acknowledgements

Writing the last words of this thesis makes me thinking about the recent period of my life, the cruises, the people, and the thesis itself. At the very beginning, I have to say, I am more than grateful that I became a victim of the self–appointed inquisitor Albert Ansmann. He is a steam engine in atmospheric science. His incredible accumulated knowledge and his persistent enthusiasm on new findings were motivation and drive for this thesis, and will stay forever an inspiring example for myself.

I thank Andreas Macke and Dietrich Althausen, who took me aboard their OCEANET project, which offered me the opportunity to write this thesis, as well as to fall in love with an old lady called Polarstern. Pictures, smells, food, and pictures again, which will never escape from my head. Steffen, Timo, Bjorn, Thomas, Michael, Harald, Chuck, John, Anna, Yann, Lisa, Henry, Amphitrite, and Karl... thanks for the scientific work between 50° N and 50° S. I thank Dietrich Althausen also for his support in my ideas to place our lidar Polly^{XT} at Punta Arenas and Stellenbosch. Each installation and problem solution of my diva Polly^{XT} was supported by Ronny Engelmann, one of my older brothers at IfT. I thank him for every email and skype response between Leipzig, the Atlantic, and especially South America 24/7. His experience helped me also during the construction of the OCEANET–Atmosphere facility. My second older brother was Patric Seifert. He gave me a good start in Leipzig, and introduced me to his scientific field of the heterogeneous ice formation. Patrics educational and scientific skills pushed me in the cloud data analysis. Thus, he was the initiator of my first publication and one of the main topics of my thesis. I also appreciate his and Ulla Wandinger's intensive proof reading of my thesis.

In addition, I want to thank the Hattrick–gamblers Matze and Holger, who showed me the different methods to analyze lidar data. The perfect style of Matze's figures were always a motivation to improve my own figures. However, there can be only one!

I am thankful for the support of additional data by Timo, John, Bernhard, Yann, the teams of CALIOP, MAN, AERONET, MODIS, GDAS, and the AWI. No measurements in Punta Arenas and Stellenbosch were possible without Ingolf, Johan, Ulli, Erich, Claudio, Ismael, Sonja, and Joaquin. In Leipzig I enjoyed the working atmosphere in the wild jungle (room 213) a lot.

I was infected by the lidar–virus by my diploma advisor Markus Pesch. The fever gained in Boulder during my first ILRC in 2008. Still the green beam of a lidar has a magic effect on me. When the night closes in and the beam becomes visible, I am fascinated to imagine what is happening with one light pulse like the first day.